

NASA Contractor Report 3746 •

**Linear and Nonlinear Interpretation
of the Direct Strike Lightning
Response of the NASA F106B
Thunderstorm Research Aircraft**

T. H. Rudolph and R. A. Perala

**CONTRACT NAS1-16984
DECEMBER 1983**



**25th Anniversary
1958-1983**

NASA

NASA Contractor Report 3746

Linear and Nonlinear Interpretation of the Direct Strike Lightning Response of the NASA F106B Thunderstorm Research Aircraft

T. H. Rudolph and R. A. Perala
Electro Magnetic Applications, Inc.
Denver, Colorado

Prepared for
Langley Research Center
under Contract NAS1-16984



National Aeronautics
and Space Administration

**Scientific and Technical
Information Branch**

1983

TABLE OF CONTENTS

CHAPTER	TITLE	PAGE
1	INTRODUCTION	1
	1.0 Background	1
	1.1 Summary	2
2	REVIEW OF INFLIGHT DIRECT STRIKE DATA	3
	2.0 Background	3
	2.1 Fourier Transform of Recorded Data	3
	2.2 Correlated 1982 Data and the Problem of Uniqueness	13
3	NONLINEAR AIR BREAKDOWN MODELING AND RESULTS	24
	3.0 Background	24
	3.1 Channel Modeling	24
	3.2 Data Interpretation Based on a Single Measurement	26
	3.3 Time Correlated Data Analysis	56
	3.4 Time Varying Channels	67
4	NONLINEAR MODELING AND RESULTS	69
	4.0 Introduction	69
	4.1 Basics of the Nonlinear Model	70
	4.2 Streamers in the Finite Difference Code	74
	4.3 Electron Avalanche Around a Streamer Tip	75
	4.4 Streamer Motion	77
	4.5 Two Dimensional Results	78
	4.6 Application of the Three Dimensional Finite Difference Code	81
	4.7 Parameter Study	82
	4.8 Application of the Nonlinear Model to the F106B Aircraft	110
5.	DISCUSSION AND RECOMMENDATIONS	143
	5.0 Data Interpretation State of the Art	143
	5.1 Recommendations for Future Test Programs	144
	REFERENCES	146
APPENDIX A	Comparison of Experimental and Numerical Results for the Interaction of a Scale Model Aircraft with a Simulated Lightning Channel	147
APPENDIX B	Fourier Transform Technique	153

LIST OF FIGURES

FIGURE	TITLE	PAGE
2.1	81-042 R1B	4
2.2	81-043 R1B	4
2.3	81-043 R2B	4
2.4	81-043 R3B	4
2.5	81-043-R4B	5
2.6	82-037 R4B	5
2.7	82-037 R4D	5
2.8	82-038 R2B	5
2.9	82-038 R2D	6
2.10	82-038 R4B	6
2.11	82-038 R4D	6
2.12	82-038 R7B	6
2.13	82-038 R7D	7
2.14	82-038 R8B	7
2.15	82-038 R8D	7
2.16	82-039 R2B	7
2.17	82-039 R2D	8
2.18	Rectangular Pulse and Isosceles Triangle Transform Pairs	11
2.19	RR for 82-037 R4	15
2.20	RR for 82-038 R2	15
2.21	RR for 82-038 R4	15
2.22	RR for 82-038 R7	15
2.23	RR for 82-038 R8	16
2.24	RR for 82-039 R2	16
2.25	Linearly Computed RR for Nose Entry, Tail Tip Exit	20
2.26	Linearly Computed RR for Nose Entry, and No Exit	20
2.27	RR for Nonlinear Attachment to Leading Edge of Left Wing, I = -100 A	21
2.28	RR for Nonlinear Attachment to Leading Edge of Left Wing, I = +100 A	21
2.29	RR for Nonlinear Attachment to Nose, I = -100 A	21
2.30	RR for Attachment to Leading Edge of Right Wing, I = + 100 A	21
2.31	RR for Nonlinear Attachment to Right Side of Tail, I = -100 A	22
3.1	Standard Current Waveform Used in Lightning Channel Impedance Study	28
3.2	Forward D-dot Response of F106 to Standard Current Pulse of Figure 3.1	29
3.3	Fourier Transform of Standard Current Shape Shown in Figure 3.1	30
3.4	Fourier Transform of D-dot Response of Figure 3.2	31
3.5	Source Independent Transfer Function Derived as Explained in the Text	32
3.6	D-dot Response of Flight 80-018	33

LIST OF FIGURES (cont'd)

FIGURE	TITLE	PAGE
3.7	Fourier Transform of D-dot Response of Flight 80-018	34
3.8	Fourier Transform of Current Source Needed to Give Forward D-dot Response of Flight 80-018	35
3.9	Time Domain Representation of Current Source Needed to Give Forward D-dot Response of Flight 80-018 (to 500 ns)	36
3.10	Time Domain Representation of Current Source Needed to Give Forward D-dot Response of Flight 80-018 (to 25 μ sec)	37
3.11	Forward D-dot Response of F106 to Current Source of Figure 3.9	38
3.12	Actual Injected Current at Nose of F106 to Obtain D-dot Response of Figure 3.11	39
3.13	Current at the Position of the Injection Point for the Case in Which the F106 Was Not Present	41
3.14	Actual Injected Current at Nose of F106 to Obtain D-dot Response of Figure 3.12 (to 6 μ s)	42
3.15	Current at the Position of the Injection Point for the Case in Which the F106 Was not Present (to 6 μ s)	43
3.16	Current Injected Into F106 ($L_\ell = 3.33 \times 10^{-7}$ h/m, $C_\ell = 3.33 \times 10^{-11}$ f/m, $R_\ell = 0$ Ω /m)	44
3.17	Current at Injection Point Without F106 ($L_\ell = 3.33 \times 10^{-7}$ h/m, $C_\ell = 3.33 \times 10^{-11}$ f/m, $R_\ell = 0$ Ω /m)	45
3.18	Current Injected Into F106 ($L_\ell = 3.33 \times 10^{-7}$ h/m, $C_\ell = 3.33 \times 10^{-11}$ f/m, $R_\ell = 0$ Ω /m, Exit Channel a Perfectly Conducting Wire)	46
3.19	Current at Injection Point Without F106 ($L_\ell = 3.33 \times 10^{-7}$ h/m, $C_\ell = 3.33 \times 10^{-11}$ f/m, $R_\ell = 0$ Ω /m, Exit Channel a Perfectly Conducting Wire)	47
3.20	Current Injected Into F106 ($L_\ell = 1.67 \times 10^{-7}$ h/m, $C_\ell = 6.67 \times 10^{-11}$ f/m, $R_\ell = 50$ Ω /m, Exit Channel a Perfectly Conducting Wire)	48
3.21	Current at Injection Point Without F106 ($L_\ell = 1.67 \times 10^{-7}$ h/m, $C_\ell = 6.67 \times 10^{-11}$ f/m, $R_\ell = 50$ Ω /m, Exit Channel a Perfectly Conducting Wire)	49
3.22	Current Injected Into F106 ($L_\ell = 5 \times 10^{-7}$ h/m, $C_\ell = 2 \times 10^{-10}$ f/m, $R_\ell = 50$ Ω /m, Exit Channel a Perfectly Conducting Wire)	50

LIST OF FIGURES (cont'd)

FIGURE	TITLE	PAGE
3.23	Current at Injection Point Without F106 ($L_\ell = 5 \times 10^{-7}$ h/m, $C_\ell = 2 \times 10^{-10}$ f/m, $R_\ell = 50 \Omega/\text{m}$, Exit Channel a Perfectly Conducting Wire)	51
3.24	Current Injected Into F106 ($L_\ell = 1.67 \times 10^{-7}$ h/m, $C_\ell = 6.67 \times 10^{-11}$ f/m, $R_\ell = 0 \Omega/\text{m}$, Exit Channel is Perfectly Conducting Wire)	52
3.25	Current at Injection Point Without F106 ($L_\ell = 1.67 \times 10^{-7}$ h/m, $C_\ell = 6.67 \times 10^{-11}$ f/m, $R_\ell = 0 \Omega/\text{m}$, Exit Channel a Perfectly Conducting Wire)	53
3.26	Current Injected Into F106 ($L_\ell = 5 \times 10^{-7}$ h/m, $C_\ell = 2 \times 10^{-10}$ f/m, $R_\ell = 0 \Omega/\text{m}$, Exit Channel a Perfectly Conducting Wire)	54
3.27	Current at Injection Point Without F106 ($L_\ell = 5 \times 10^{-7}$ h/m, $C_\ell = 2 \times 10^{-10}$ f/m, $R_\ell = 0 \Omega/\text{m}$, Exit Channel a Perfectly Conducting Wire)	55
3.28	D-dot Response of Flight 82-039	57
3.29	B-dot Response of Flight 82-039	58
3.30	Injected Current for Calculated D-dot Source	59
3.31	Time Derivative of Injected Current for D-dot Source	60
3.32	Calculated D-dot Response for D-dot Source	61
3.33	Calculated B-dot Response for D-dot Source	62
3.34	Injected Current for B-dot Source	63
3.35	Time Derivative of Injected Current for B-dot Source	64
3.36	Calculated B-dot Response for B-dot Source	65
3.37	Calculated D-dot Response for B-dot Source	66
3.38	Forward D-dot Response for the Case in Which the Exit Channel has a Temporally Varying Resistance per Unit Length	68
4.1	Streamer Tip Geometry	75
4.2	Rod-Plane Gap Geometry of Collins & Meek [7]	78
4.3	Measured Electric Fields for Experiment of Collins & Meek [7]	79
4.4	Comparison of Experimental Data of Collins and Meek [7] With the Prediction of the Nonlinear Computer Code	80
4.5	Predicted Electric Fields for the Case of a Negatively Charged Rod	81
4.6	Nonlinear Response of Bar for Positive Charge, 0% Water Content, .5 Relative Air Density	84
4.7	Nonlinear Response of Bar for Positive Charge, 0% Water Content, 1 Relative Air Density	87

LIST OF FIGURES (cont'd)

FIGURE	TITLE	PAGE
4.8	Nonlinear Response of Bar for Positive Charge, 6% Water Content, 1 Relative Air Density	90
4.9	Nonlinear Response of Bar for Positive Charge, 6% Water Content, .5 Relative Air Density	93
4.10	Nonlinear Response of Bar for Negative Charge, 0% Water Content, .5 Relative Air Density	96
4.11	Nonlinear Response of Bar for Negative Charge, 0% Water Content, 1 Relative Air Density	99
4.12	Nonlinear Response of Bar for Negative Charge, 6% Water Content, 1 Relative Air Density	102
4.13	Nonlinear Response of Bar for Negative Charge, 6% Water Content, .5 Relative Air Density	105
4.14	Geometry of Breakdown Process on the Finite Difference Code	108
4.15	F106 Model Showing Nonlinear Attachment Points and Sensor Points	112
4.16	Illustration of Finite Difference Cell Containing Charge Located Directly in Front of Aircraft Nose	113
4.17	Nonlinear Response of F106B for Positive Charge and Nose Attachment	115
4.18	Nonlinear Response of F106B for Negative Charge and Nose Attachment	118
4.19	Nonlinear Response of F106B for Positive Charge and Tail Attachment	121
4.20	Nonlinear Response of F106B for Negative Charge and Tail Attachment	124
4.21	Nonlinear Response of F106B for Positive Charge and Left Wing Attachment	127
4.22	Nonlinear Response of F106B for Negative Charge and Left Wing Attachment	130
4.23	Nonlinear Response of F106B for Positive Charge and Right Wing Attachment	133
4.24	Nonlinear Response of F106B for Negative Charge and Right Wing Attachment	136
4.25	Measured D-dot of Flight 82-039	140
4.26	Measured B-dot of Flgith 82-039	141

LIST OF TABLES

TABLE	TITLE	PAGE
2.1	1981 B Data Summary for Direct Strikes	9
2.2	1982 B and D Data Summary for Direct Strikes	10
2.3	Summary of Peaks for Response Ratios	17
2.4	Low Frequency Response Ratios for Selected 1982 Simultaneous Data	19
4.1	Air Chemistry Coefficient Formulas	72

CHAPTER 1

INTRODUCTION

1.0 Background

The NASA Langley Research Center is engaged in obtaining in-flight nearby and direct strike lightning data on an instrumented F-106B thunderstorm research aircraft. The aircraft is equipped with sensors which measure surface electric fields, surface magnetic fields, and current on the pitot boom with a data system incorporating a transient digitizer. The objective of this research is to characterize the lightning environment in such a way that it is applicable to other aircraft as well. The aircraft has encountered numerous direct lightning strikes during the summers of 1980, 1981, and 1982, and has likewise recorded numerous electromagnetic transient waveforms.

In order to derive the lightning environment from these measurements, the effects of the aircraft have to be removed from the data to yield the environment which would be there without the aircraft present. The objective of the research discussed in this report is to develop a methodology to determine this environment and to apply it to the existing data. This research is a continuation of a previous effort reported in [1], in which an initial data interpretation approach was developed. This reference provides much of the background for the results presented here. This includes a discussion of the three dimensional finite difference technique used to model the electromagnetic response of the F-106B, preliminary work in nonlinear analysis, and an initial interpretation methodology development.

The following general research areas are discussed in this report:

1. Review of 1981 and 1982 Data (Chapter 2)
2. Interpretation Methodology Development (Chapter 3).
3. Nonlinear Air Breakdown Modelling (Chapter 4).
4. Model Validation Studies (Appendix A).

Item 4 above was published as a conference paper and is included in Appendix A as such. Finally, a discussion of the overall results and suggestions for improving the test program are given in Chapter 5.

1.1 Summary

The emphasis in this research has been the development of methodologies and tools which can be applied to the data interpretation problem. One of these tools is a linear approach for obtaining the lightning channel current in the absence of the aircraft as a function of various channel parameters. When applied to only one measurement point, however, the result is not unique. Initial attempts to obtain a unique answer from correlated 1982 measurements met with limited success, indicating that the proper channel parameters were not included.

The concept of finding ratios of Fourier transforms of simultaneous responses was introduced with the objective of overcoming the problem concerning uniqueness. Although this concept needs to be further developed and applied, initial results are encouraging.

It should be emphasized that it is not certain that linear analysis is sufficient to properly understand the in-flight data. With this in mind, a nonlinear air breakdown model based on first principles, was developed and applied. The results indicate that it is entirely possible that most of the data obtained thus far can be interpreted as the nonlinear attachment of a leader channel to the aircraft.

Future efforts will concentrate on application of these tools to the measured data, and further exploitation of simultaneous measurements taken in 1982.

CHAPTER 2

REVIEW OF INFLIGHT DIRECT STRIKE DATA

2.0 Background

In this chapter, a review of direct strike inflight data from 1981 and selected data from 1982 is given. This includes Fourier transform analysis to identify resonances and nulls. Simultaneous data from 1982 is discussed along with its usefulness in helping to solve the problem of uniqueness in data interpretation.

2.1 Fourier Transforms of Recorded Data

Fourier transforms are presented for data gathered both during 1981 and 1982. Transforms are presented in a log-linear format in Figures 2.1 - 2.17. The vertical axis is dB, where $\text{dB} = 20 \log_{10} |F(\omega)|$, where $F(\omega)$ is the Fourier transform expressed in MKS units of $\dot{B}(t)$ or $\dot{D}(t)$, as appropriate. The Fourier transforms were calculated using the algorithm described in Appendix B. The horizontal scale is in frequency from zero to 30 MHz. Although the measured data has a useful bandwidth up to 50 MHz, which was used for the analysis done in Chapter 3, it was decided to present the data here with a smaller bandwidth and on a linear scale because it was found that this provided the best resolution of the aircraft resonances.

In the interest of brevity, the time domain data is not presented here. The 1981 data can be found in a published report [2], and the 1982 data will be contained in a future report.

The captions require some explaining. The first 7 characters give the flight and run number, and the 8th digit indicates whether the measurement is B or D. For example, 81-042R1B means that the data shown is B for flight number 42, run 1, during the 1981 thunderstorm season.

Data for 1981 is given in Figures 2.1 - 2.5, and selected data for 1982 is given in Figures 2.6 - 2.17. The latter data is important because it consists of correlated B and D records for the same lightning event, a feature which will be discussed later in more detail.

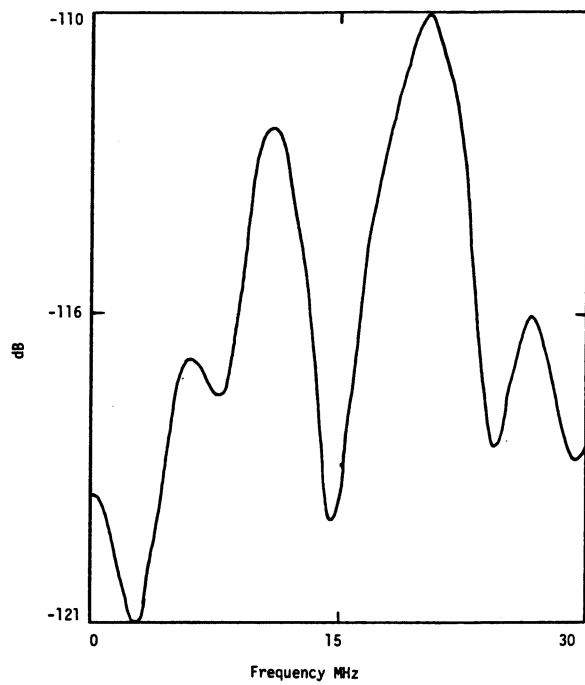


Figure 2.1 81-042 R1B

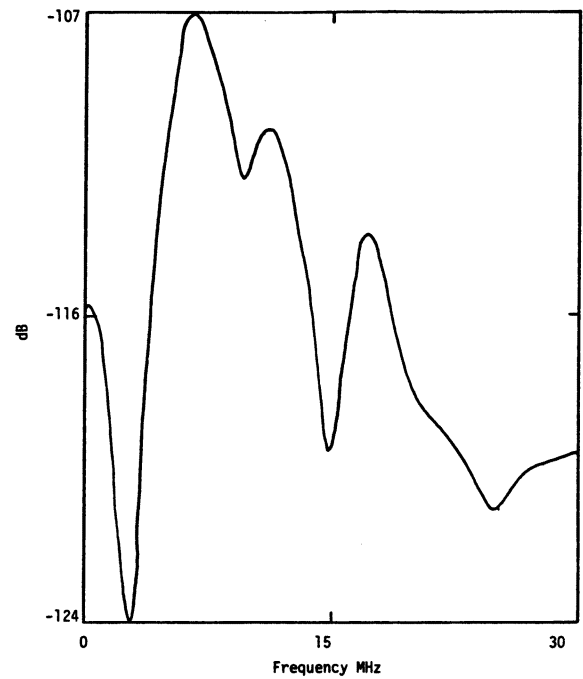


Figure 2.2 81-043 R1B

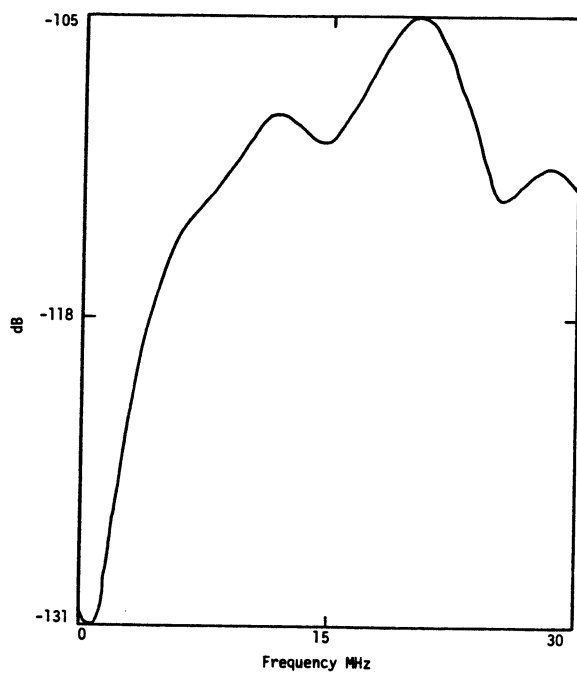


Figure 2.3 81-043 R2B

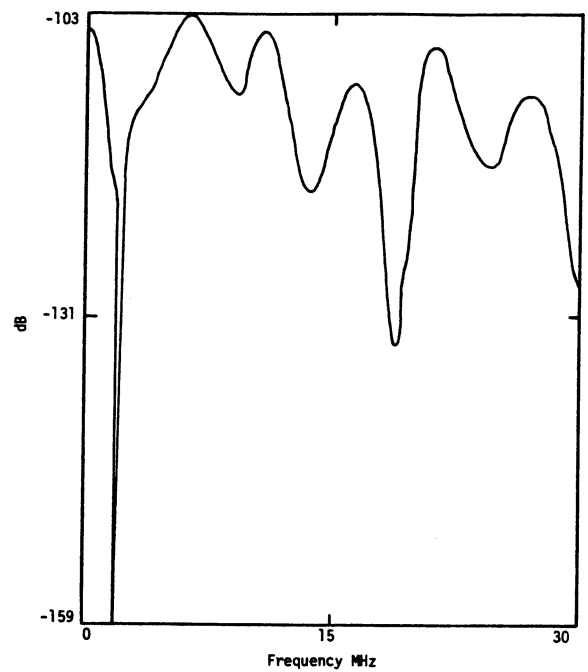


Figure 2.4 81-043 R3B

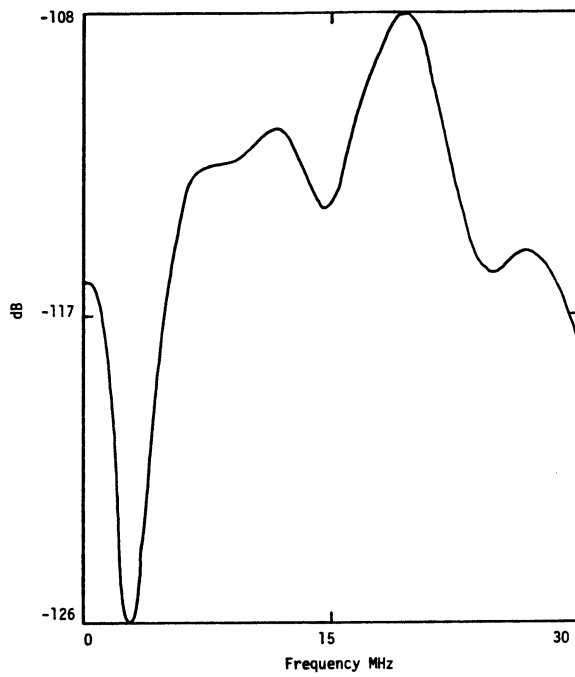


Figure 2.5 81-043 R4B

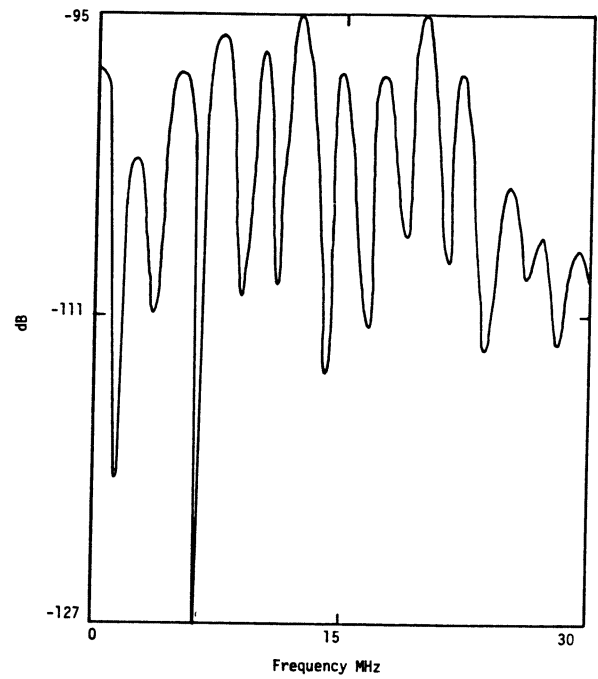


Figure 2.6 82-037 R4B

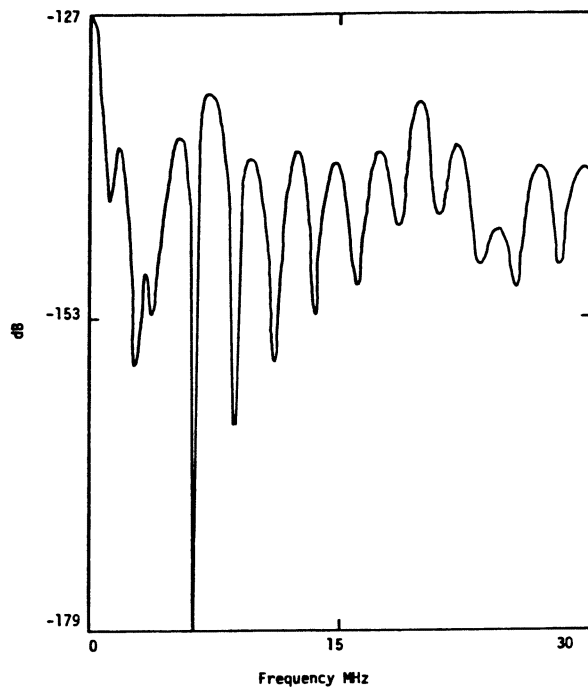


Figure 2.7 82-037 R4D

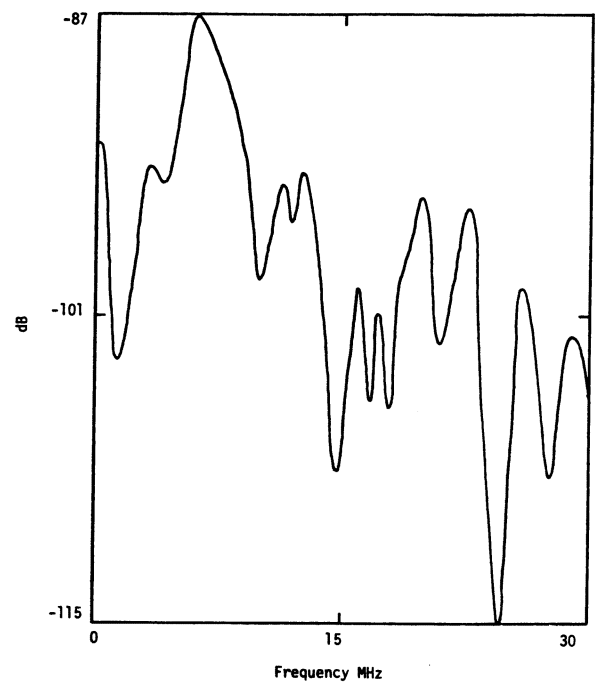


Figure 2.8 82-038 R2B

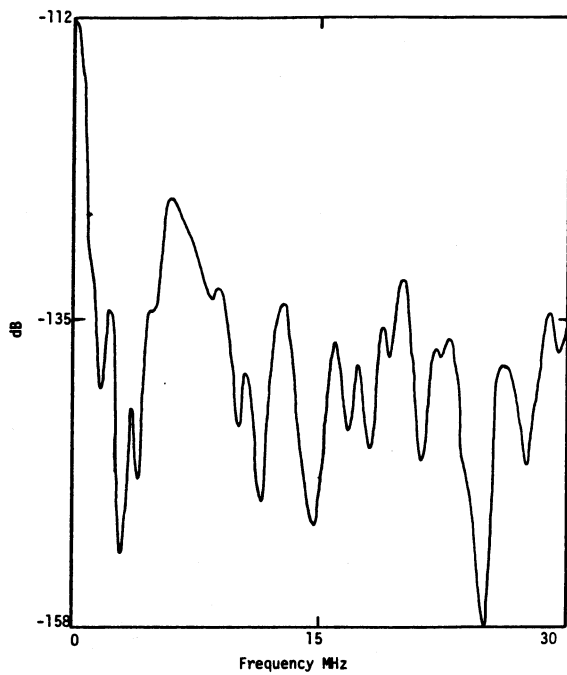


Figure 2.9 82-038 R2D

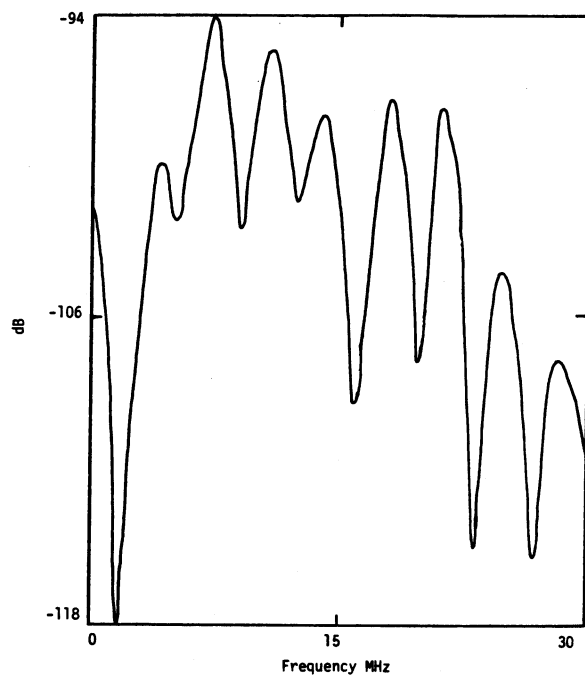


Figure 2.10 82-038 R4B

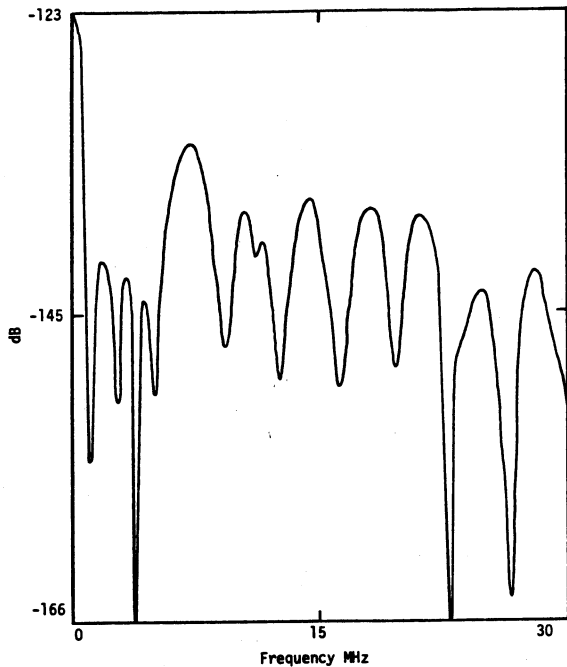


Figure 2.11 82-038 R4D

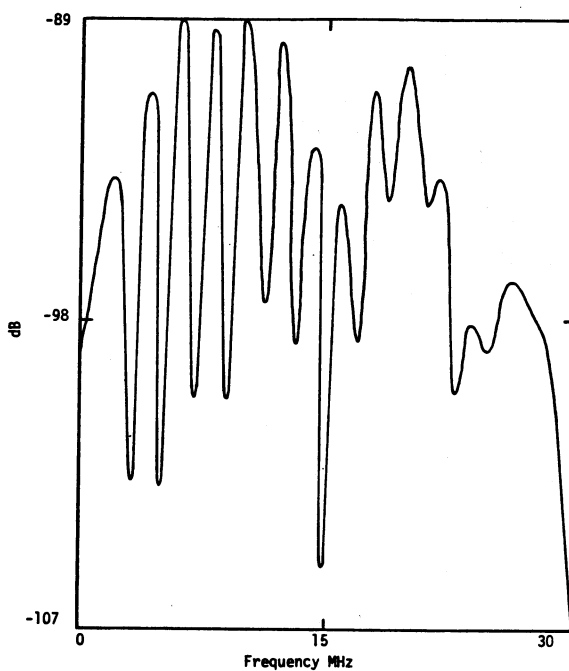


Figure 2.12 82-038 R7B

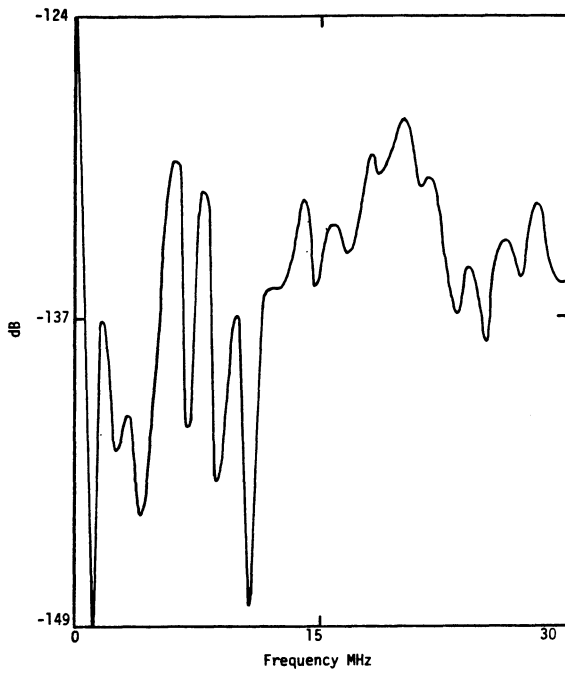


Figure 2.13 82-038 R7D

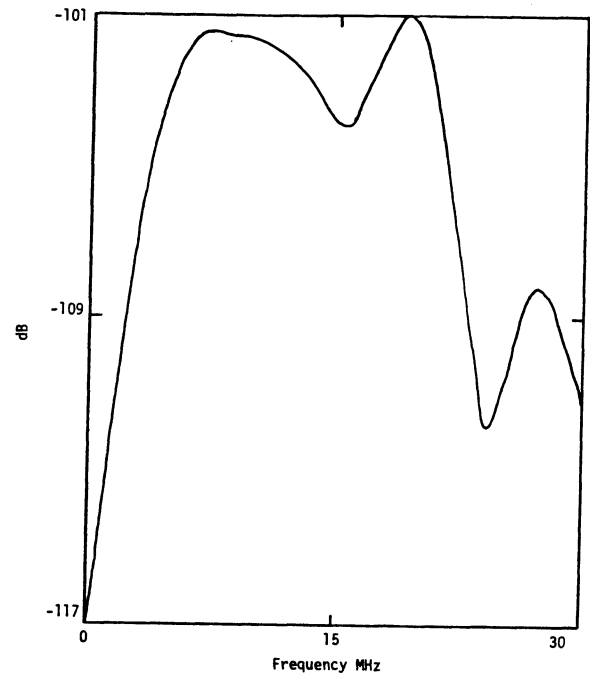


Figure 2.14 82-038 R8B

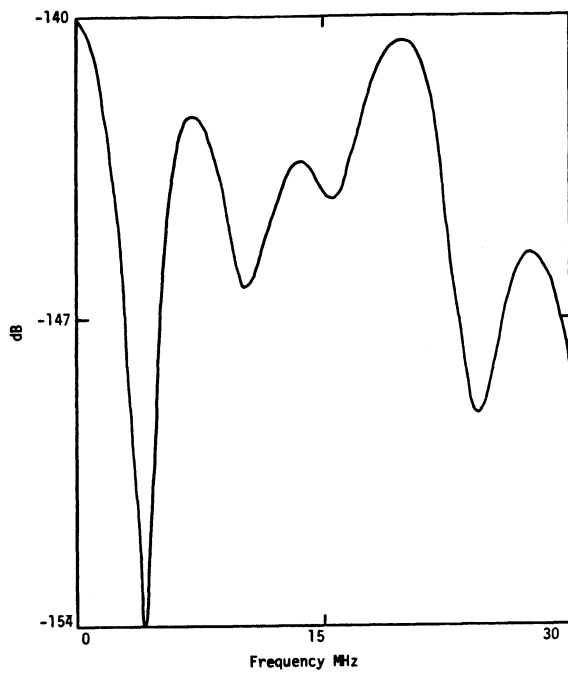


Figure 2.15 82-038 R8D

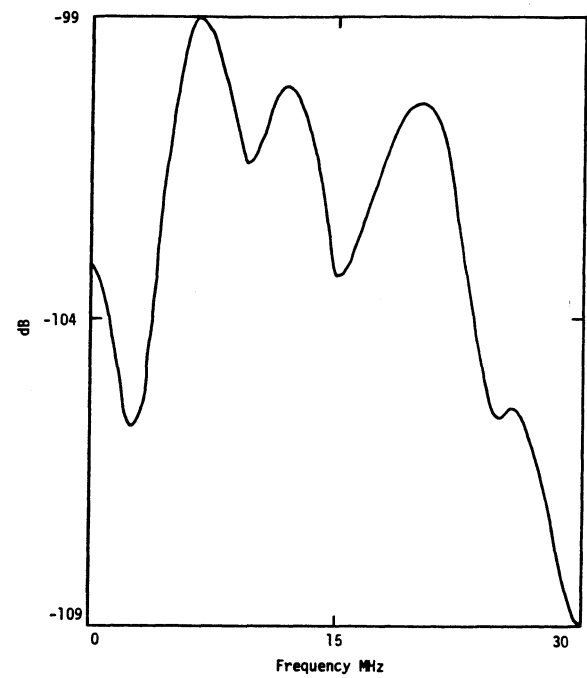


Figure 2.16 82-039 R2B

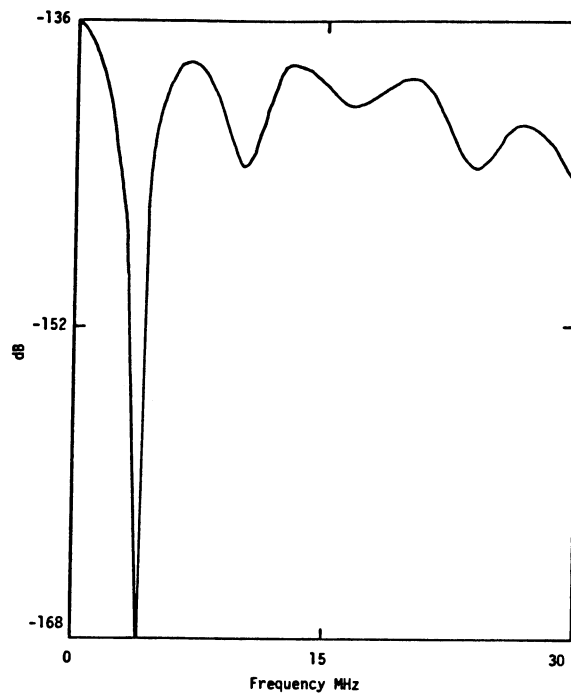


Figure 2.17 82-039 R2D

Tables 2.1 and 2.2 summarize the dynamic range, the inverse (time domain) record length, and the exact frequencies of the nulls and peaks for the 1981 and 1982 data, respectively. The first column describes the event, and the second column gives the estimated dynamic range, which is $20 \log_{10}(N)$, where N is the maximum number of discrete levels used in the time domain data record. This number is an indication of the dynamic range of the Fourier transform data as well. It is observed that the 1982 data has a somewhat better dynamic range.

The nulls in the data, especially the ones at the lower frequencies, are of interest because if they can be shown to occur because of aircraft resonance effects, something might be learned

TABLE 2.1

1981 B Data Summary for Direct Strikes

EVENT	DYNAMIC RANGE dB	[RECORD LENGTH] ⁻¹ MHz	NULLS MHz	PEAKS MHz
81-042 R1 B	14	4.3	<u>2.85</u> , 14.9	6.25, 11.4, <u>20.9</u>
81-043 R1 B	14	4	<u>2.77</u> , 9.75, 14.6	<u>6.65</u> , 11.4, 17.3
81-043 R2 B	17	5.9	<u>.86</u> , 15.4	12.5, <u>20.4</u>
81-043 R3 B	19	2	<u>2.0</u> , 9.3, 19.2	<u>6.4</u> , 11.2, 21.7
81-043 R4 B	17	5.3	<u>3.0</u> , 15	11.9, <u>19.6</u>

about the channel impedances and attach point locations. For example, identification of $\lambda/4$ resonances could give indications that the aircraft has either high or low impedance channel loading, depending upon whether the resonance is observed in D or B, and the attach point locations. It is of great interest to determine if the nulls are caused by aircraft resonances or if they are related to the record length. The inverse of the time domain record length was computed for correlation with these nulls. It is observed that there is no obvious correlation of the lowest frequency nulls with the record length, although this does not prove that they are not related. For example, consider the two Fourier transform pairs in Figure 2.18. Clearly, the nulls in the amplitude spectrum occur at frequencies related differently to the pulse width. Other transforms were computed for various arbitrary triangles and other simple waveforms, which showed that the

TABLE 2.2
1982 B and D Data Summary for Direct Strikes

EVENT	DYNAMIC RANGE dB	[RECORD LENGTH] ⁻¹ MHz	NULLS MHz	PEAKS MHz
82-037 R4 D	25	1.37	1.33, 2.86, <u>6.4</u> , 8.99	1.88, 3.39, 5.5, <u>7.5</u> , 10.1, 17.8, <u>20.0</u>
B	24	1.5	1.43, 3.75, <u>6.33</u> , 16.4	2.54, 5.19, 7.6, 10.2, <u>12.4</u> , 17.8, 20.2
82-038 R2 D	34	.71	<u>2.85</u> , 11.4, 14.9	<u>6.0</u> , 12.0, 16.2
B	30	1.06	1.30, 10.1, <u>14.9</u>	<u>5.9</u> , 16.0, 20.2
82-038 R4 D	23	1.1	1.22, 2.77, <u>3.87</u> , 9.4	2.17, 3.3, <u>7.54</u>
B	23	1.9	<u>1.70</u> , 5.46, 9.23, <u>16.4</u>	7.27, 11.1, 18.3
82-038-R7 D	29	1.2	<u>1.27</u> , 4.25, <u>10.8</u>	1.88, 6.1, <u>20.2</u>
B	22	1.37	3.1, 5.0, 7.0, 9.0, 11.1, 13.1, <u>15.0</u>	2.0, 4.1, <u>6.1</u> , <u>8.0</u> , <u>10.0</u> , <u>12.1</u>
82-038-R8 D	21	5.3	<u>3.84</u> , 10.45	7.2, 13.6, <u>20.0</u>
B	21	4.8	<u>15.6</u>	<u>7.4</u> , <u>19.4</u>
82-039 R2 D	20	5.0	<u>3.7</u> , 10.4, 16.8	<u>7.1</u> , <u>13.9</u> , <u>19.9</u>
B	26	4.2	<u>2.83</u> , 9.75, 15.5	<u>6.83</u> , 12.1, 20.5

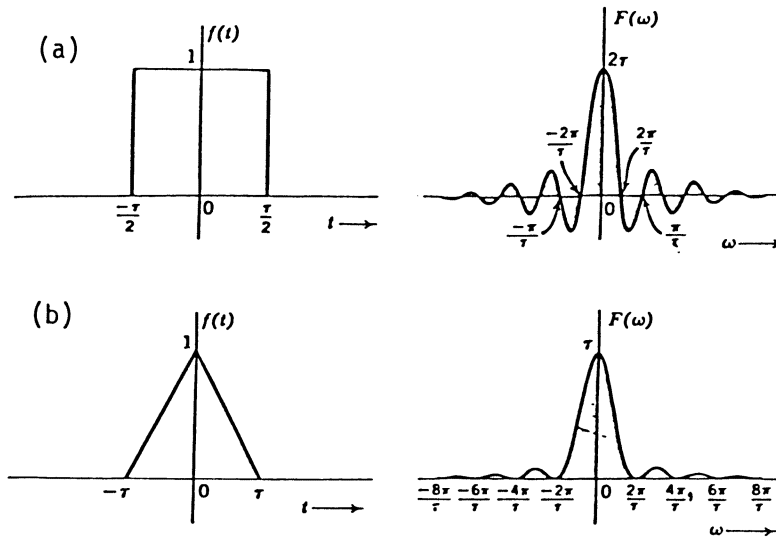


Figure 2.18 Rectangular Pulse and Isosceles Triangle Transform Pairs

resulting nulls cannot be simply related to the record length, but are related to other peculiarities of the waveforms. Thus it is believed that the lower frequency nulls in the data cannot be proven to be related to aircraft resonances, and must be assumed to be caused by some other source. In addition, the lower frequency nulls do not correlate with the basic $\lambda/4$ resonance at about 3.5 MHz.

The peaks in the data are shown in the last column. Because of the complex nature of the Fourier transform waveforms, it is difficult to tell whether a peak occurs because of an aircraft resonance, or simply because it is between two nulls. The converse is also true. In spite of this however, there are certain frequencies which consistently appear in much of the data.

The 1981 B data show fairly consistent peaks at 6-7 MHz, 11-12 MHz, and 20-21 MHz. This is in general agreement with the resonances reported by Trost [3] for the 1980 data. There is also a rather consistent null at ~ 10 and ~ 15 MHz.

The 1982 data is similar in character. Peaks in the vicinity of ~ 7 , 12 and ~ 20 MHz are common. Nulls at ~ 10 and ~ 15 MHz are also evident.

It is likely that these resonances are related to aircraft dimensions. For example, the half wavelength resonance based on structural length of the fuselage including the pitot boom is 7.0 MHz, and is 8.8 MHz without the pitot boom. The wing tip to wing tip resonance is on the order of 13 MHz. One would expect that the fatness of the aircraft would reduce these frequencies on the order of 5-10%.

The null data and peak data shown in Tables 2.1 and 2.2 is based on a Fourier transform technique which assumes a straight line interpolation between measured data points. The frequencies indicated are accurately determined from the computer numerical output directly. The frequency of the deepest null or largest peak is underlined. In the case in which there is more than one frequency underlined, then the depths or peaks at these frequencies are within 10%. The nulls and peaks are given only for frequencies less than 20 MHz, in order to keep the data set small and to emphasize the primary and first few resonances. It should be noted that not all peaks and nulls are given, but only those that appear to be significant, which involves some judgment.

Inspection of the transforms in Figures 2.1 - 2.17 results in some interesting observations. First, there is a great deal of variety in the transform structure. The data for 1981 (Figures 2.1 - 2.5), for example, has a few broad peaks and valleys, whereas the 1982 data (Figures 2.6 - 2.17) shows much more structure with considerably more peaks and nulls. This difference may be caused by the lower dynamic

range of the 1981 data with respect to the 1982 data. Another possible cause might be that the 1982 strikes were encountered at much higher altitudes (~ 9 km) than were the 1981 strikes (~ 6 km). For example, 82-037R4D and 82-038R4D show periodic nulls and dips every 2.3 - 2.6 MHz. Similarly, 82-038R4D and 82-038R4B show this pattern at 3.2 - 3.6 MHz intervals. Again, the same type of pattern is observed in 82-038R7D and 82-038R7B at 2 MHz intervals. This latter feature is probably caused by the presence of a second pulse in the time domain waveforms delayed 490 ns from the initial pulse. These responses can be contrasted with the much less complex structure of 82-038R8D and 82-038R8B.

2.2 Correlated 1982 Data and the Problem of Uniqueness

The data shown for 1982 is of special interest because it involves simultaneous \dot{B} and \dot{D} records. These records are not correlated accurately enough to identify which one began first, but they are correlated to the extent that they can be identified as being caused by the same lightning strike event. Because whatever lightning environment is postulated must simultaneously cause these two responses, it is expected that confidence in the uniqueness of that environment is much greater than that for one derived from a single measurement point.

For a particular channel configuration (impedance, velocity of propagation, attach points, etc.) transfer functions $T_D^*(\omega)$ and $T_B^*(\omega)$ can be defined as

$$T_D^*(\omega) = \frac{\dot{D}(\omega)}{\dot{I}(\omega)} \quad (2.1)$$

and

$$T_B^*(\omega) = \frac{\dot{B}(\omega)}{\dot{I}(\omega)} \quad (2.2)$$

where $I(\omega)$ is the channel current, and linearity is assumed. It is easy to show then that

$$\frac{\dot{D}(\omega)}{\dot{B}(\omega)} = \frac{T_D(\omega)}{T_B(\omega)} \quad (2.3)$$

If $\dot{D}(\omega)$ and $\dot{B}(\omega)$ are measured quantities, and $T_D(\omega)$ and $T_B(\omega)$ are determined from analysis of aircraft response to certain channel configurations, one should be able to reduce the uncertainty in the uniqueness problem by finding the channel configuration given $T_D(\omega)/T_B(\omega)$ which most nearly matches the measured ratio $\dot{D}(\omega)/\dot{B}(\omega)$.

These ratios must be identical at all frequencies, which at this point seems to present a difficult problem in view of the possible large number of combinations of channel parameters and attach points. Nevertheless, this question must be addressed.

The response ratio RR can be defined in logarithmic form as

$$RR = 20 \log \left| \frac{\dot{B}(\omega)}{\dot{D}(\omega)} \right|, \quad (2.4)$$

with \dot{D} and \dot{B} expressed in MKS units.

Figures 2.19 - 2.24 are plots of these ratios determined from the measured data. It is noted, of course, that they are not identical, although there are certain peak frequencies which are evident in much of the data. The differences between the figures arise from different channel parameters, attach points, or nonlinear effects. A summary of the peaks for the measured waveforms, as well as for some computed waveforms, is given in Table 2.3.

Because the response at low frequencies is easier to understand than that at high frequencies, it seems reasonable to assume that the low frequency response ratio could be indicative of attach point locations. That is, one would expect this ratio to be different for nose-tail, nose-wing, or wing-wing configurations, for example. However, it is found that the dynamic range (or alternately, the granularity of the amplitude resolution of the digitized data) is not

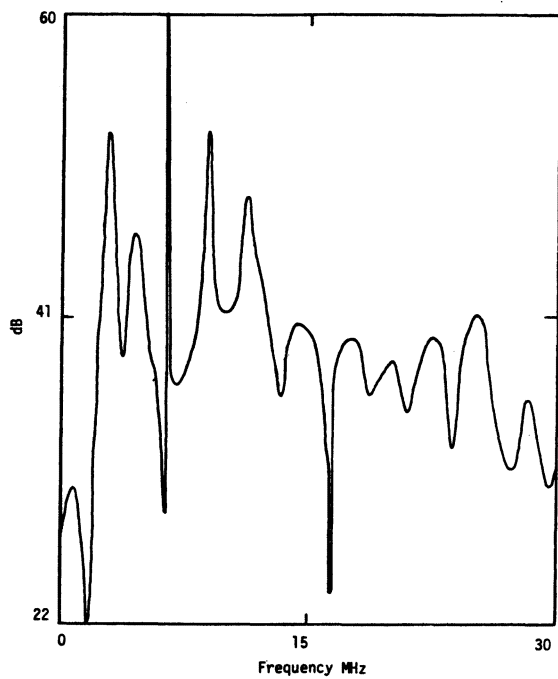


Figure 2.19 RR for 82-037 R4

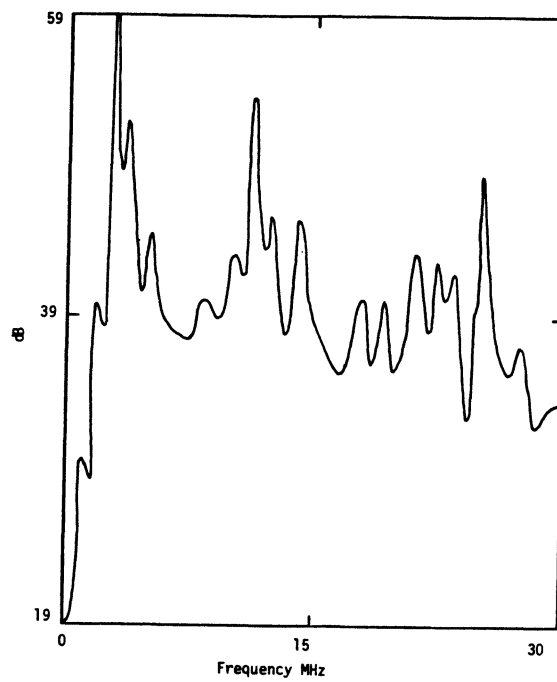


Figure 2.20 RR for 82-038 R2

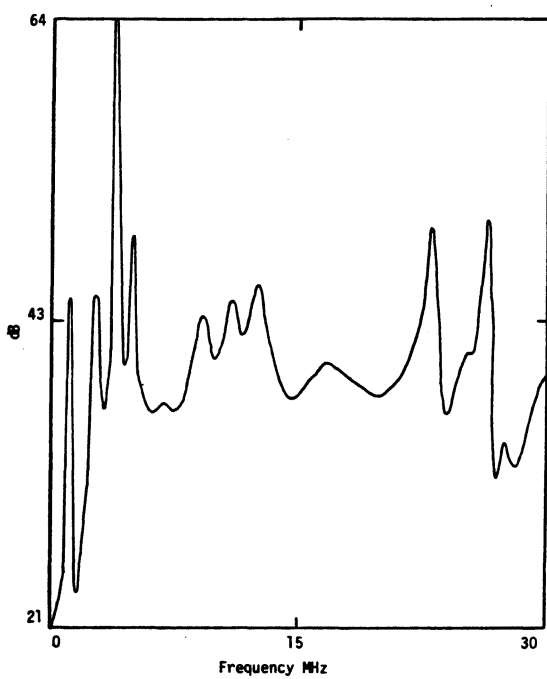


Figure 2.21 RR for 82-038 R4

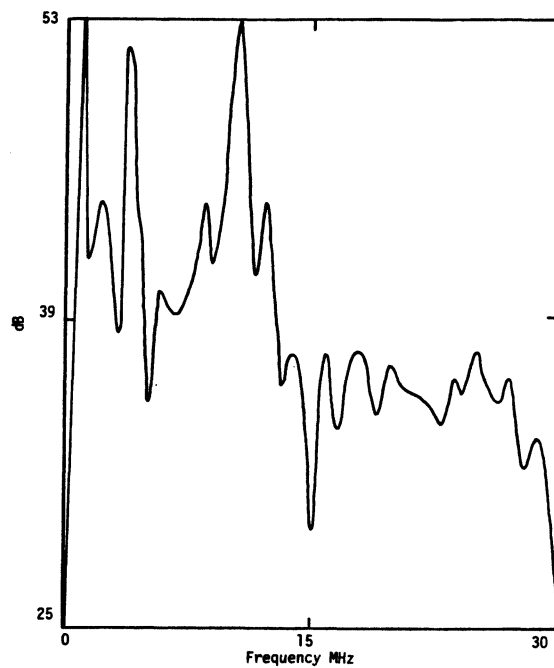


Figure 2.22 RR for 82-038 R7

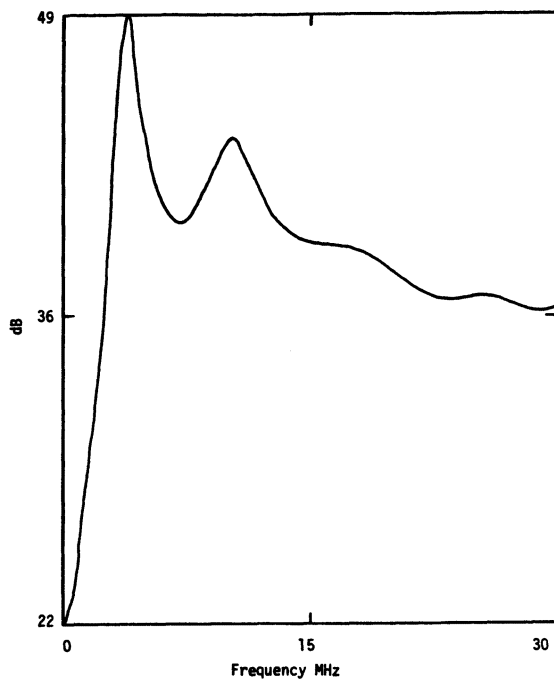


Figure 2.23 RR for 82-038 R8

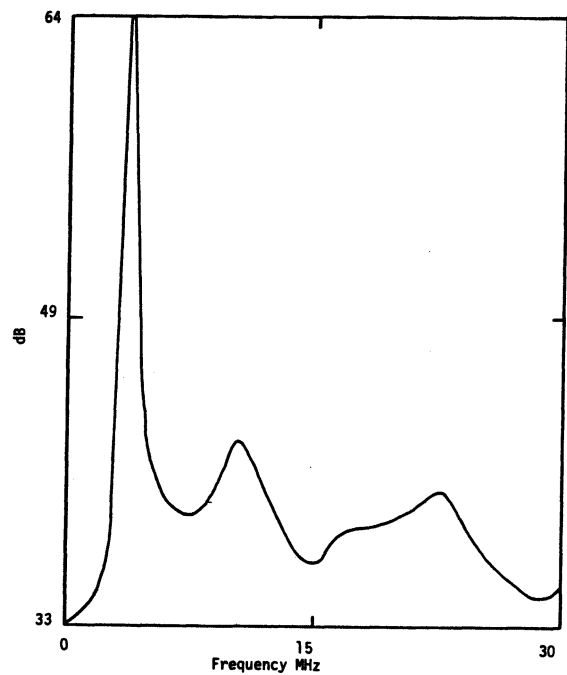


Figure 2.24 RR for 82-039 R2

sufficient for accurate determination of the low frequency levels. This is particularly true for \dot{B} data, which is almost always bipolar and has the property that the $\int_0^t \dot{B} dt$ (which is the same as the low frequency value of the Fourier transform of \dot{B}) is very close to zero, that is, it has a small DC value. This DC value is of the same size (or smaller) as the value one would obtain by assuming an error of $1/2$ of the amplitude digitization resolution over the entire record length. The latter value is a measure of the absolute best accuracy one could obtain with the discrete data system. Therefore, errors in \dot{B} at low frequencies were computed to be in the range of $-\infty$ dB (which corresponds to $\int_0^t \dot{B} dt < \text{max digitization error}$) to $+10$ dB. Errors in DC values of \dot{D} are smaller, because \dot{D} tends to have a significant DC value. The errors for \dot{D} were computed to be in the range of -4 dB to $+3$ dB. The results are summarized in Table 2.4. The second column shows the response ratio at DC as obtained directly from the Fourier

TABLE 2.3
Summary of Peaks for Response Ratios

<u>EVENT</u>	<u>FREQUENCY, MHz</u>	<u>RATIO dB</u>
82-037 R4	2.854	53.2
	4.348	46.8
	6.382	60.1
	9.00	52.5
	11.44	48.5
82-038 R2	1.792	40.3
	2.845	58.6
	3.574	52.4
	5.167	44.6
	10.00	43.8
	11.44	53.7
82-038 R4	1.207	44.9
	2.782	44.4
	3.871	64.5
	4.915	49.0
	9.568	44.2
	11.17	44.7
82-038 R7	1.27	52.9
	2.512	45.0
	4.213	52.0
	8.713	44.7
	10.72	53
82-038 R8	3.889	49.4
	10.45	44.1
82-039 R2	3.727	63.8
	10.54	42.5
Computed linearly: Nose Entry	2.548	42.2
Tail Tip Exit, $Z_o = 100 \Omega$,	12.52	41.7
$v_p = 3 \times 10^8$, $R/\ell = 0$		
Computed linearly: Nose Entry	2.305	50.2
No Exit, $Z_o = 100 \Omega$,	11.2	41.4
$v_p = 3 \times 10^8$, $R/\ell = 50 \Omega/m$		

TABLE 2.3 (CONT'D)

Summary of Peaks for Response Ratios

<u>EVENT</u>	<u>FREQUENCY, Mhz</u>	<u>RATIO, dB</u>
Computed Nonlinearly		
A. Leading Edge of Left Wing I = -100A	1.594	24.0
	3.817	29.9
	5.338	35.0
	6.103	35.0
	7.372	40.4
	9.57	40.1
	10.5	36.9
	11.7	39.2
	12.61	42.8
	25.03	51.9
Computed Nonlinearly		
B. Leading Edge of Left Wing I = +100A	1.522	18.6
	2.674	30.8
	4.339	44.8
	6.418	44.8
	7.03	38.4
	8.578	40.2
	10.45	38.33
Computed Nonlinearly		
C. Nose, I = -100A	2.602	44.1
	4.411	37.0
	6.571	36.3
	8.605	36.9
	10.99	40.0
	12.34	33.8
Computed Nonlinearly		
D. Leading Edge of Right Wing I = +100A	2.197	40.4
	4.312	52.1
	6.382	50.2
	8.308	45.4
	9.89	46.0
	11.89	41.5
	27.8	65.4
Computed Nonlinearly		
E. Right Side of Tail I = -100A	1.81	36.9
	4.339	39.9
	6.877	41.24
	9.244	42.5
	11.53	49.5
	13.06	59.3
	26.83	70.8

TABLE 2.4
Low Frequency Response Ratios for Selected 1982 Simultaneous Data

EVENT	RESPONSE RATIO at DC (dB)	POSSIBLE VARIATION (dB)
82-037 R4	28.3	(-16.9, + 8.5)
82-038 R2	19.4	(-8.9, + 6.2)
82-038 R4	21.4	(-∞, +9)
82-038 R7	25.0	(-29, + 8.3)
82-038 R8	22.2	(-∞, + 14.4)
82-039 R2	33.2	(-8.2, + 5.9)

transforms. The third column shows the possible variation in this ratio, as determined from the error analysis of B and D. The symbol ∞ means that the possible error is larger than the calculated DC value, thus allowing the possibility that the DC value is zero. Even apart from those two special cases, the allowable spread can be as great as 37 dB, which clearly indicates that the data is not sufficiently accurate to allow the use of DC levels to infer attach points. This problem can be helped by increasing the dynamic range of the instrumentation. It is understood that there are plans to replace the current 6 bit digitizer with an 8 bit unit, which will allow up to a maximum of 12 dB increase in the dynamic range.

It thus seems that if the response ratio's DC values cannot be used to help in the uniqueness problem, then the peaks of the response ratios may provide some insight. The response ratios have been calculated for two linear channel configurations indicated in Figures 2.25 and 2.26 and for five nonlinear attachment cases shown in Figures 2.27 to 2.31. These nonlinear cases correspond to those of section 4.6 with 6% water content and a relative air density of .5. These can be compared directly with the measured ratios in Figures 2.19 - 2.24. Table 2.3 also gives the peak values for the computed ratios. Several items are worthy of mention.

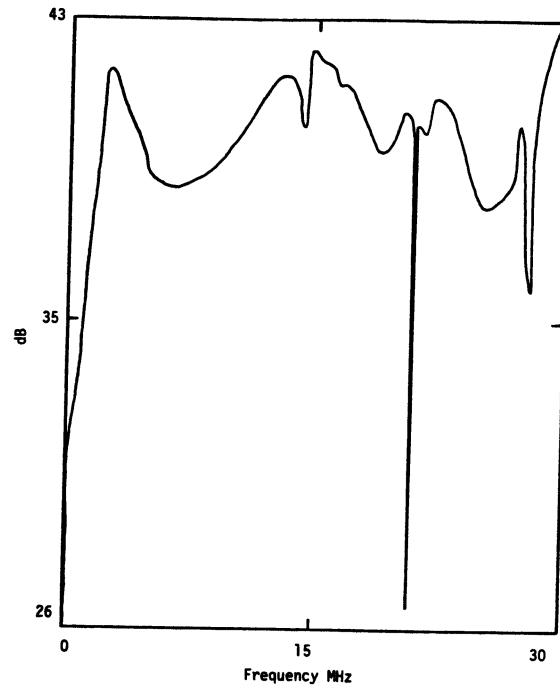


Figure 2.25

Linearly Computed RR for Nose
Entry, Tail Tip Exit, $Z_0 = 100 \Omega$,
 $R/\lambda = 0$, $v_p = 3 \times 10^8$ m/sec

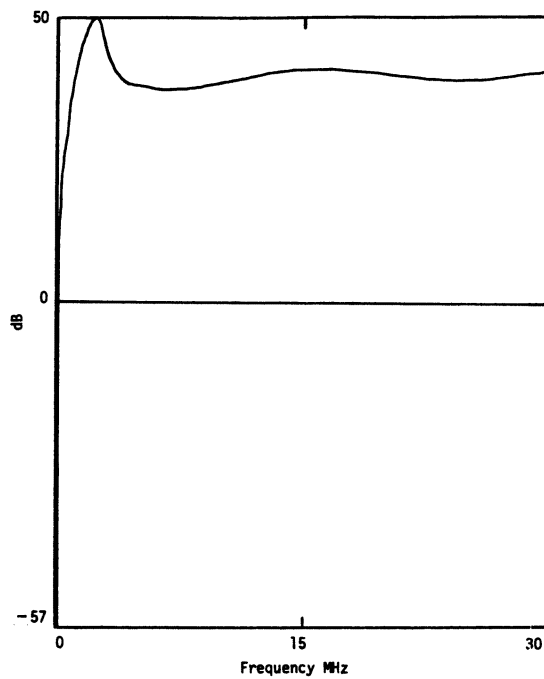


Figure 2.26

Linearly Computed RR for Nose
Entry and No Exit, $Z_0 = 100 \Omega$,
 $R/\lambda = 50 \Omega/m$, $v_p = 3 \times 10^8$ m/sec

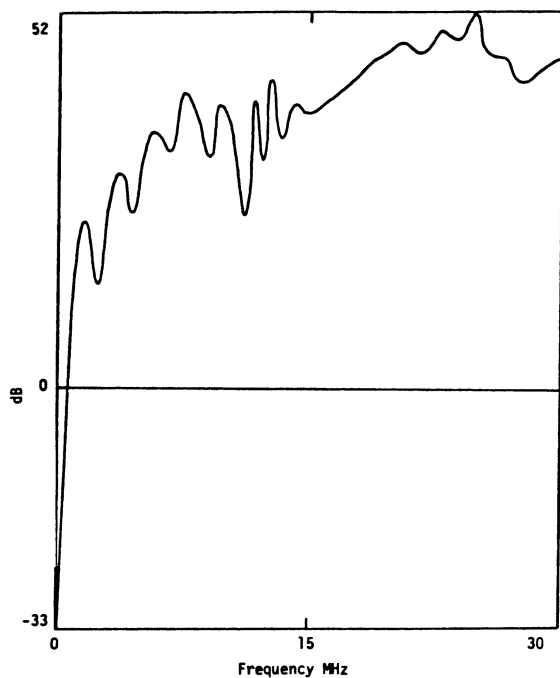


Figure 2.27

RR for Nonlinear Attachment to Leading Edge of Left Wing, $I = -100$ A

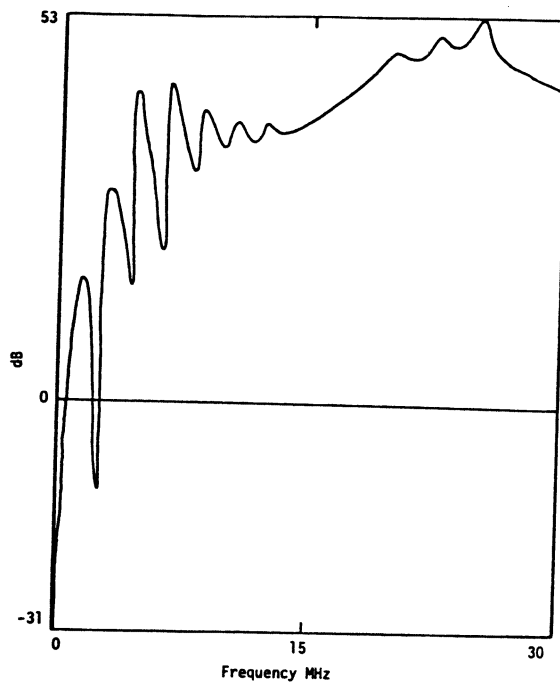


Figure 2.28

RR for Nonlinear Attachment to Leading Edge of Left Wing $I = +100$ A

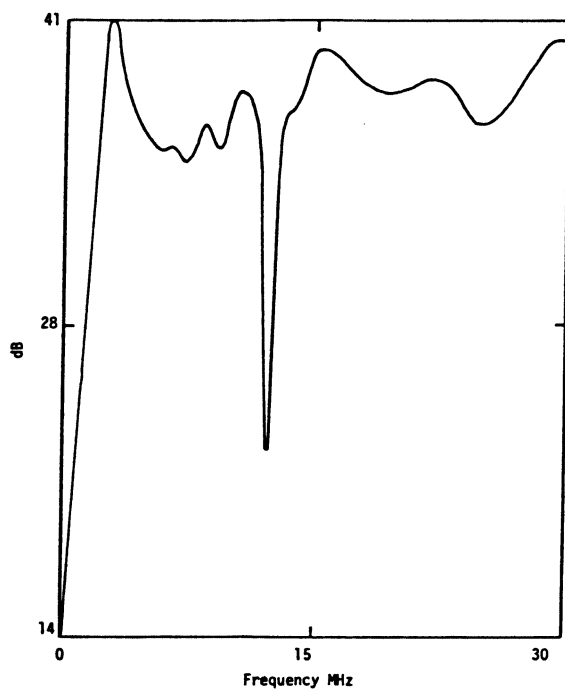


Figure 2.29

RR for Nonlinear Attachment to Nose, $I = -100$ A

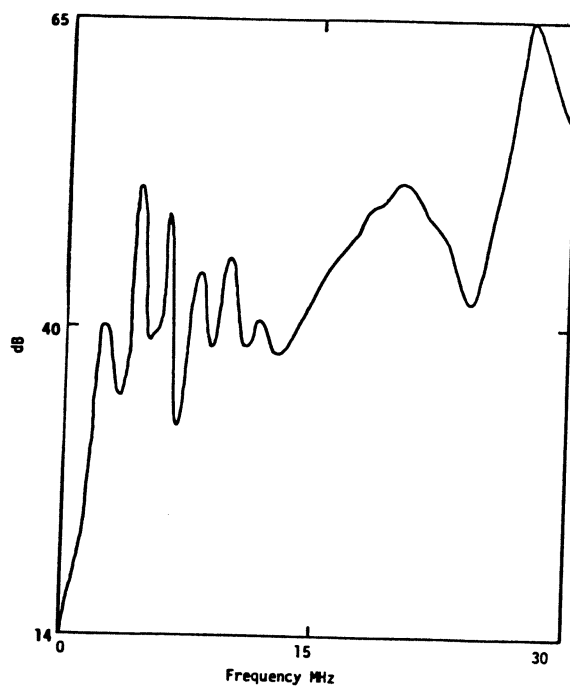


Figure 2.30

RR for Attachment to Leading Edge of Right Wing $I = +100$ A

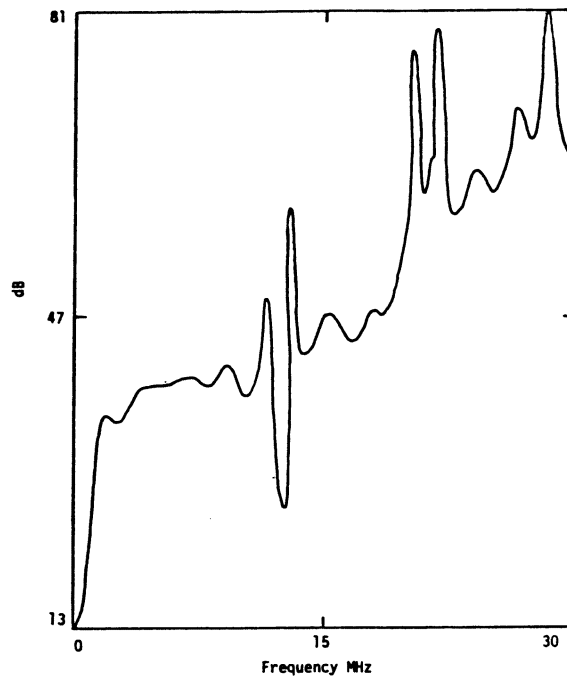


Figure 2.31

RR for Nonlinear Attachment to
Right Side of Tail, $I = -100$ A

First, the computed ratios have a larger dynamic range than the measured ones. This is so, however, because the computed data has a larger dynamic range (> 100 dB) than does the measured data (20-30 dB), and thus no significance can be attached to this difference.

Second, the measured ratios often have considerably more structure in them than do the linearly computed ratios, and the non-linearly computed ratios have more structure in them than do the linearly calculated ones.

Third, the peaks for measured ratios are not free from noise problems either. In many cases, the peaks occur because of nulls in $|D(\omega)|$. The depth of these nulls is greater than what the dynamic range of the original data would allow. Thus, the validity of the amplitude of the peaks has to be determined on an individual basis by studying the original waveforms.

Fourth, there are some modest agreements between the computed and some of the measured ratios. For example, the ratio for 82-038R8 has features quite similar to those of Figure 2.26. Also, the computed peak frequencies of about 11 and 2.4 MHz are evident in several of the measured waveforms. Thus there appears to be some hope for using this type of technique to help resolve the uniqueness problem.

Fifth, there is a great variety in structure of both measured and computed ratios. This is particularly true for the ratios obtained from responses computed nonlinearly.

Finally, the utility of the response ratios has not been fully evaluated at this point. Work in this area began near the end of this research period, and more work is planned for future efforts. In particular a whole catalogue of ratios for various attach points and channel parameters needs to be developed, and ratios from other 1982 correlated data sets need to be computed.

CHAPTER 3

INTERPRETATION METHODOLOGY DEVELOPMENT

3.0 Background

The response of an aircraft to a lightning strike can be significantly affected by the character of the lightning channel. Consider as an example two different channels containing a given current, one with a high characteristic impedance and the other a low impedance. When the high impedance channel interacts with an aircraft, the current in the channel is not greatly changed, and the current flowing onto the aircraft is approximately the original value in the channel. When the low impedance channel interacts, the current in the channel can be changed significantly, and the current flowing onto the aircraft is usually larger than the initial value in the channel. Since this current is the primary source for the aircraft response, it is clear that the channel impedance must be considered when studying the aircraft response.

Another characteristic of the lightning channel is the propagation velocity of the current flowing in it. Stepped leaders, dart leaders, and return strokes all propagate with different speeds because of the different physical processes occurring in them. Even within a given category of lightning phenomena the propagation speed can vary over a relatively wide range. This channel characteristic is important in that for propagation velocities much less than the speed of light, the aircraft response will begin long before the lightning current reaches the sensor point, because the electromagnetic fields from the current produce a polarization of the aircraft.

3.1 Channel Modeling

In order to calculate a realistic aircraft response, it is necessary to model the channel impedance and propagation velocity properly. The linear finite difference code used in this study achieves that by representing the lightning channel as a thin wire [4].

In this approximation the channel is required to be much smaller than the cell size which for the F106 code is one-half meter. The thin wire formalism characterizes the channel impedance and propagation velocity through a per unit length inductance and capacitance. The following relationships hold:

$$\begin{aligned} Z_0 &= \sqrt{L_\ell / C_\ell} \\ V_p &= [L_\ell C_\ell]^{-1/2}, \end{aligned} \tag{3.1}$$

where Z_0 = characteristic impedance, (Ω),
 V_p = propagation velocity (m/sec),
 L_ℓ = per unit length inductance (h/m),
 C_ℓ = per unit length capacitance (f/m).

It should be noted at this point the per unit length inductance and capacitance in Equation (3.1) are not to be considered the real physical values for the lightning channel. The thin wire formalism is a mathematical construction which allows one to model a current path in the finite difference code which is smaller than the cell size. The per unit length inductance and capacitance used in the formalism are those appropriate for a coaxial cable with inner conductor radius a , and outer shield radius $\frac{\Delta S}{2}$, where ΔS is the spatial grid dimension of the code. Thus C_ℓ and L_ℓ may be written,

$$\begin{aligned} C_\ell &= 2\pi\epsilon / \ln \left(\frac{\Delta S}{2a} \right) \\ L_\ell &= \frac{\mu_0}{2\pi} \ln \left(\frac{\Delta S}{2a} \right) \end{aligned} \tag{3.2}$$

In addition to specifying Z_0 and V_p , the thin wire formalism allows the inclusion of a resistance per unit length along the channel. In principle all of these quantities can be time varying, and some cases were run in which the resistance was allowed to vary. However, the majority of the cases reported in this chapter did not allow any time variation. By requiring time invariance of the channel, the problem of the aircraft response to a given excitation became amenable

to Fourier analysis. This greatly simplified the methodology used in finding a source to produce a given aircraft response.

In addition to the thin wire formalism, two other methods were used to model the lightning channel. The first is simply a variation of the thin wire method, in which the exit channel is changed from a thin wire to a line of zeroed electric fields, corresponding to a perfectly conducting exit channel of dimensions one-half meter by one-half meter. This was done to see if the characteristics of the exit channel were important in the aircraft response. Slight differences were seen between the perfectly conducting and thin wire channels as can be seen in the data to be presented later.

The second alternate method of modeling the channel was to simply force the injected current to be a particular value regardless of the channel characteristics. This method was used in the early part of the channel studies and corresponds to a very high impedance channel for which the current is unaffected by the presence of the aircraft. This is unlikely to be true physically and is unable to predict the correct relationship between time correlated response measurements on the aircraft. Results for this method will therefore be omitted from this report.

3.2 Data Interpretation Based on a Single Measurement

To illustrate how the channel study was done, one set of parameters will be analyzed in detail, with each step in the analysis explained. The entry channel for the study always ran from the outer boundary of the finite difference code to the nose of the F106 in a straight line. The exit channel ran directly to the boundary from the exit point. The source used to drive the code was a transparent current source located at the boundary of the code at the end of the entry channel. By "transparent" source is meant one that allows reflections coming back along the lightning channel from the F106 to pass through without reflection.

The case to be discussed had inductance per unit length of 3.33×10^{-7} h/m, capacitance per unit length of 3.33×10^{-11} f/m, and

resistance per unit length of $50\Omega/\text{m}$. The exit and entry channels both used the same parameters. The first step in analyzing the channel was to use a standard sine-squared pulse shape (shown in Figure 3.1) as a current source. This source was chosen so as to have significant frequency content at all relevant frequencies. The finite difference code was run with this source to determine the response of the F106. The forward \dot{D} response is shown in Figure 3.2. Then the waveforms of Figures 3.1 and 3.2 were Fourier transformed to obtain the frequency content. The results are shown in Figures 3.3 and 3.4, respectively. Next the frequency transform of the F106 response was divided by the frequency transform of the source current to obtain the transfer function between source and response. The result is shown in Figure 3.5. This transfer function is a source independent quantity for the linear problem here considered. That is, regardless of the source current waveform, the Fourier transform of the response divided by the Fourier transform of the source results in the same transfer function. This knowledge was then used in conjunction with the measured data. The measured \dot{D} response of flight 80-018 (Figure 3.6) was digitized and Fourier transformed, the result of which is shown in Figure 3.7. Then this transform was divided by the transfer function to give the Fourier transform of the current source needed to produce the response of flight 80-018. The transform of that source is shown in Figure 3.8. The frequency representation of that source current was then transformed back into the time domain, the results of which are shown in Figures 3.9 and 3.10 on two different time scales. The derived time domain source current was then used to drive the finite difference code. This was done for two reasons. The first was to check that the source actually reproduced the measured waveform; that is, that there were no major errors in deriving the source. The second reason was to determine the actual injected current, which in general can be quite different from the source current. The forward \dot{D} response of the aircraft is shown in Figure 3.11 and the injected current in Figure 3.12. Note that Figure 3.11 does match the measured \dot{D} quite closely, as it must if there were no errors in the analysis. The last step in the analysis is to use the source current in the finite difference code once again, but this time

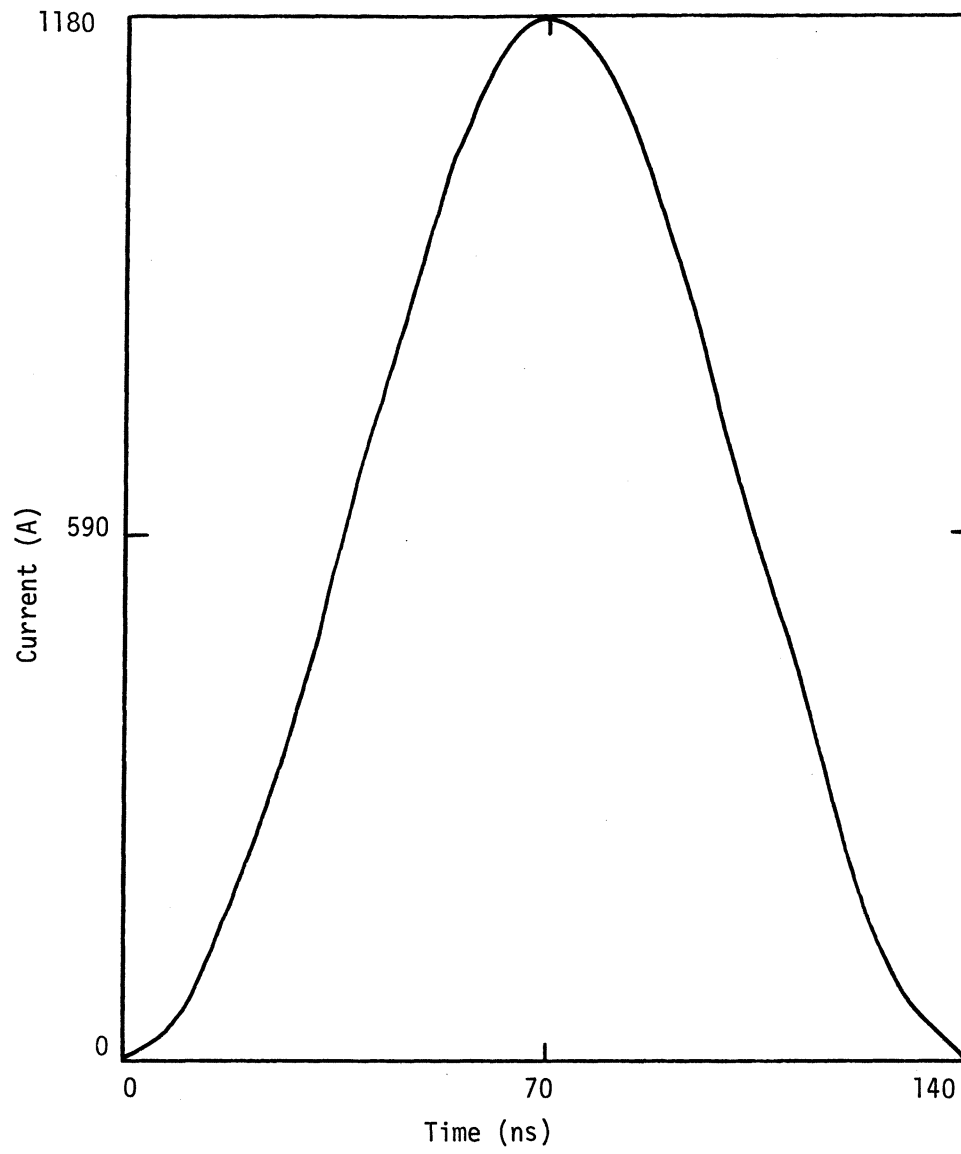


Figure 3.1 Standard Current Waveform Used in Lightning Channel Impedance Study

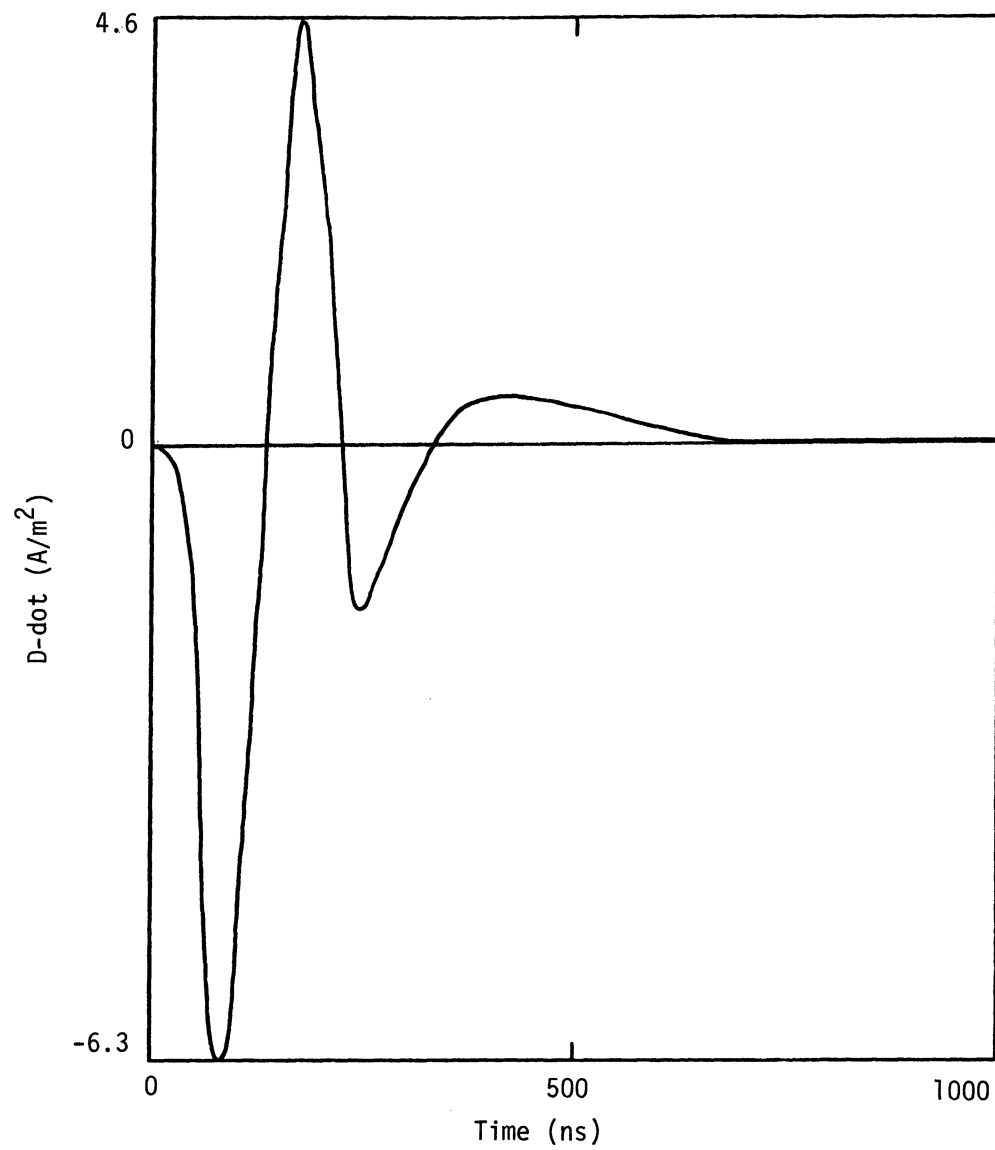


Figure 3.2 Forward D-dot Response of F106 to Standard Current Pulse of Figure 3.1

$$\begin{aligned}
 (L_{\ell} &= 3.33 \times 10^{-7} \text{ h/m} \\
 C_{\ell} &= 3.33 \times 10^{-11} \text{ f/m} \\
 R_{\ell} &= 50 \text{ } \Omega/\text{m})
 \end{aligned}$$

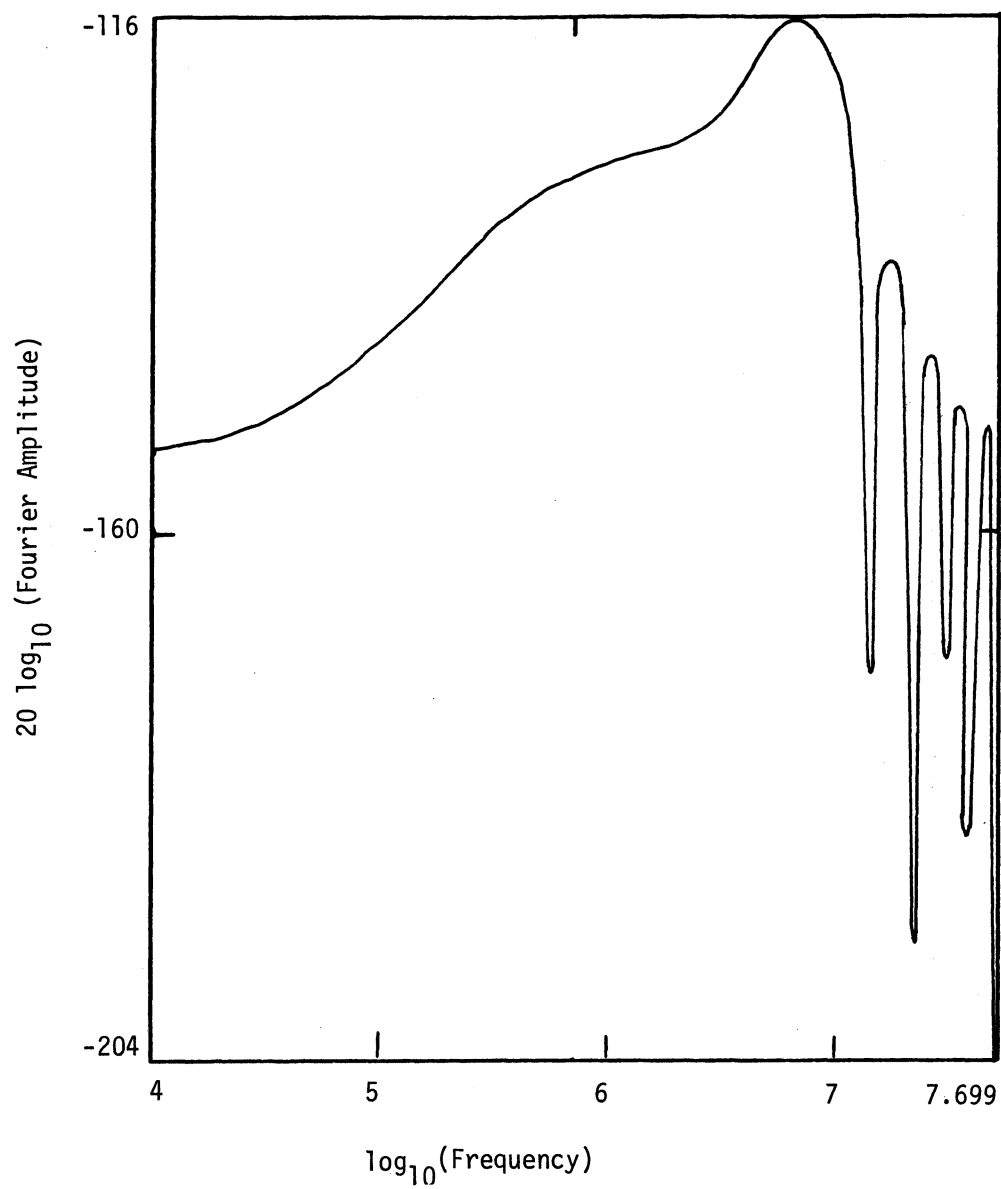


Figure 3.3 Fourier Transform of Standard Current Shape Shown in Figure 3.1

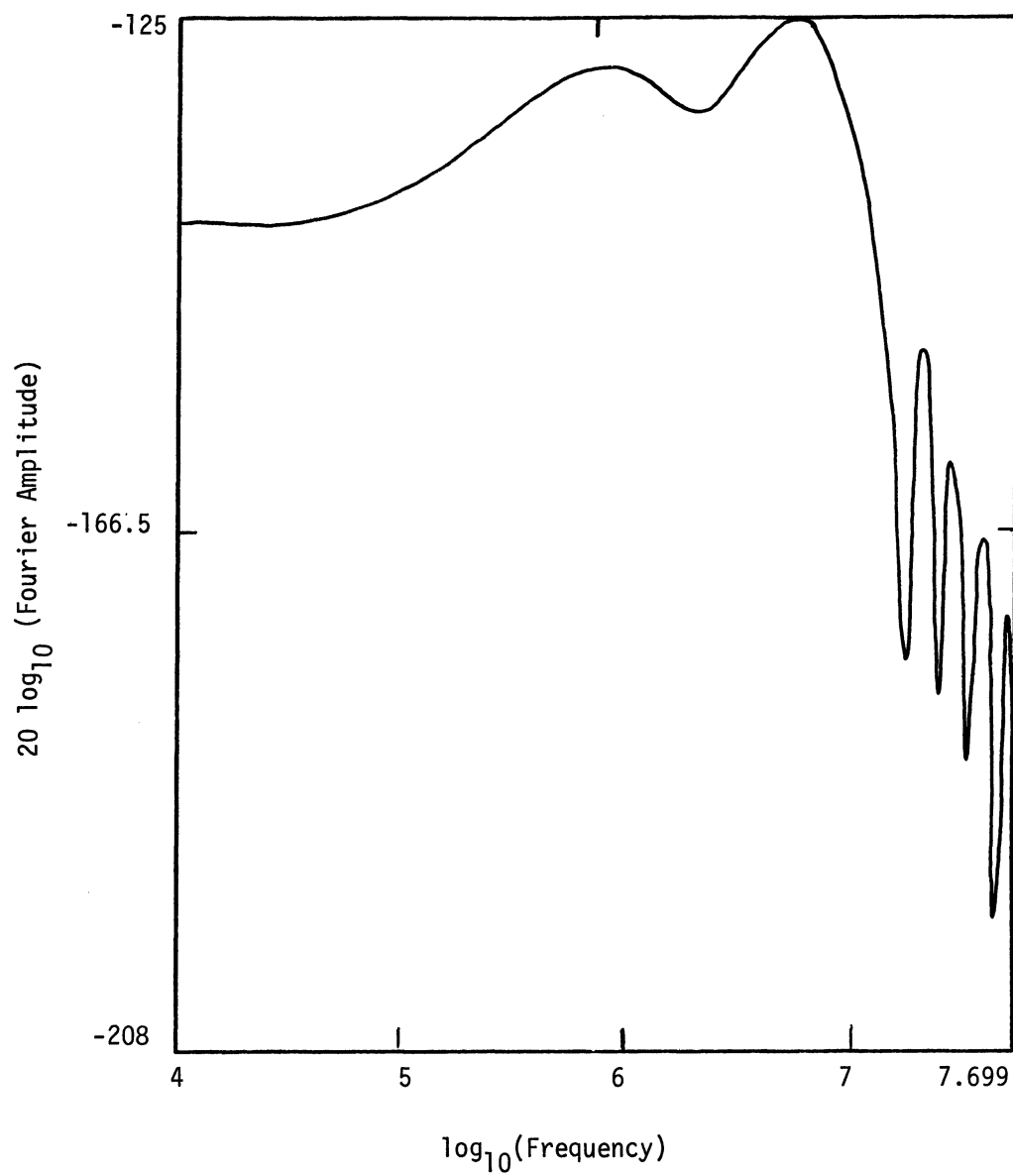


Figure 3.4 Fourier Transform of D-dot Response of Figure 3.2

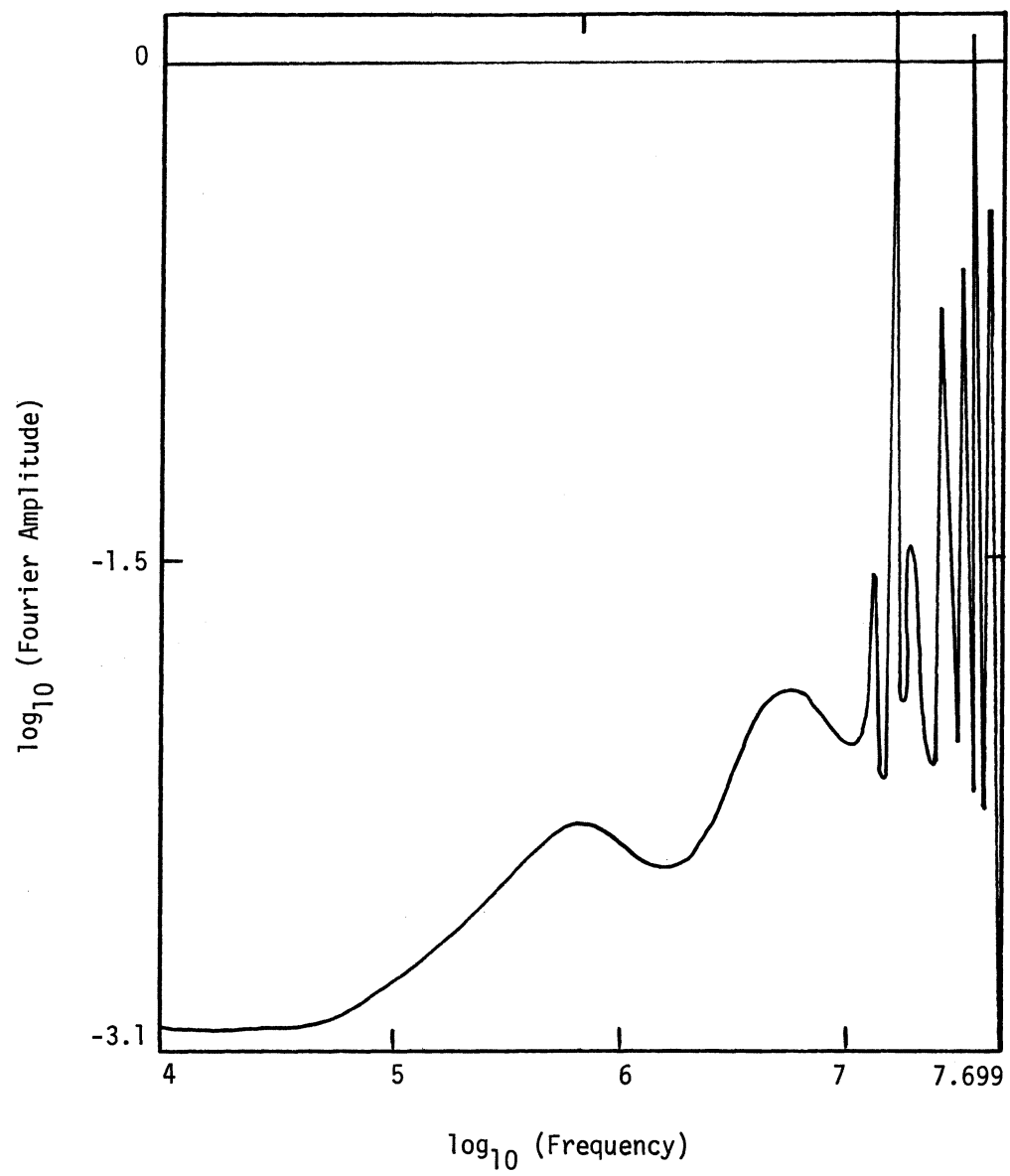


Figure 3.5 Source Independent Transfer Function Derived as Explained in the Text

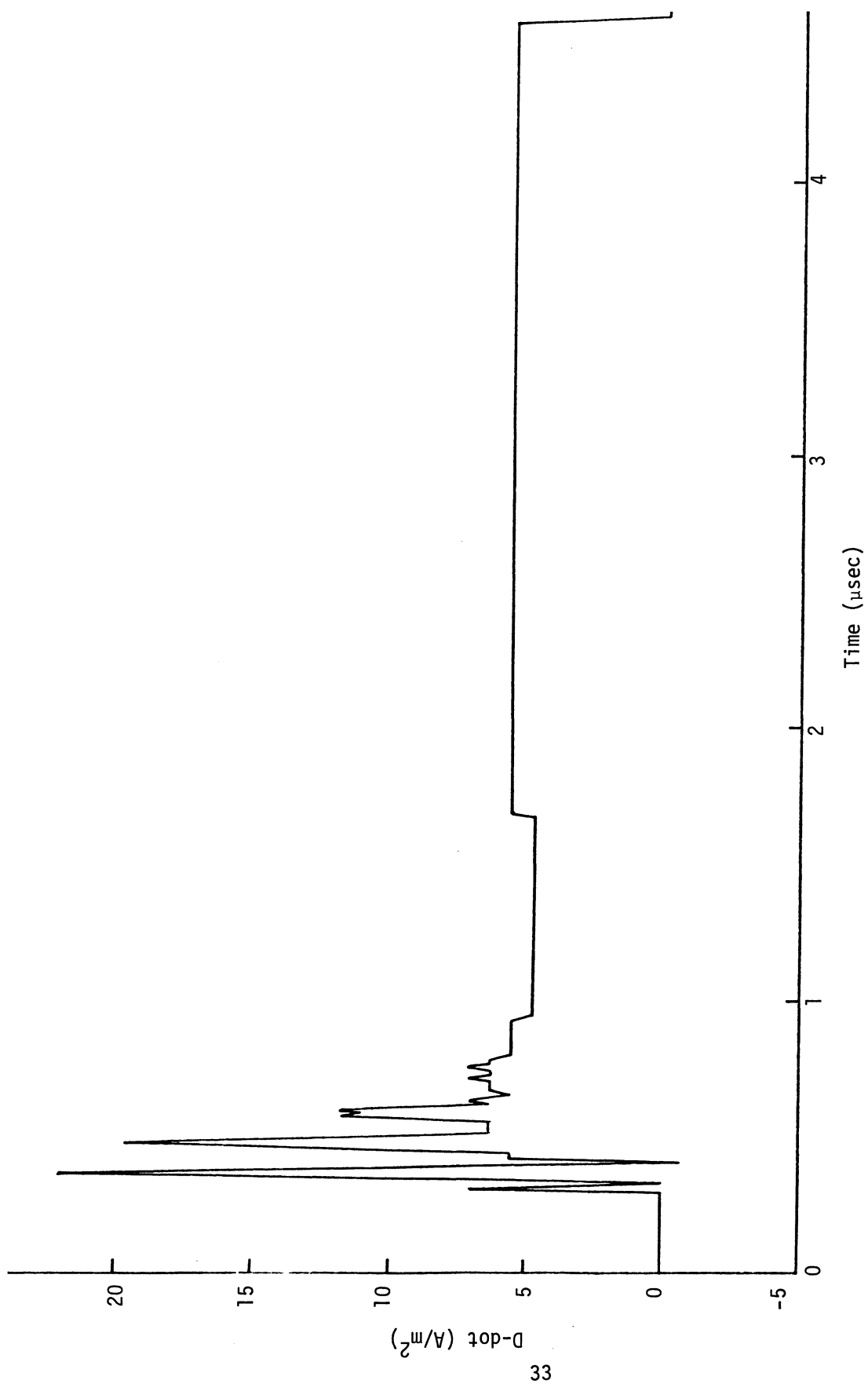


Figure 3.6 D-dot Response of Flight 80-018

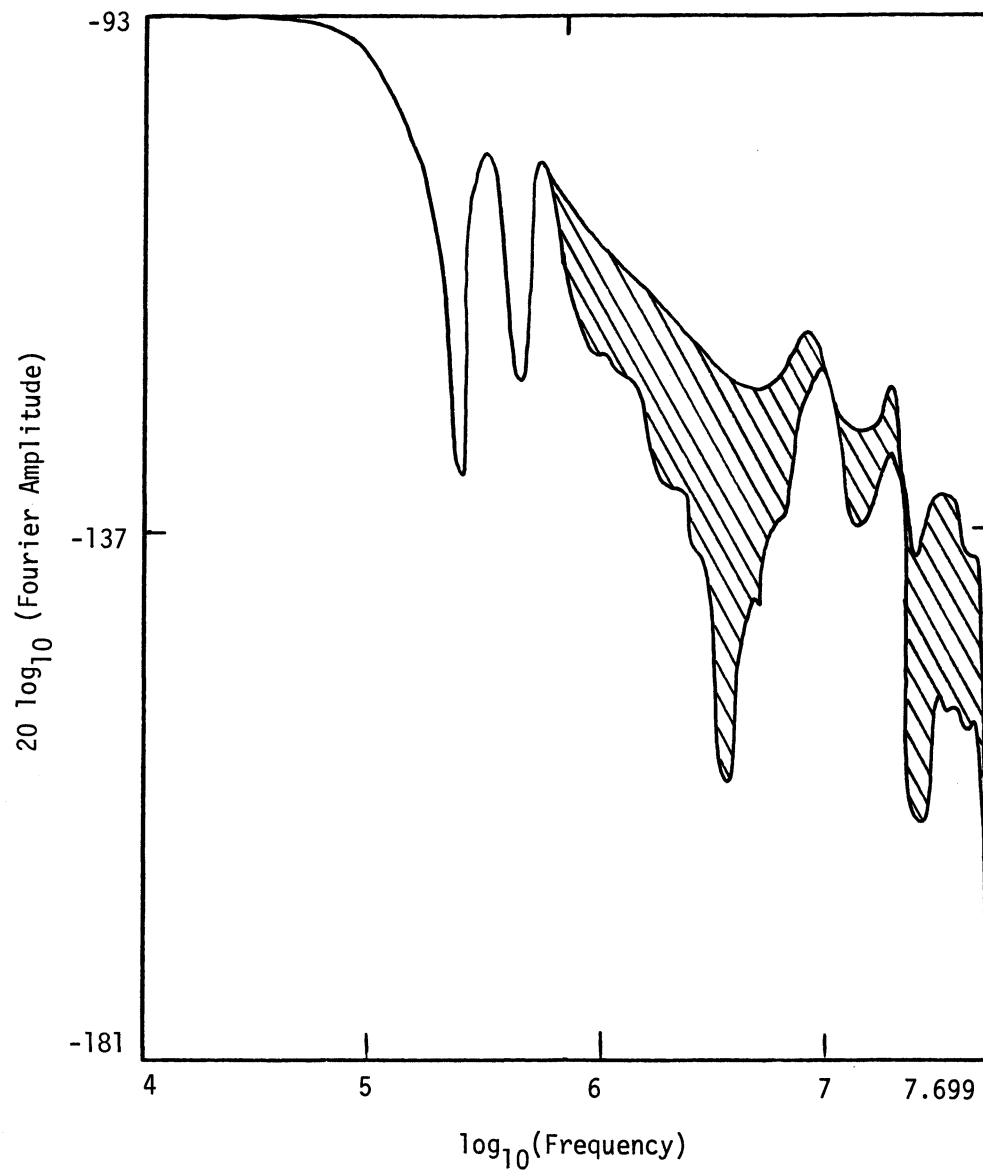


Figure 3.7 Fourier Transform of D-dot Response of Flight 80-018
(Hatched Area Indicates Closely Spaced Resonances)

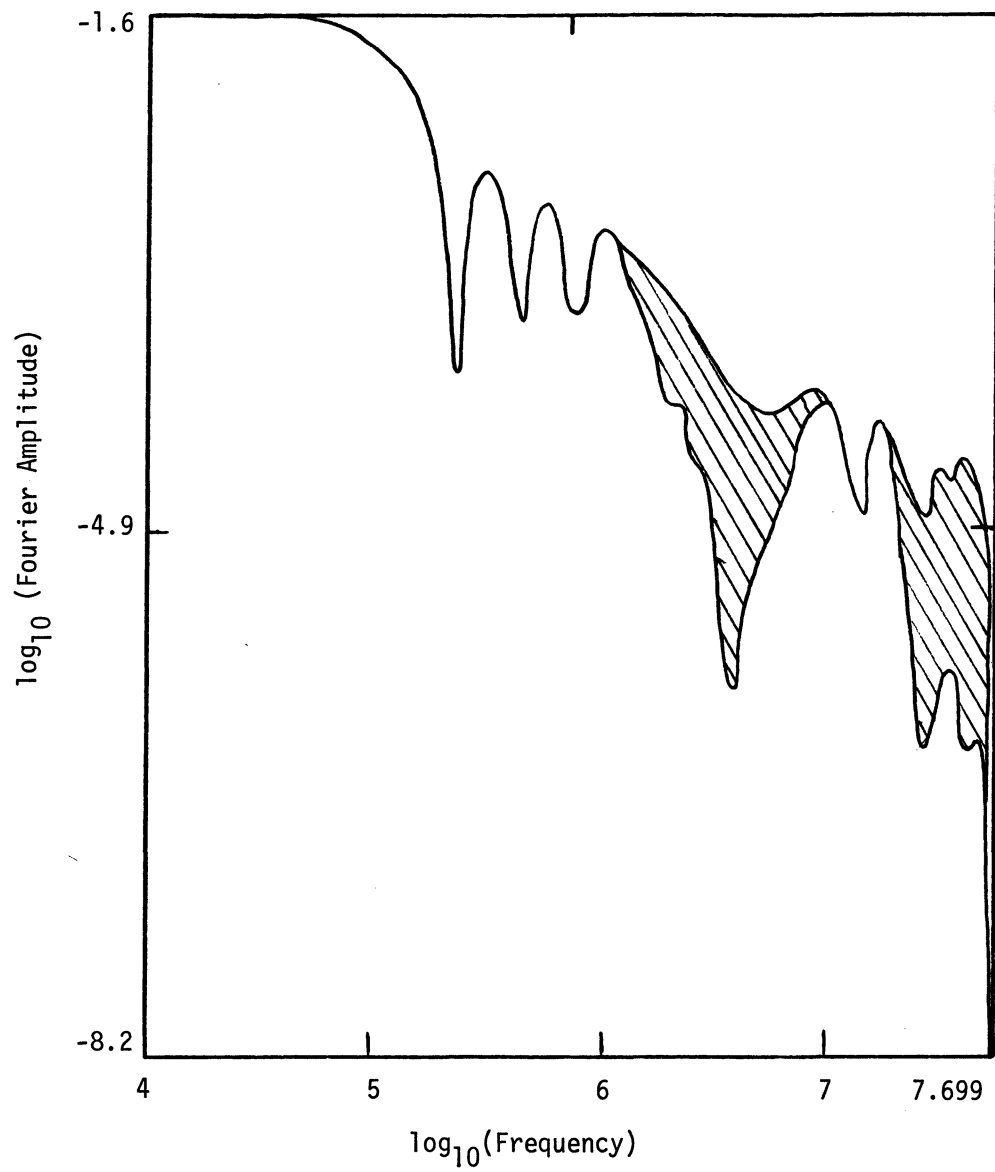


Figure 3.8 Fourier Transform of Current Source Needed to Give Forward D-dot Response of Flight 80-018

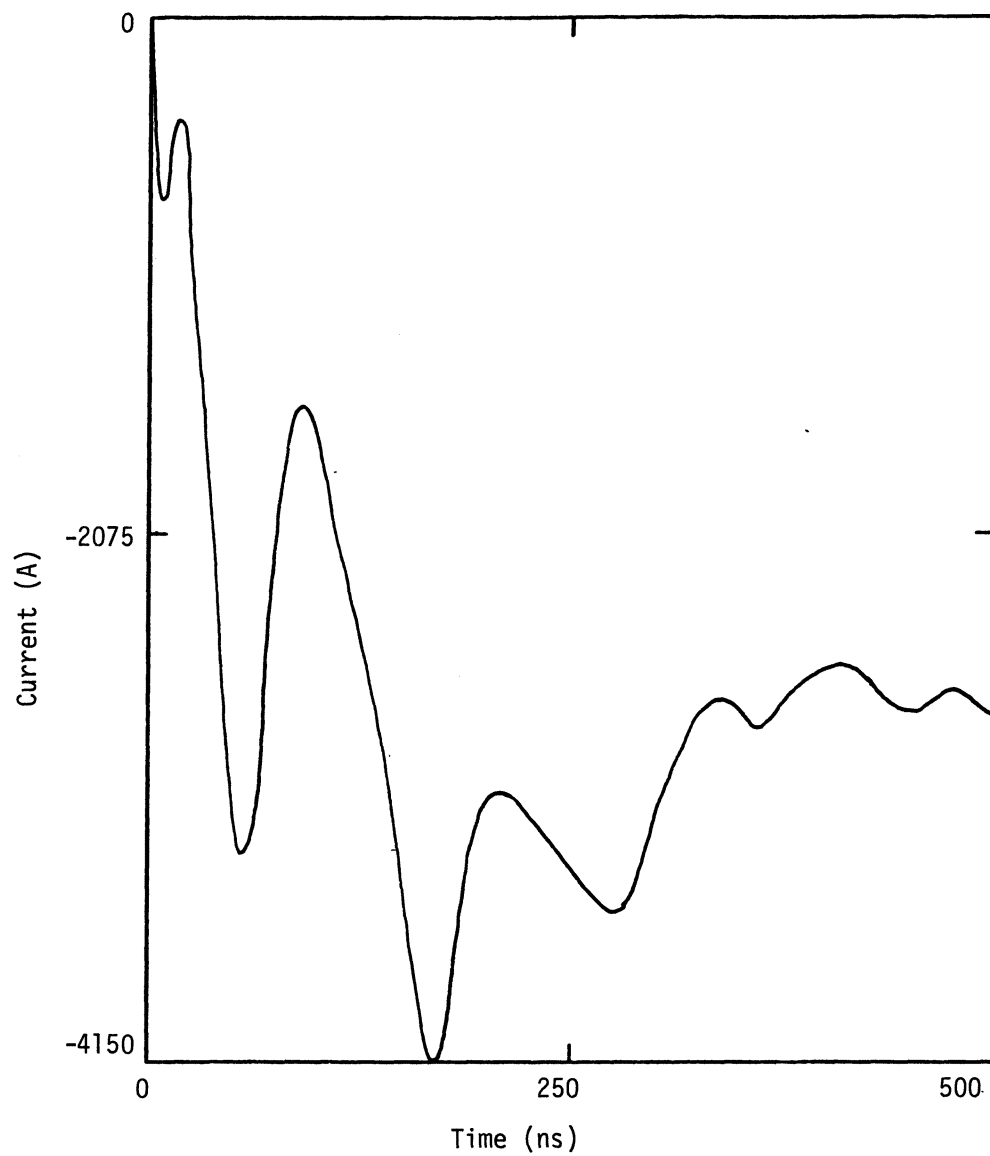


Figure 3.9 Time Domain Representation of Current Source Needed to Give Forward D-dot Response of Flight 80-018 (to 500 ns)

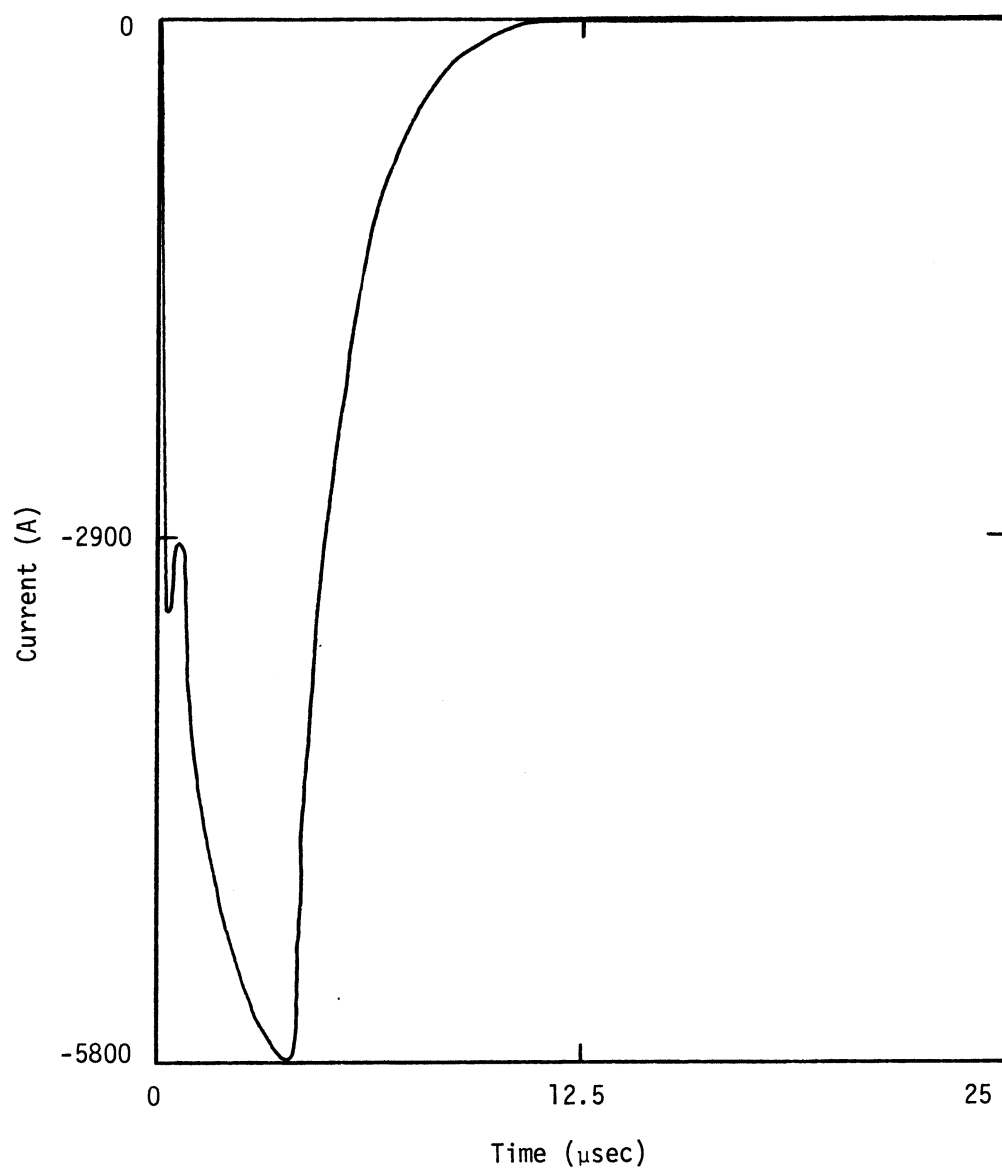


Figure 3.10 Time Domain Representation of Current Source Needed to Give Forward D-dot Response of Flight 80-018 (to 25 μsec)

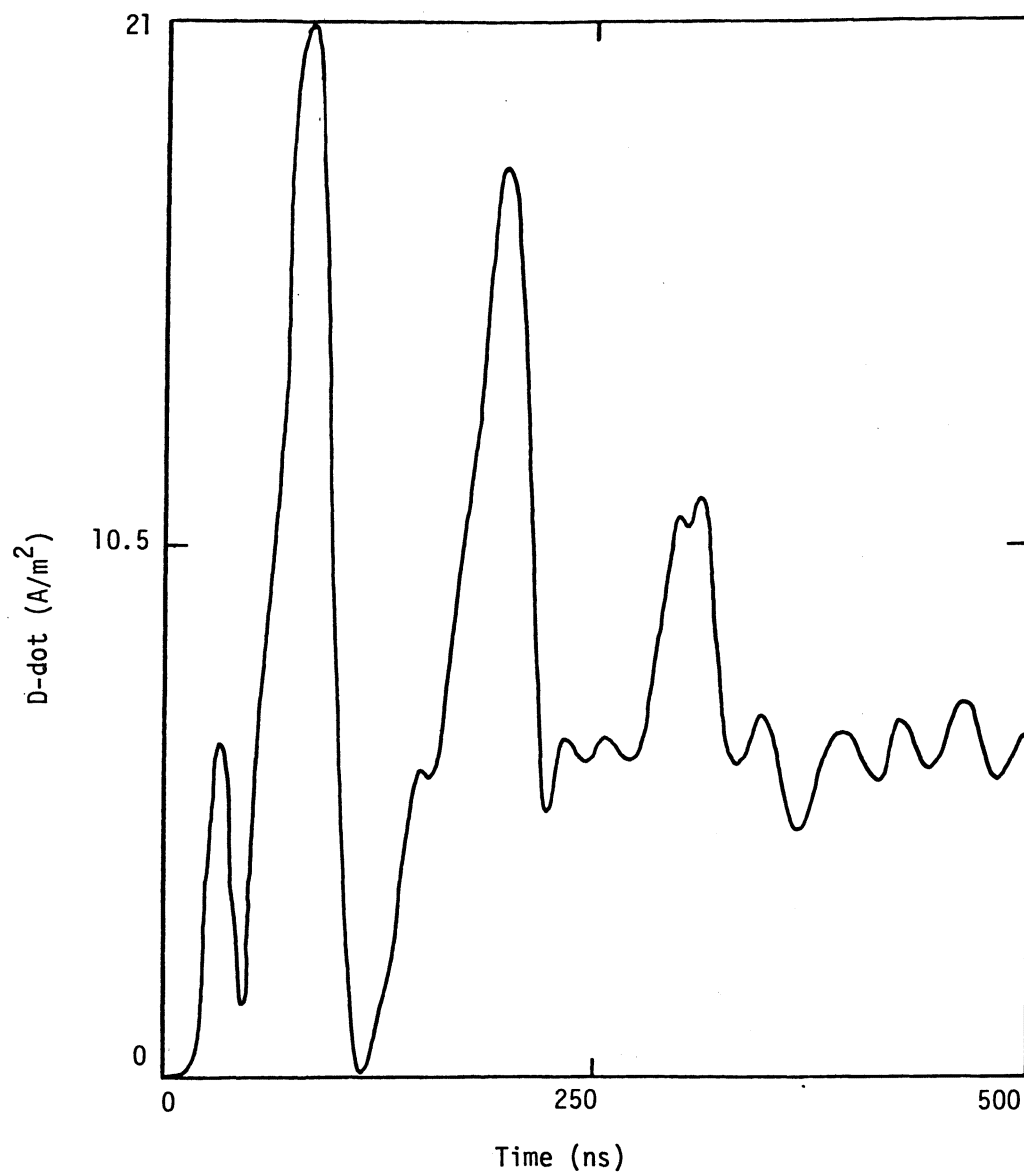


Figure 3.11 Forward D-dot Response of F106 to Current Source o
Figure 3.9

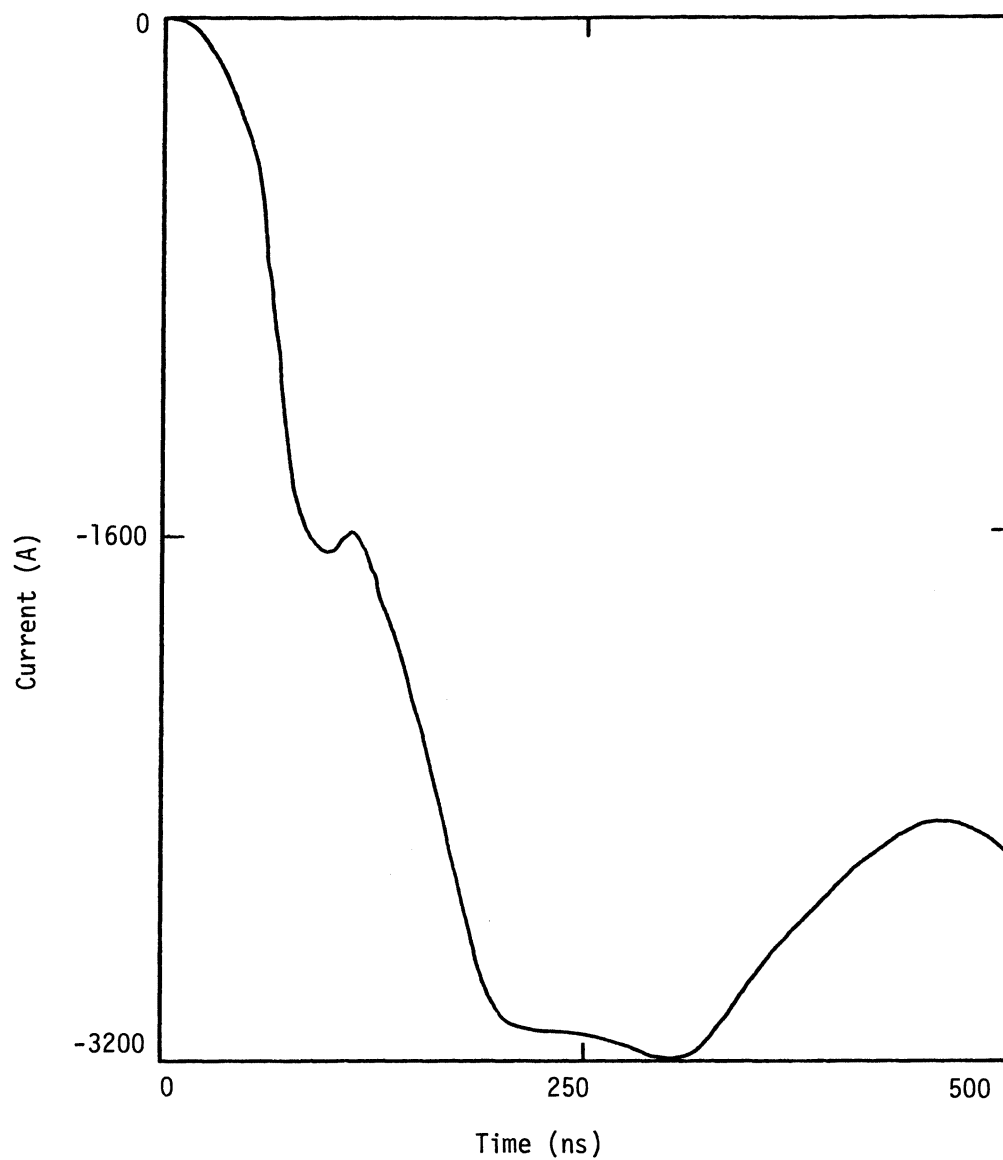


Figure 3.12 Actual Injected Current at Nose of F106 to Obtain D-dot Response of Figure 3.11

without the F106 present. That is, the lightning channel ran completely across the finite difference problem space. The current at the former position of the nose of the F106 was monitored, and it is shown in Figure 3.13. In principle, this current should be an indication of the lightning environment. It is the current flowing in the lightning channel in the absence of the aircraft. Figures 3.14 and 3.15 are the same as Figures 3.12 and 3.13, except on a larger time scale to illustrate peak values.

Figures 3.16 - 3.27 show the injected current at the nose of the F106 and the current at that position without the F106 present for a variety of channel parameters as indicated on the figures. The currents are all appropriate to produce the measured D-dot response of Figure 3.6. In all cases the exit channel ran from the base of the tail to the boundary. There are several cases in which the exit channel from the aircraft is listed as being a perfectly conducting wire. This does not affect the run that was made with the F106 removed. The channel for that run had no perfectly conducting section and was a uniform thin wire across the entire problem space.

Some things should be noted about Figures 3.14 - 3.27. First, all of the currents injected at the nose of the F106 are very similar, both in character and amplitude. This is a reflection of the fact that the transfer function between the current injected at the nose and the D-dot response is dependent almost entirely on the geometry of the aircraft, and only incidentally on the channel parameters. However, the current flowing at the same positions without the F106 present is strongly dependent on channel parameters, as expected. The amplitude of the injected current which produces the measured D-dot should also be noticed. This amplitude for a given D-dot will in general be a function of two variables, the peak amplitude of the D-dot record and the length of the record in time. That is, large injected currents must result in either large D-dot peaks or long time records. The record of flight 80-018 is both largest in amplitude and longest in time of the measured D-dot responses. Hence it is reasonable to infer that the injected current calculated for that record is the largest seen so far in the measured D-dot's, so all lightning strikes which produced D-dot records must have had peak currents of less than 10,000 amperes. In fact, since most of the D-dot records are significantly smaller both in peak amplitude

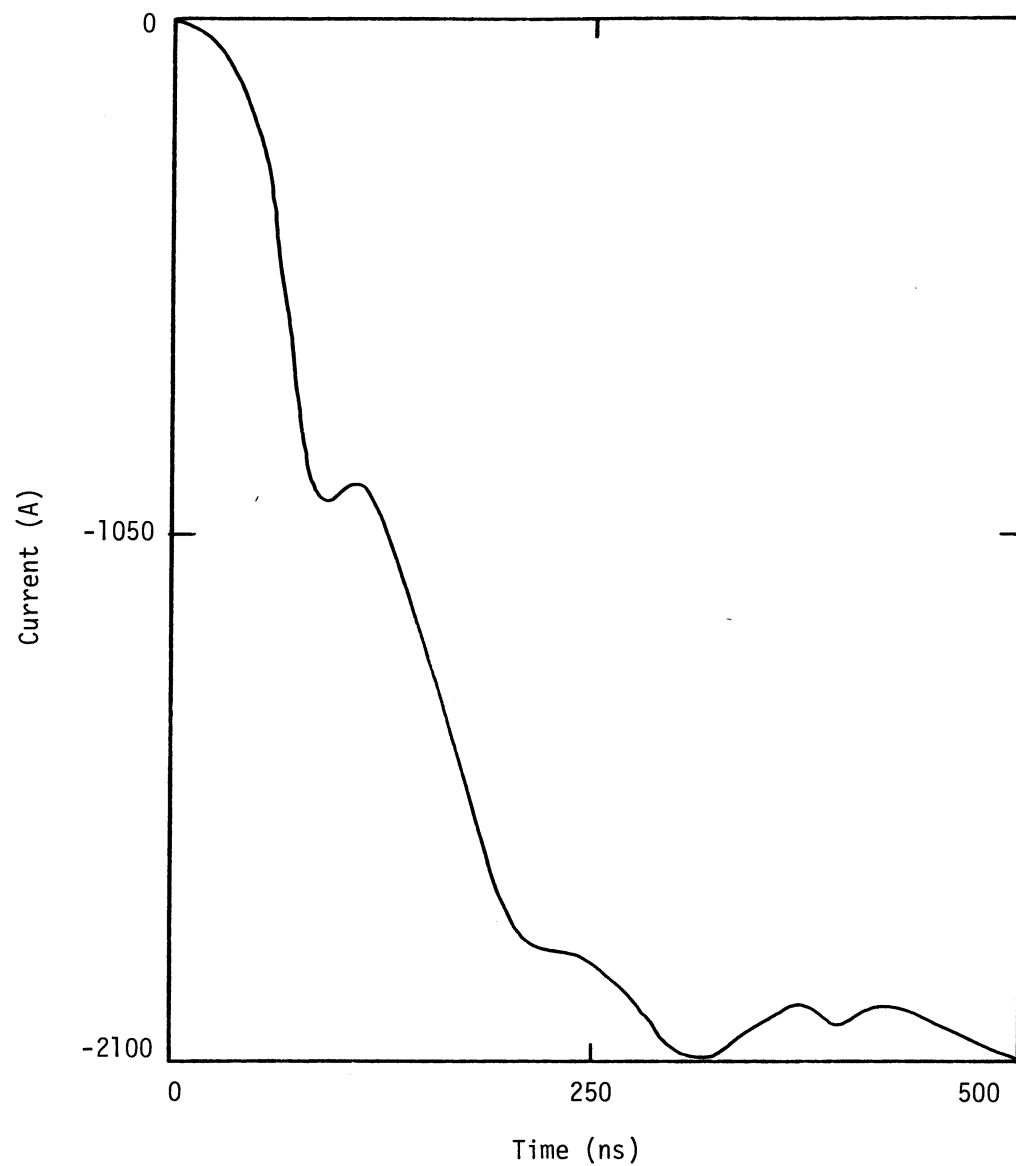


Figure 3.13 Current at the Position of the Injection Point for the Case in Which the F106 Was Not Present

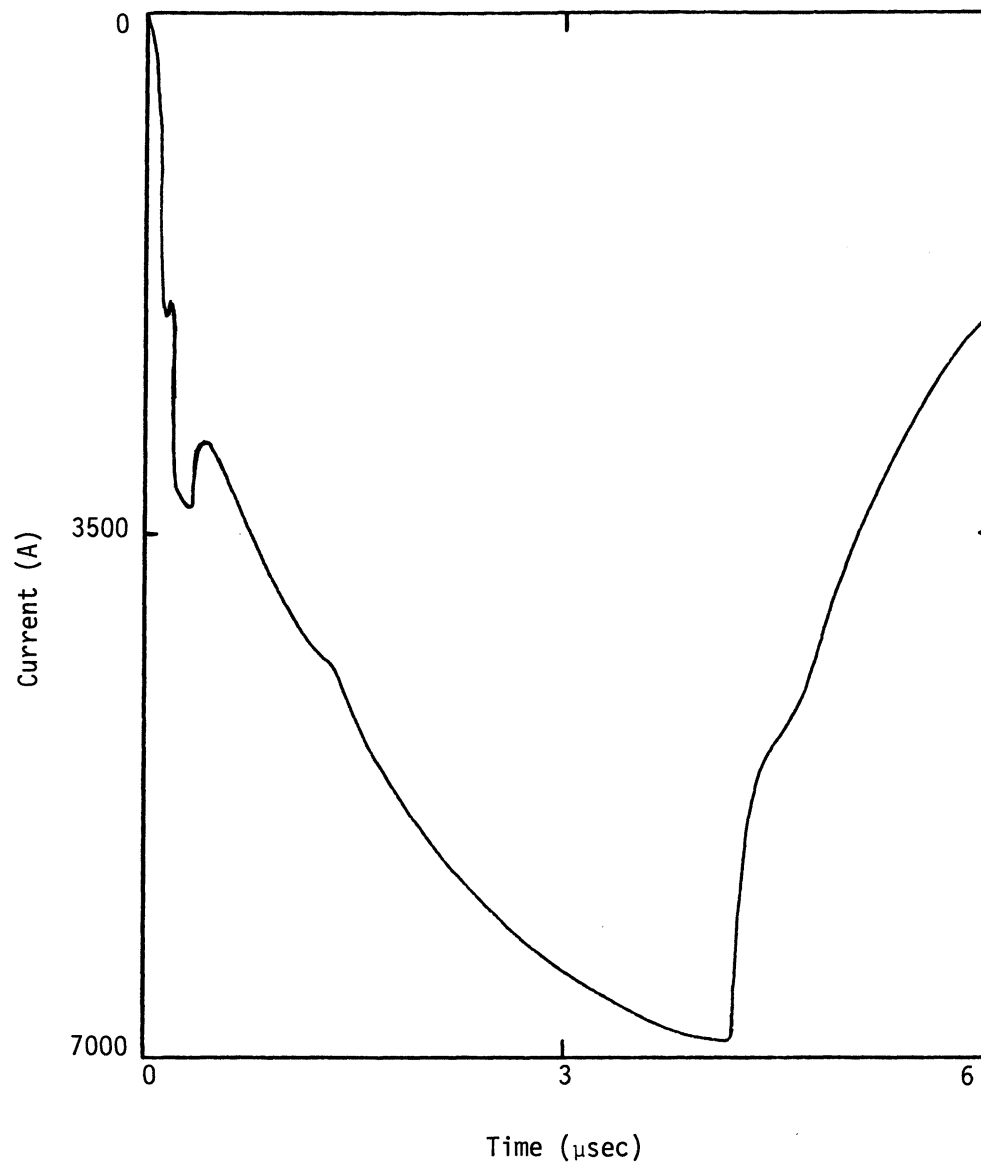


Figure 3.14 Actual Injected Current at Nose of F106 to Obtain D-dot Response of Figure 3.12 (to 6 μ s)

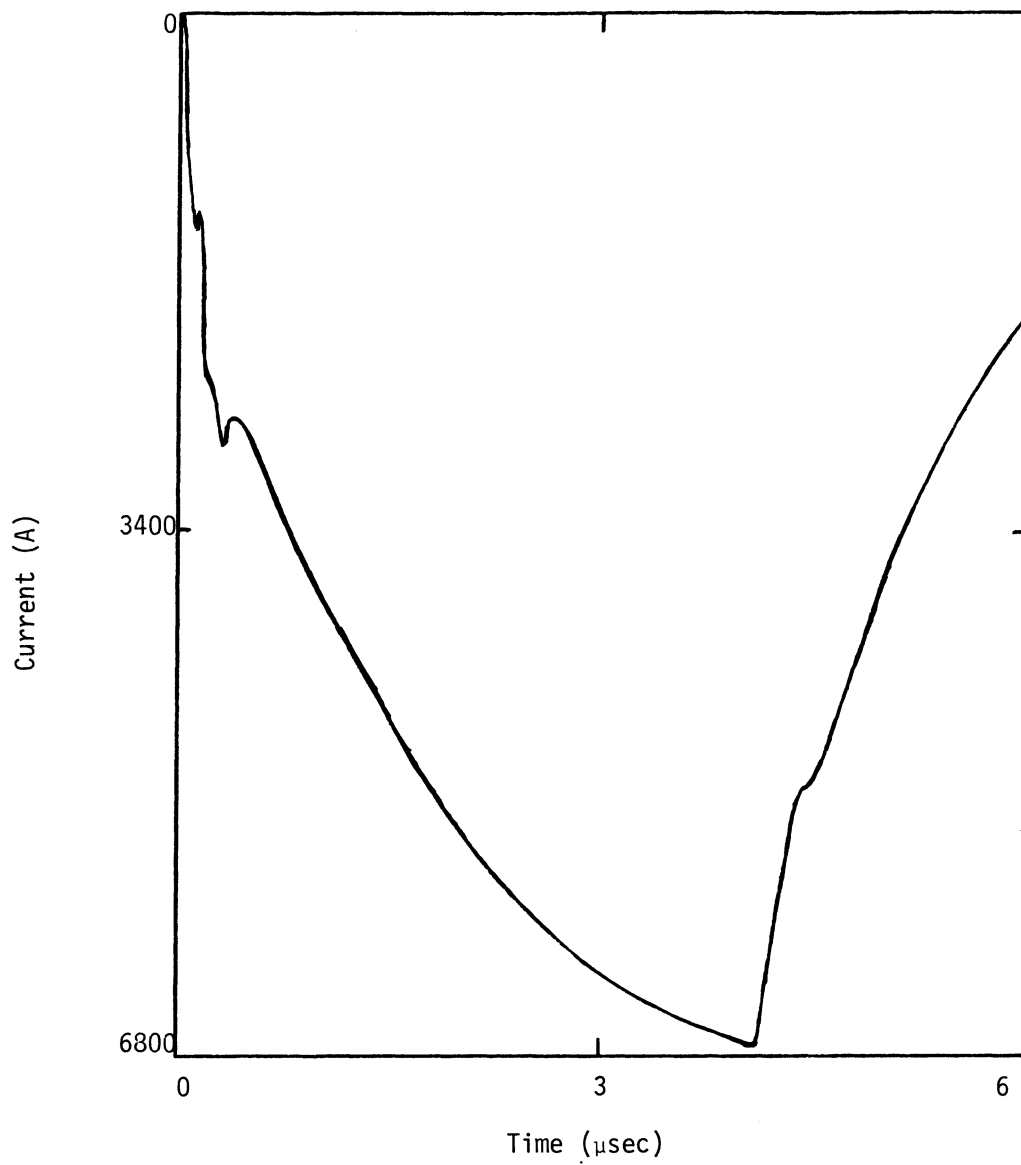


Figure 3.15 Current at the Position of the Injection Point for the Case in Which the F106 was Not Present (to 6 μs)

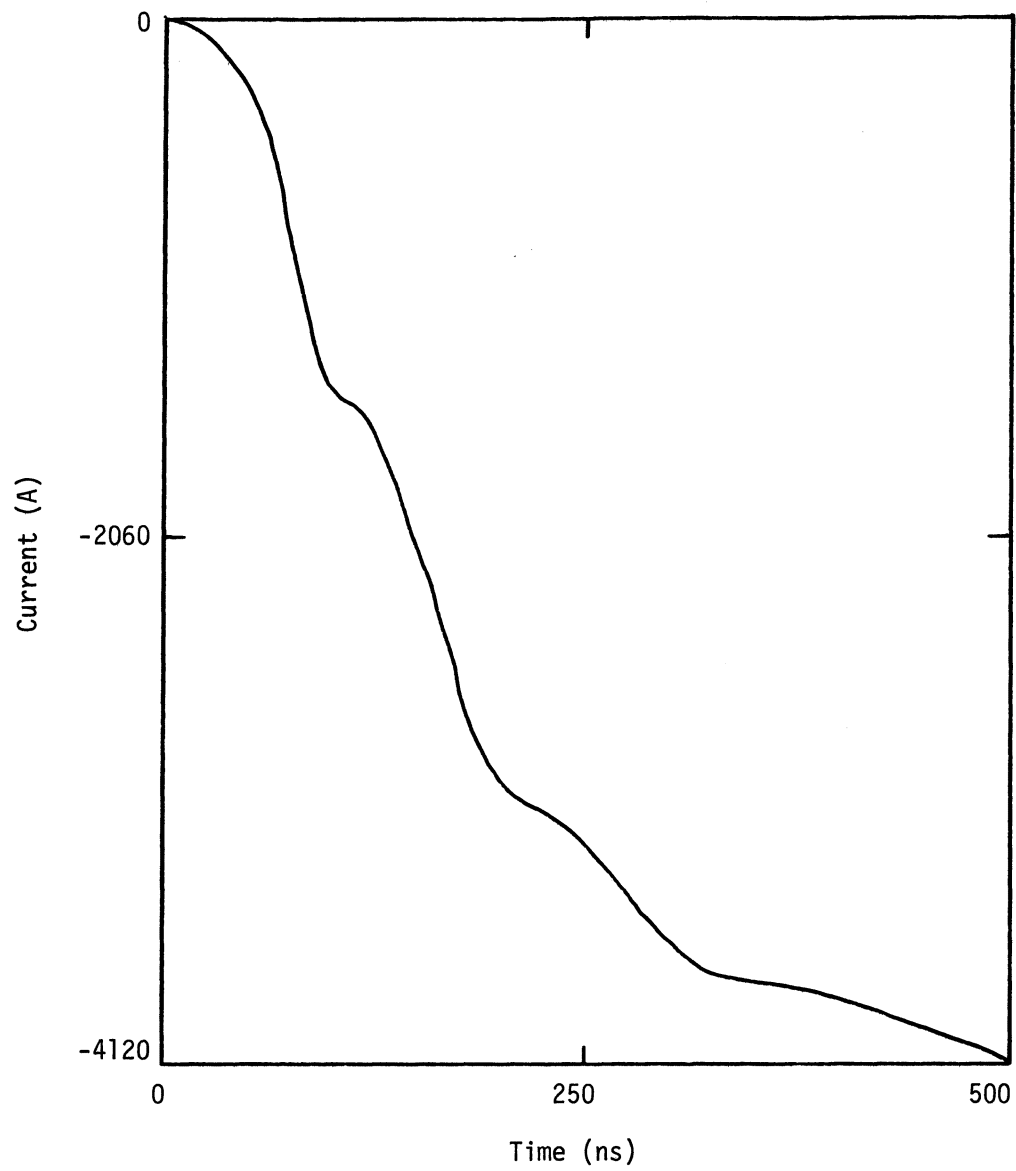


Figure 3.16 Current Injected Into F106 ($L_\ell = 3.33 \times 10^{-7}$ h/m
 $C_\ell = 3.33 \times 10^{-11}$ f/m
 $R_\ell = 0 \Omega/m$)

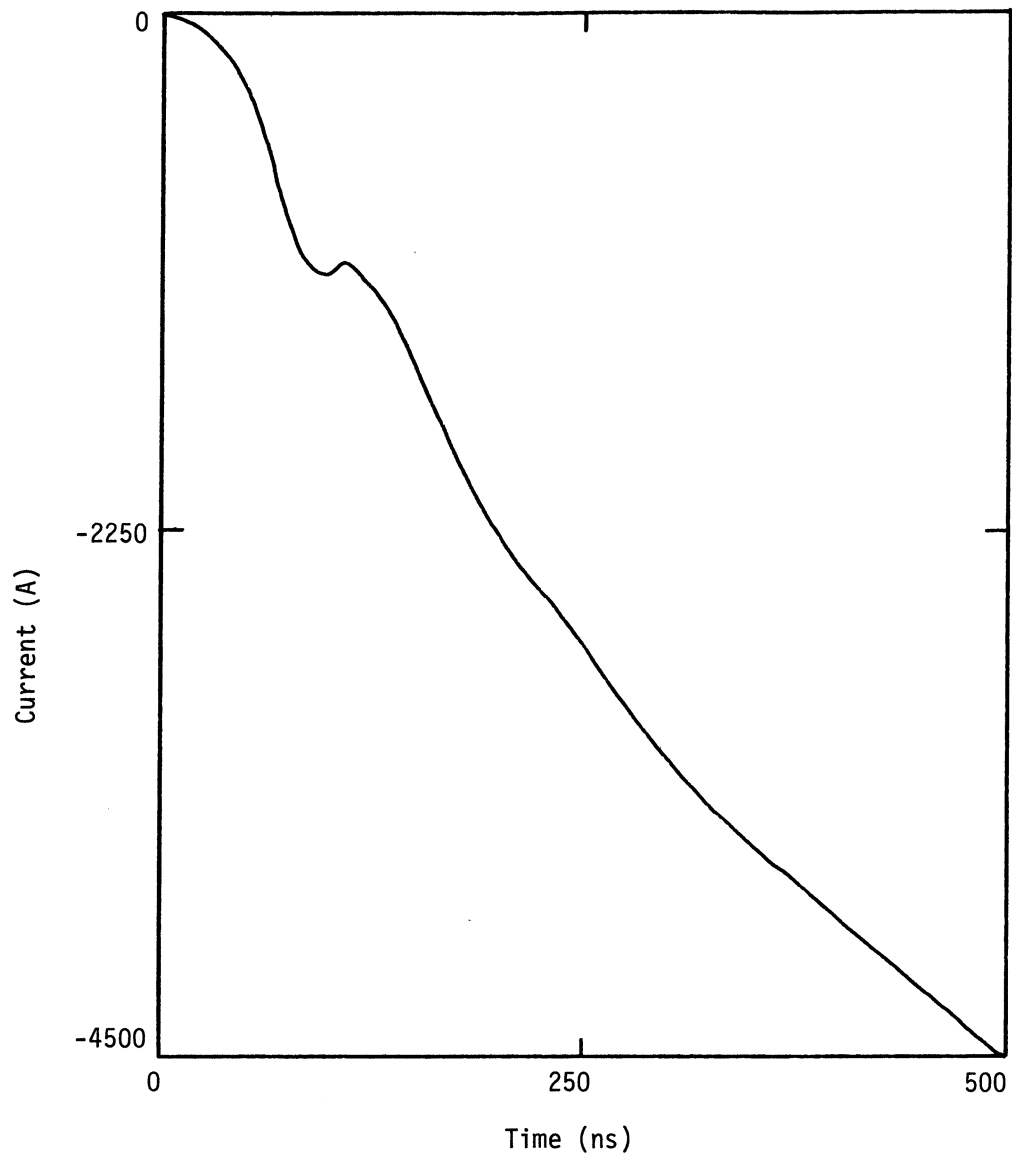


Figure 3.17 Current at Injection Point Without F106

$$\begin{aligned}
 (L_{\ell} &= 3.33 \times 10^{-7} \text{ h/m} \\
 C_{\ell} &= 3.33 \times 10^{-11} \text{ f/m} \\
 R_{\ell} &= 0 \text{ } \Omega/\text{m})
 \end{aligned}$$

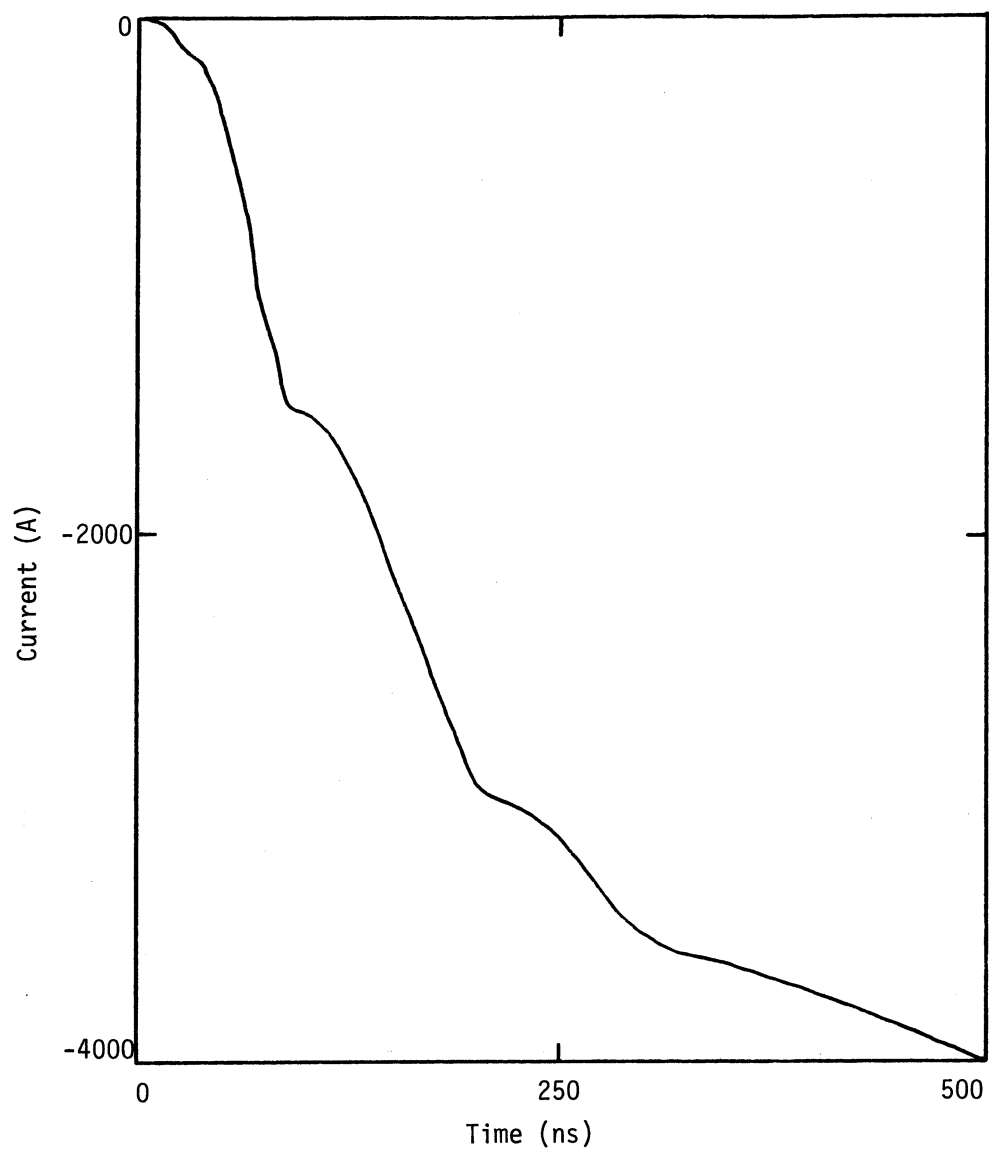


Figure 3.18 Current Injected Into F106 ($L_\ell = 3.33 \times 10^{-7}$ h/m
 $C_\ell = 3.33 \times 10^{-11}$ f/m
 $R_\ell = 0 \Omega/m$
 Exit Channel a Perfectly
 Conducting Wire)

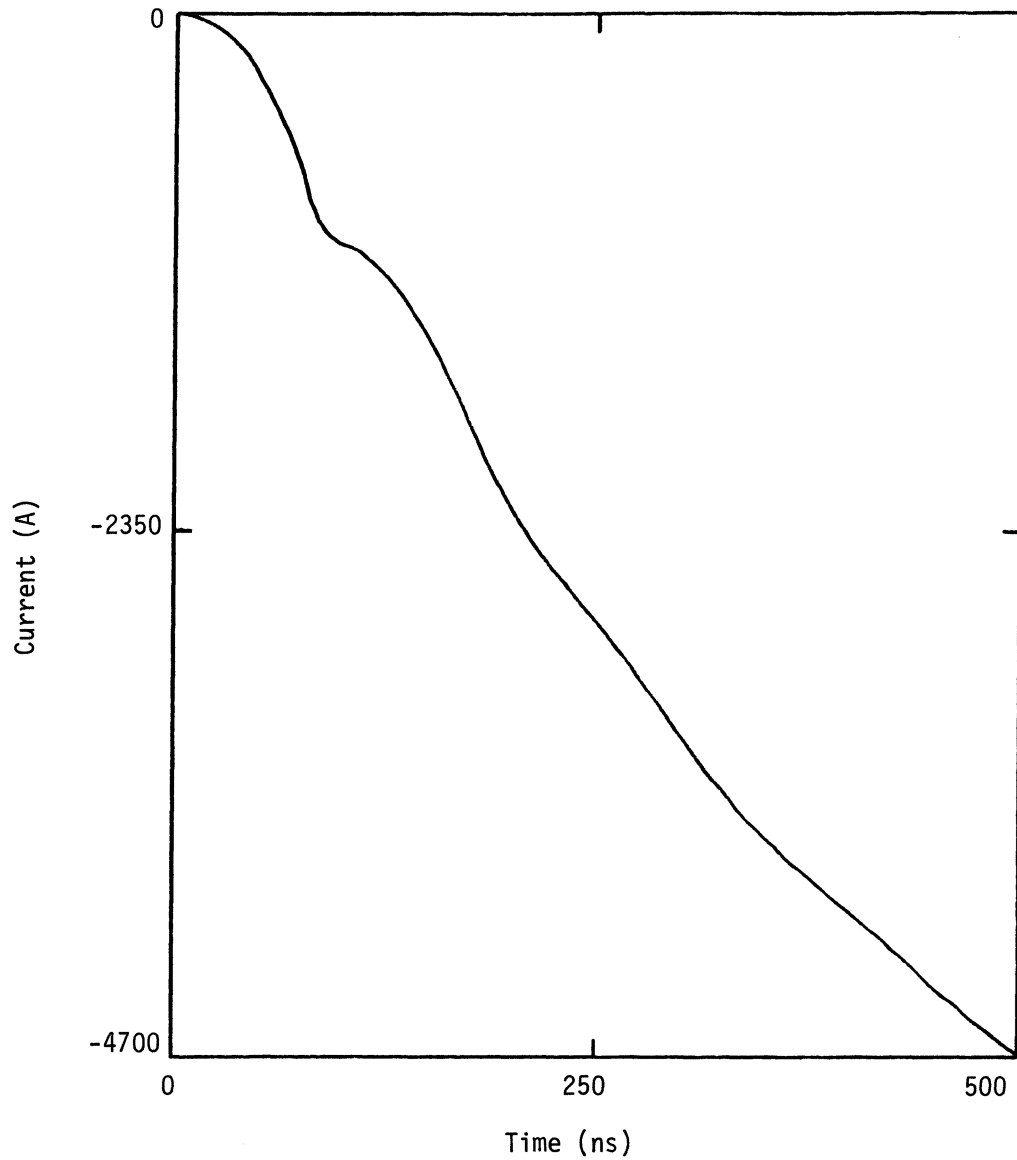


Figure 3.19 Current at Injection Point Without F106

$$\begin{aligned}
 (L_{\lambda} &= 3.33 \times 10^{-7} \text{ h/m} \\
 C_{\lambda} &= 3.33 \times 10^{-11} \text{ f/m} \\
 R_{\lambda} &= 0 \text{ } \Omega/\text{m}
 \end{aligned}$$

Exit Channel a Perfectly
Conducting Wire)

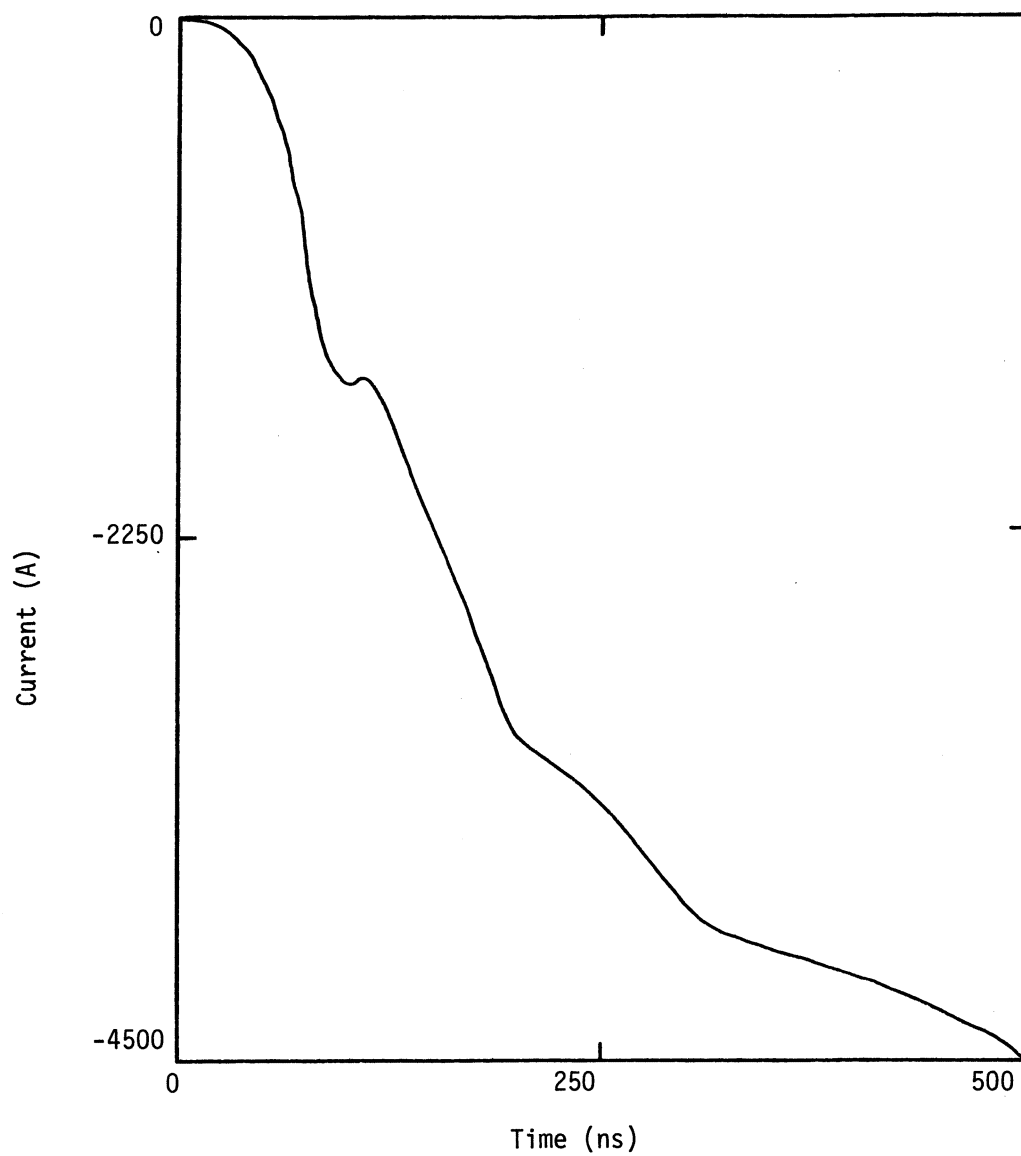


Figure 3.20 Current Injected Into F106 ($L_\ell = 1.67 \times 10^{-7}$ h/m
 $C_\ell = 6.67 \times 10^{-11}$ f/m
 $R_\ell = 50 \Omega/\text{m}$
Exit Channel a Perfectly
Conducting Wire)

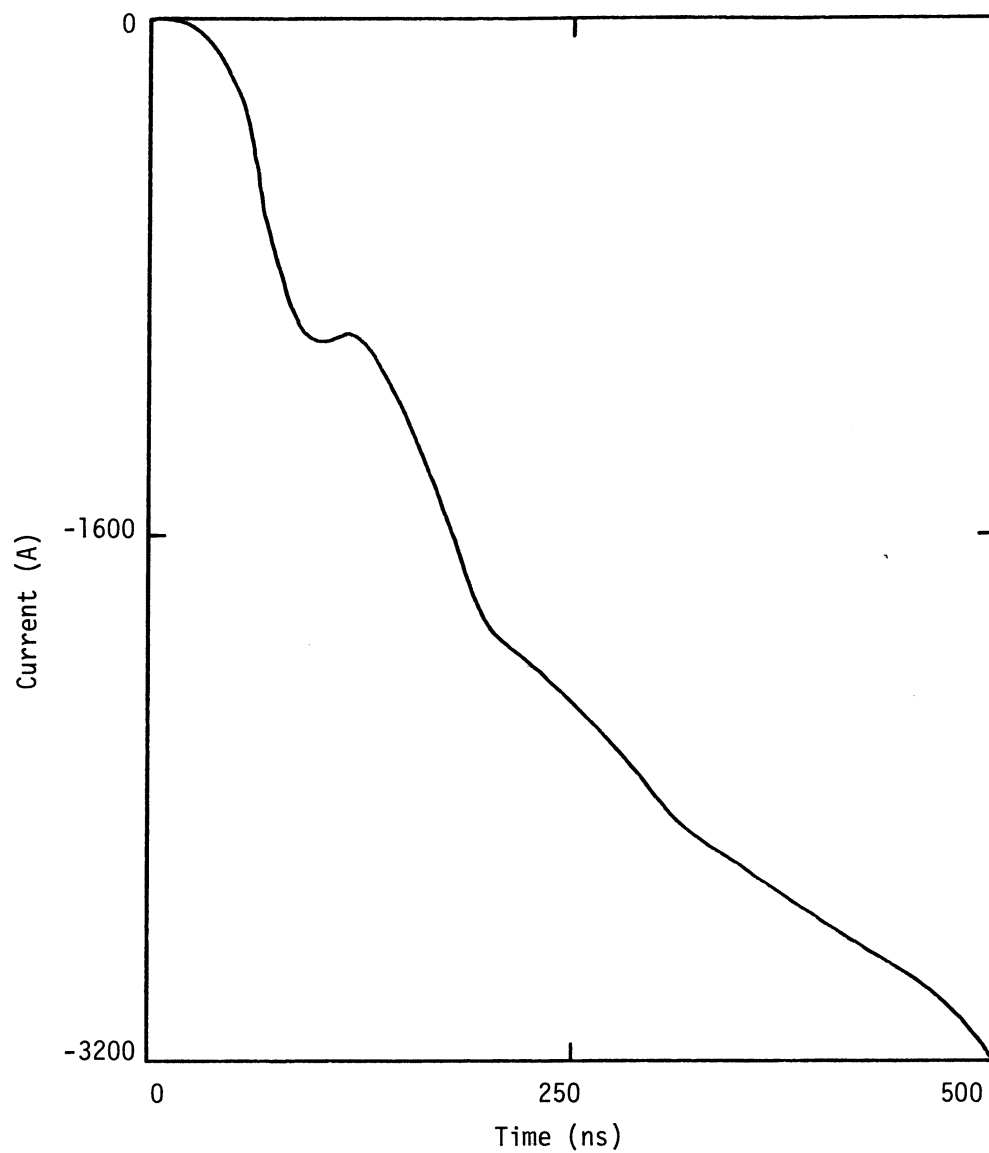


Figure 3.21 Current at Injection Point Without F106

$$(L_{\ell} = 1.67 \times 10^{-7} \text{ h/m})$$

$$C_{\ell} = 6.67 \times 10^{-11} \text{ f/m}$$

$$R_{\ell} = 50 \text{ } \Omega/\text{m}$$

Exit Channel a Perfectly
Conducting Wire)

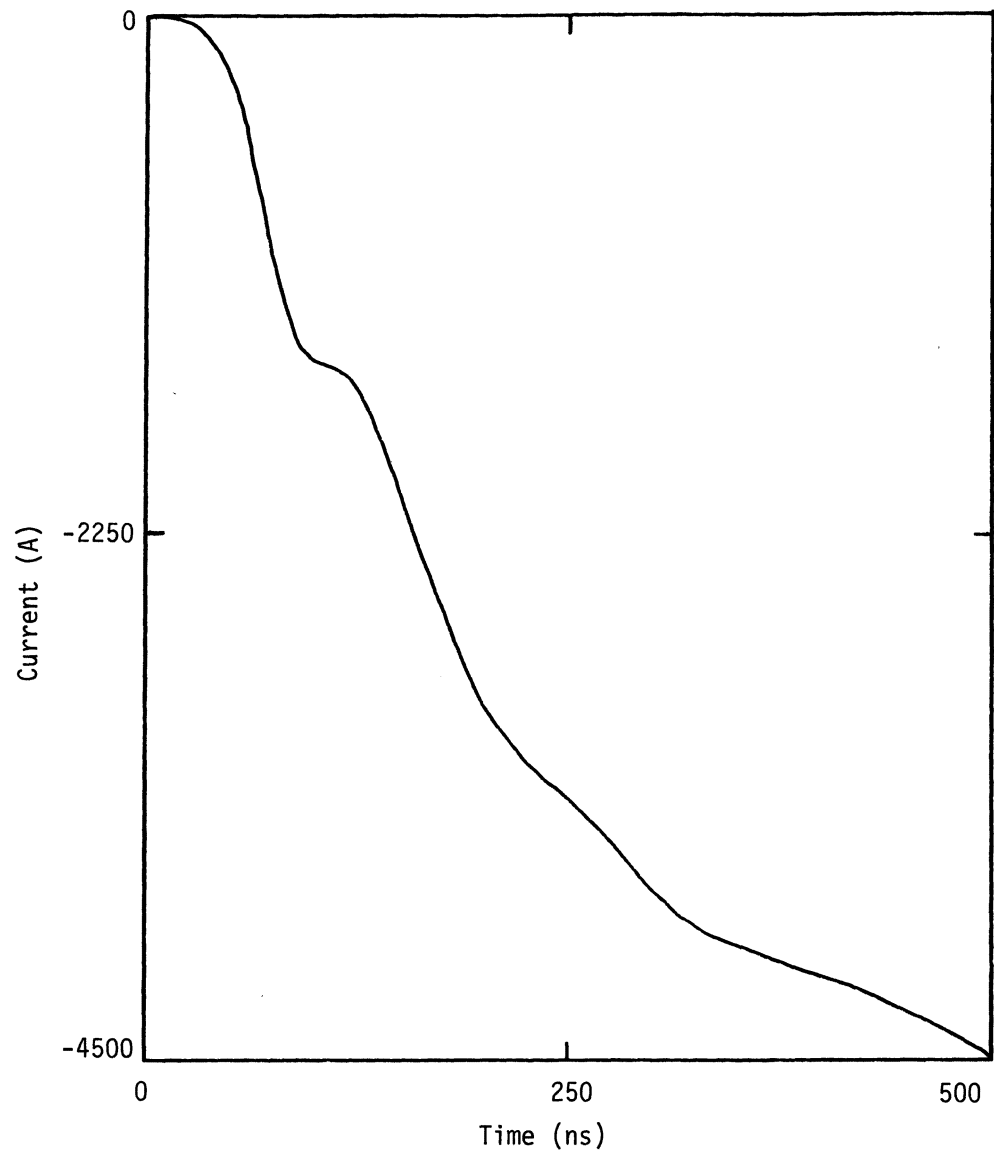


Figure 3.22 Current Injected Into F106 ($L_\ell = 5 \times 10^{-7}$ h/m
 $C_\ell = 2 \times 10^{-10}$ f/m
 $R_\ell = 50 \Omega/\text{m}$
Exit Channel a Perfectly
Conducting Wire)

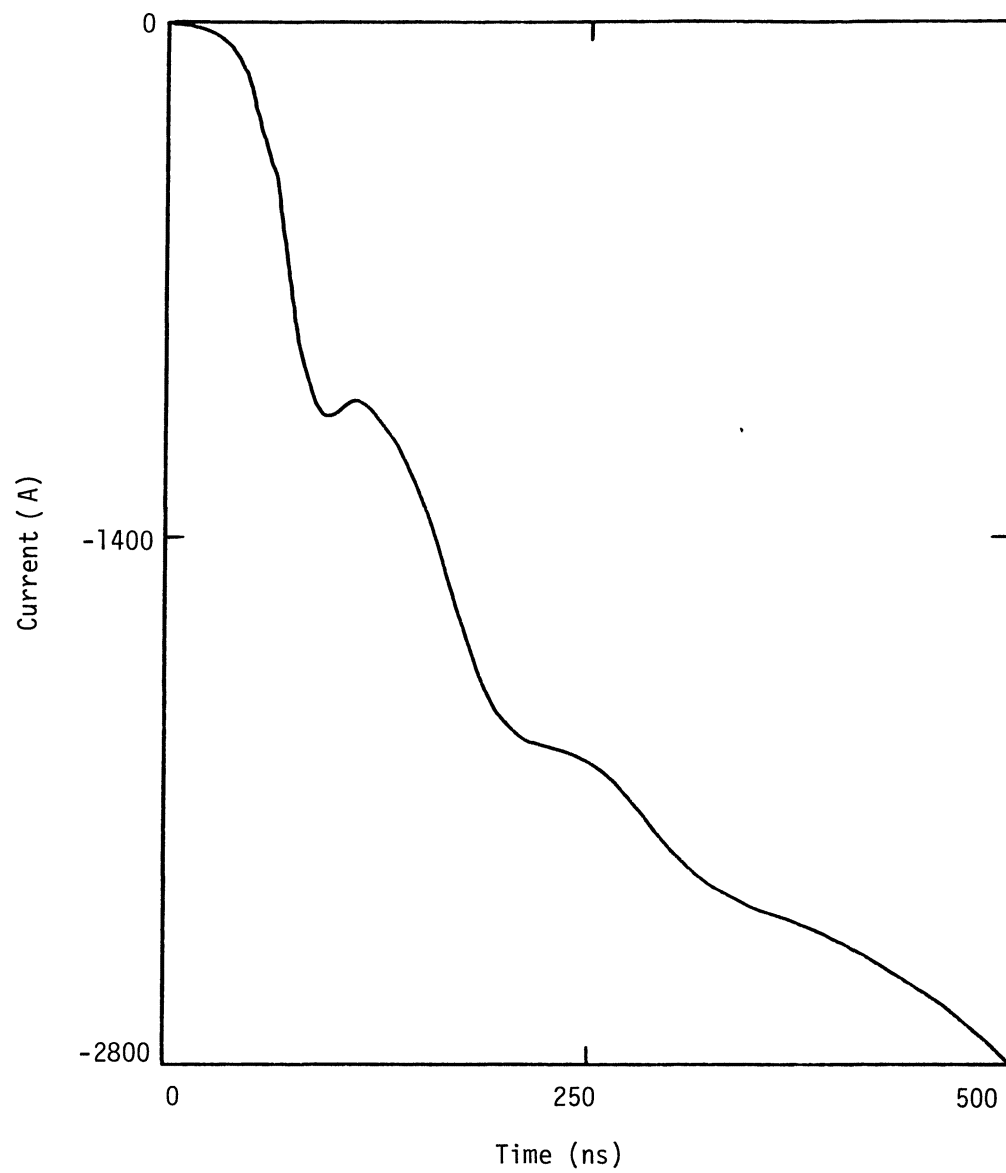


Figure 3.23 Current at Injection Point Without F106

$$\begin{aligned}
 (L_{\ell} &= 5 \times 10^{-7} \text{ h/m} \\
 C_{\ell} &= 2 \times 10^{-10} \text{ f/m} \\
 R_{\ell} &= 50 \text{ } \Omega/\text{m}
 \end{aligned}$$

Exit Channel a Perfectly
Conducting Wire)

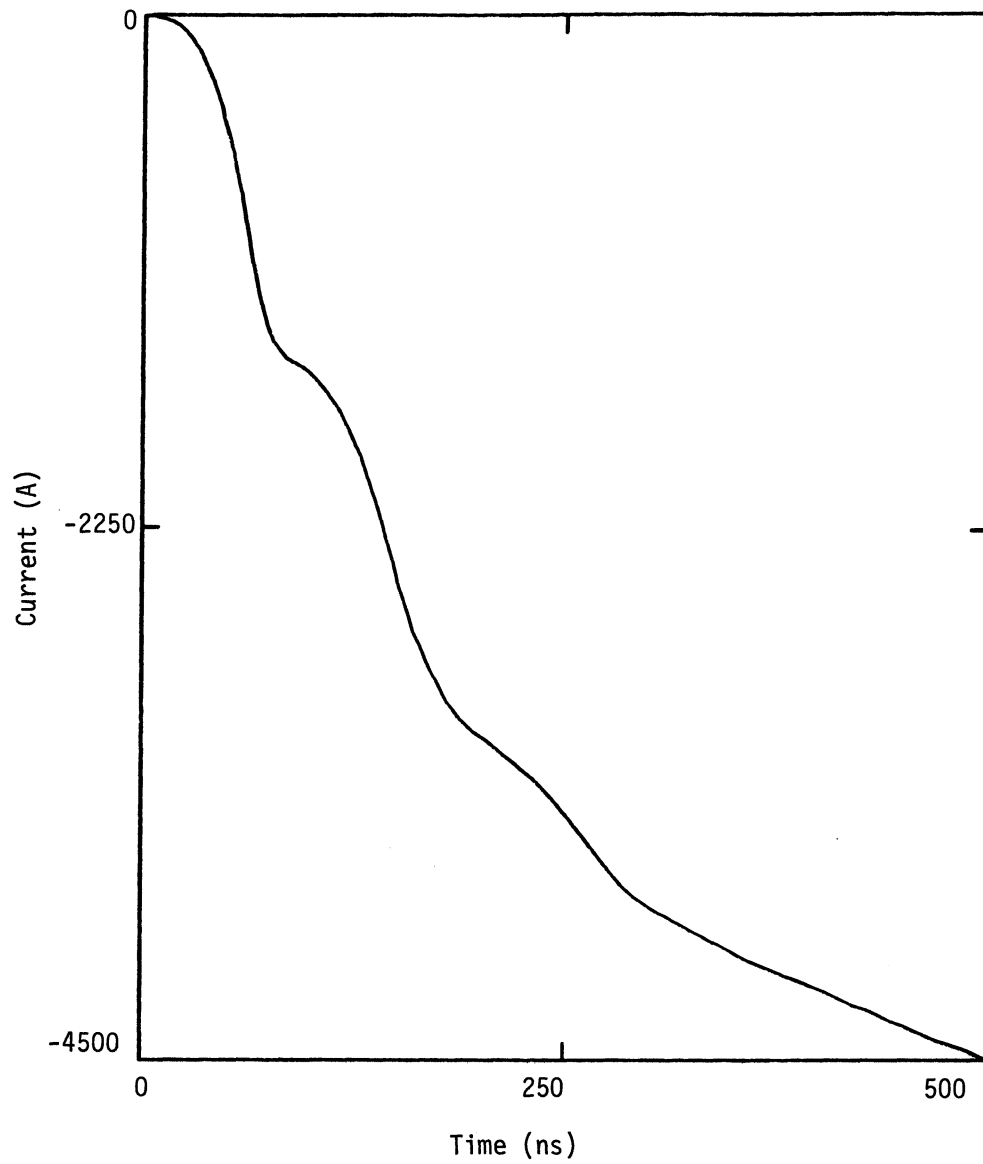


Figure 3.24 Current Injected Into F106 ($L_{\ell} = 1.67 \times 10^{-7}$ h/m
 $C_{\ell} = 6.67 \times 10^{-11}$ f/m
 $R_{\ell} = 0 \Omega/m$
Exit Channel is Perfectly
Conducting Wire)

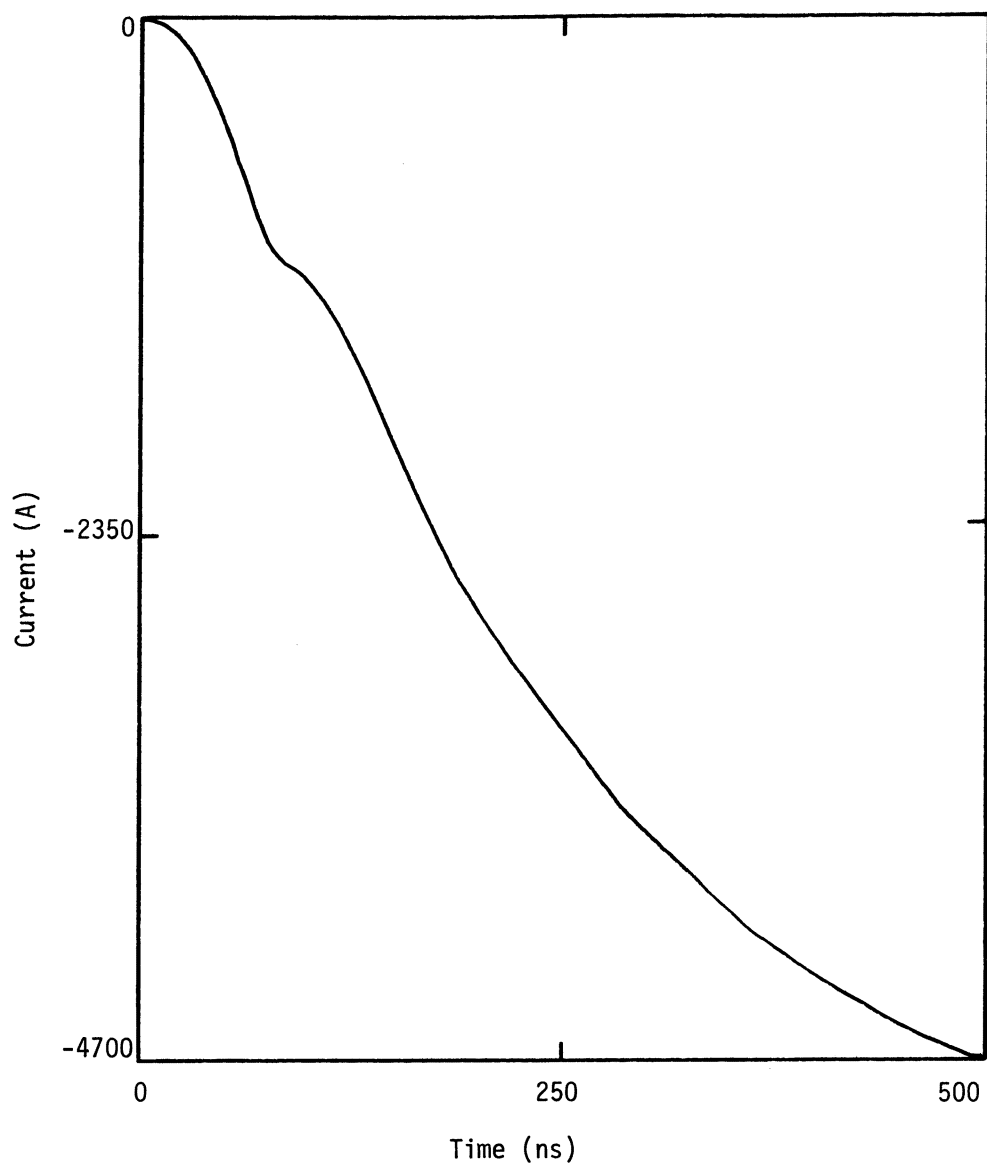


Figure 3.25 Current at Injection Point Without F106

$$(L_{\ell} = 1.67 \times 10^{-7} \text{ h/m})$$

$$C_{\ell} = 6.67 \times 10^{-11} \text{ f/m}$$

$$R_{\ell} = 0 \text{ } \Omega/\text{m}$$

Exit Channel a Perfectly
Conducting Wire)

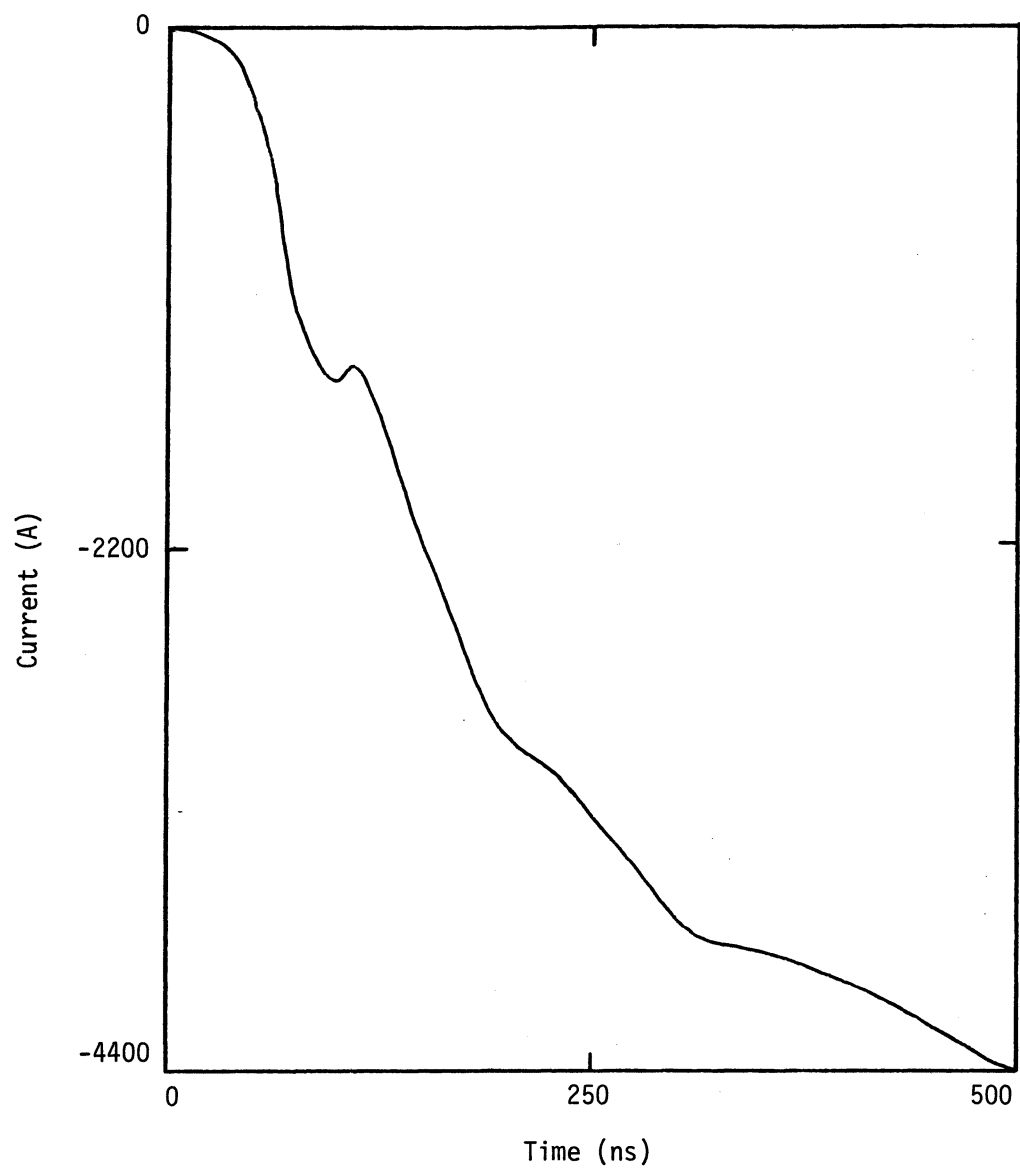


Figure 3.26 Current Injected Into F106 ($L_\ell = 5 \times 10^{-7}$ h/m
 $C_\ell = 2 \times 10^{-10}$ f/m
 $R_\ell = 0 \Omega/\text{m}$
Exit Channel a Perfectly
Conducting Wire)

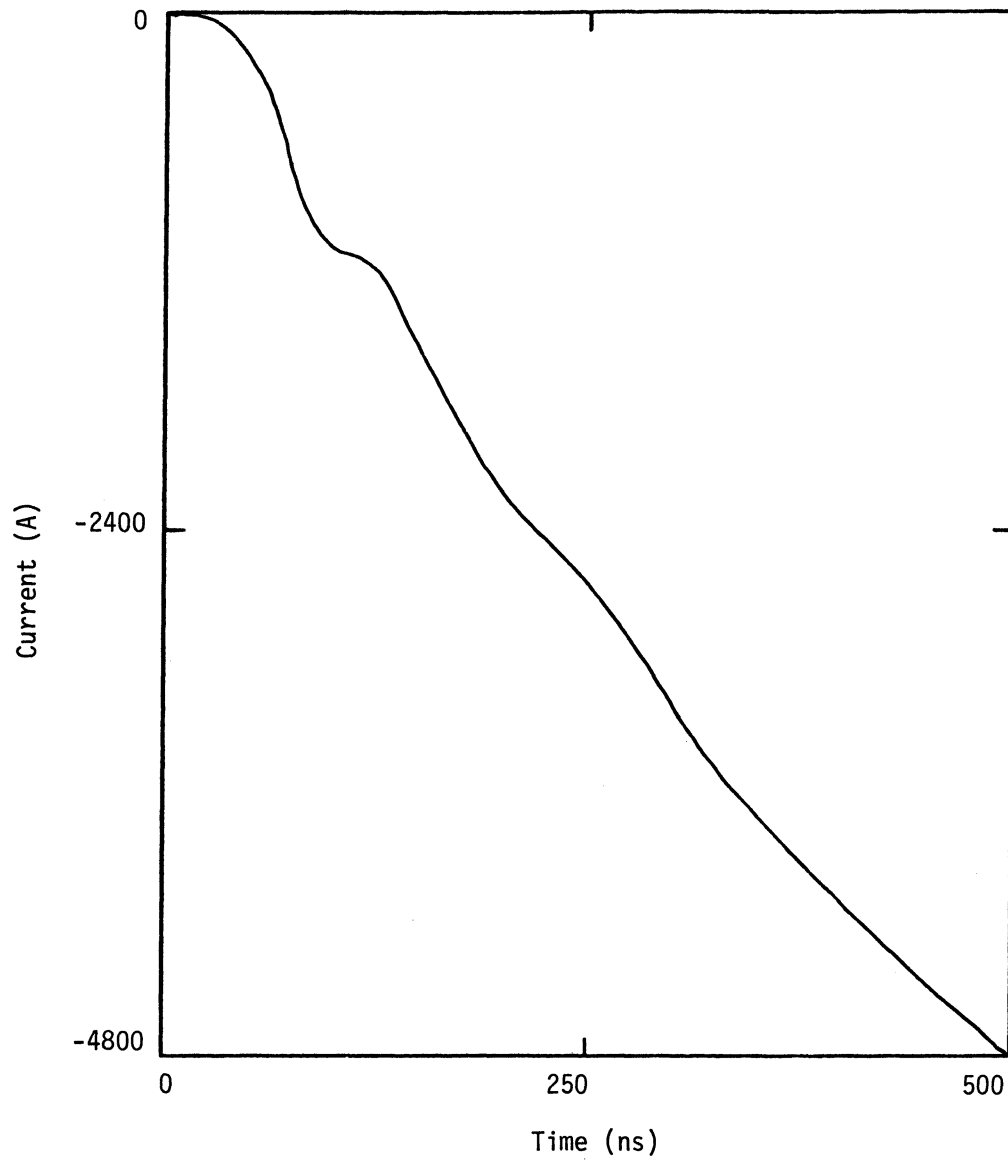


Figure 3.27 Current at Injection Point Without F106

$$(L_{\ell} = 5 \times 10^{-7} \text{ h/m})$$

$$C_{\ell} = 2 \times 10^{-10} \text{ f/m}$$

$$R_{\ell} = 0 \text{ } \Omega/\text{m}$$

Exit Channel a Perfectly
Conducting Wire)

and duration, it is probable that a majority of the recorded strikes so far have had current amplitudes of less than a thousand amperes.

3.3 Time Correlated Data Analysis

Near the end of the contract period work began on the time correlated D-dot and B-dot measurements taken on the F106 aircraft during the summer of 1982. These records have similar features which allow one to recognize that both were produced by a single lightning event. There is no information, however, on which record led the other in time; that is, whether the B-dot or D-dot event occurred first. The methodology for analyzing these records is basically the same as for single records. A channel is chosen and a source determined as previously described for a single record, either B-dot or D-dot. Then the analysis is done for the second of the time correlated measurements and a second source determined. In general the two sources will be different. This indicates that something about the chosen lightning channel is incorrect. By varying the channel parameters and orientation it should be possible to bring the two calculated sources into agreement, so that the one remaining source will produce both of the measured records. At this point, though the calculated source is not mathematically unique, it is hoped that it can be regarded as physically unique, in the sense that if a third response on the aircraft were measured, it would automatically be predicted by the calculated source. If this were not the case, the process of varying the channel characteristics would need to be redone until one source produced all three responses.

The analysis of the time correlated measurements has concentrated on the records from flight 82-039 (Figures 3.28 and 3.29). because of their relatively large dynamic range and short record length. These factors contribute to accuracy and shorter computer runs respectively. Figures 3.30 - 3.37 give an example of the methodology used in dealing with the time correlated data. A channel was chosen and a source derived from the measured D-dot record. This was then used to drive the finite difference code. The resulting injected current is shown in Figure 3.30 and its time derivative in Figure 3.31.

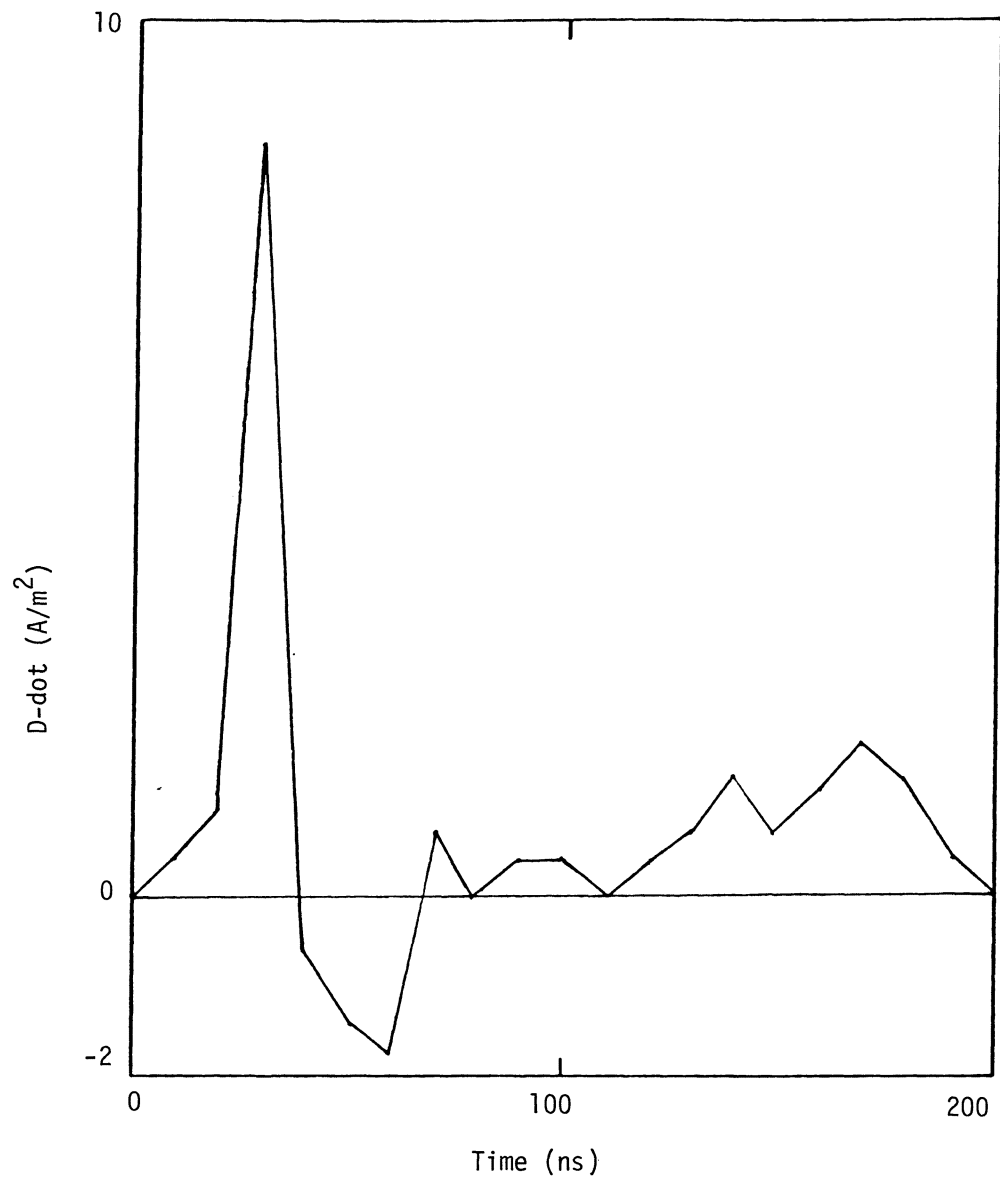


Figure 3.28 $D\text{-dot}$ Response of Flight 82-039

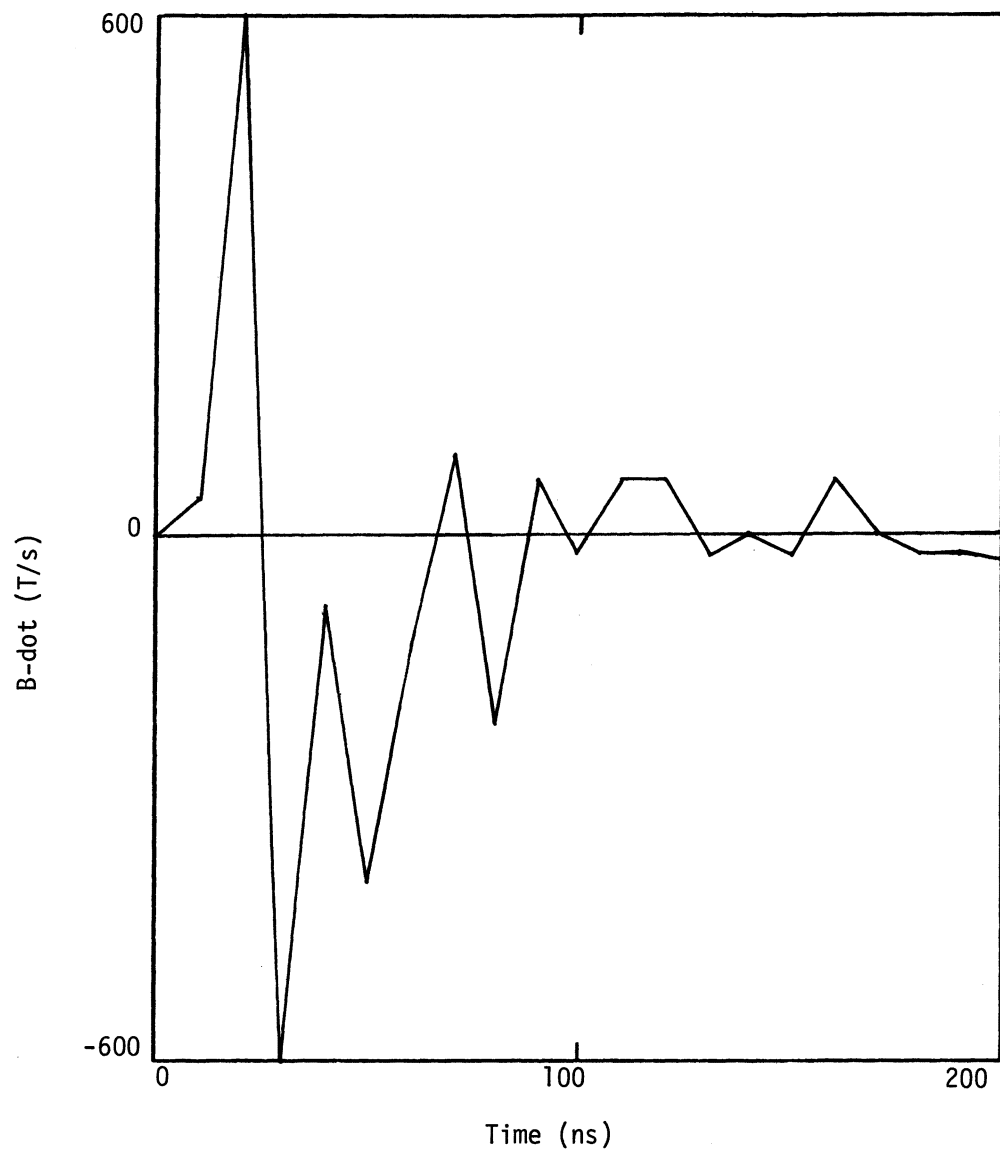


Figure 3.29 B-dot Response of Flight 82-039

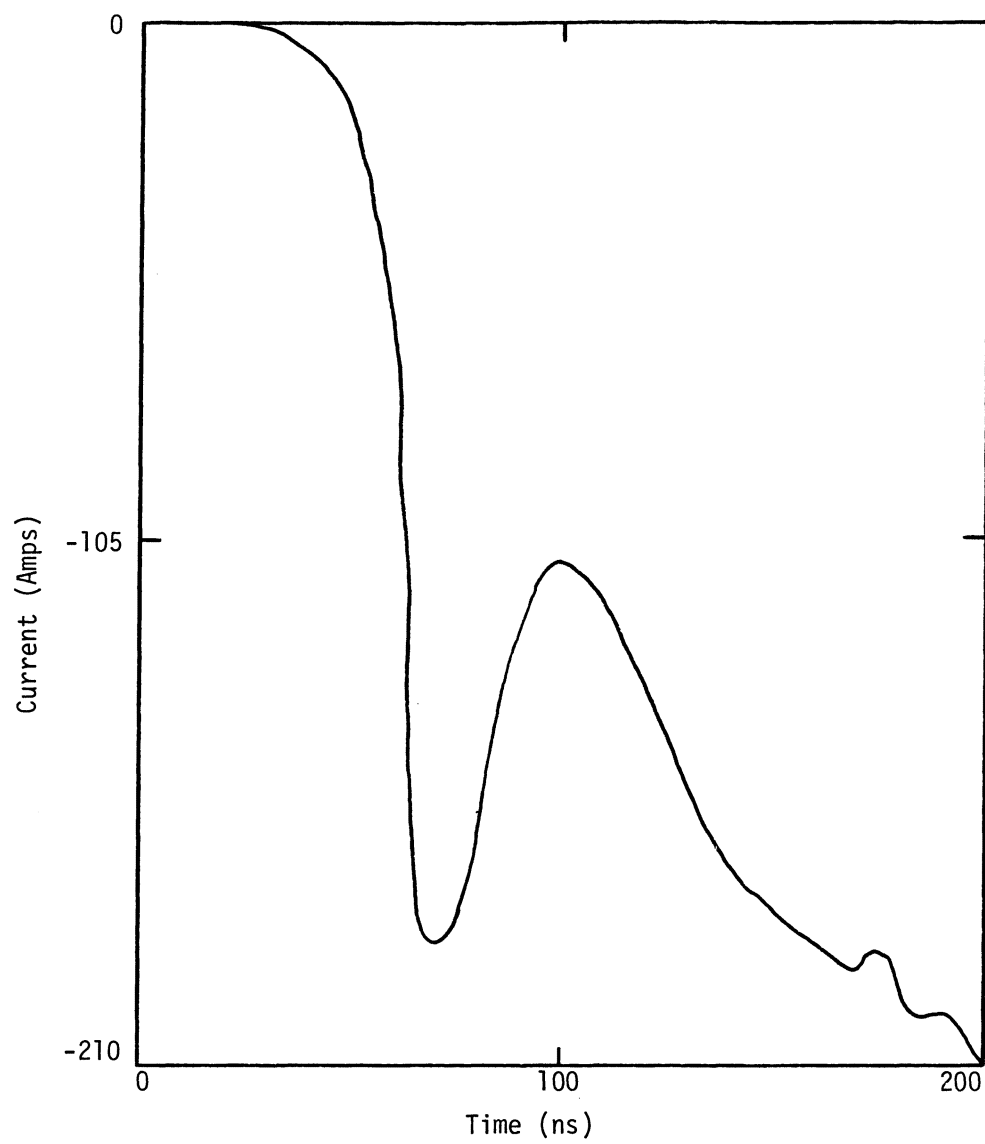


Figure 3.30 Injected Current for Calculated D-dot Source

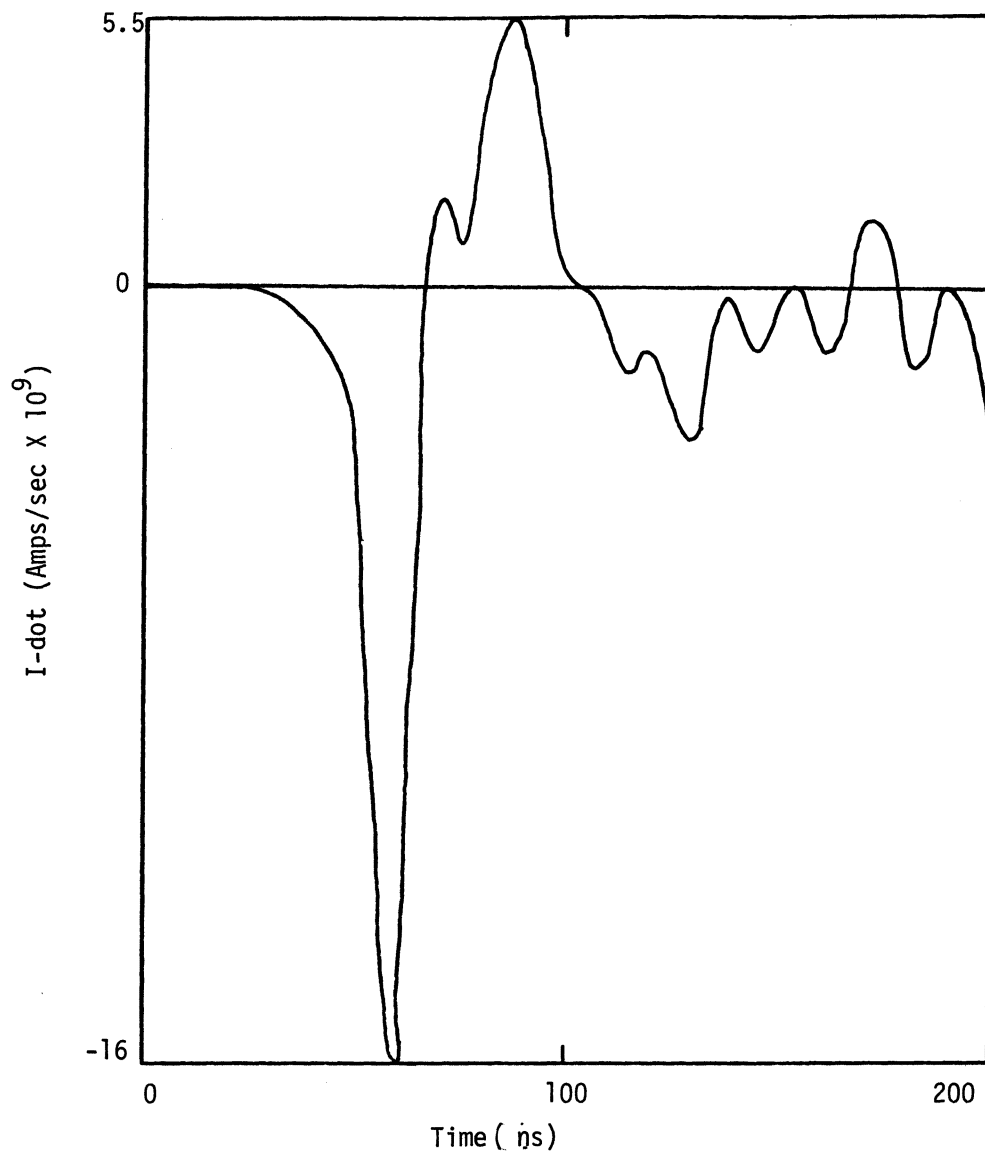


Figure 3.31 Time Derivative of Injected Current for D-dot Source

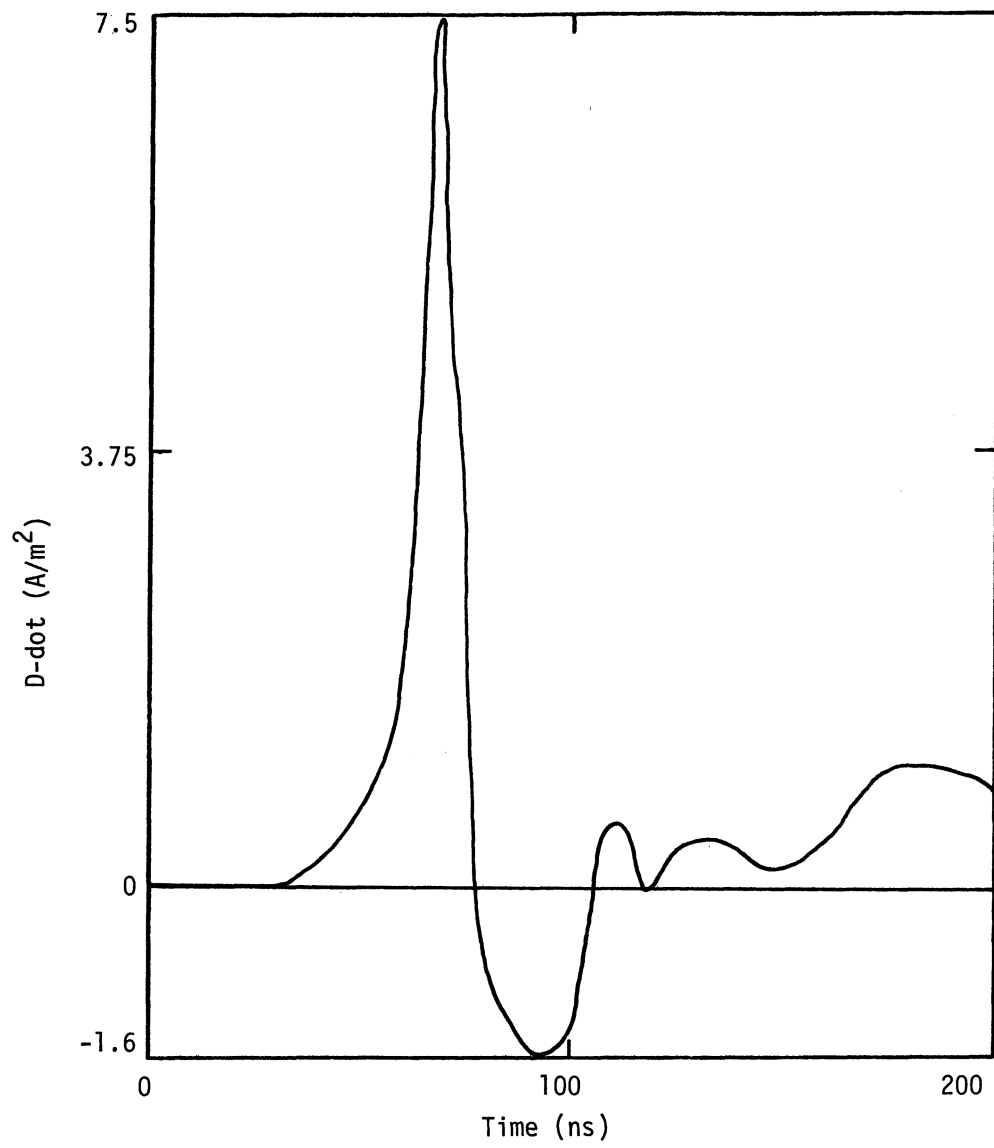


Figure 3.32 Calculated D-dot Response for D-dot Source

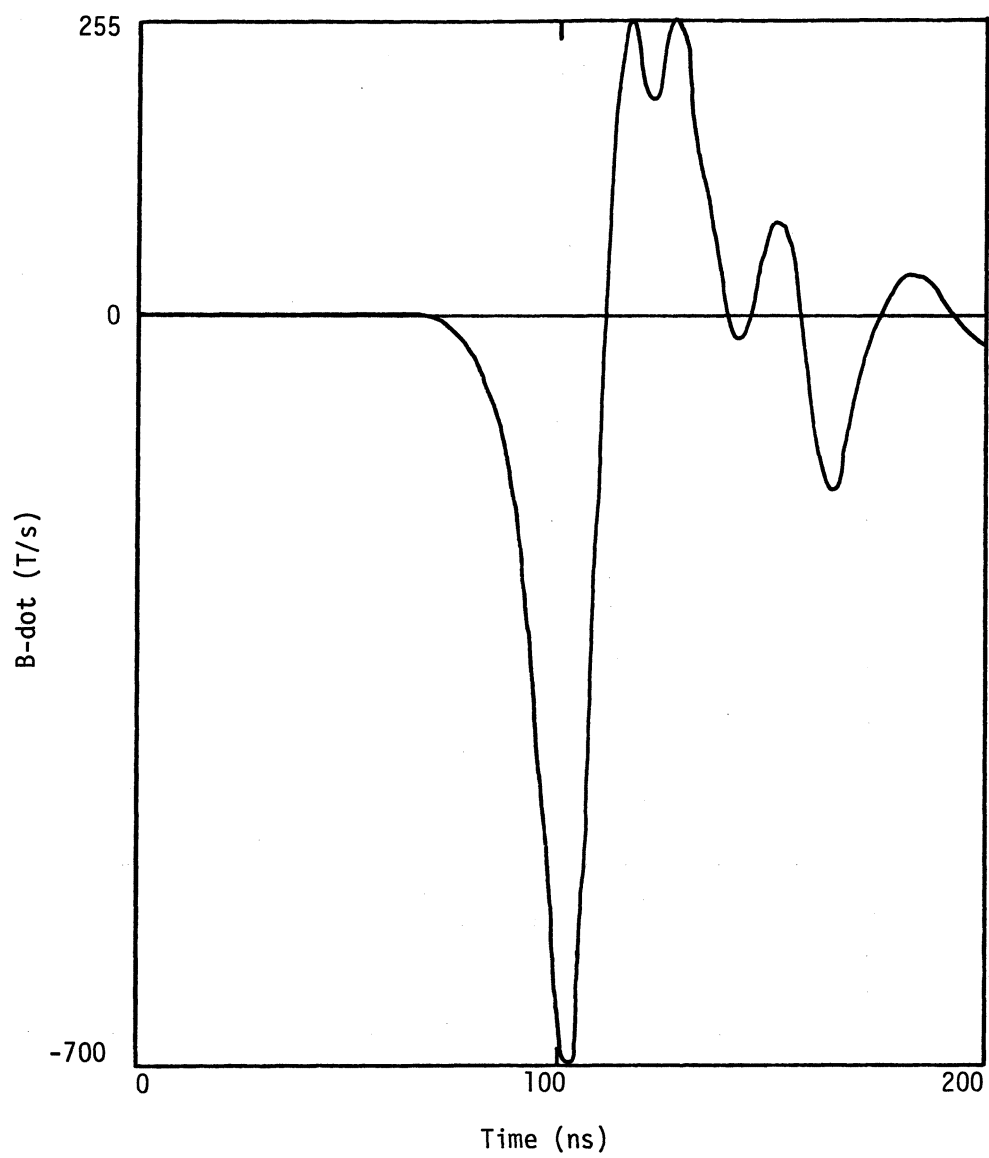


Figure 3.33 Calculated B-dot Response for D-dot Source

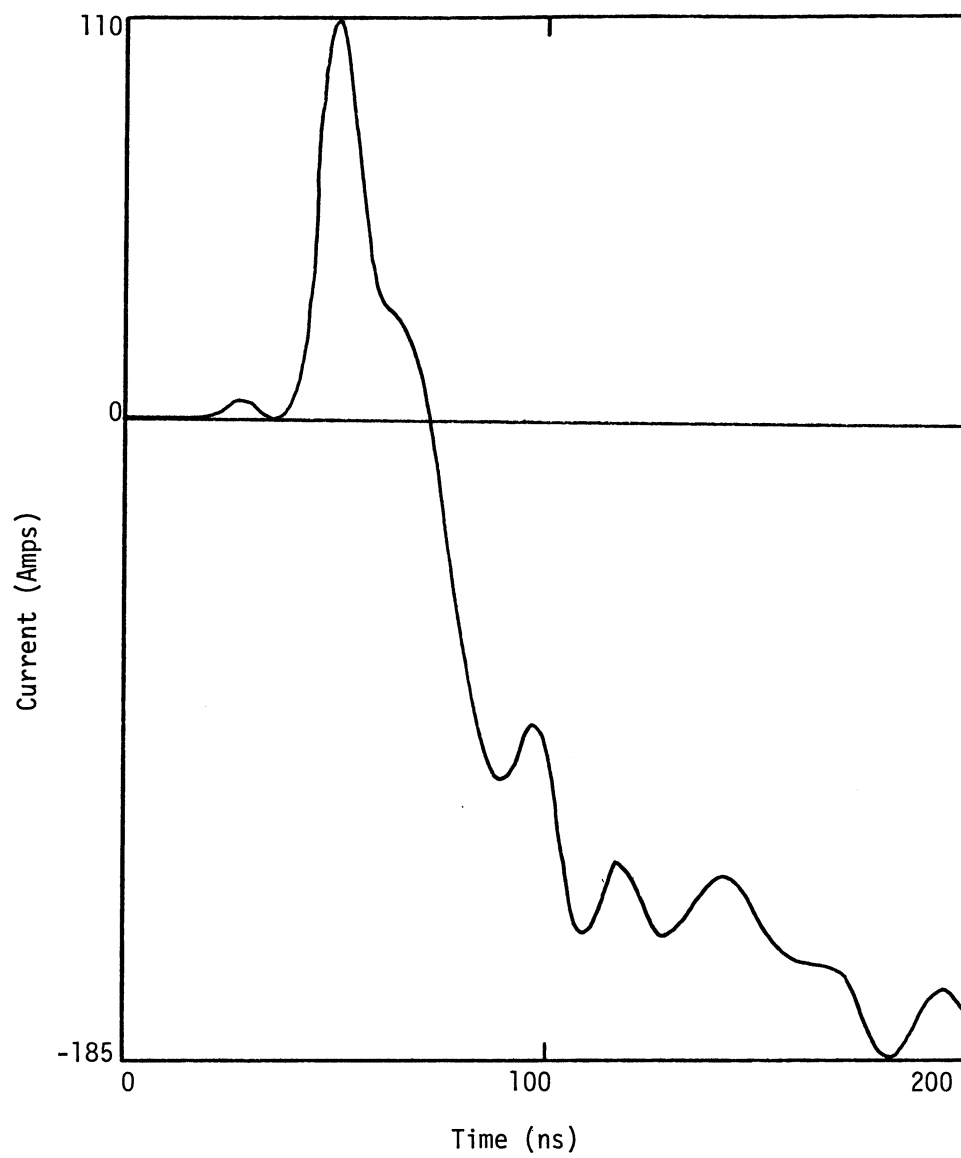


Figure 3.34 Injected Current for B-dot Source

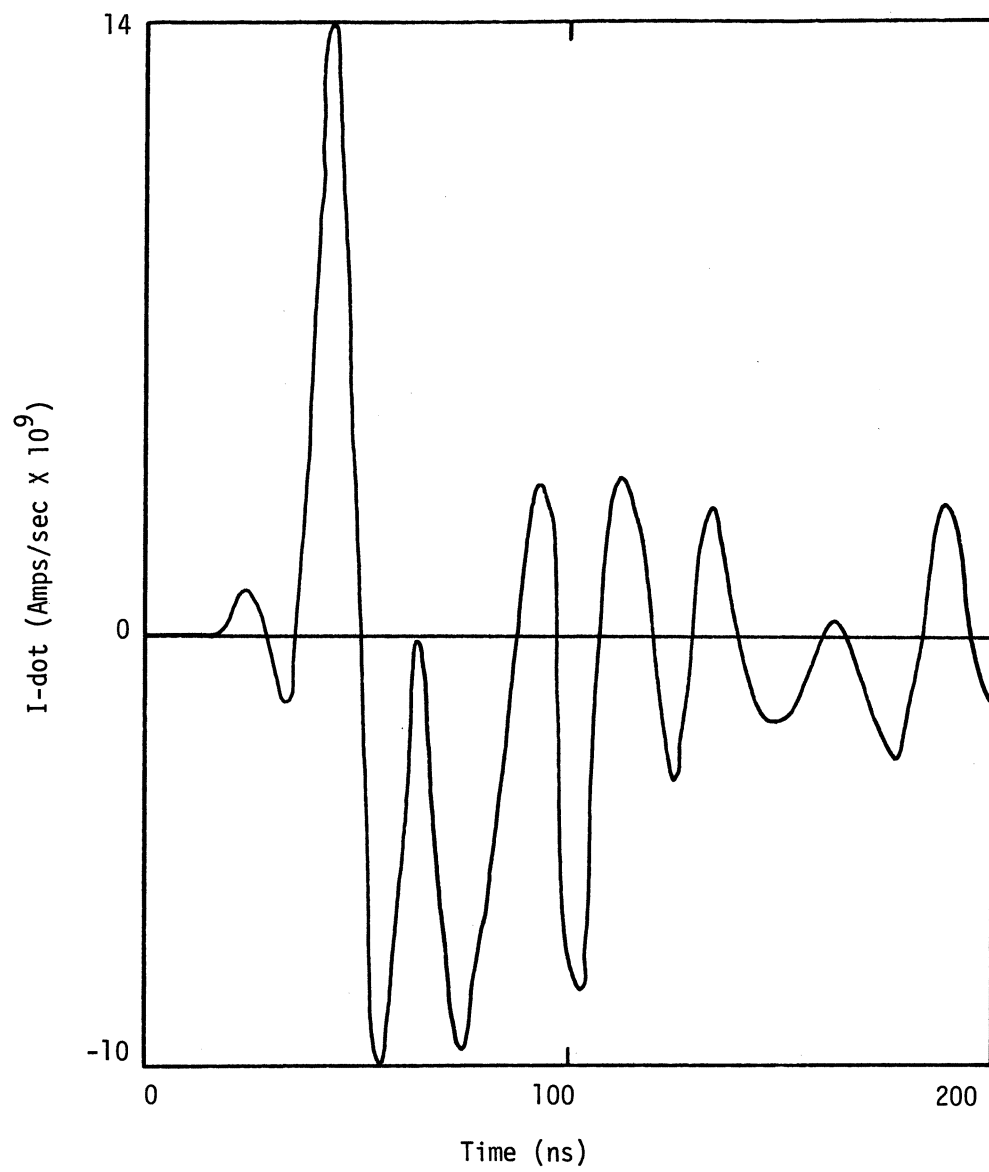


Figure 3.35 Time Derivative of Injected Current for B-dot Source

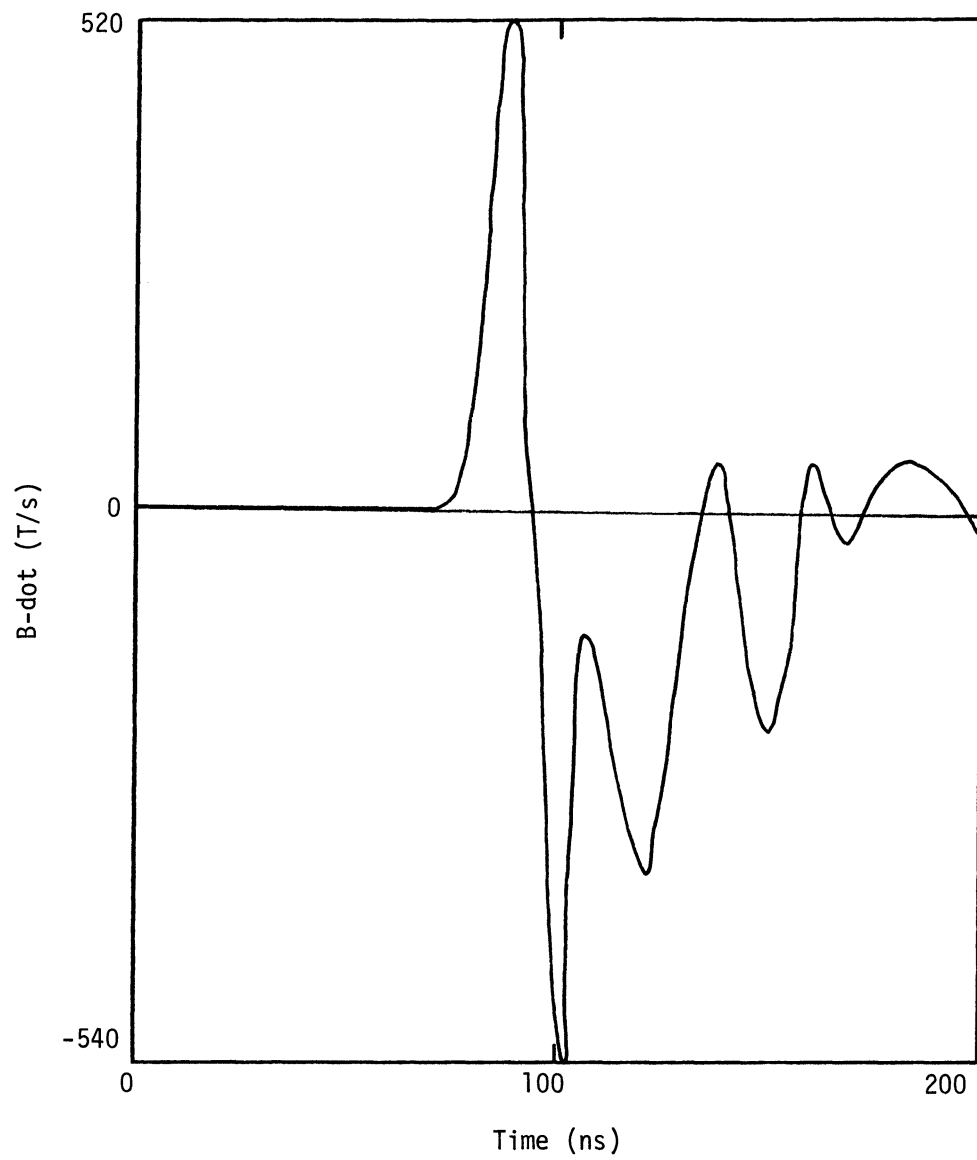


Figure 3.36 Calculated B-dot Response for B-dot Source

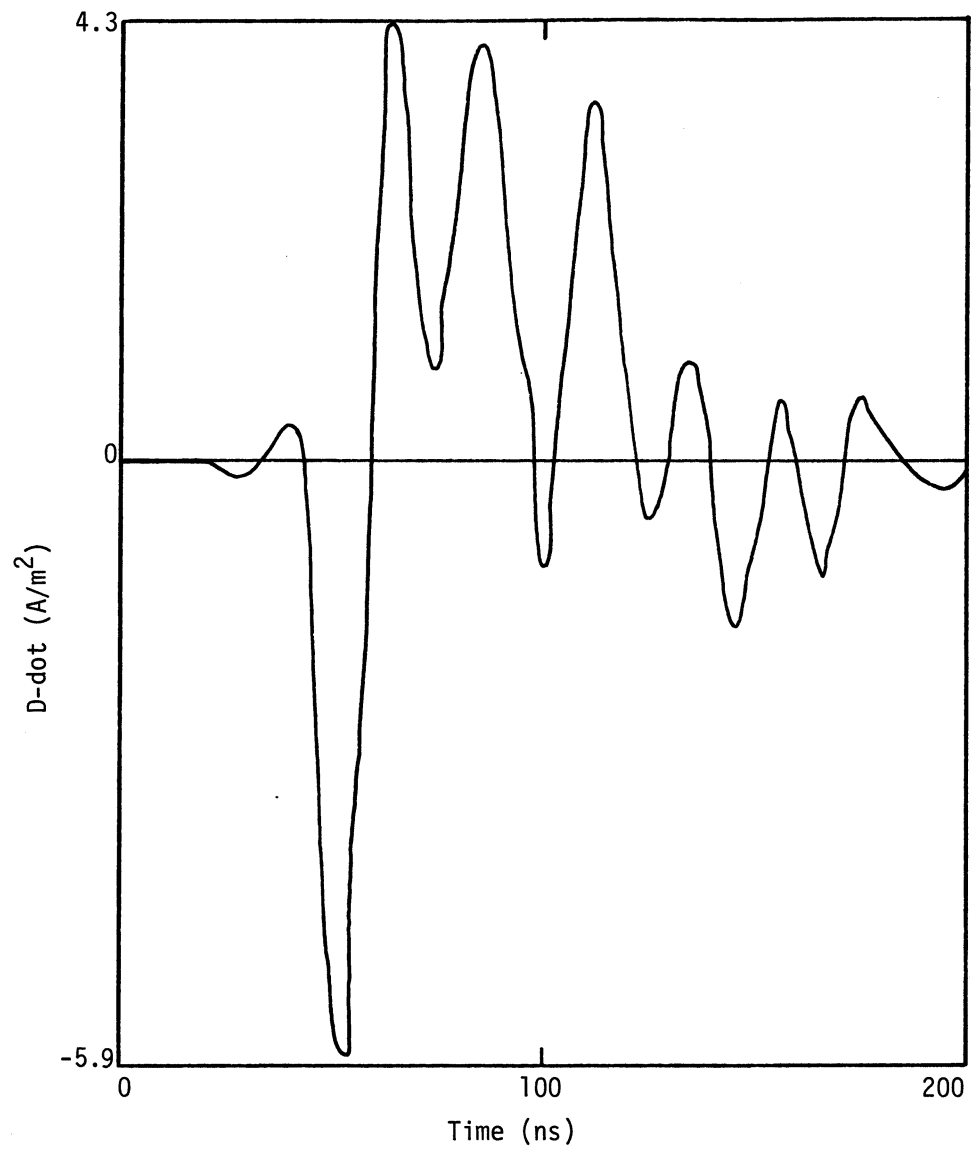


Figure 3.37 Calculated D-dot Response for B-dot Source

The calculated D-dot response is given in Figure 3.32. Note that it corresponds quite well to the measured D-dot response. In Figure 3.33 is shown the calculated B-dot response, which is clearly quite different from the measured response. Hence the chosen channel must be in error and needs adjusting. The reverse process was also done, in which a source was calculated for the B-dot record and used to drive the finite difference code. The injected current and its time derivative for this case are shown in Figures 3.34 and 3.35 respectively. Figure 3.36 gives the calculated B-dot response which again closely matches the measured response. In Figure 3.37 is shown the predicted D-dot response. The obvious difference between measured and calculated response verifies that the channel parameters chosen were in error.

It should be pointed out that another possibility for error exists in addition to the possible error in the channel. That possibility is that the correlated responses were produced by a nonlinear event, in which case the model itself is in error and the analysis will be unable to derive a correct source. For this possibility a more sophisticated and yet undeveloped methodology will be needed.

3.4 Time Varying Channels

As mentioned earlier, some rudimentary work has been done for the case in which the channel resistance varied in time. An example of the results is shown in Figure 3.38 which is the calculated D-dot response for a step function current of amplitude 1000 amps and rise time 44 nano-seconds. The rear channel resistance per unit length varied as,

$$R_{\ell} = \frac{1 \times 10^8}{I^2} \text{ } \Omega/\text{m}, \quad I > 447 \text{ A}$$

$$= 500 \text{ } \Omega/\text{m} \quad , \quad I \leq 447 \text{ A}.$$

In addition the resistance was forced to be a monotonically decreasing function. That is, if the current I decreased, R_{ℓ} stayed at its minimum value. This models in a crude way the breakdown of the air as a lightning current flows through it. Since the model is not able to be analyzed by Fourier methods, little effort has been expended on it. More interesting results would be obtained by implementing real time varying channel models from the literature into the finite difference code.

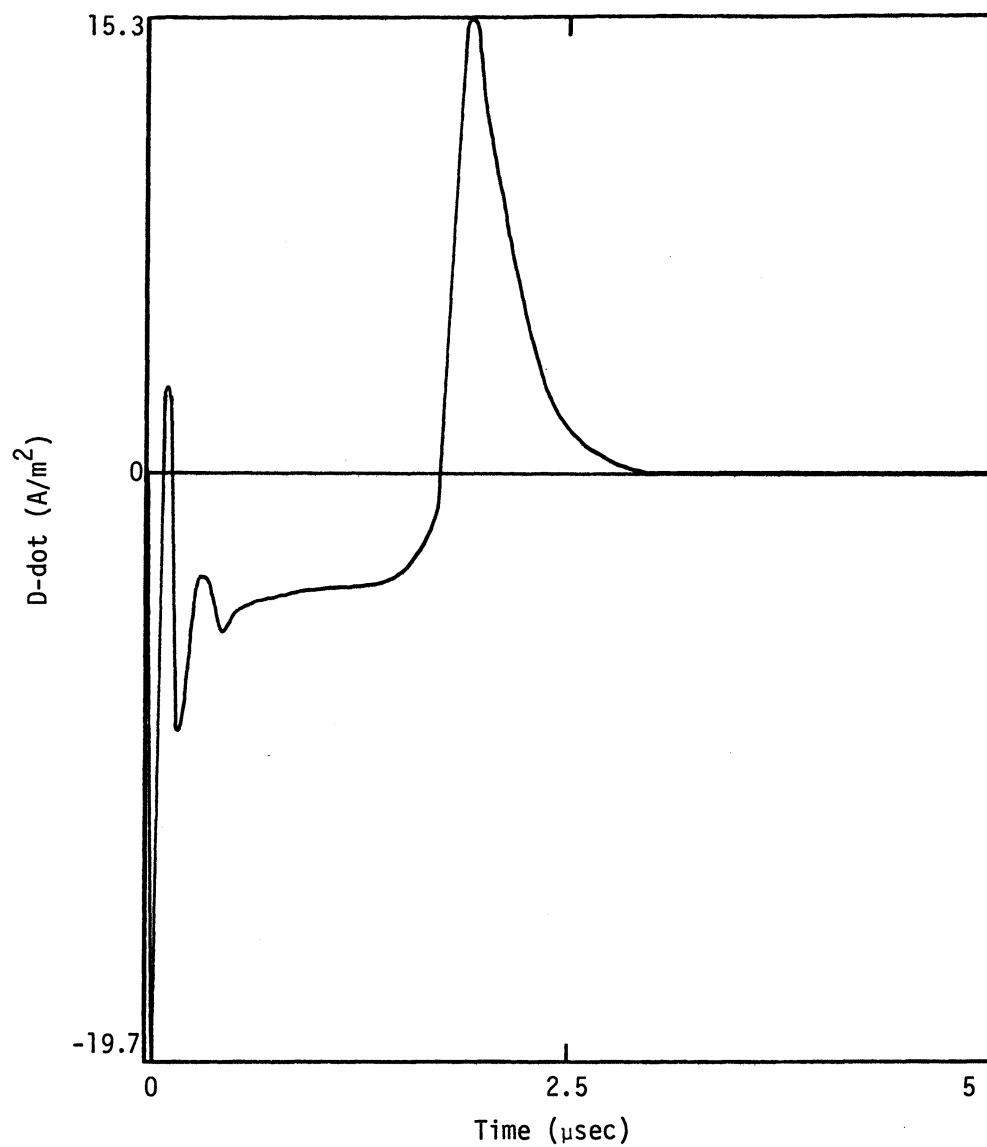


Figure 3.38 Forward D-dot Response for the Case in Which the Exit Channel has a Temporally Varying Resistance Per Unit Length

CHAPTER 4

NONLINEAR AIR BREAKDOWN MODELING AND RESULTS

4.0 Introduction

The interaction of lightning with an aircraft in flight is a nonlinear event. The initial attachment to the aircraft by the stepped leader is of necessity nonlinear, as is the development of an exit channel after the aircraft has charged to a sufficiently high level. Other aspects of the interaction, possible return strokes, K-changes, or dart leaders, also involve nonlinear processes, although it may be that the nonlinear effects are less important for these, because a conducting channel has been established previously. To accurately model these events, especially the initial leader, it is necessary to include electrical corona formation and air breakdown. It may also be necessary to take into account the effects of streamers.

It is not difficult to understand in an elementary fashion what occurs as a lightning leader approaches an aircraft. The leader tip is a region of high charge density with correspondingly high electric field levels near it. As the leader approaches the aircraft the field intensity is largest in the direction of the aircraft. Free electrons in the air are accelerated in this high field until they collide with a neutral atom or molecule. If the electron's kinetic energy is large enough at the time of the collision, the neutral particle can have an electron separated from it, producing a second free electron and a positive ion. The free electrons are then again accelerated by the field, possibly suffering more collisions and producing more free electrons and ions. If the rate of production of free electrons is larger than the rate of loss (by recombination, and attachment to form negative ions), an electron "avalanche" occurs, in which sufficient numbers of electrons and ions are produced to substantially alter the electrical conductivity of

the air. The electrons and positive ions move in opposite directions under the influence of the electric field, constituting a current in the direction of the field. This has the net effect of neutralizing the electric field at the position of the leader tip, but enhancing the field at a point nearer the aircraft. That point now has a large charge density and is the new tip of the leader.

The preceding description contains only what are commonly known as "primary" effects. There also exist "secondary" effects which may be important in lightning.

The most significant of these is the photoionization process which allows for streamer propagation. A streamer is a luminous pulse of ionization which extends from the high electric field region into regions of lower field. The tip of the streamer is believed to consist of positively charged ions with a high enough density that breakdown or near-breakdown electric fields exist in some region around the tip. Also, some of these ions (which were created through collisions between electrons and neutral gas molecules) are likely to be in excited states which can decay and emit a photon. The energetics of the situation are such that this photon can ionize a gas molecule in advance of the streamer tip. The electron produced in the ionization can then avalanche in the field around the streamer tip, and the avalanche electrons drift back toward the tip leaving behind the positive ions formed in the avalanche. These positive ions become the new tip of the streamer. In this way a streamer can advance from regions of high field to regions where the field may be very low.

4.1 Basics of the Nonlinear Model

The model developed here to account for electrical corona is a variation of that commonly in use in nuclear electromagnetic pulse (NEMP) work for the calculation of air conductivity. The NEMP model solves for the air conductivity by calculating the densities of positive ions, negative ions, and electrons as a function of space and time through the use of detailed balancing. Physical processes included are electron avalanching, electron attachment to neutral molecules to form negative ions, electron-positive ion recombination,

and negative-positive ion recombination.

The air conductivity for this model is a nonlinear function of the total electric field. It is given by

$$\sigma = q(n_e \mu_e + (n_- + n_+) \mu_i) .$$

Here q is the charge on one electron 1.6×10^{-19} coulombs,
 n_e is the number density of secondary electrons [m^{-3}],
 n_- and n_+ are the number densities of negative and
 positive ions [m^{-3}], and
 μ_e and μ_i are the electron and ion mobilities in
 [$m^2/(volt \ sec)$].

The electron and ion densities are computed from the ambient
 ionization rate $\dot{Q}(t)$:

$$\frac{\partial n_e}{\partial t} + [\beta n_+ + \alpha_e - G] n_e = \dot{Q}(t)$$

$$\frac{\partial n_-}{\partial t} + [\delta n_+] n_- = \alpha_e n_e$$

$$n_+ = n_e + n_-$$

Here α_e is the electron attachment rate (sec^{-1}),
 G is the electron avalanche rate (sec^{-1}),
 β is the electron-ion recombination coefficient ($m^3 \cdot sec^{-1}$), and
 δ is the negative-positive ion recombination coefficient
 ($m^3 \cdot sec^{-1}$).

The coefficients are defined in Table 4.1.

TABLE 4.1 Air Chemistry Coefficient Formulas [5]

Calculation of Erel:

$$E_{rel} = \frac{E}{\rho_r} / (1 + 2.457P^{0.834}) \text{ for } \frac{E}{\rho_r} < 0.07853(1 + 2.457P^{0.834})$$

$$E_{rel} = \frac{E}{\rho_r} - 1.195P^{0.834} \text{ for } \frac{E}{\rho_r} > 3.015 + 1.195P^{0.834}$$

$$E_{rel} = \sqrt{\frac{E}{\rho_r} + \left(\frac{0.6884P^{0.834}}{2} \right)^2 - \frac{0.6884P^{0.834}}{2}} \text{ for all other } \frac{E}{\rho_r}$$

Where P is the percent water vapor and ρ_r is relative air density. Note: E is in esu, where Eesu = Emks/ 3×10^4 .

Calculation of Electron Attachment Rate α_e :

$$\alpha_e = \frac{100-P}{100} (\alpha_3(1+0.344P) + \alpha_2)$$

$$\alpha_2 = 1.22 \times 10^8 \rho_r e^{-21.15/E_{rel}}$$

$$\alpha_3 = \rho_r^2 (6.2 \times 10^7 + 8. \times 10^{10} E_{rel}^2) / (1 + 10^3 E_{rel}^2 (E_{rel}(1 + 0.03 E_{rel}^2))^{1/3})$$

Calculation of Avalanche Rate, G:

$$G = 5.7 \times 10^8 \rho_r Y^5 / (1 + 0.3Y^{2.5}); Y = \frac{E_{rel}}{100}$$

Calculation of Electron-Ion Recombination Coefficient δ , and Ion-ion Neutralization Coefficient, β :

$$\delta = 2 \times 10^{-13} + \rho_r 2.1 \times 10^{-12} \text{ (m}^3/\text{sec)}$$

$$\beta = 2 \times 10^{-13} + 2.8 \times 10^{-12} (P)^{1/3} \text{ (m}^3/\text{sec)}$$

Calculation of Electron Mobility, μ_e :

$$\mu_e = \frac{100\mu_a}{100-P+P \times R}; R = 1.55 + 210 / (1 + 11.8 E_{rel} + 7.2 E_{rel}^2) \frac{\text{m/sec}}{\text{volts/meter}}$$

$$\mu_a = (((16.8 + E_{rel}) / (0.63 + 26.7 E_{rel}))^{0.6}) / (3. \times \rho_r)$$

Calculation of Ion Mobility, μ_i :

$$\mu_i = \frac{2.5 \times 10^{-4}}{\rho_r} \frac{\text{m/sec}}{\text{volts/m}}$$

Some of the weaknesses of the model are evident from the equations. The rate equations involving $\frac{\partial n}{\partial t}$ terms have no provision for motion of the charges, so electrons and ions must remain at the location where they were formed. This may be an adequate approximation for very fast events such as those seen in NEMP work, but is not adequate for the relatively slow processes occurring in lightning. Also the equations require local neutrality by specifying that the density of positive ions be equal to the sum of the densities of electrons and negative ions. This certainly is not true in the case of lightning. Finally, the physics of streamers is not included.

In order to account for these difficulties, the equations have been modified in the following way. The rate equations involving $\frac{\partial n}{\partial t}$ terms and the local neutrality condition $n_+ = n_e + n_-$ have been replaced by a continuity equation for each species separately. These equations are shown below.

$$\begin{aligned} \frac{\partial n_e}{\partial t} + \nabla \cdot (n_e \vec{v}_e) + [\beta n_+ + \alpha_e - G] n_e &= \dot{Q}(t) \\ \frac{\partial n_-}{\partial t} + \nabla \cdot (n_- \vec{v}_-) + \delta n_+ n_- &= \alpha_e n_e \\ \frac{\partial n_+}{\partial t} + \nabla \cdot (n_+ \vec{v}_+) + \beta n_e n_+ + \delta n_- n_+ &= \dot{Q}(t) + G n_e \end{aligned} \tag{4.1}$$

Note here that the source terms remain formally unchanged from the previous equations, and that the convective derivative has replaced the previous simple partial derivative, allowing for charge motion. The reason that the source terms are said to be formally unchanged is that the addition of streamer physics to the model changes the value of the avalanche rate G . Also a current of positive charge has been included in the convective derivative term to account for the effective motion of streamers. It should also be noted that the velocities $\vec{v}_e, \vec{v}_+, \vec{v}_-$ in Equations (4.1) are calculated as the product of mobility and electric field, $\vec{v}_s = \pm \mu_s \vec{E}$. The exception to this is the

case of \vec{v}_+ when streamer propagation is included.

4.2 Streamers in the Finite Difference Code

The addition of photoionization and streamers to a finite difference code is a nontrivial matter, because the grid size is normally by necessity much larger than the radius of a streamer tip. Hence the code cannot sense the presence of streamers directly, because the effects of averaging over a spatial cell mask the streamer tip field. This makes it necessary to use special techniques and some assumptions in order to determine whether streamers exist in a given cell. The assumptions made are listed below.

- 1) All net positive charge above a certain threshold is in the form of streamers.
- 2) All streamer tips are in the form of spheres with an experimentally determined average radius and charge density.
- 3) All streamers move with a uniform speed in the direction of the maximum electric field at the tip.

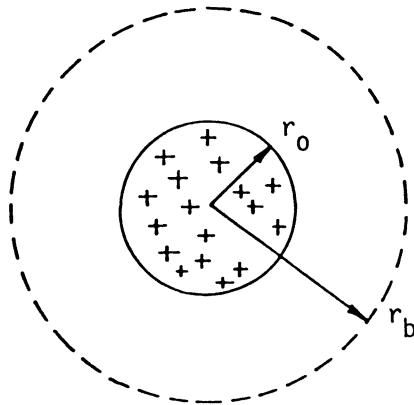
None of these simplifying assumptions corresponds exactly to the physical situation, but they should be reasonable in an average sense. Since the finite difference code is dealing with quantities averaged over a spatial cell, it should be possible to get an accurate overall response from average streamer properties.

The nonlinear finite difference code makes use of the above three assumptions in the following ways. Assumption (1) allows the code to determine which cells have streamers in them. These cells are then treated differently than cells without streamers. Assumption (2) allows the code to calculate the net positive charge density threshold and the number of streamer tips in a cell. That is, the experimentally determined radius and charge density of a streamer tip specifies the total positive charge in the tip. The net positive charge in a cell (volume of cell $\times (n_+ - n_e - n_-)$) must be larger than this total positive charge in order for the cell to contain a streamer. If this is true then the total number of streamers in the cell is the total net positive

charge divided by the total charge in the standard streamer tip. Assumption (2) also allows the calculation of the electron avalanche occurring around the streamer tip. This is covered in more detail in the next section. Assumption (3) allows the code to model streamer motion by defining a current of positive charge in cells containing streamers. This current is proportional to the net positive charge density in the cell and also to the uniform speed chosen for the streamer. This uniform speed assumption is a weakness of the model, since streamers are known to move slowly as they form and then to speed up as they mature.

4.3 Electron Avalanche Around a Streamer Tip

In order to determine the effect a streamer has on the air conductivity it is necessary to calculate the magnitude of the electron avalanche which occurs around the streamer tip. To do this the streamer tip will be modeled as a uniform sphere of positive charge as shown in Figure 4.1. The charge density and radius will be assumed to be experimentally determined quantities. It will also be assumed that all avalanching occurs outside the streamer tip (i.e. $r > r_0$).



$$\begin{aligned}
 n_0 &\approx 1 \times 10^{21} \text{ m}^{-3} &= \text{Uniform Positive Charge Number Density} \\
 r_0 &\approx 2 \times 10^{-5} \text{ m} &= \text{Radius of Streamer Tip} \\
 r_b &&= \text{Radius at Which Nominal Breakdown Electric Field Occurs}
 \end{aligned}$$

Figure 4.1 Streamer Tip Geometry

The number of electrons being produced per unit volume, per unit time, around the streamer is $G(r) n_e^P(r)$, where $G(r)$ is the avalanche rate, given in Table 4.1, and $n_e^P(r)$ is the number of photoelectrons per unit volume. The latter quantity is given [6] as

$$n_e^P(r) = N_s \frac{p p_q}{p+p_q} \frac{\psi}{r^2}, \quad (4.2)$$

where N_s = number of positive ions in the streamer tip,

p = gas pressure,

p_q = quenching pressure, and

$\psi = \frac{\text{number of photoelectrons generated/steradian/cm/Torr}}{\text{number of ions formed in avalanching}}.$

$G(r)$ is given in Table 4.1 as a function of electric field. Because the field variation around the model streamer tip is known, this can easily be transformed to a function of radial distance. The result is;

$$G(r) = 5.7 \times 10^8 \rho_r \frac{(r_b/r)^{10}}{1+3(r_b/r)^5} \text{ sec}^{-1} \quad (4.3)$$

The total number of electrons produced per unit time in the streamer avalanche is then just the integral of $G(r) n_e^P(r)$ over the volume surrounding the streamer tip.

$$N_e^{\text{streamer}} = \frac{1}{2} \times 4\pi \int_{r_0}^{\infty} G(r) n_e^P(r) r^2 dr. \quad (4.4)$$

The factor of one-half is included because the streamer tip is expected to be connected to a conducting channel, so high electric field and therefore the electron avalanche are confined to the half space in advance of the streamer. The number of electrons per unit volume per unit time produced in the finite difference cell by the single streamer is then,

$$n_e^{\text{streamer}} = \frac{N_e^{\text{streamer}}}{V_{\text{cell}}} = \frac{N_s p p_q \psi}{V_{\text{cell}} (p+p_q)} 1.14 \times 10^9 \pi \int_{r_0}^{\Delta r} \frac{(r_b/r)^{10}}{1+3(\frac{r_b}{r})^5} dr, \quad (4.5)$$

where Δr is the approximate radius of the cell. The replacement

of the infinite upper bound in Equation (4.4) with Δr is a good approximation as long as $\Delta r \gg r_b$. This is true in most cases. The integral in Equation (4.5) is easily transformed to give,

$$n_e^{\text{streamer}} = 1.14 \times 10^9 \pi \frac{N_s p p_q \psi}{V_{\text{cell}} (p + p_q)} r_b \int_{r_b/\Delta r}^{r_b/r_0} \frac{u^8}{1 + 1.3 u^5} du. \quad (4.6)$$

The remaining integral can be performed numerically since r_b , r_0 , and Δr are known.

Equation (4.6) gives the number of electrons per unit volume and time produced in a cell due to the presence of a single streamer. Assuming no interaction between streamers, the number of electrons per unit volume and time due to all streamers is,

$$n_e^{\text{all streamers}} = N n_e^{\text{streamers}}, \quad (4.7)$$

where N is the total number of streamers in a cell. To calculate N it is assumed that any net positive charge in a cell above a certain threshold is in the form of streamers. The threshold is the positive charge contained in a single streamer tip. So for the finite difference code to classify a cell as containing streamers, it must be the case that $Q_{\text{net positive}}^{\text{cell}} > \frac{4}{3} \pi r_0^3 n_0 q$. It follows directly from this that the total number of streamers in a given cell can be written as

$$N = \frac{(n_+ - n_e - n_-) V_{\text{cell}}}{4/3 \pi r_0^3 n_0} \text{ for } (n_+ - n_e - n_-) V_{\text{cell}} \geq \frac{4}{3} \pi r_0^3 n_0$$

$$= 0 \text{ for } (n_+ - n_e - n_-) V_{\text{cell}} < \frac{4}{3} \pi r_0^3 n_0 \quad (4.8)$$

The quantity $N n_e^{\text{streamer}}$ then is the number of electrons per unit volume and time generated in a cell by all the streamer tips which are present. This term is then added to the right sides of the

$\frac{\partial n_e}{\partial t}$ and $\frac{\partial n_+}{\partial t}$ equations in (4.1) as a source term.

4.4 Streamer Motion

The physical motion of a streamer tip is incorporated into the finite difference code as a current of positive charge. It couples into

the rate equations for the charge densities through the convective derivative term. The magnitude of this current is determined by the experimentally observed average streamer velocity, 2×10^5 m/s [7]. The current has the effect in the code of depleting a cell of any net positive charge, which stops the streamer avalanche in that cell.

4.5 Two Dimensional Results

The nonlinear corona model just described has been implemented in a two dimensional finite difference code which assumes cylindrical symmetry. This was done in order to model the rod-plane gap experiment of Collins and Meek [7]. Their experiment consisted of a positively charged rod and a negative plane as shown in Figure 4.2. The voltage applied between the rod and plane was such that electrical corona formed around the end of the rod. Time domain measurements were made of the electric field at the tip of the rod and on the plane directly below the rod. The results for a 64 kilovolt applied voltage are shown in Figure 4.3. The dotted line indicates the geometric field, which is the field that would be seen in the absence of corona.

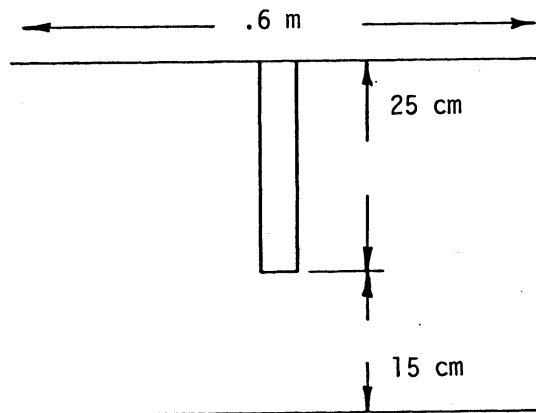


Figure 4.2 Rod-plane Gap Geometry of Collins & Meek [7].

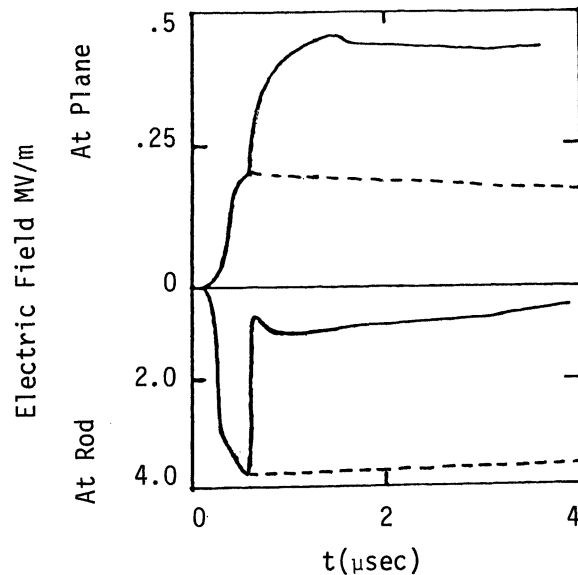


Figure 4.3 Measured Electric Fields for Experiment of Collins and Meek [7].

The calculated fields from the two dimensional nonlinear code are shown in Figure 4.4, overlaid on the Collins and Meek data. The major differences are in the final level of the field at the plane, and in the behavior of the field at the rod tip during corona formation. The excess of the measured field over the predicted field at the plane indicates that the experimental corona is larger spatially than that calculated by the computer code. It is likely that inaccuracies in the streamer formalism (e.g. average size, average velocity, etc.) included in the code are the reason for this. It should be noted, however, that without the streamer model in the code, the calculated field at the plane rose just slightly ($\sim 5\%$) above the geometric field.

The calculated and experimental fields at the rod tip differ in the amount of decrease seen during corona formation. The experimental field drops sharply to about .5 MV/m and then rises slightly

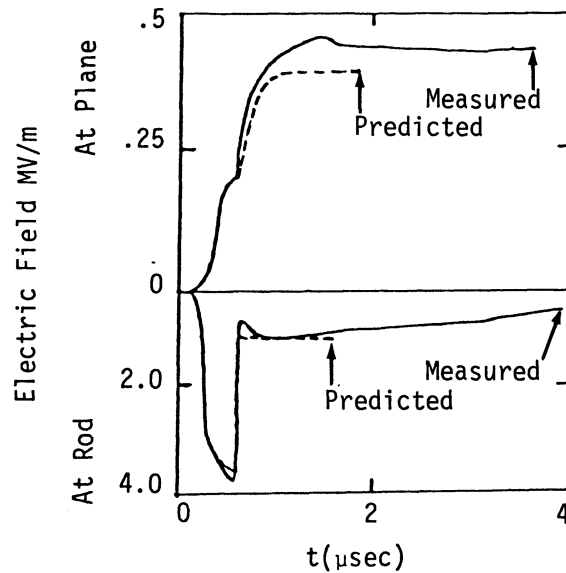


Figure 4.4. Comparison of Experimental Data of Collins and Meek [7] With the Prediction of the Nonlinear Computer Code

before beginning a long slow fall. The calculated field also drops sharply but only to about 1 MV/m. From that point it continues to drop slowly, exhibiting no rise as is seen experimentally. It is felt that the cause of this difference is in the choice of propagation velocity for the streamers. It is known experimentally that this velocity is slower for streamers which are forming, and faster for mature streamers. Computationally, then, the use of an average velocity removes the streamers from the rod tip area too soon. Hence the electron avalanche around streamer tips occurs for a shorter time near the rod than it should, and the electric field stays artificially high. Presumably this defect in the model could be removed by a more appropriate variation of streamer velocity.

Although Collins and Meek did not report results for a negatively charged rod, the prediction of the nonlinear code is shown in Figure 4.5.

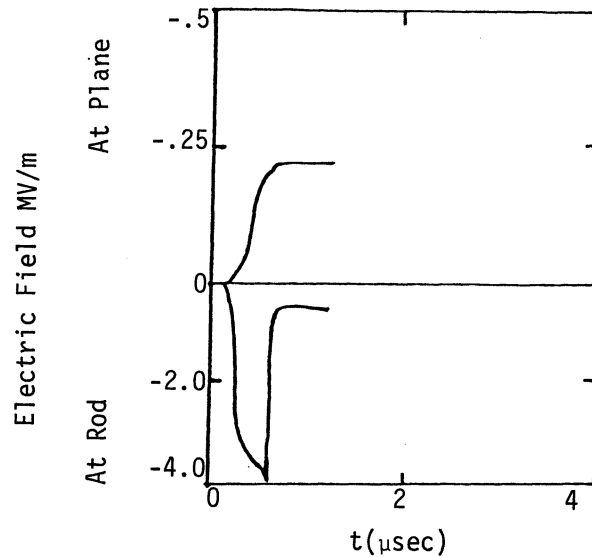


Figure 4.5 Predicted Electric Fields for the Case of a Negatively Charged Rod

Note that the field at the rod is much the same as in the positive rod case, but the field at the plane is essentially the geometric field. In this case, then, the spatial extent of the corona around the rod tip is much smaller than for the positively charged rod. This effect is confirmed by experimental observation.

4.6 Application to the Three Dimensional Finite Difference Code

Two applications were made of the nonlinear corona model to the three dimensional finite difference code. The first consisted of a perfectly conducting bar in free space and an electric charge near one end. This was done in order to study the effects of water vapor content of the air and relative air density on the attachment process. The second application was to study the attachment of an electric charge to the F106 aircraft. In this case the charge was placed near an extremity of the aircraft (i.e. wing tip, nose, tail tip) where lightning usually attaches. The objective of this application was to study the response of the F106 to nonlinear attachment.

It was found that for the cell sizes appropriate for these two problems (~ 1 meter), the treatment of streamers is inaccurate. This occurs because of the way in which the streamer threshold (Equation 4.8) for a cell is calculated. In a cell with a small volume the difference $n_+ - n_e - n_-$ must be large in order for Equation 4.8 to flag the cell as one having streamers. However, for the three dimensional codes of this chapter the necessary size of $n_+ - n_e - n_-$ is of the same order as the roundoff error of the computer. Therefore, streamer cells cannot be accurately flagged. This problem could be resolved by using a smaller cell size or performing the computations in double precision, both of which require extraordinary computational resources. Hence, in the three dimensional results, the streamer formalism was not used, but the new terms involving charge motion were included.

4.7 Parameter Study

A parameter study was conducted with a small version of the nonlinear code in order to determine the effects of water vapor and air density on the attachment process. The size of the problem space was reduced to $8\text{ m} \times 8\text{ m} \times 29\text{ m}$ in order to decrease the running time of the code. A rectangular bar five meters long and one square meter in cross section was placed in the center of the space. A line current was then introduced into the space in such a way that an electrical charge appeared at a point two meters from the end of the bar. This charge was then allowed to grow in magnitude (as the time integral of the line current). Eventually the electric field between the charge and the bar reached air breakdown level, and a conducting channel appeared. The line current then could flow directly onto the bar.

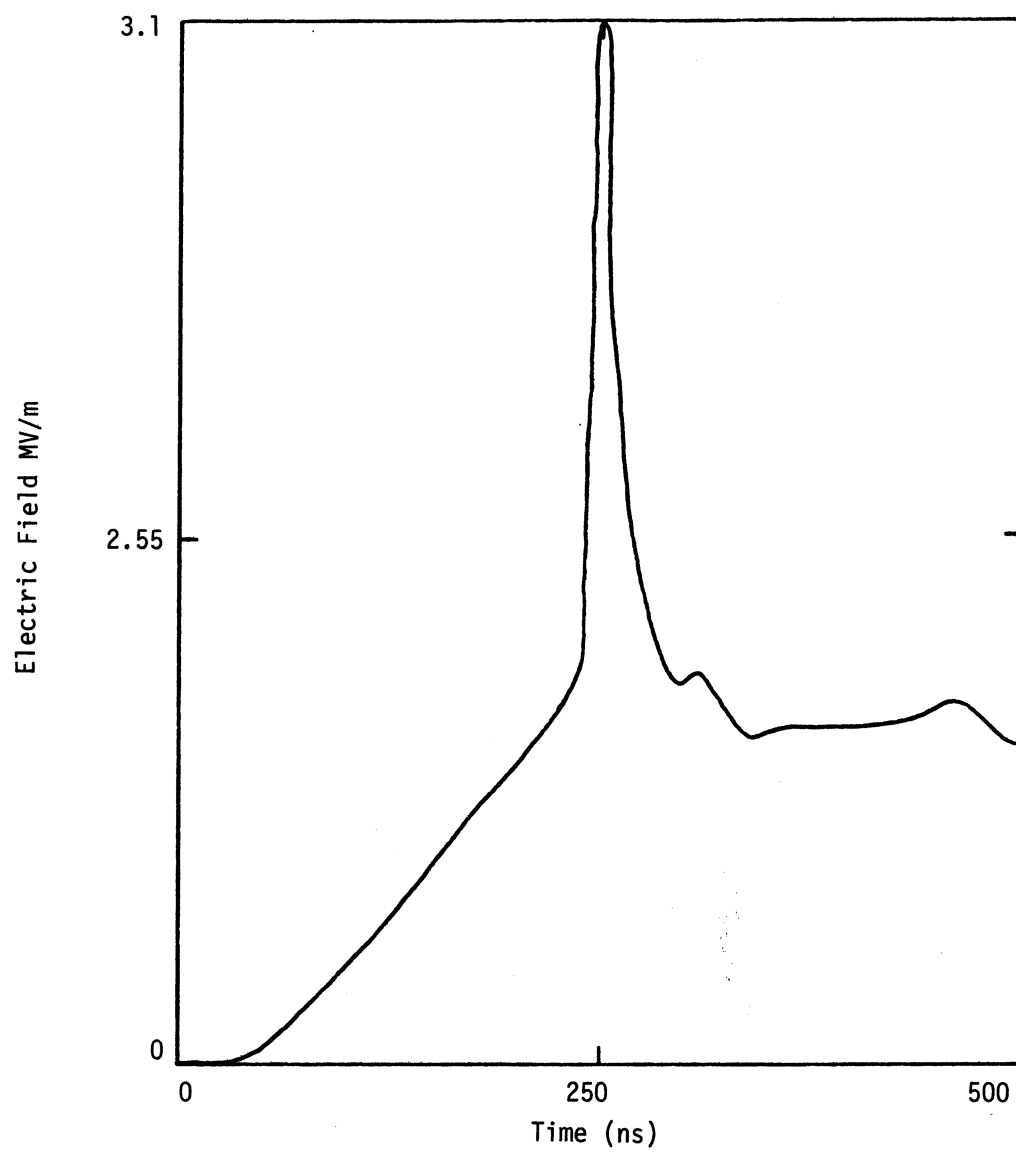
The parameters which were varied were the water vapor content of the air and the relative air density. The water vapor content is defined as the percentage of water vapor molecules by number in the air. The amount of water vapor in the air was allowed to be either 0% or 6%, and the relative air density was either 1 or .5. Zero percent water vapor with relative air density of one corresponds to dry air at sea level, while six percent water vapor and relative air density of one-half corresponds to a thunderstorm at high altitude ($\sim 5.2\text{ km}$). The line current used to form the charge was in all cases the same, and was chosen to be a step function with sine-squared leading edge of amplitude 1000 amperes and rise time of 100 nsec. The outputs from the code were normal electric fields

and tangential magnetic fields on the bar, representative of charges and currents on its surface.

The results of the parameter study are shown in Figures 4.6 - 4.13 in groups of three. The (a) in each group is the normal electric field at the end of the bar facing the charge; (b) is the normal electric field at the end of the bar away from the charge; and (c) is the current at the end of the bar facing the charge. Note that this current includes a component due to polarization of the bar, which is also present in the linear case.

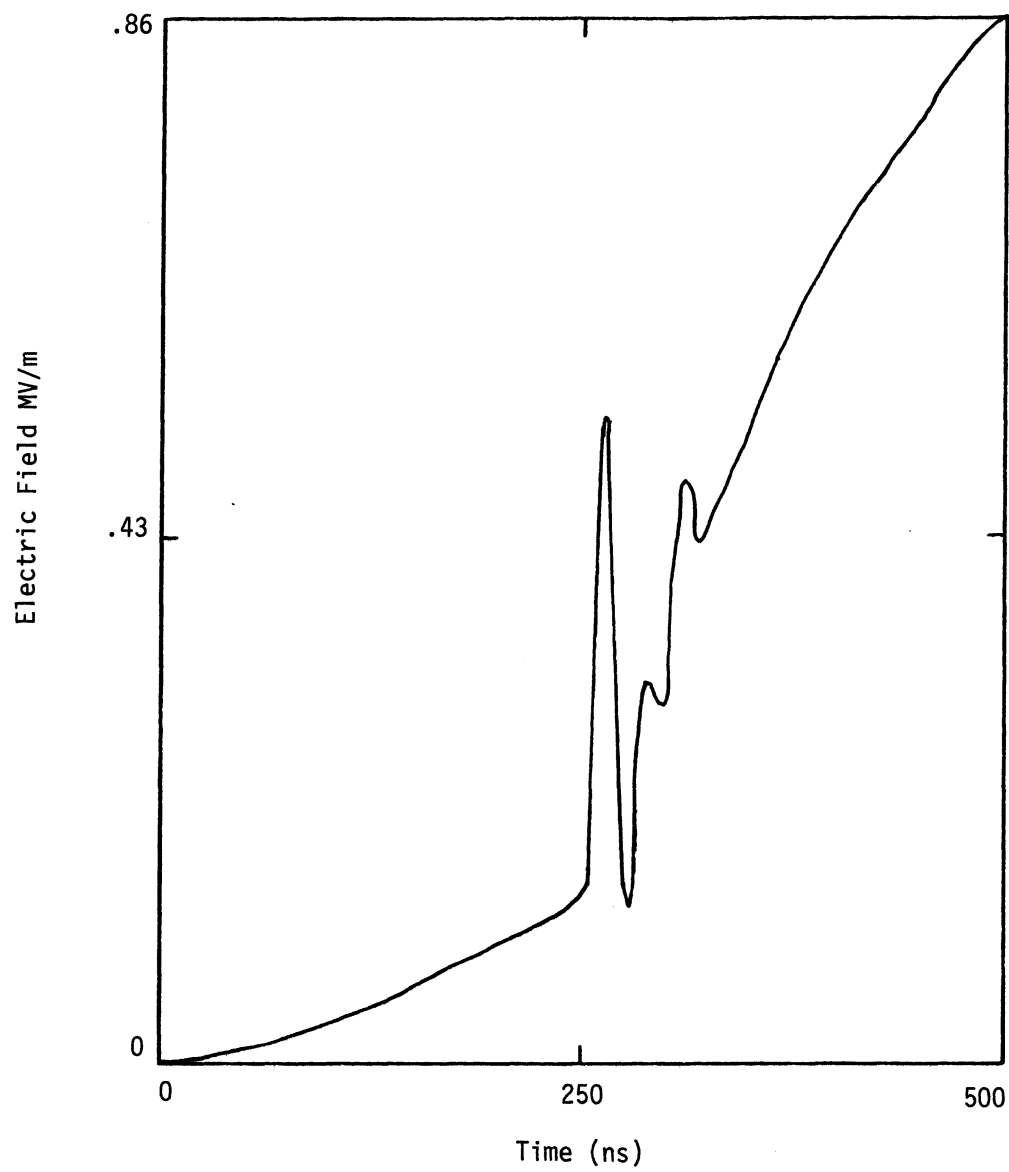
There are a few things about Figures 4.6 - 4.13 which may appear puzzling at first glance. First of all, in some cases the fields seem to break down at levels which are lower than nominal values. This is entirely due to the "graininess" of the finite difference code. Corona and air breakdown are, of course, most likely to occur around pointed objects such as the nose of an aircraft. These are regions of high electric field which causes the necessary electron avalanche. However, these regions in general also have the largest spatial gradients of the electric field. Therefore this field in a finite difference code can change markedly between two adjacent cells. One of the cells may have a field which is significantly above nominal air breakdown level and the other significantly below. The air conductivity in the nonlinear finite difference code is calculated at spatial positions between electric field points. Hence for corona to form in the code it is necessary that the average of the fields in two adjacent cells reach breakdown level. So in the parameter study a field breaking down at a lower level than one would normally expect simply means that the field next to it was sufficiently high to make the average field between the two of breakdown intensity.

Another characteristic of the parameter study which may be puzzling is the behavior of the field at the end of the bar facing the charge. In the case when the charge is positive the electric field first exhibits a slow rise followed by a sharp rise and then a steep fall when nonlinear levels are reached. The case of the negative charge is similar but shows no sharp rise. This is again partly due to graininess in the code, but another factor is also involved. Figure 4.14 will help to clarify the situation. In (a) is shown the case of the



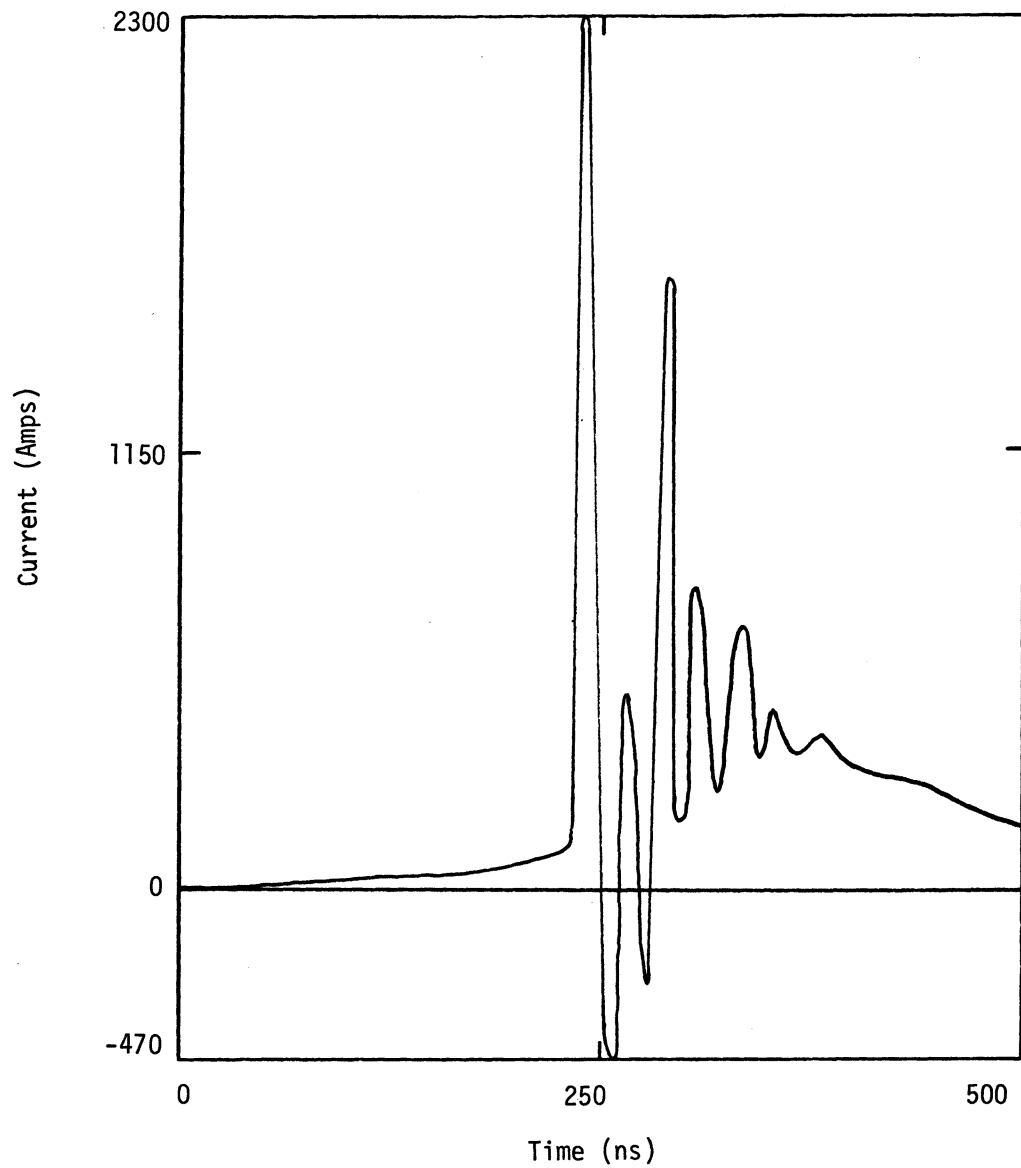
Charge - Positive
Water Vapor Content - 0%
Relative Air Density - .5

Figure 4.6a



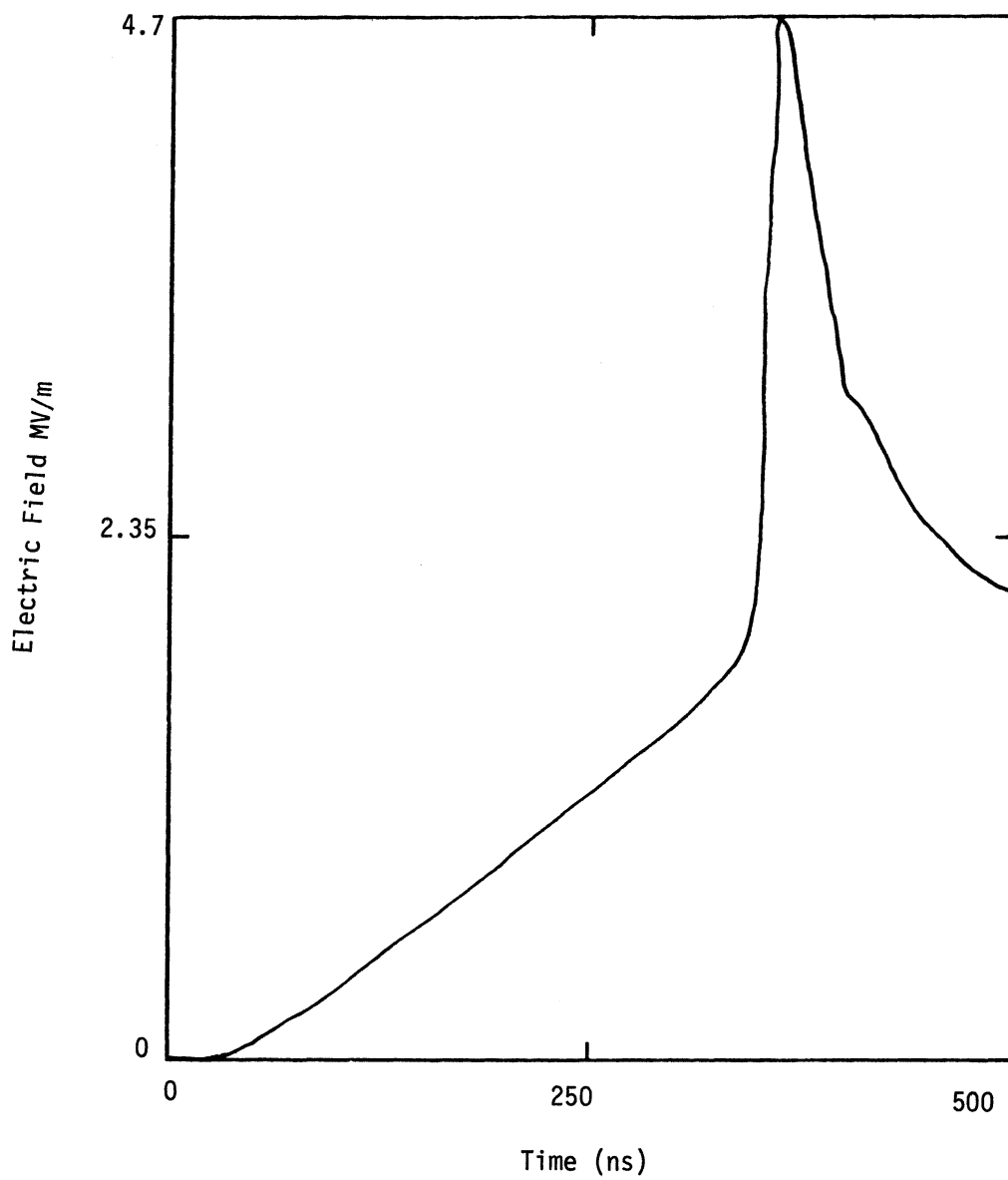
Charge - Positive
Water Vapor Content - 0%
Relative Air Density - .5

Figure 4.6b



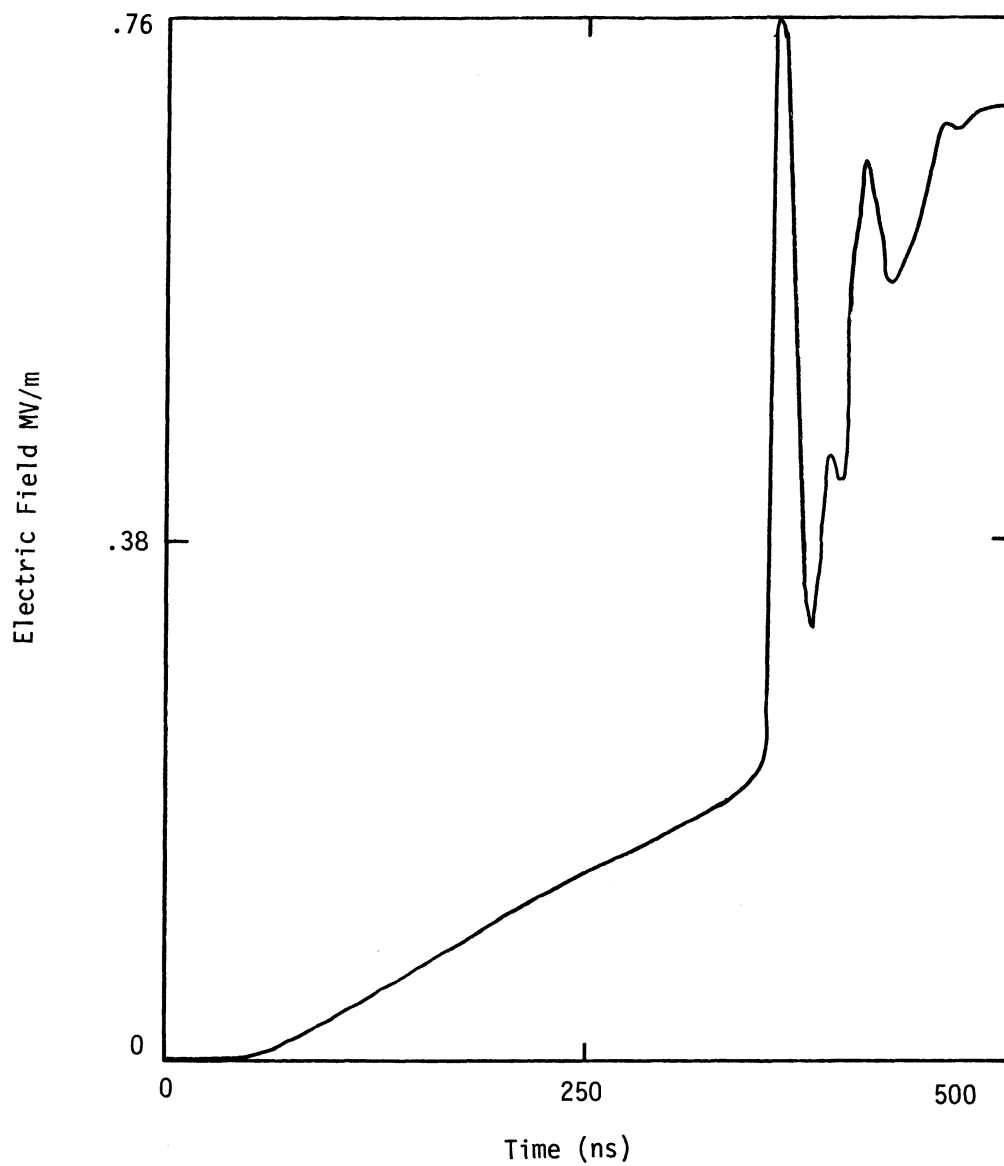
Charge - Positive
Water Vapor Content - 0%
Relative Air Density - .5

Figure 4.6c



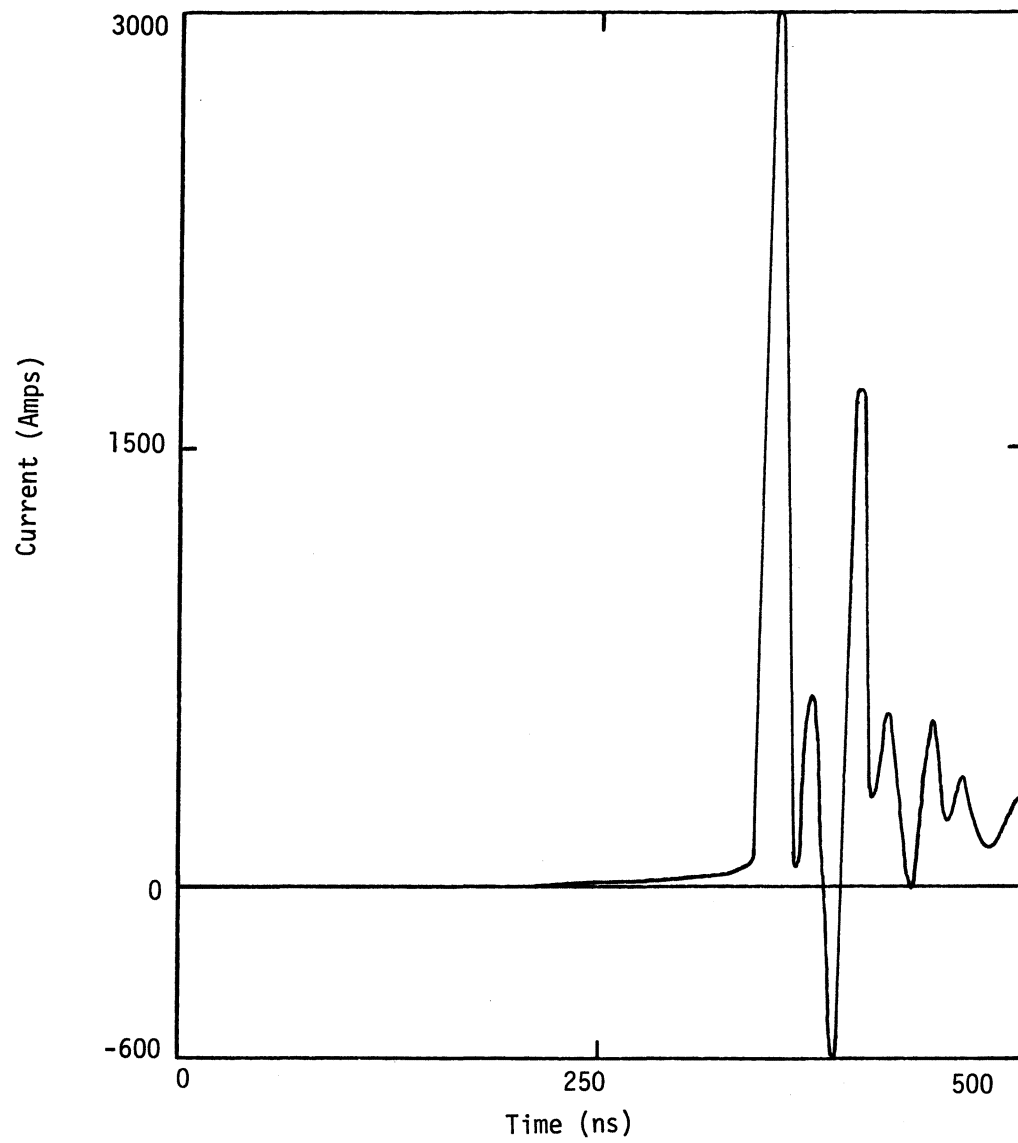
Charge - Positive
Water Vapor Content - 0%
Relative Air Density - 1

Figure 4.7a



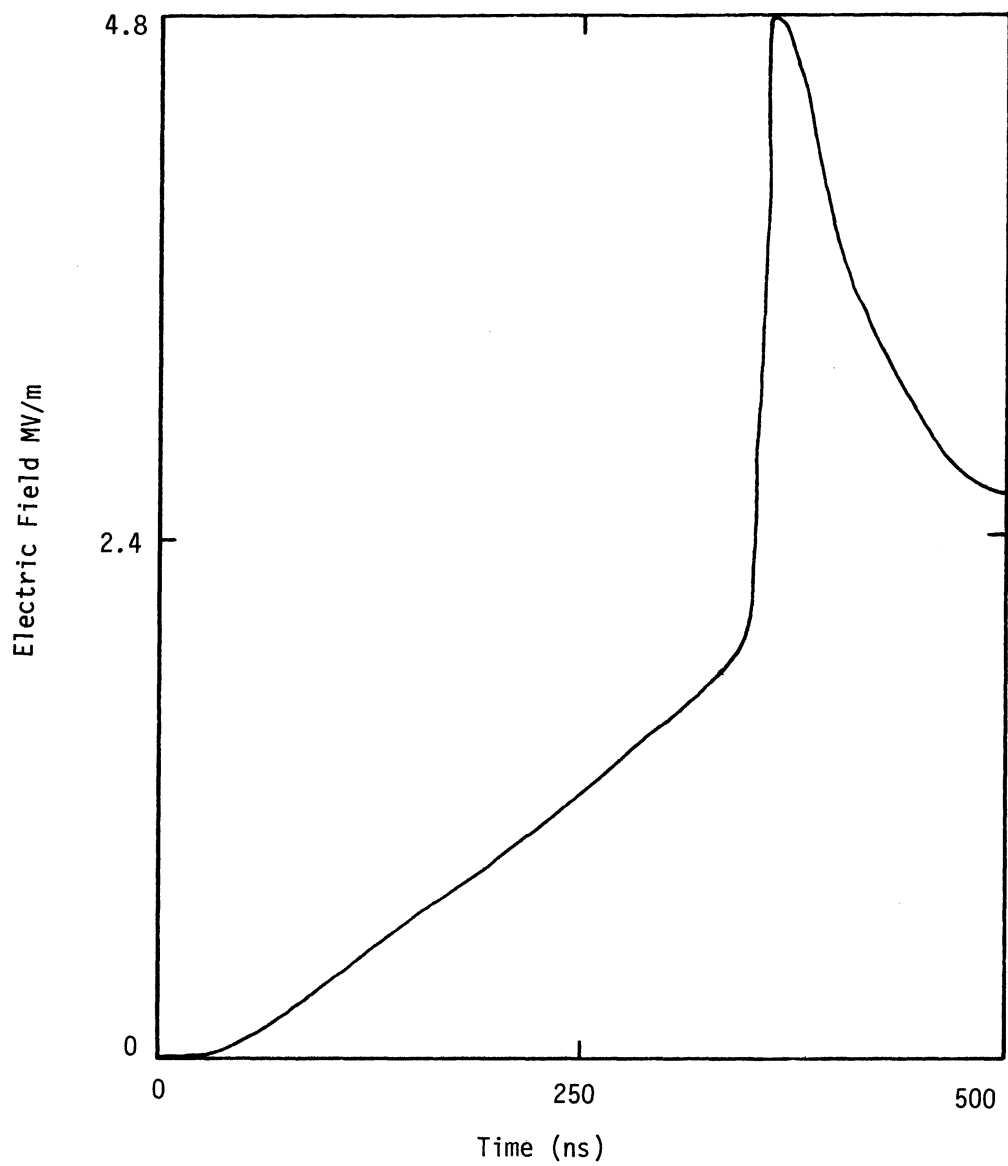
Charge - Positive
Water Vapor Content - 0%
Relative Air Density - 1

Figure 4.7b



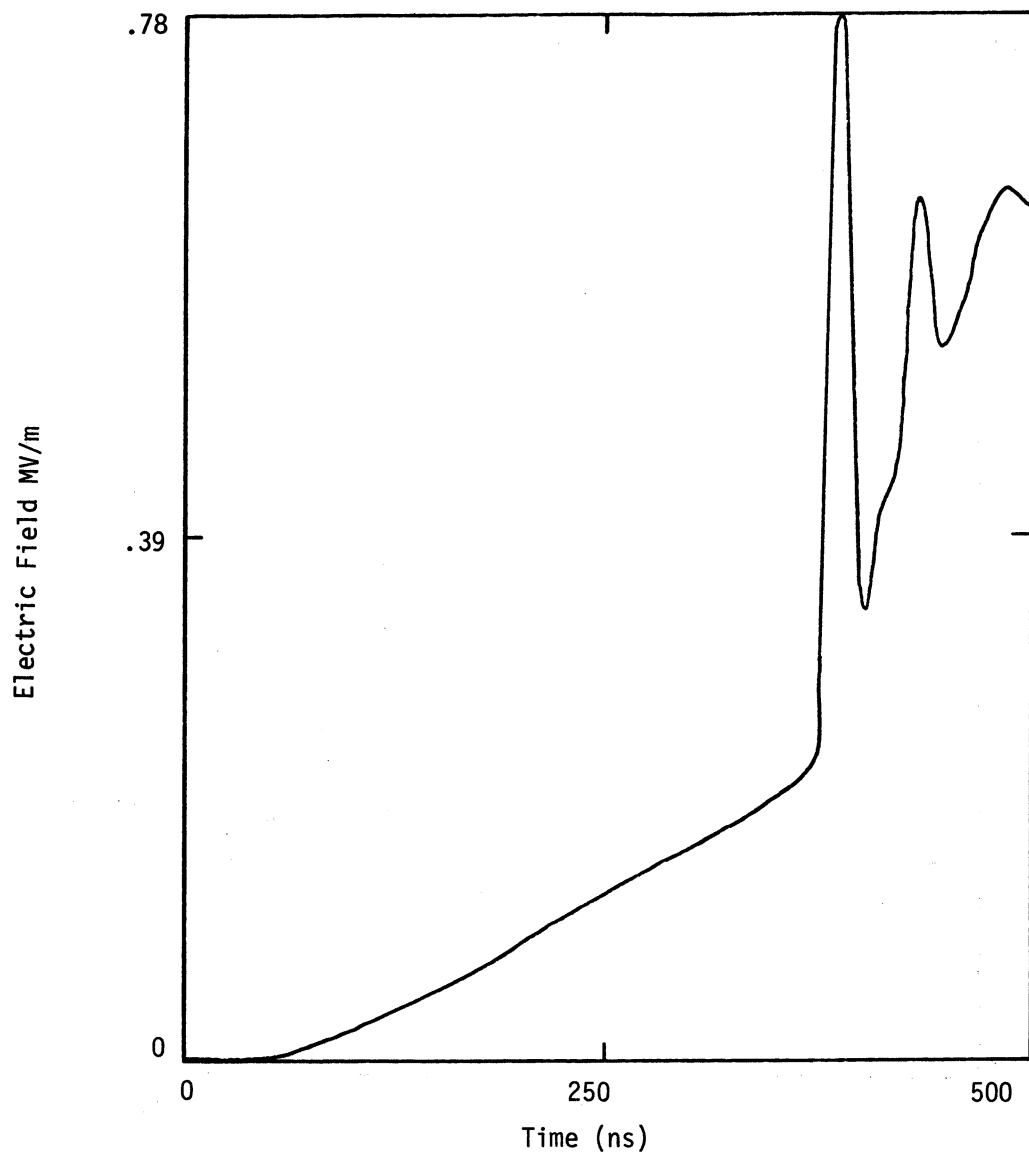
Charge - Positive
Water Vapor Content - 0%
Relative Air Density - 1

Figure 4.7c



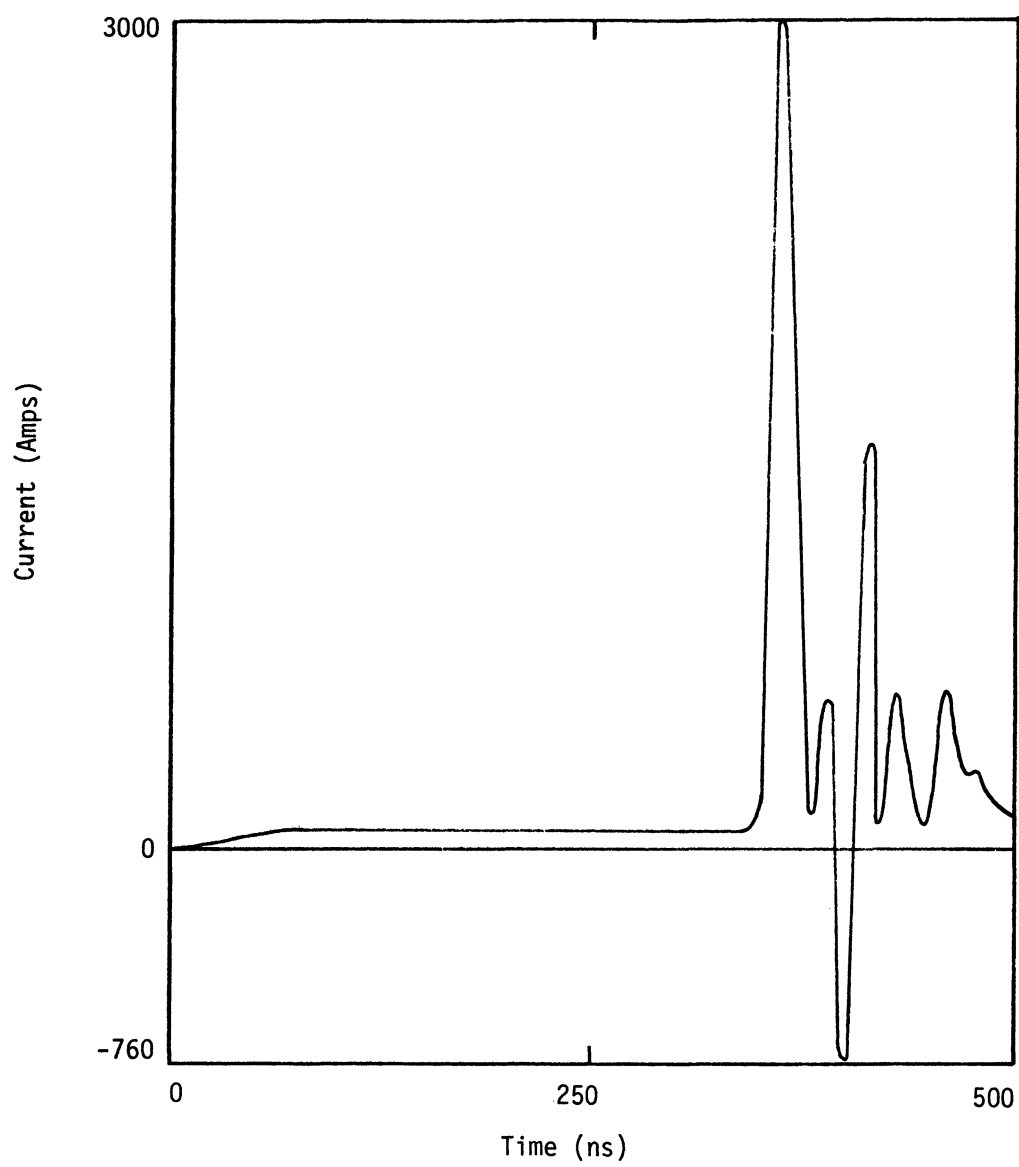
Charge - Positive
Water Vapor Content - 6%
Relative Air Density - 1

Figure 4.8a



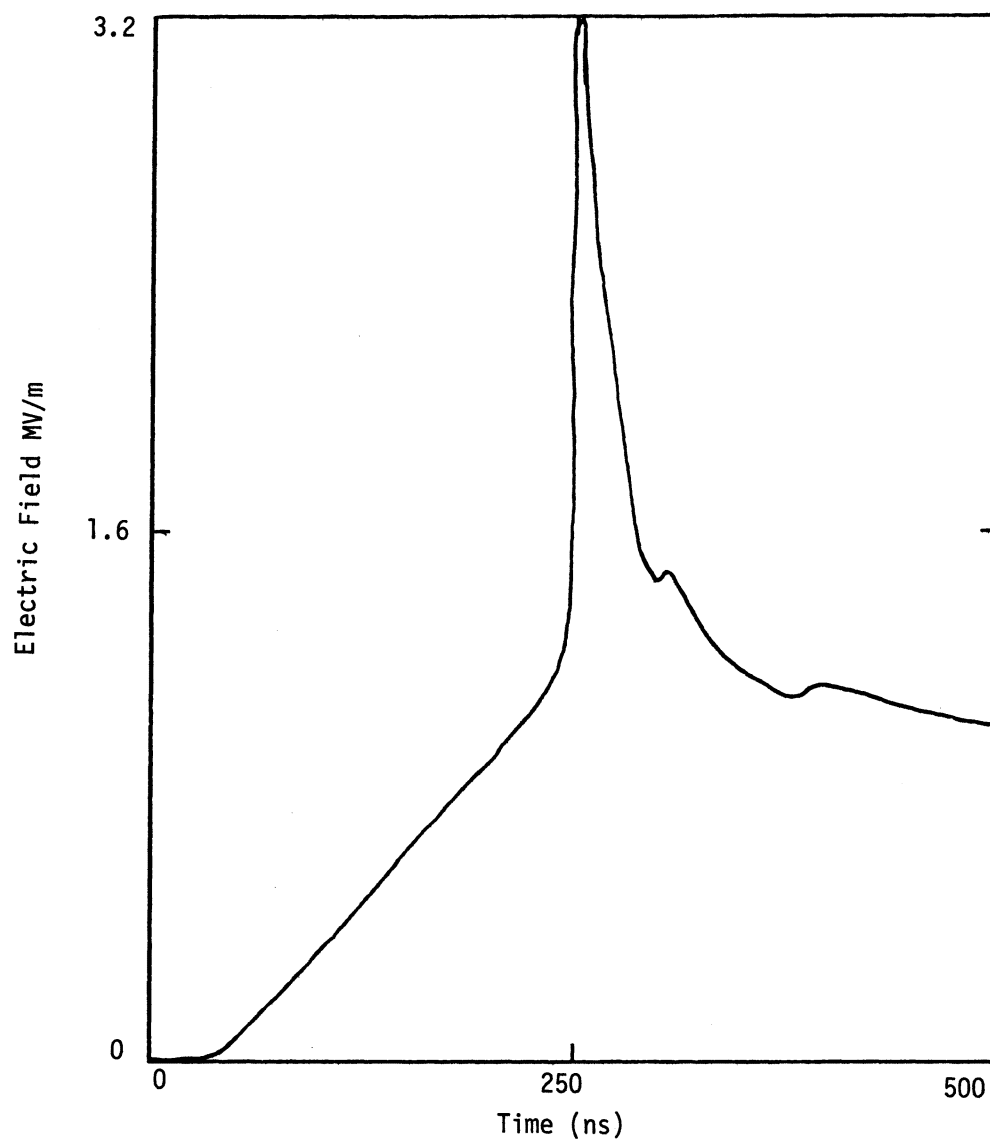
Charge - Positive
Water Vapor Content - 6%
Relative Air Density - 1

Figure 4.8b



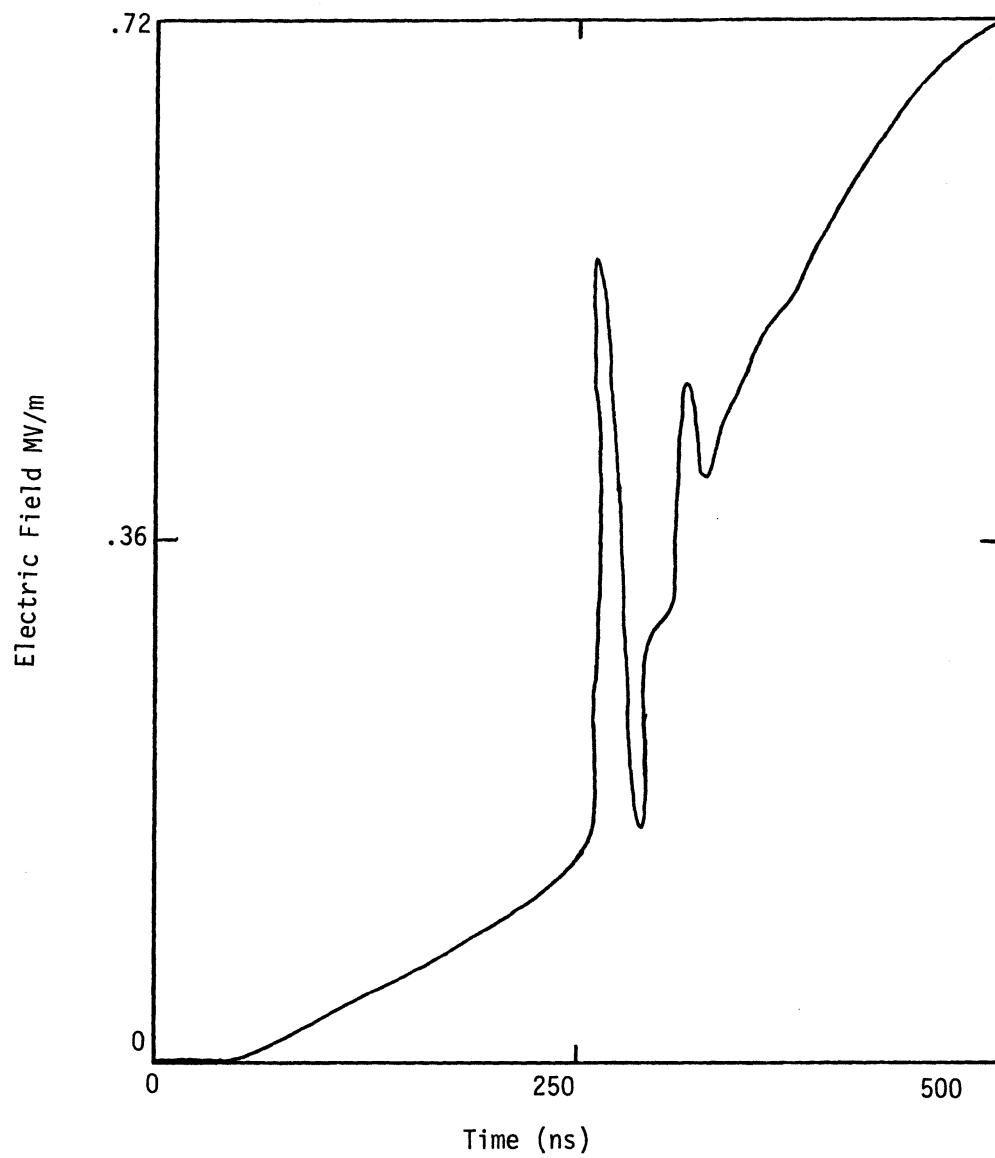
Charge - Positive
Water Vapor Content - 6%
Relative Air Density - 1

Figure 4.8c



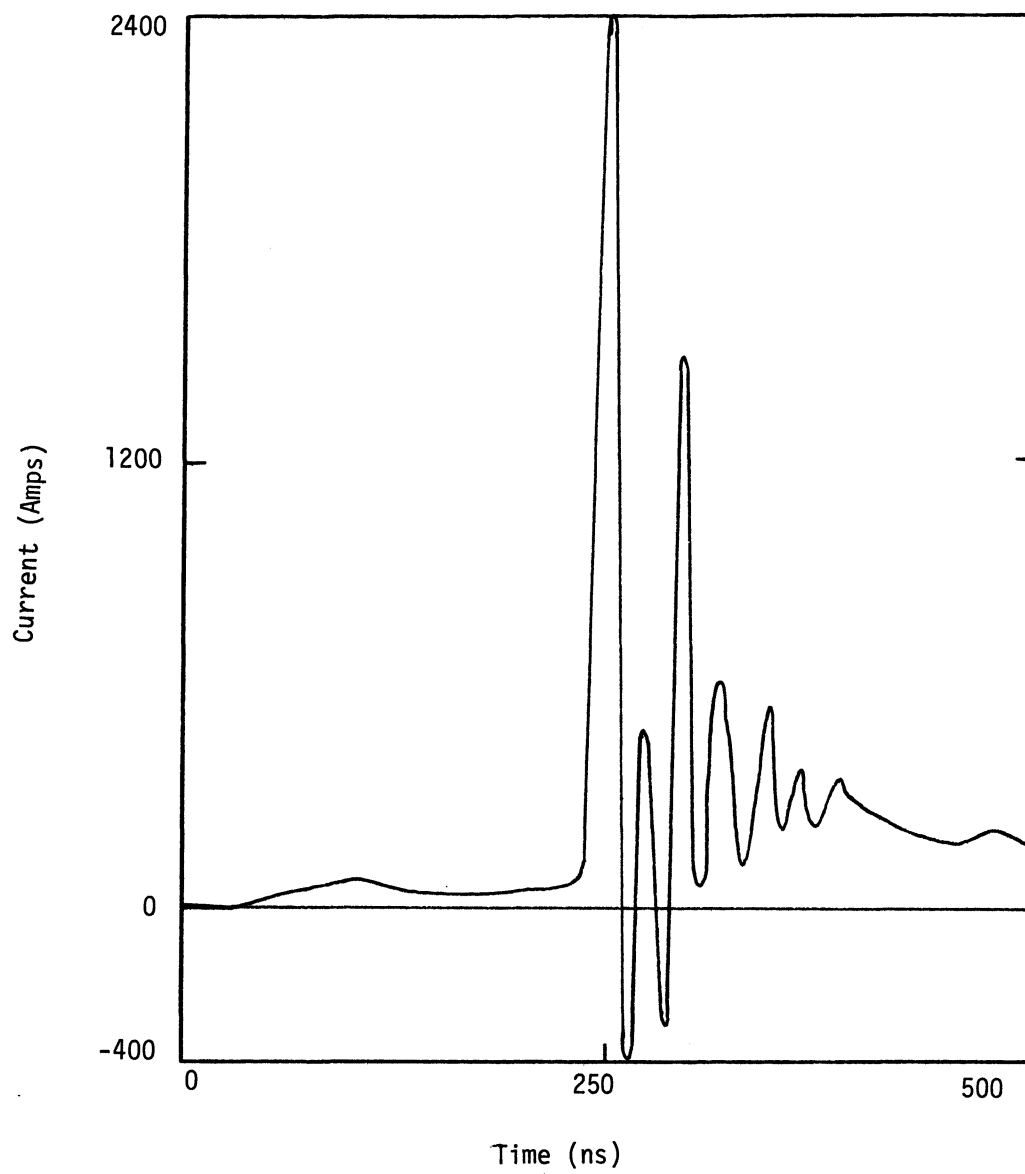
Charge - Positive
Water Vapor Content - 6%
Relative Air Density - .5

Figure 4.9a



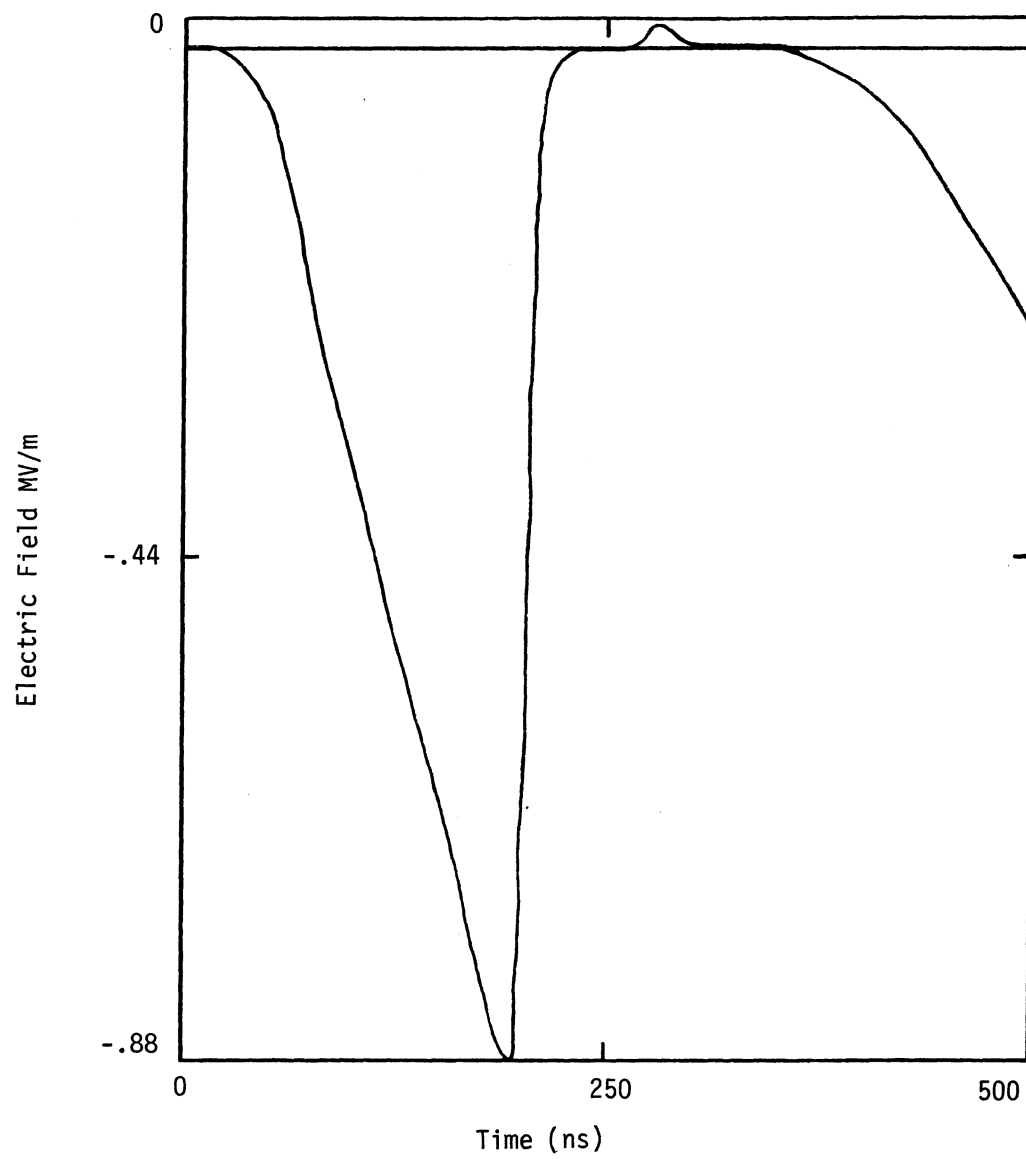
Charge - Positive
Water Vapor Content - 6%
Relative Air Density - .5

Figure 4.9b



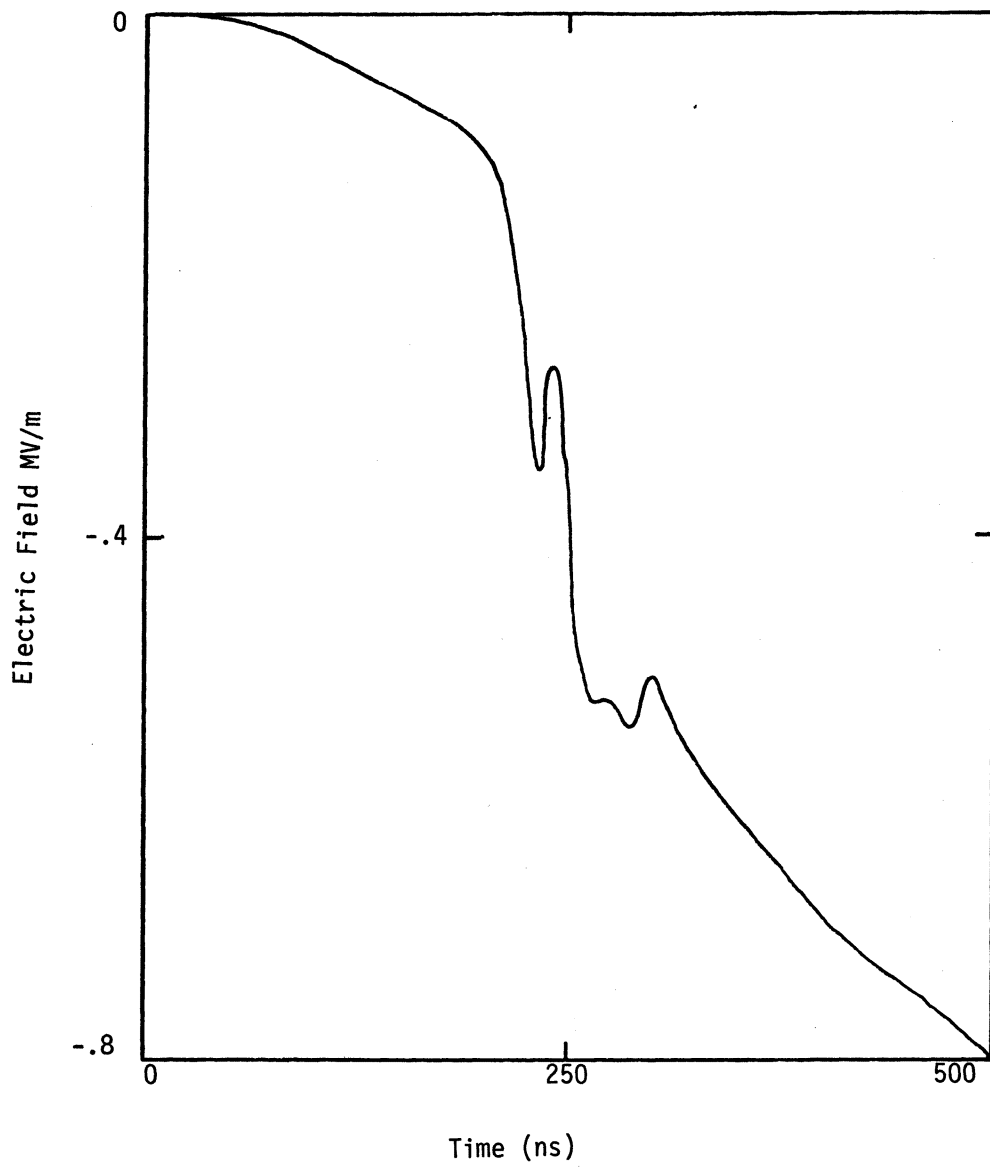
Charge - Positive
Water Vapor Content - 6%
Relative Air Density - .5

Figure 4.9c



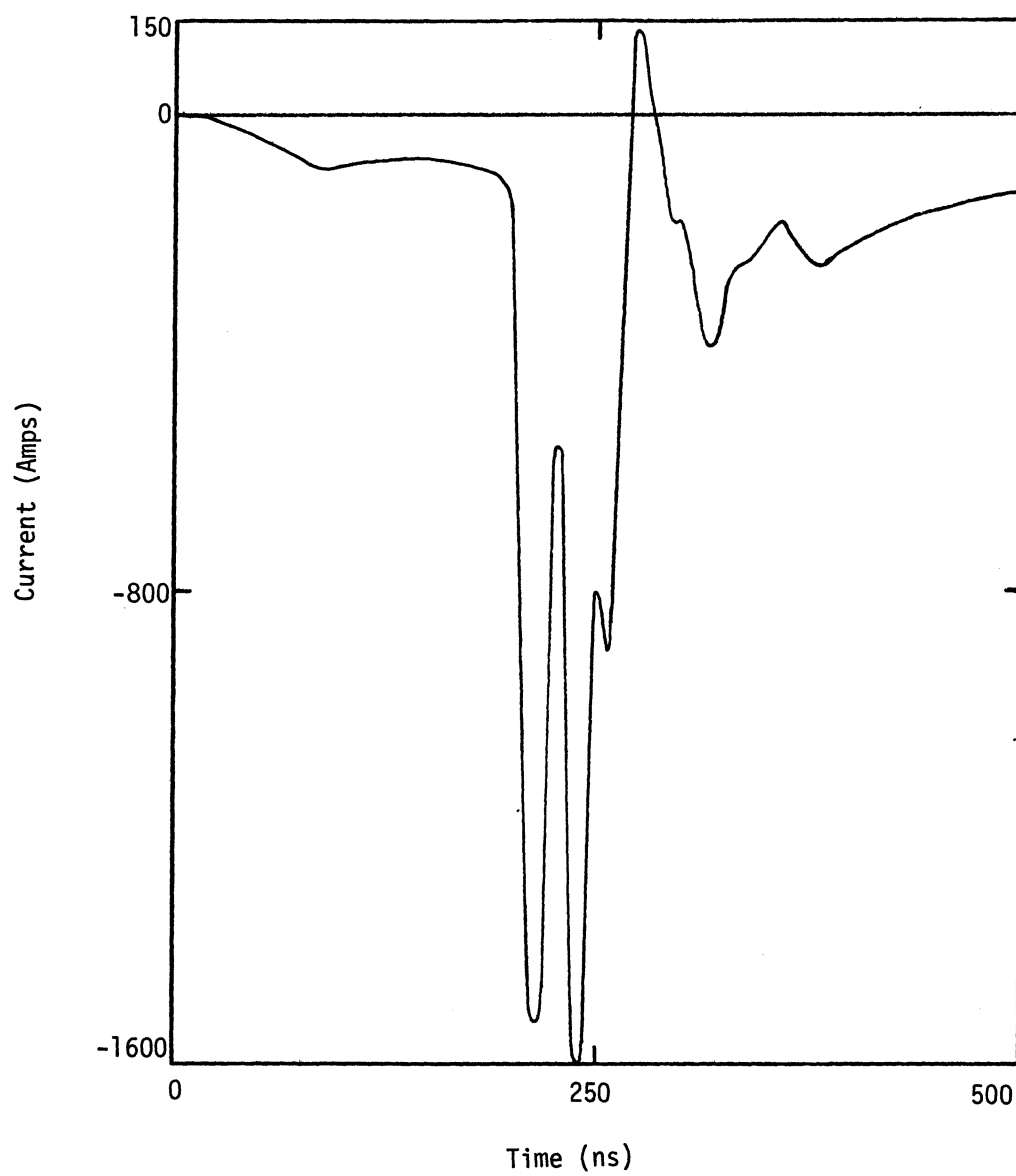
Charge - Negative
Water Vapor Content - 0%
Relative Air Density - .5

Figure 4.10a



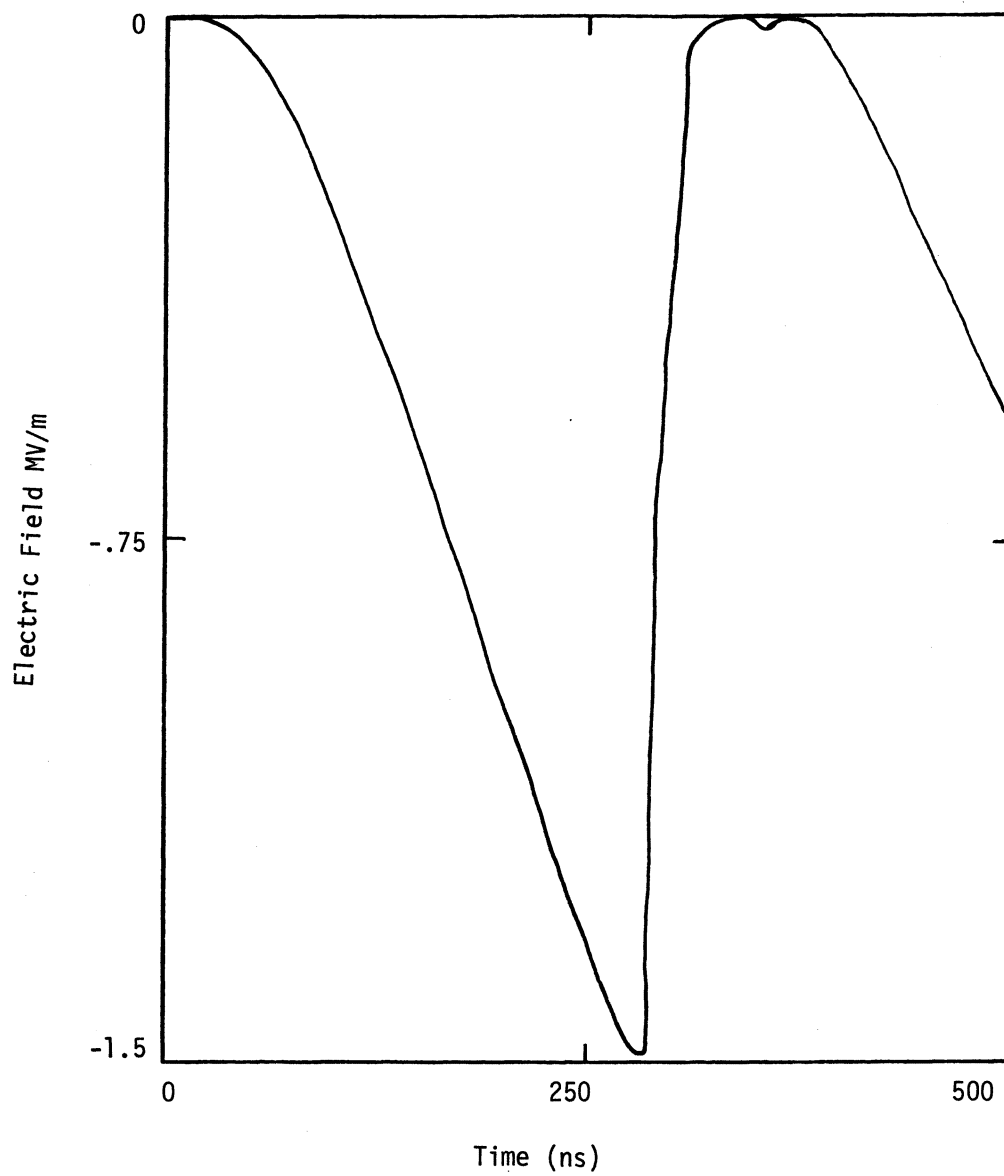
Charge - Negative
Water Vapor Content - 0%
Relative Air Density - .5

Figure 4.10b



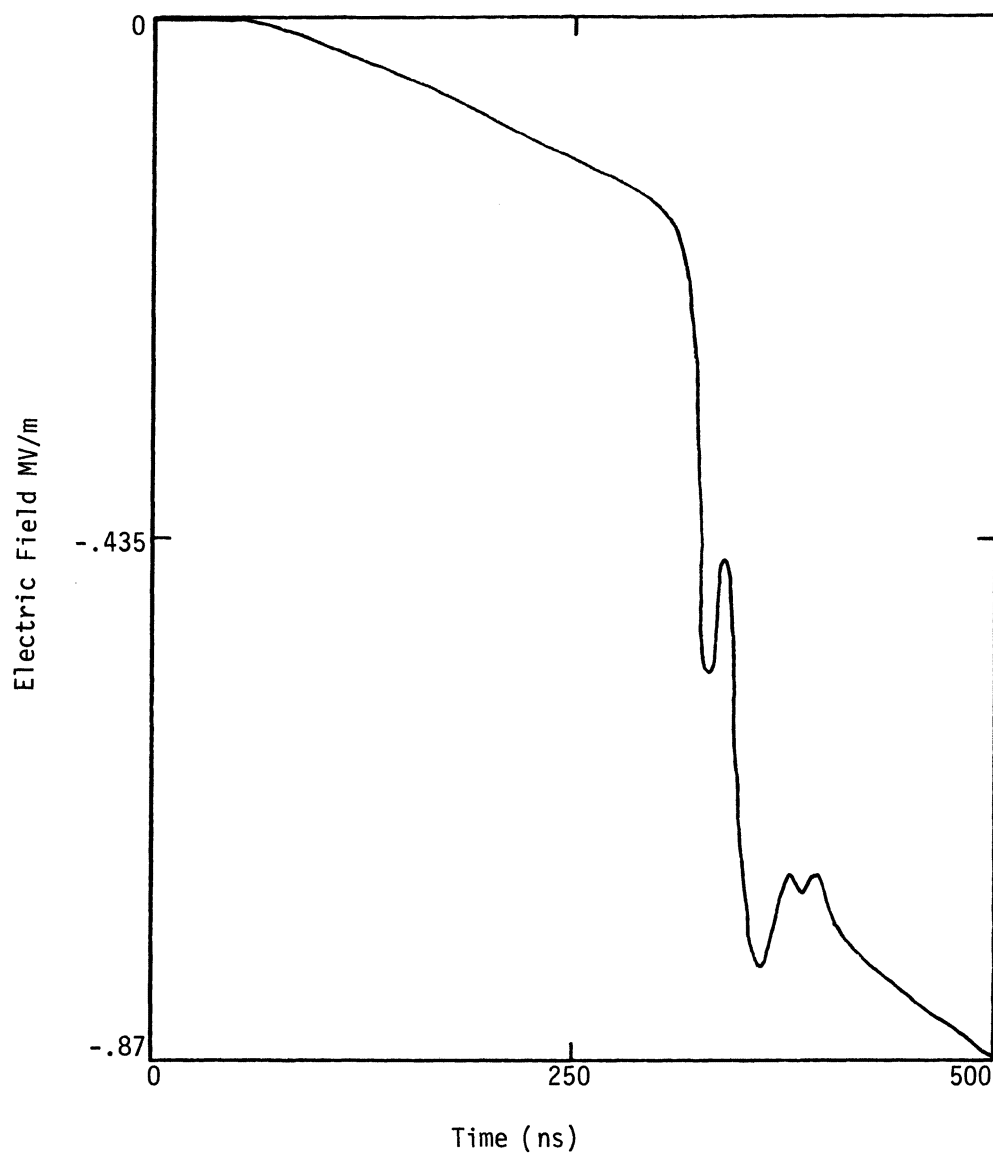
Charge - Negative
Water Vapor Content - 0%
Relative Air Density - .5

Figure 4.10c



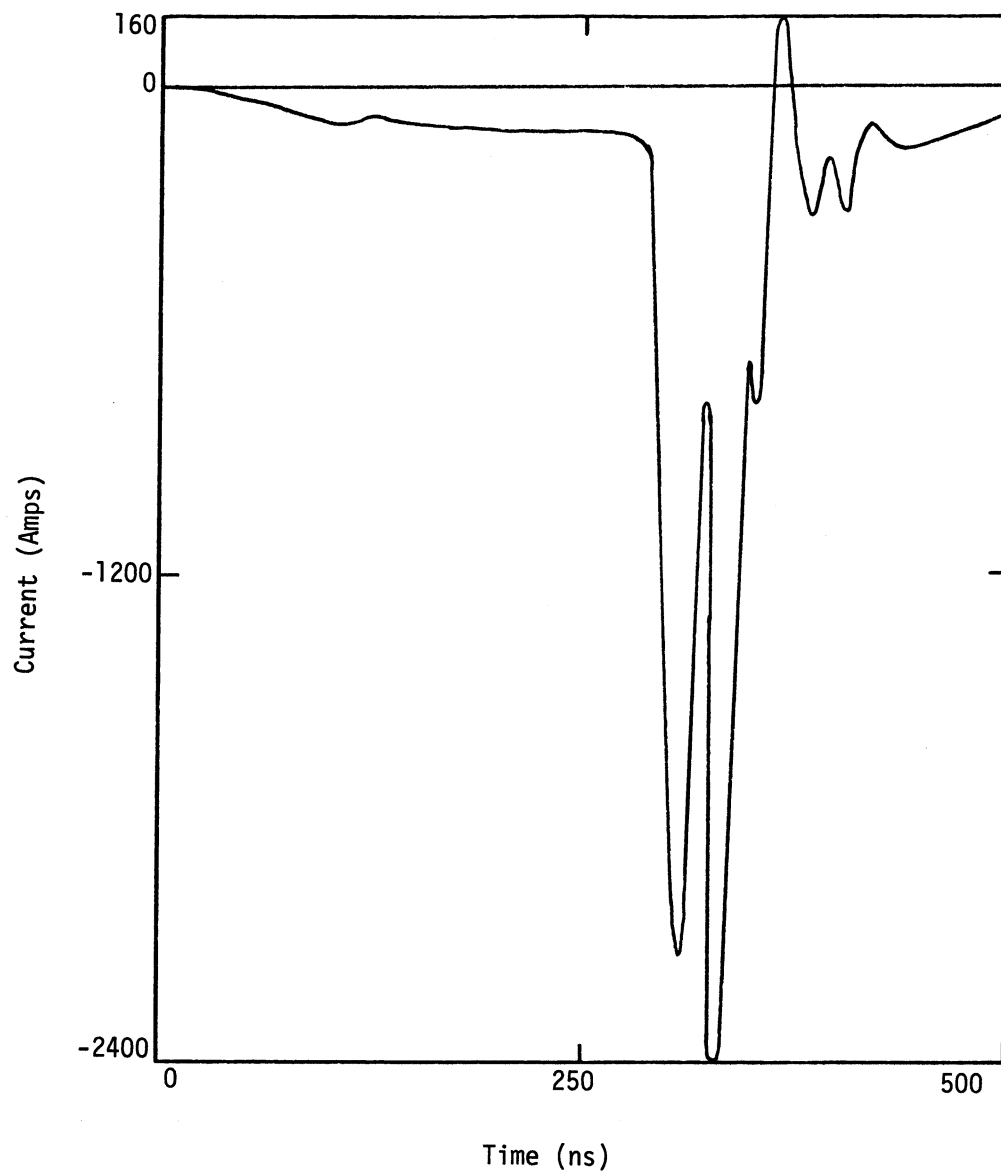
Charge - Negative
Water Vapor Content - 0%
Relative Air Density - 1

Figure 4.11a



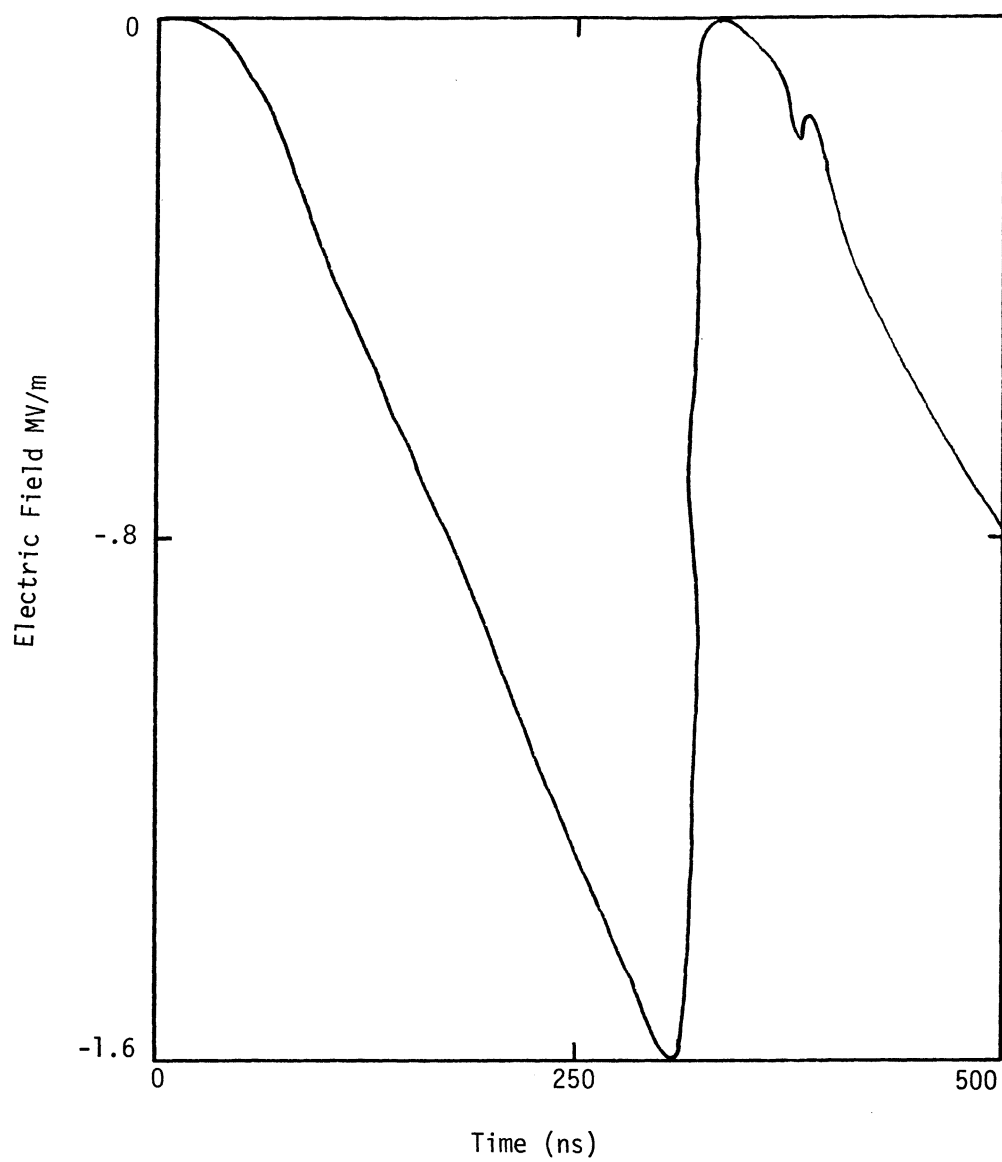
Charge - Negative
Water Vapor Content - 6%
Relative Air Density - 1

Figure 4.11b



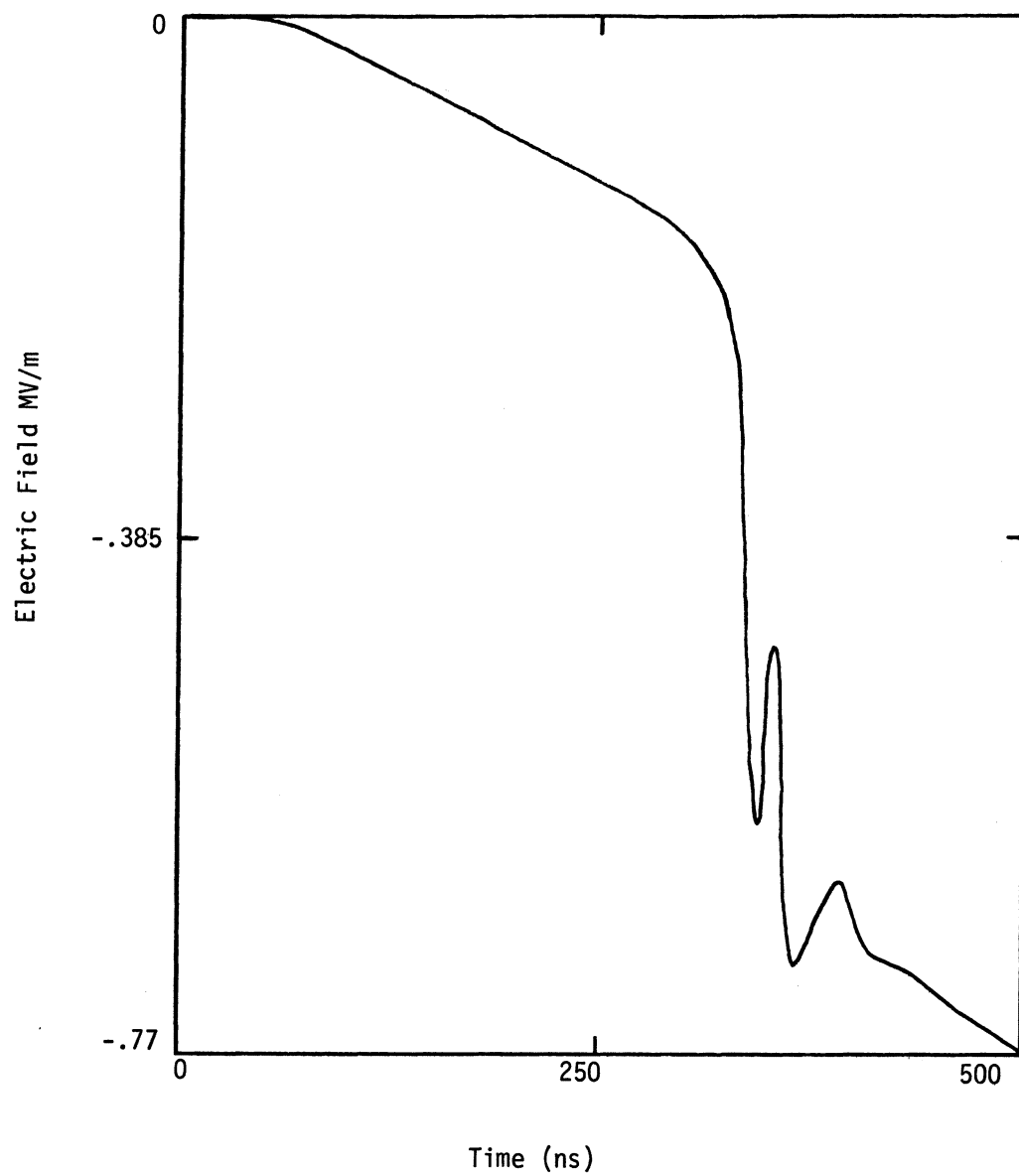
Charge - Negative
Water Vapor Content - 0%
Relative Air Density - 1

Figure 4.11c



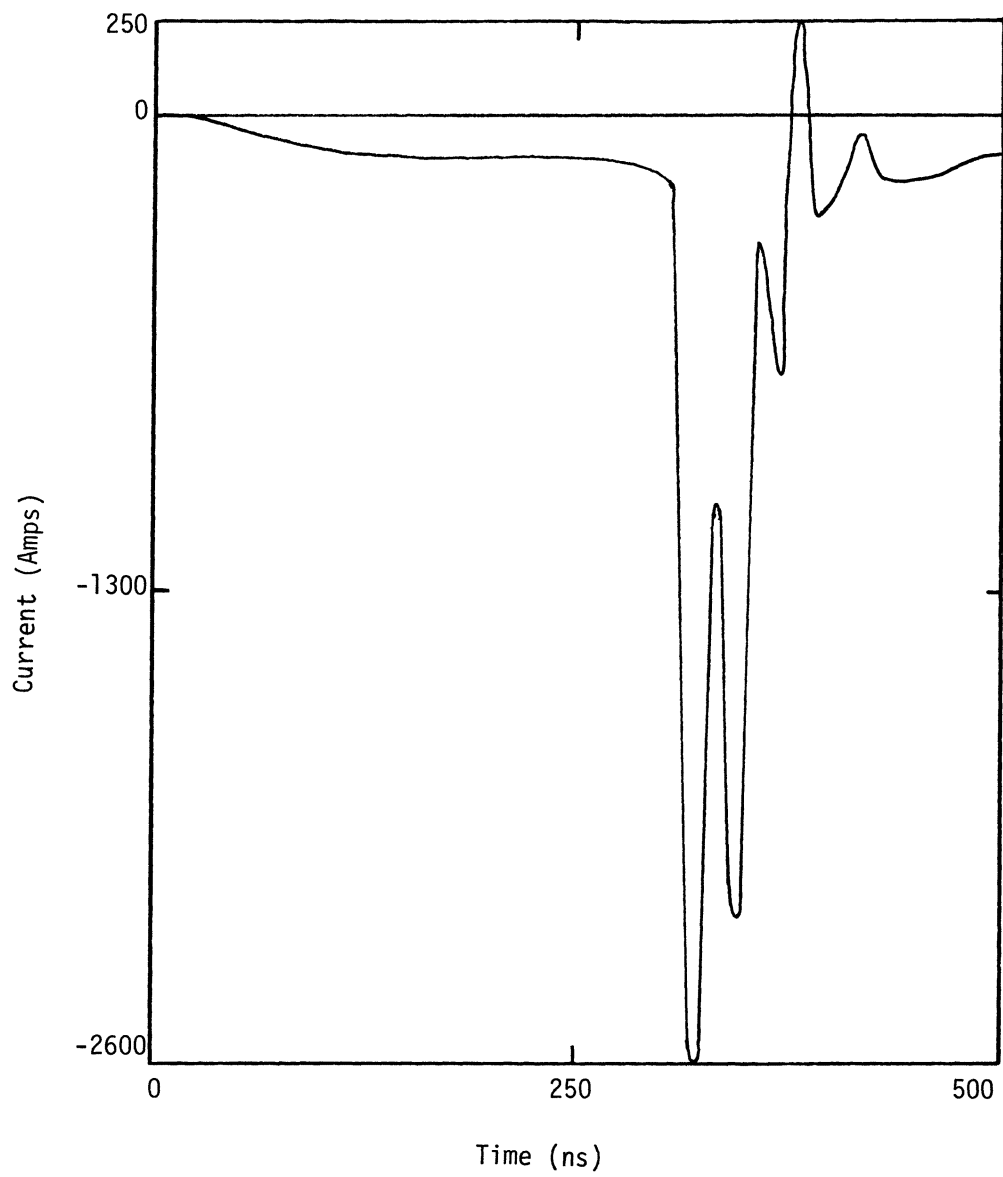
Charge - Negative
Water Vapor Content - 6%
Relative Air Density - 1

Figure 4.12a



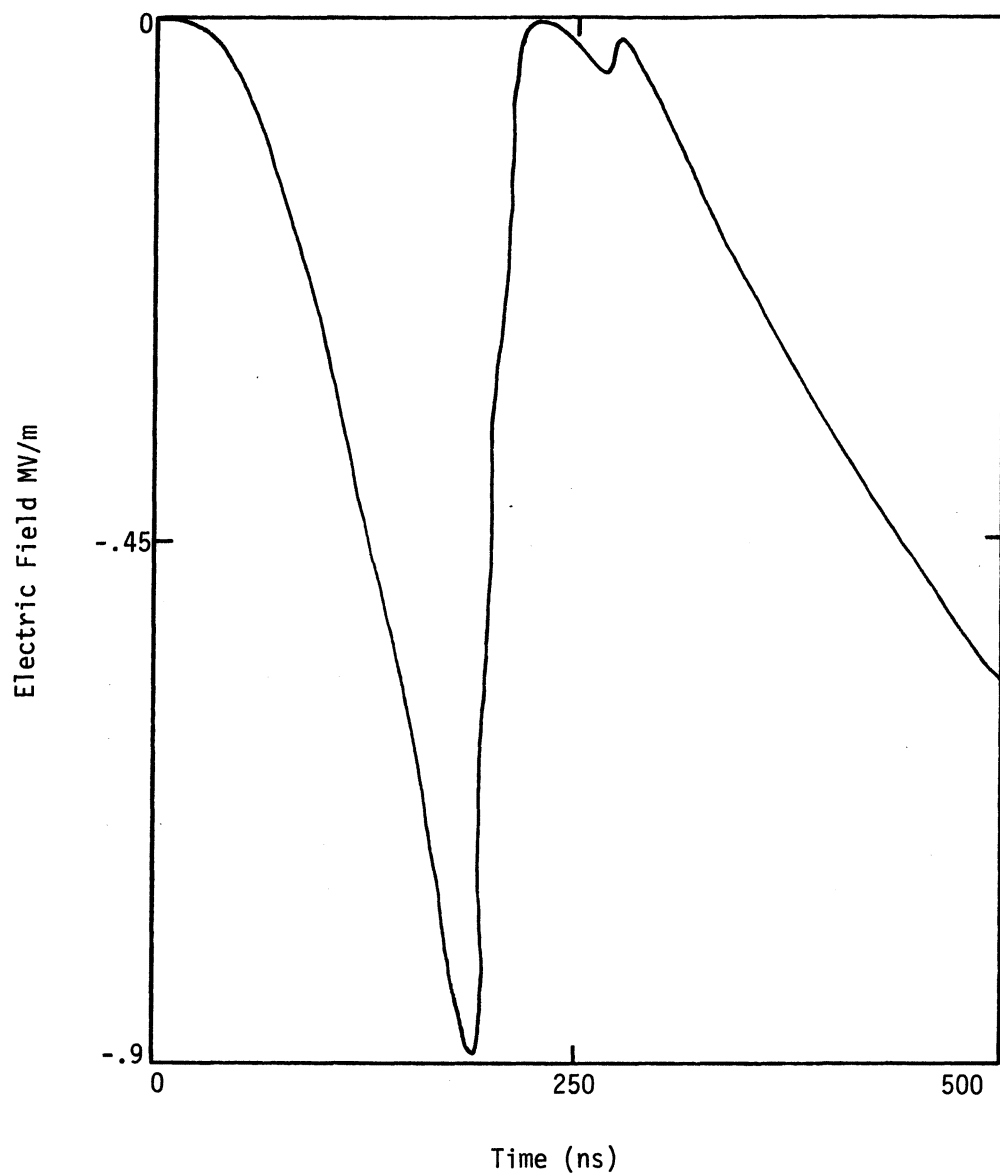
Charge - Negative
Water Vapor Content - 6%
Relative Air Density - 1

Figure 4.12b



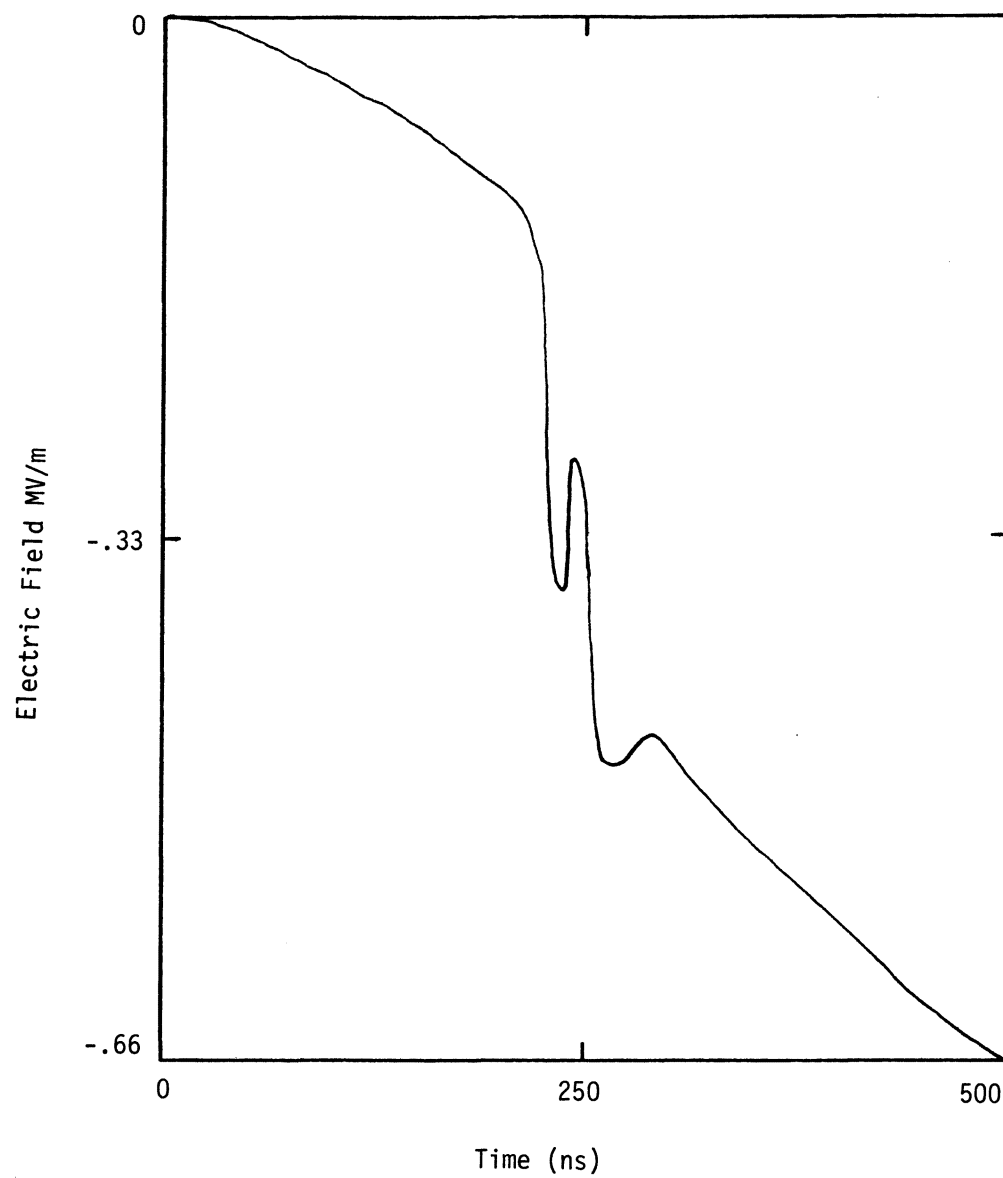
Charge - Negative
Water Vapor Content - 6%
Relative Air Density - 1

Figure 4.12c



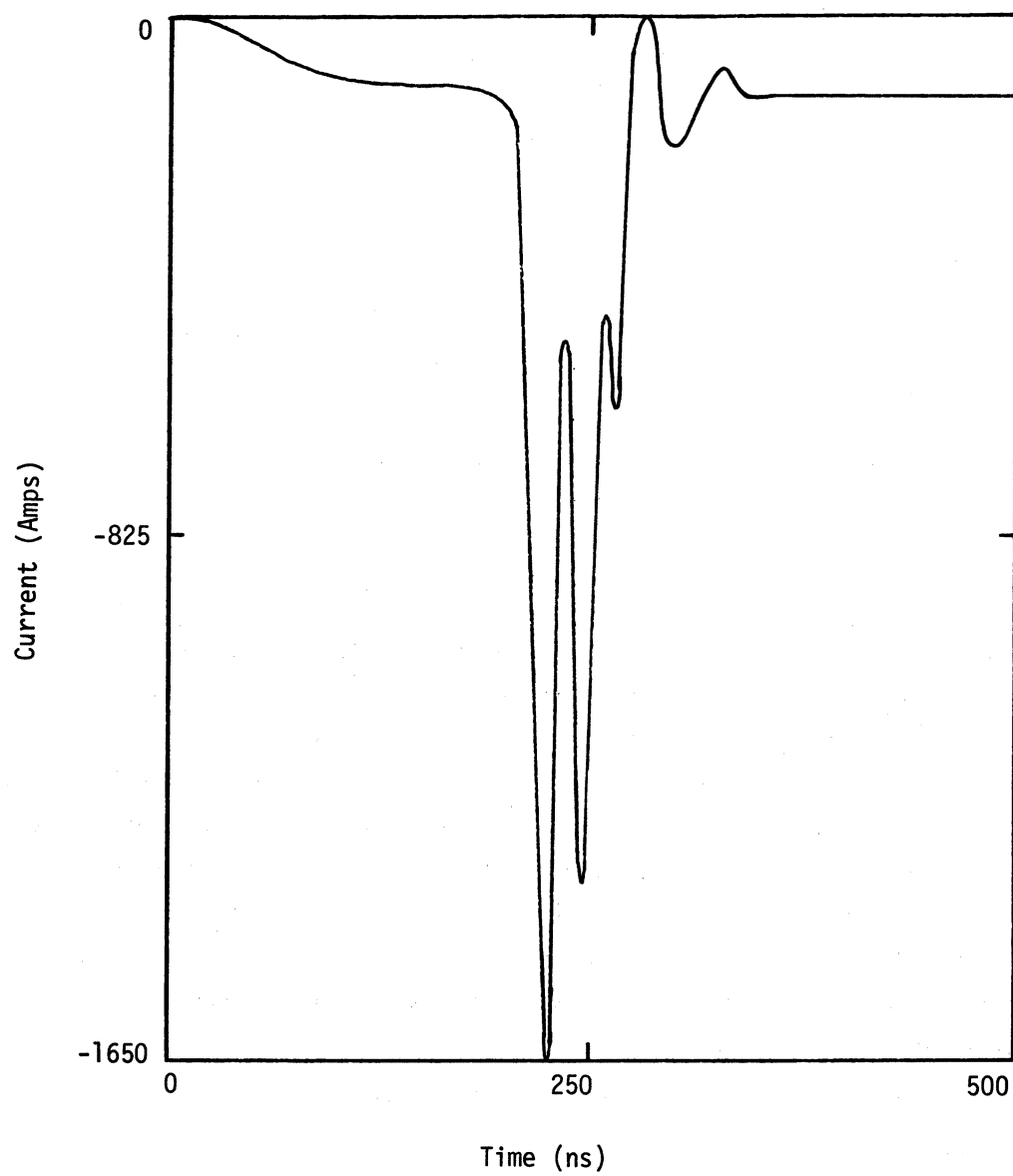
Charge - Negative
Water Vapor Content - 6%
Relative Air Density - .5

Figure 4.13a



Charge - Negative
Water Vapor Content - 6%
Relative Air Density - .5

Figure 4.13b



Charge - Negative
Water Vapor Content - 6%
Relative Air Density - .5

Figure 4.13c

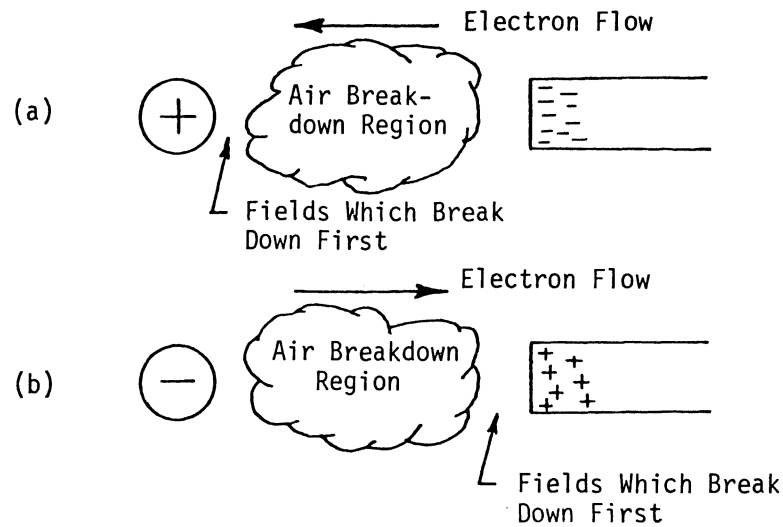


Fig. 4.14 Geometry of Breakdown Process in the Finite Difference Code

positive charge and in (b) is the negative charge case. In both cases the air conductivity rises in the same place, between the charge and the end of the bar. The difference is in the direction of electron flow in the two cases.

In (a) flow is toward the charge, which will neutralize the electric field near the charge but enhance the field at the end of the bar. The positive ions in the breakdown region will flow in the opposite direction. This will tend to neutralize the field at the end of the bar, but since the mobility of these ions is so much less than the electron mobility the effect will be very small at first. The enhancement of the field at the end of the bar will cause the breakdown region to extend all the way to the bar's surface. This is what causes the sharp drop in the field after the enhancement is seen.

In (b) electron flow from the breakdown region is in the opposite direction, causing the field at the end of the bar to be neutralized first. If one were to monitor the fields on the charge side of the breakdown region, an initial enhancement would be seen there, followed by a sharp drop.

The question must now be asked as to whether the preceding is correct physical behavior or not, and whether or not the discreteness of

the finite differencing and the necessary spatial averaging have destroyed the physics of the attachment process. In the microscopic sense the answer is yes, in that the attachment does not take place exactly as one would expect. Physically, because of the cell size in the code, the bar has a relatively blunt end and also the maximum fields should be seen very near the charge. These fields should break down first producing an enhancement in the field at the end of the bar, regardless of the sign of the charge. But one must remember that the finite difference code cannot model in detail phenomena on a scale smaller than the cell size, and the initial air breakdown around the charge is surely smaller than that. The code can only model the breakdown in an average sense. That is, details such as the exact location of the initial electron avalanche are lost, but the overall behavior should be approximately correct. In particular, fields far from the attachment point should be relatively insensitive to the fine details of the breakdown and their behavior should be more characteristic of the average that the finite difference code calculates.

One last characteristic of Figures 4.6 - 4.13 which may be confusing is the drop in the field at the end of the bar when attachment occurs. Notice that where a positive charge is present the field drops to a relatively low level ($\approx 2 \times 10^6$ V/m) and stays there. In the case of a negative charge, however, the field drops to zero. This again is because of spatial averaging in the code and the direction of electron flow out of the breakdown region, as shown in Figure 4.14. The electrons are much more effective than the ions in neutralizing a field, so the fields toward which the electrons flow will drop to zero, and those on the other side will not. Again the average behavior of the fields is what is important to the attachment study.

Some general comments can be made about the results of the parameter study. As expected, in all cases breakdown of the air around the charge is accompanied by a large pulse of current flowing onto the bar. This current rapidly drops after the initial breakdown to a much lower steady level. The magnitude of the current pulse is relatively insensitive to the water content of the air, but

is quite sensitive to the relative air density. This is because a low air density allows breakdown at a lower electric field intensity. The attachment, therefore, occurs at an earlier time when less charge has built up at the end of the bar. Hence a smaller current pulse is seen.

The same type of phenomena is seen when comparing the current pulses for the two cases of positive and negative charge. The negative charge case shows an earlier and smaller current pulse for equal water content and relative air density. This occurs because the negative charge is composed of electrons which are available to start the electron avalanche earlier than in the positive charge case. So again, less charge has accumulated at the end of the bar when attachment occurs, and a smaller current pulse is seen.

In none of the runs done for the parameter study was breakdown observed at the back of the bar. Observation of the normal fields along the length of the bar at late time ($\sim 1 \mu\text{sec}$) showed that the charge was being distributed fairly evenly, with less than a factor of two difference in charge density between the center of the bar and the back end. This implies that the formation of a conducting channel at the back end of the bar is likely to occur several microseconds after attachment. It is also likely to happen more slowly than the initial attachment, because there is no enhancement of the electric field as is seen between the charge and the bar in attachment. This is important to the F106 study in that it would appear that the initial attachment of a lightning channel to the aircraft and the initial exit will be quite widely separated in time, particularly for the small currents that are commonly seen. Of course, it should be kept in mind that the F106 aircraft has much more pointed structures, such as wing and tail tips, than the bar in the parameter study. These allow for much larger electric fields locally, and may cause exit channels to form significantly earlier than would be predicted from a study of the behavior of the bar.

4.8 Application of the Nonlinear Model to the F106B Aircraft

To determine the response of the F106 aircraft to a lightning attachment, the nonlinear corona model was applied to the finite

difference model of the F106. The linear version of the F106 model was described in detail in [1]. Addition of corona and air conductivity necessitated one change to the basic finite difference code. This was a reduction in the problem space size by three cells in each of the three coordinates, corresponding to a three meter reduction in the dimension along the length of the aircraft, and one and one-half meters in the other two dimensions. The problem space size for the nonlinear code was, therefore, 16 meters in the wing to wing dimensions, 28 meters along the fuselage, and 9-1/2 meters vertically. The reduction was necessary in order to bring the computer run time of the code down to an acceptable level, because air conductivity calculations are costly in both storage and time. Even with the reduction the calculations took approximately 30 CPU seconds per time step on a Data General MV8000 with 1 megabyte of central memory.

Attachments were done at four points on the aircraft for both positive and negative charges. These points were the right side of the fuselage near the nose, the tip of the tail, and the leading edges of the right and left wings near the tip (Figure 4.15). The attachment was forced to occur by introducing a line current into the problem space and terminating it at a point one meter from the expected attachment point. This resulted in a charge building up at the end of the line current until the electric field between the charge and the aircraft reached breakdown level. Then a conducting channel formed between the charge and the aircraft allowing the charge and the line current to flow directly onto the aircraft. The waveform for the line current used to form the charge was a step function of amplitude 100 amperes and sine-squared leading edge with rise time 100 nanoseconds. It was found that this current led to attachment at approximately 500 nanoseconds and that the attachment was slow enough that the one nanosecond time step of the code could resolve it. Larger currents resulted in earlier attachment with very fast field changes which the code was unable to track with a one nanosecond time step. Smaller currents took an unacceptably long time to produce breakdown field levels. In addition, 100 amperes is thought to be the average value of current in a stepped leader [8,9], which the nonlinear

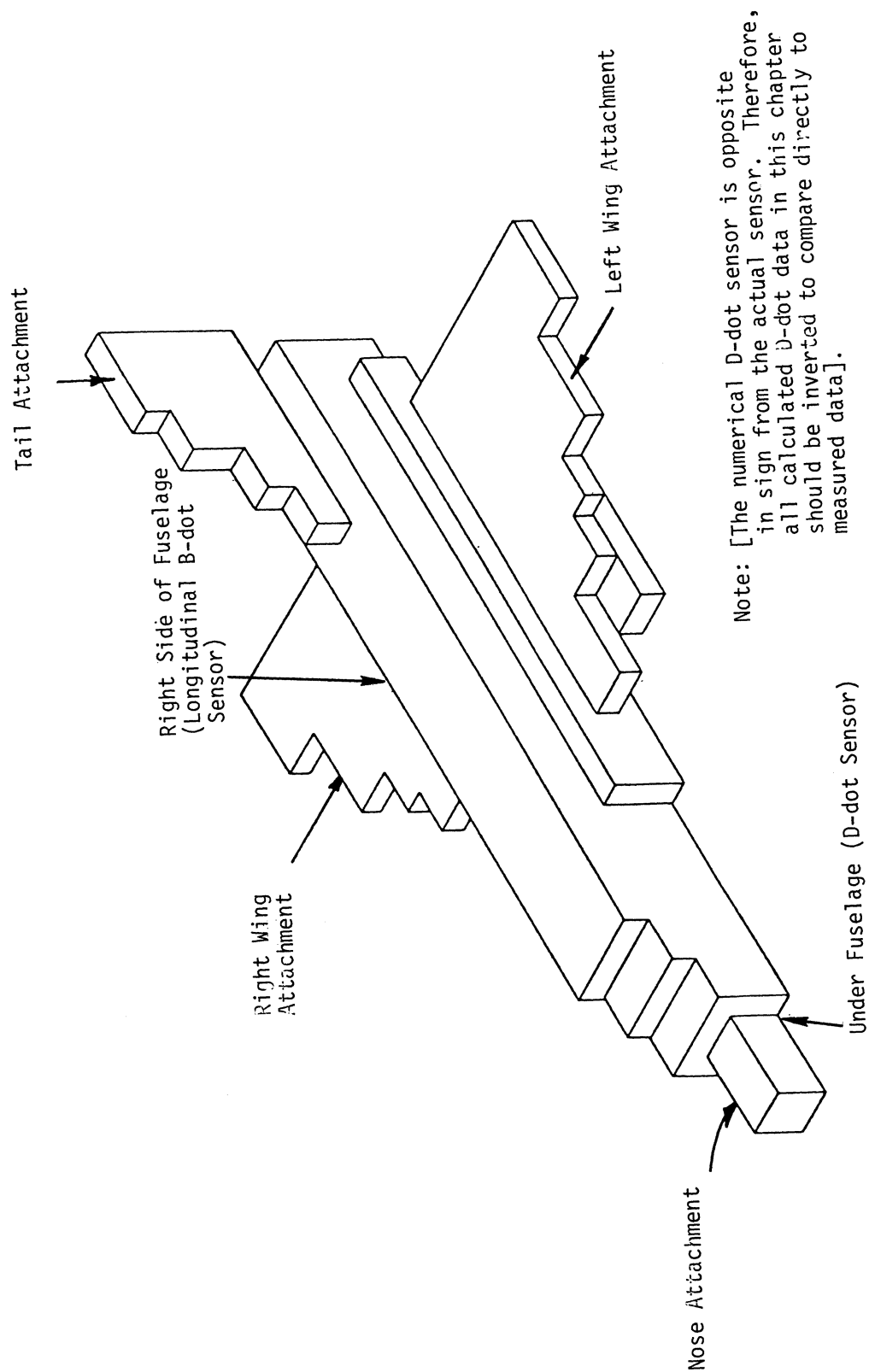


Figure 4.15 F106 Model Showing Nonlinear Attachment Points and Sensor Points

code is attempting to model. The air parameters used in all of the attachments were a water vapor content of 6 percent, corresponding to thunderstorm and rainy conditions, and a relative air density of .5, corresponding roughly to the altitude (5.2 km) at which the F106 has been struck by lightning. Monitor points on the model aircraft were E and D-dot underneath the fuselage near the nose, H and B-dot on the fuselage above the right wing, and the current and its time derivative at the expected attachment point. The magnetic field monitor point was positioned so as to sense currents flowing longitudinally along the fuselage. The D-dot and B-dot monitor points correspond to those which are measured experimentally when the F106 is struck by lightning, so these responses can be compared directly with the measured data.

The reader may be curious as to why one of the attachments was done to the side of the nose rather than directly onto the nose of the aircraft. The explanation has to do with the noncubical cells used in the nonlinear code. Figure 4.16 shows the geometric situation for a charge directly in front of the nose of the aircraft. The field

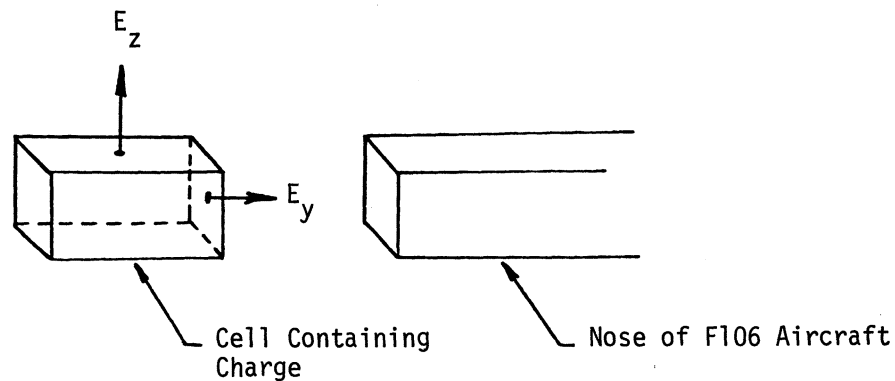


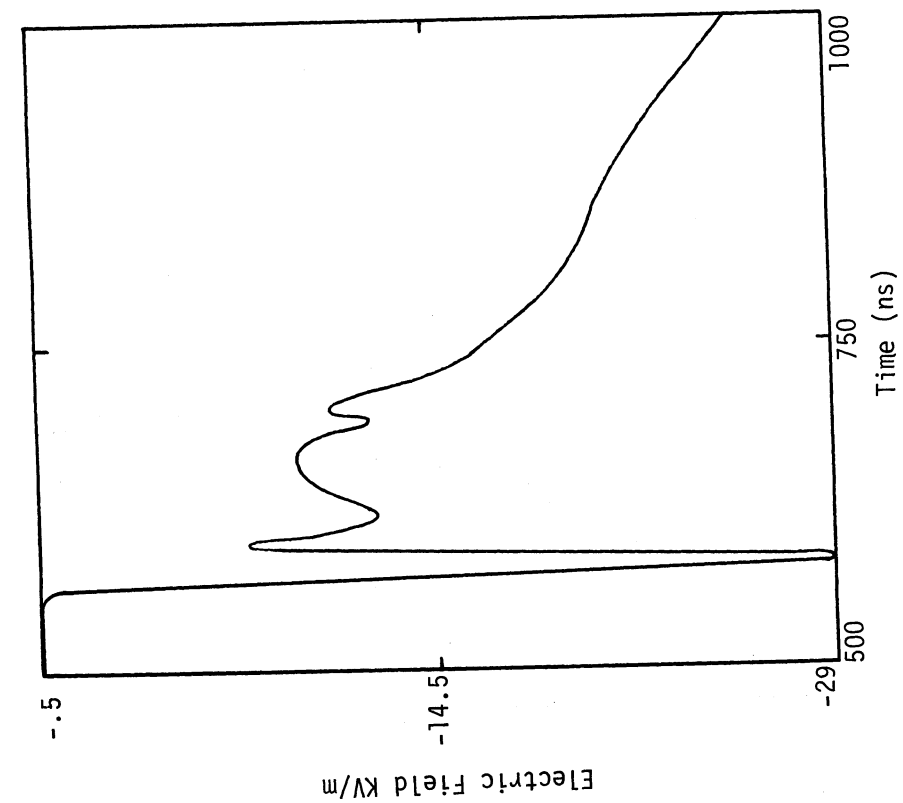
Figure 4.16 Illustration of Finite Difference Cell Containing Charge Located Directly in Front of Aircraft Nose

labelled E_y should be the largest field because of the presence of the nose of the aircraft. However, because the unit cell is twice as long in that direction as in the two perpendicular directions, the field labelled E_z is effectively closer to the charge than is E_y . Therefore the nonlinear code finds that E_z is larger than E_y and when breakdown occurs, the charge moves predominantly in the directions perpendicular to E_y . Physically the charge is attempting to achieve a lower energy state by becoming spherical, or at least as spherical as possible in a Cartesian coordinate space. But this expansion perpendicular to E_y delays attachment and eventually causes the attachment to be a diffuse one over all points on the nose of the aircraft. Of course, this is not seen physically, and so must be avoided. By forcing the attachment to occur on the side of the nose, the expansion does not take place, and a much more localized area is involved. The response of the aircraft should not be affected drastically by this shift in attachment point. It is also observed that attachment from the side is a physically realistic situation.

The aircraft responses for the attachment calculations are shown in Figures 4.17 - 4.24. Only a window around the time of attachment is shown in each case to emphasize the fast field and derivative changes that are seen. In all cases the attachment of a negative charge is seen to be somewhat gentler than that of a positive charge, as evidenced by smaller peak fields and time derivatives. This is consistent with the results in the study of the bar reported in the previous section. There is little difference in the current injected onto the aircraft at the four attachment points. Peak currents range from 450 to 540 amperes with rise times of the order of 30 nanoseconds. Peak $I\text{-dot}$ ranges from 3×10^{10} to 8×10^{10} amperes/second.

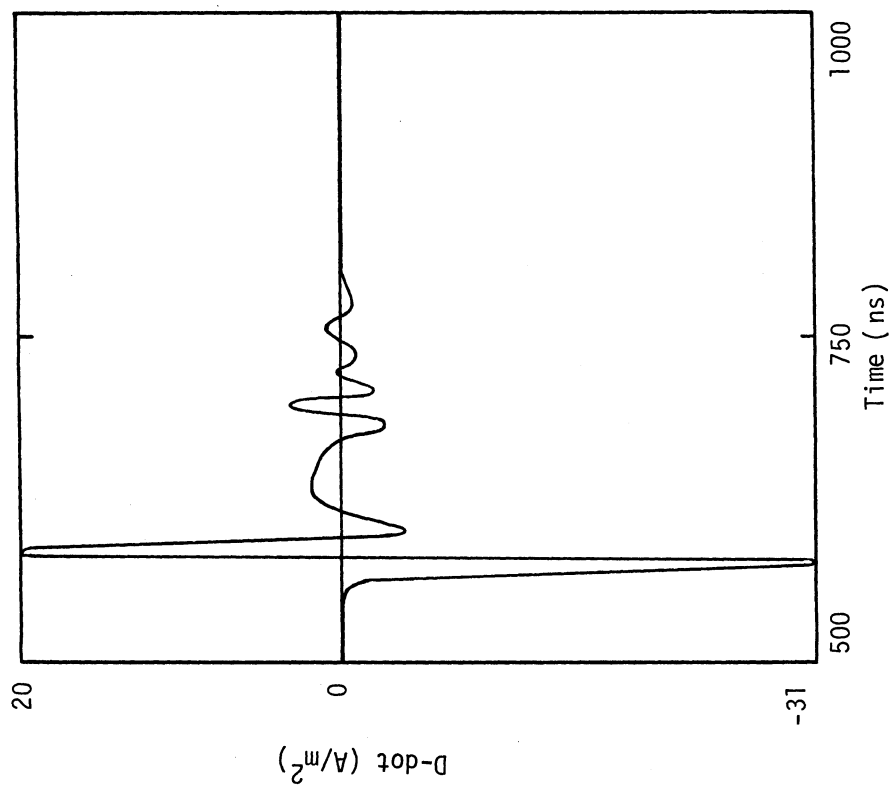
As expected, there is greater variation in fields recorded at the other monitor points. Peak values of $D\text{-dot}$ are largest for nose attachment, and peak values of $B\text{-dot}$ are largest for right wing attachment, although the corresponding H field for that attachment is not largest.

An explanation is necessary as to the difference in responses for left and right wing attachment, which should be symmetric.



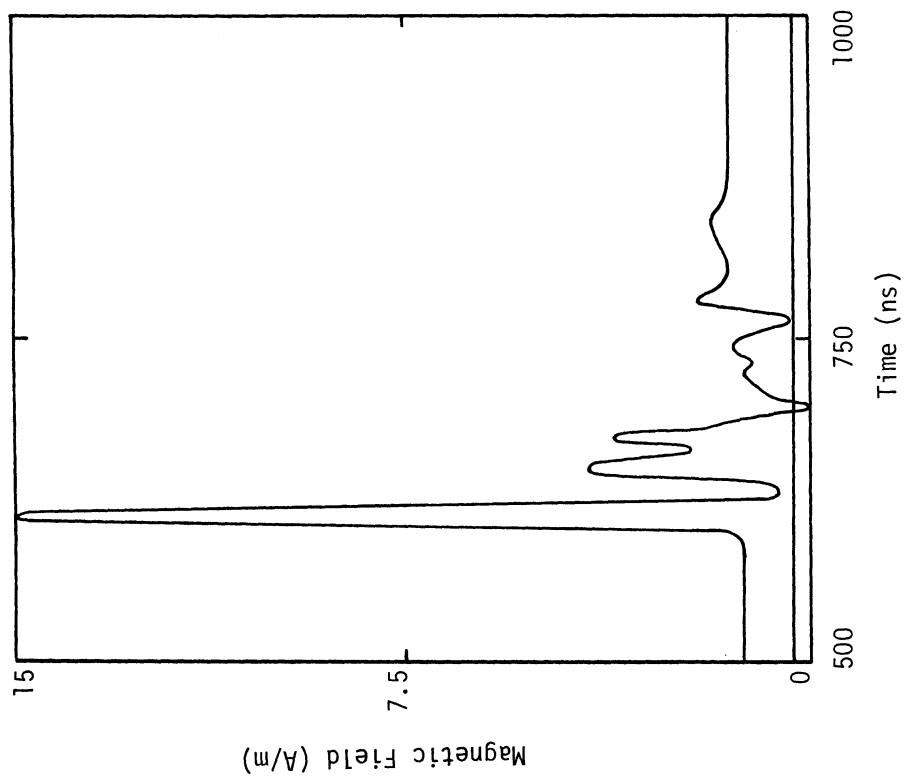
Charge - Positive
Attachment Point - Nose

Figure 4.17a. Electric Field at Forward Sensor Point



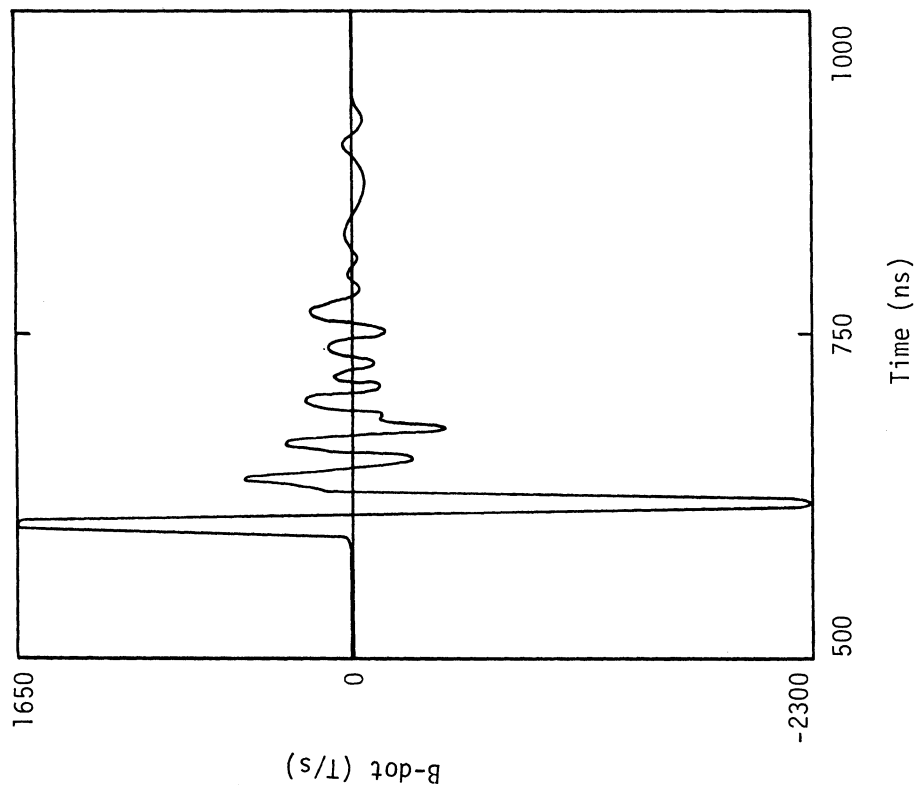
Charge - Positive
Attachment Point - Nose

Figure 4.17b. D-dot at Forward Sensor Point



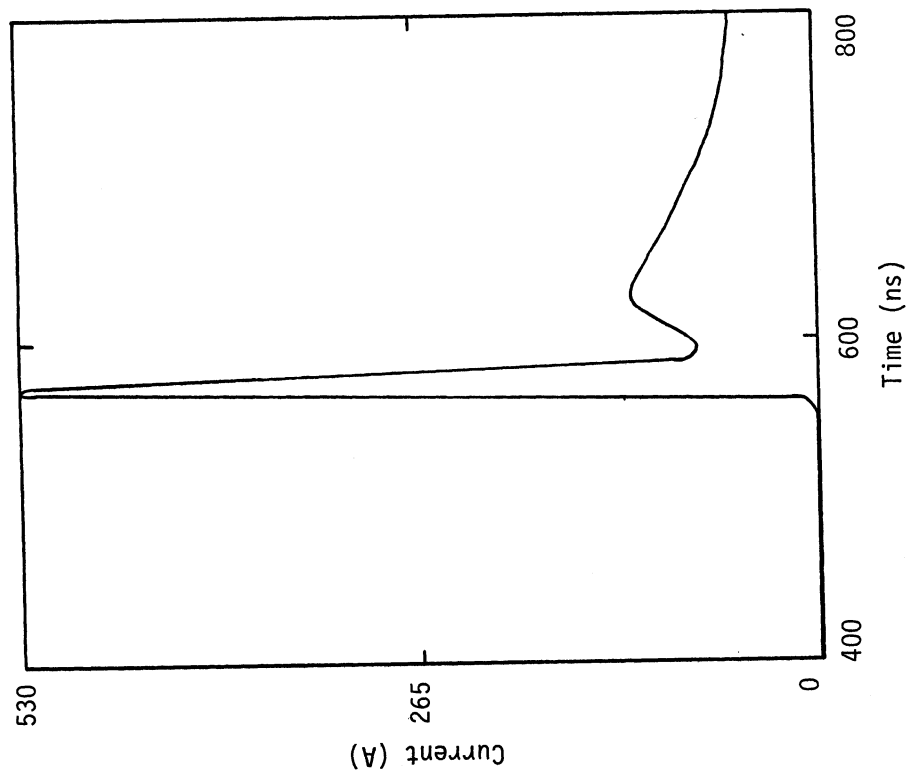
Charge - Positive
Attachment Point - Nose

Figure 4.17c. Magnetic Field (H) at Longitudinal
Fuselage Sensor Point



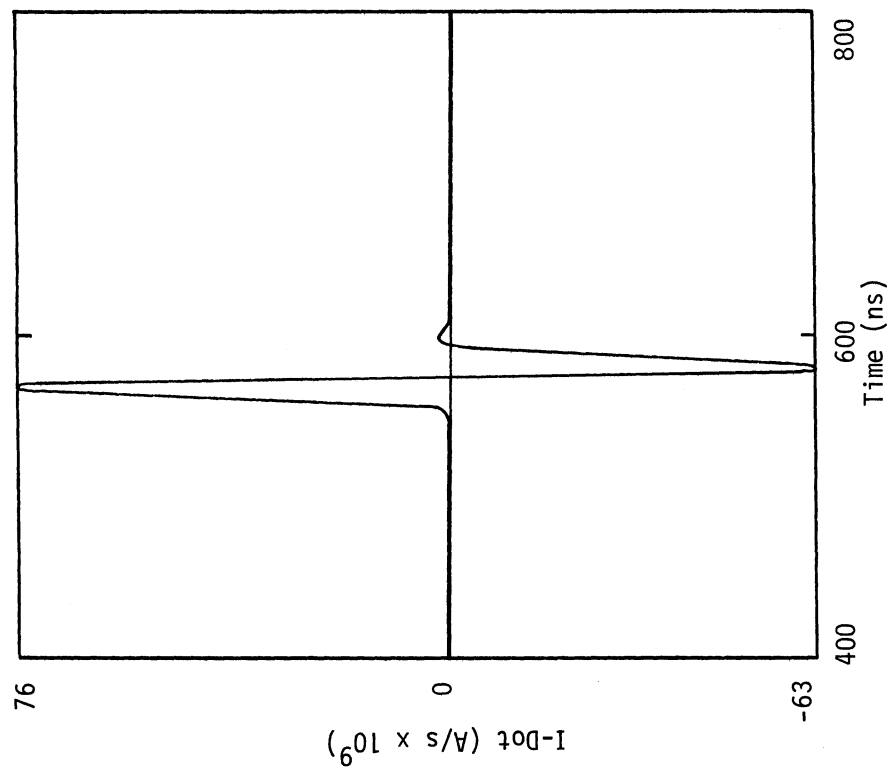
Charge - Positive
Attachment Point - Nose

Figure 4.17d. B-dot at Longitudinal Fuselage
Sensor Point



Charge - Positive
Attachment Point - Nose

Figure 4.17e. Injected Current at Attachment Point



Charge - Positive
Attachment Point - Nose

Figure 4.17f. I-dot at Attachment Point

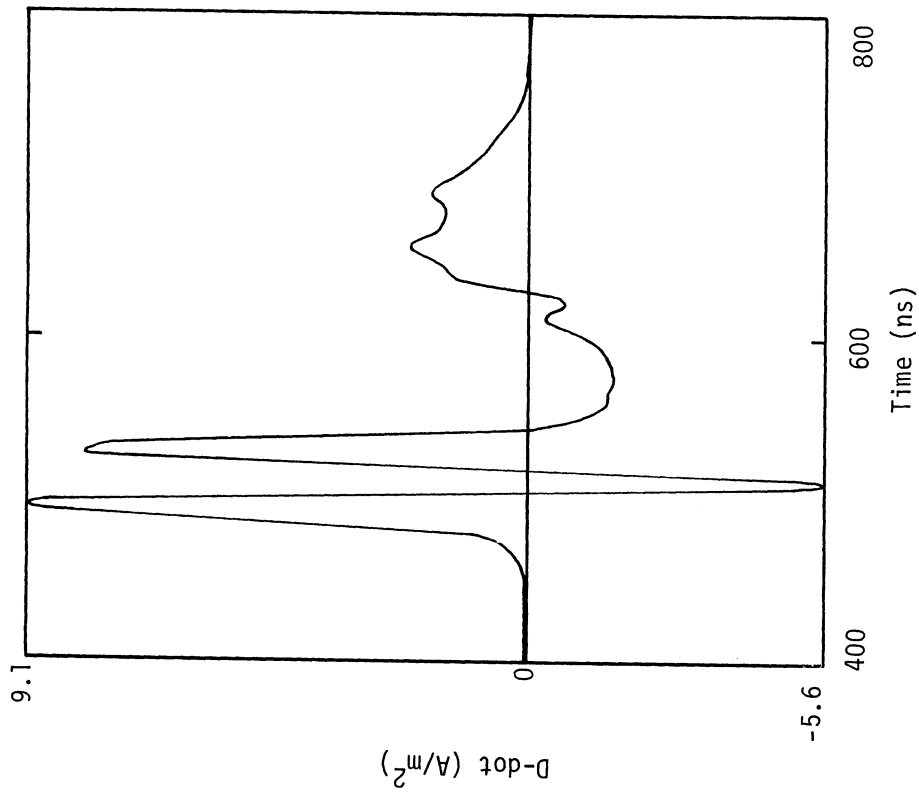


Figure 4.18a. Electric Field at Forward Sensor Point

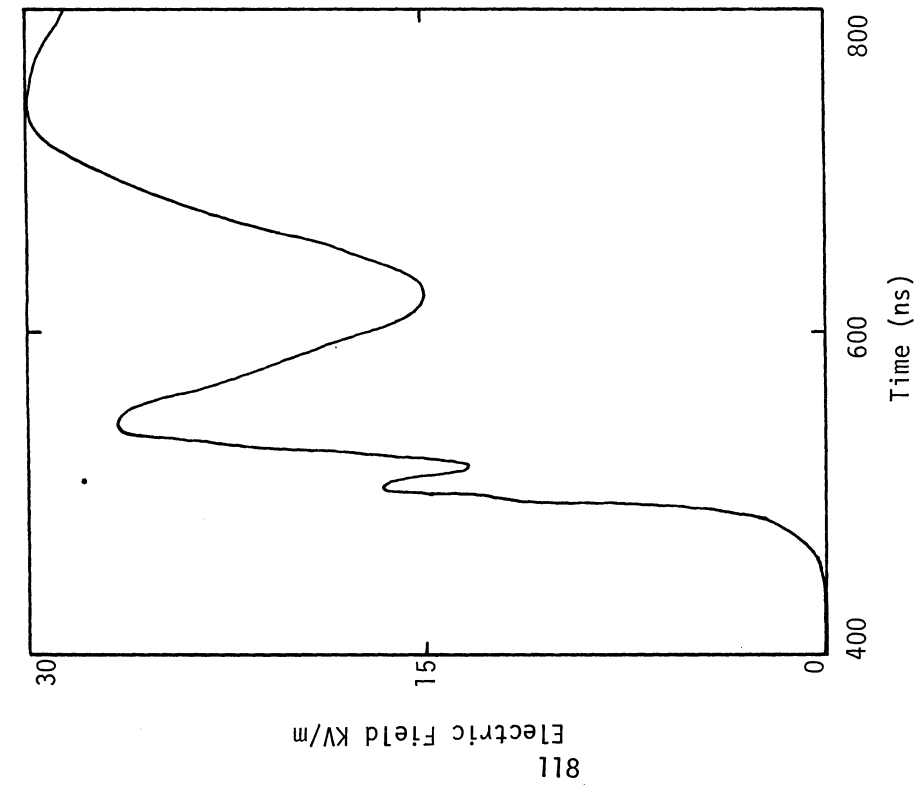
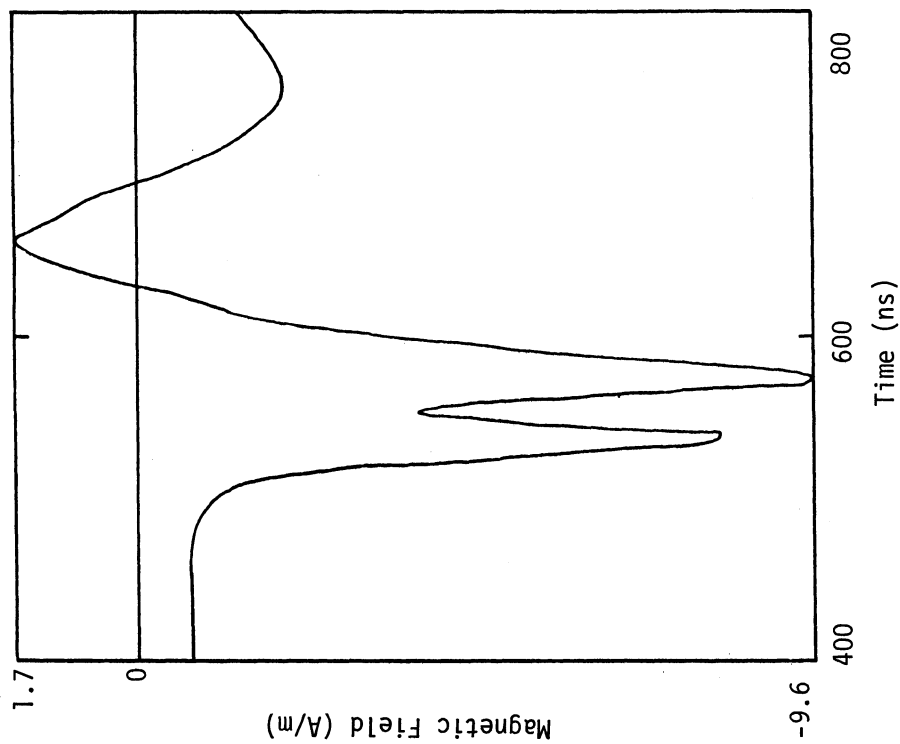
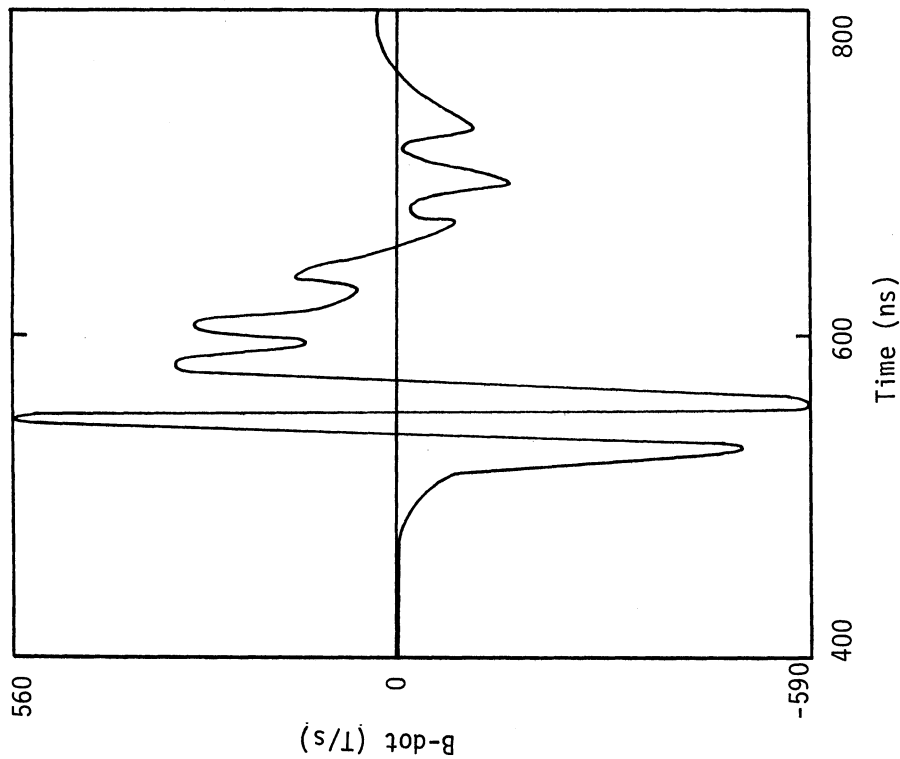


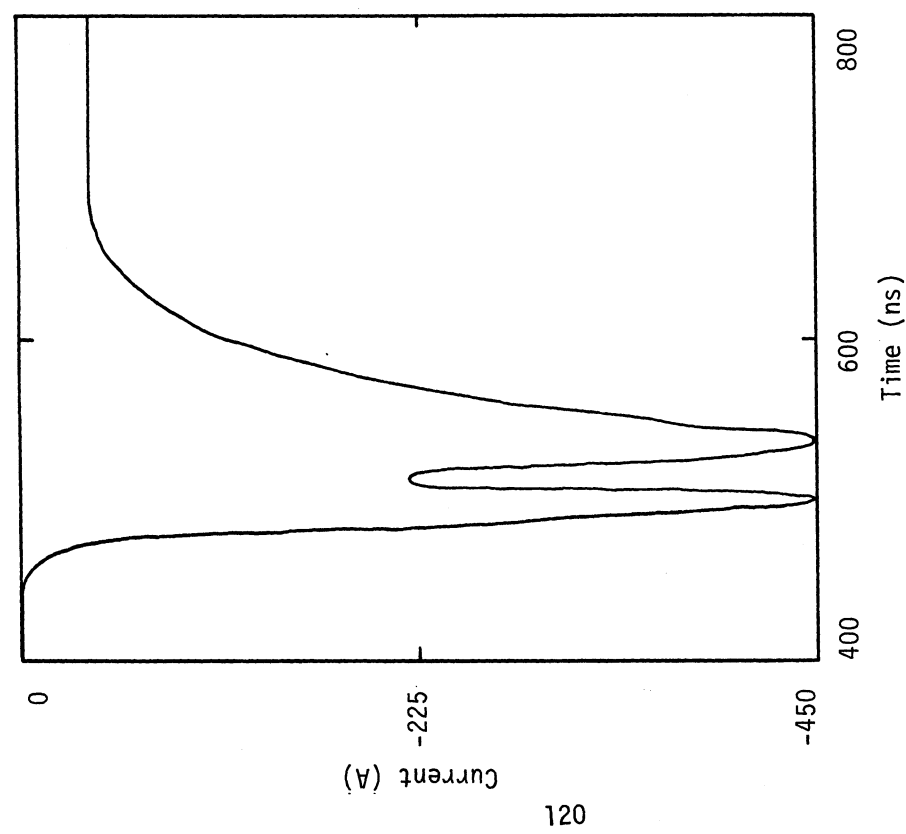
Figure 4.18b. D-dot at Forward Sensor Point



Charge - Negative
Attachment Point - Nose
Figure 4.18c. Magnetic Field (H) at Longitudinal
Fuselage Sensor Point

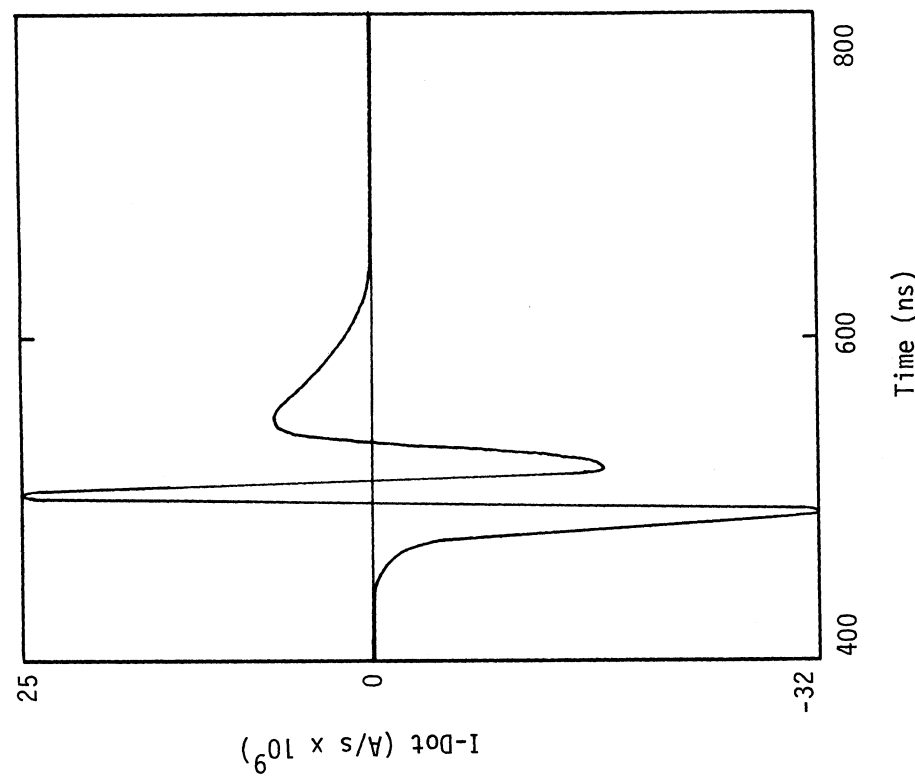


Charge - Negative
Attachment Point - Nose
Figure 4.18d. B-dot at Longitudinal Fuselage
Sensor Point



Charge - Negative
Attachment Point - Nose

Figure 4.18e. Injected Current at Attachment Point



Charge - Negative
Attachment Point - Nose

Figure 4.18f. I-dot at Attachment Point

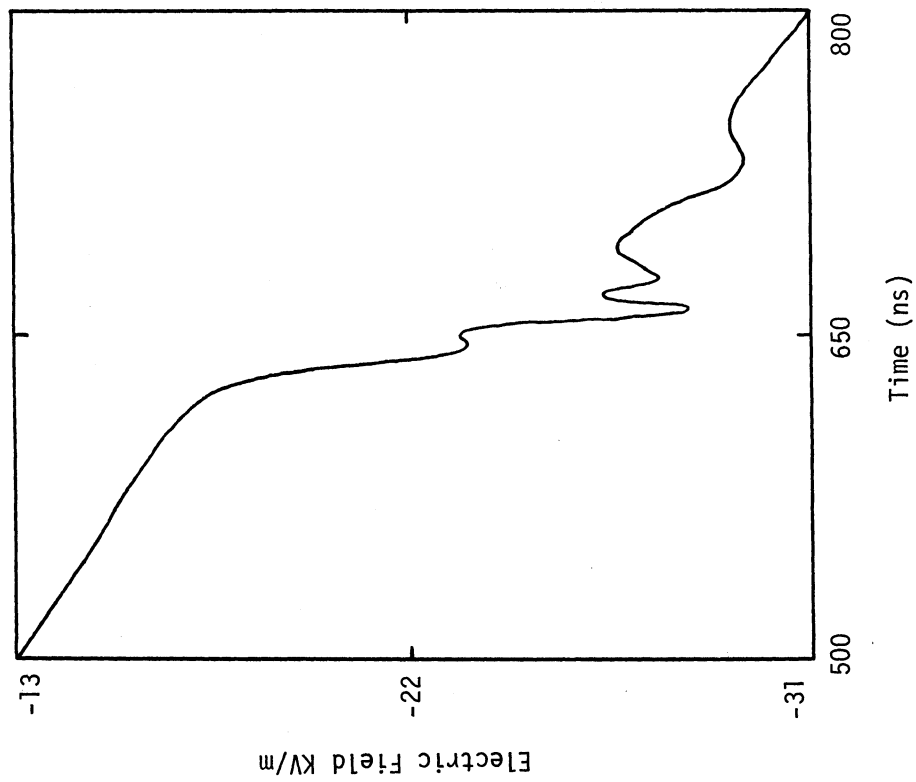


Figure 4.19a. Electric Field at Forward Sensor Point

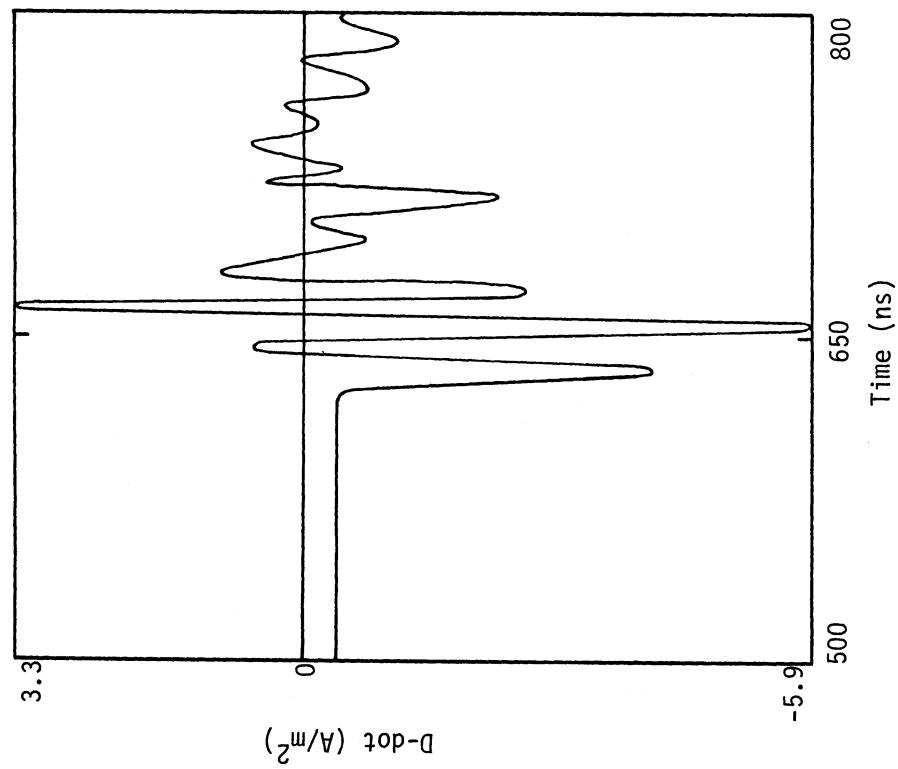


Figure 4.19b. D-dot at Forward Sensor Point

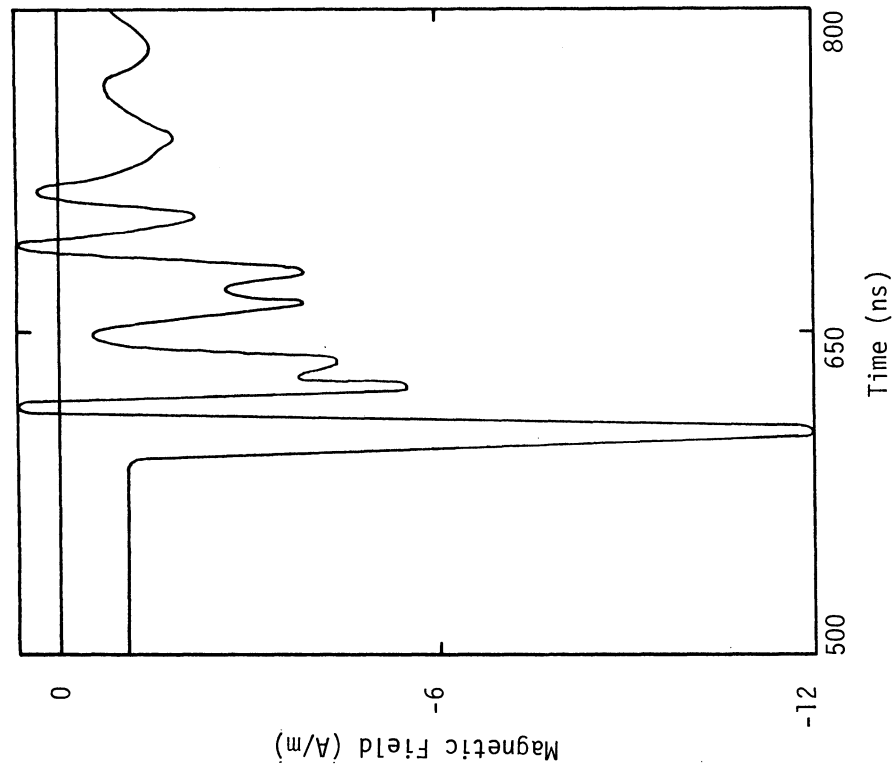


Figure 4.19c. Magnetic Field (H) at Longitudinal Fuselage Sensor Point

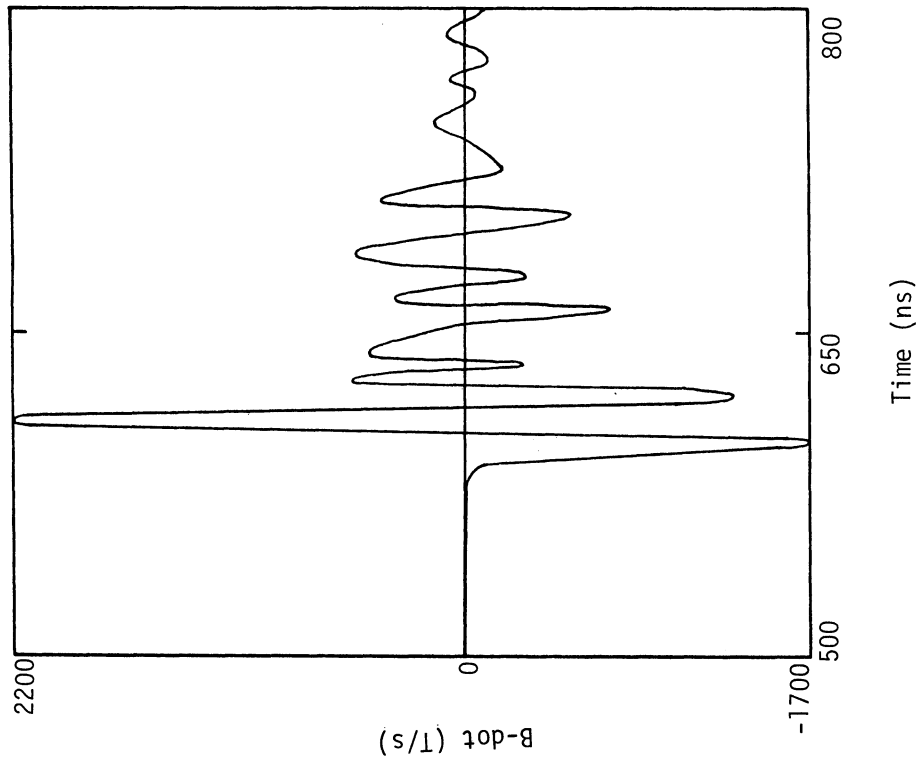


Figure 4.19d. B-dot at Longitudinal Fuselage Sensor Point

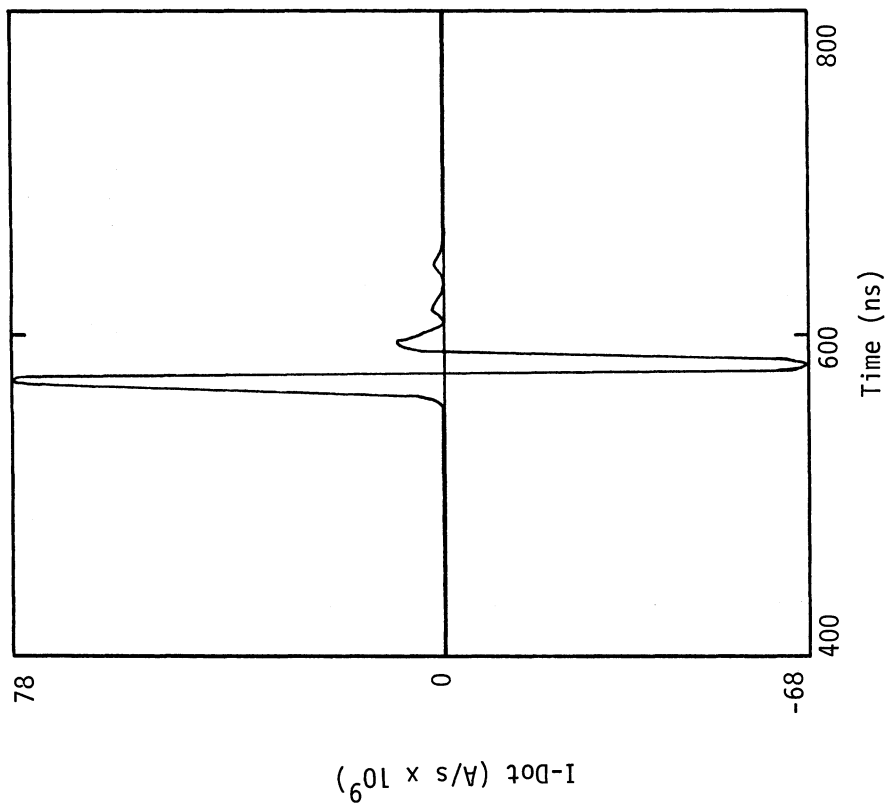


Figure 4.19f. I-dot at Attachment Point

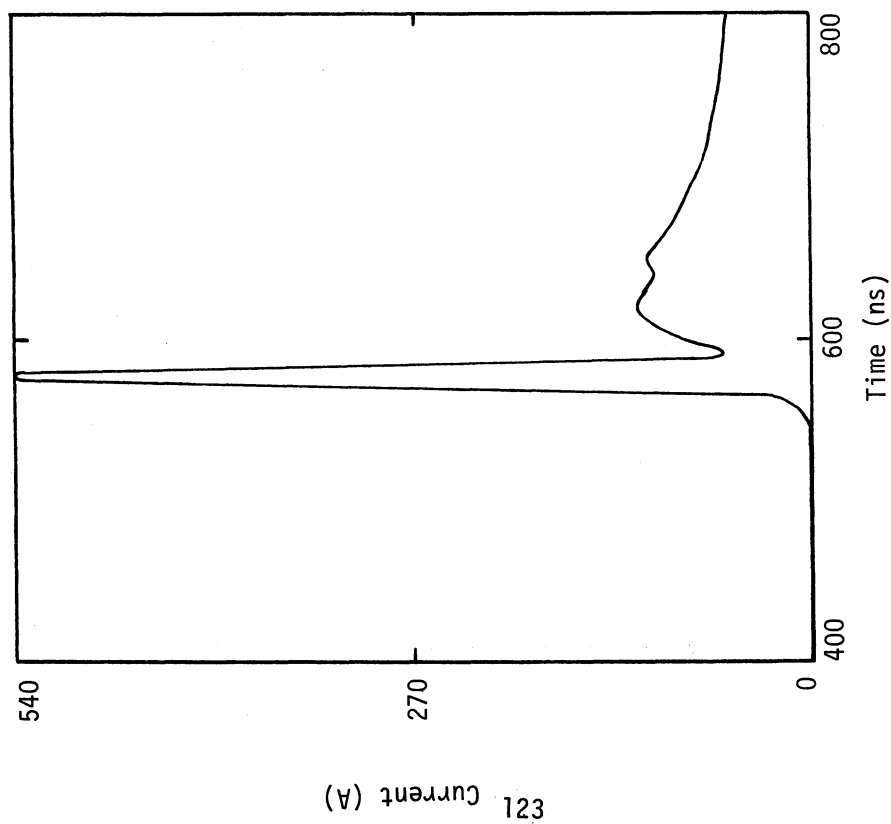
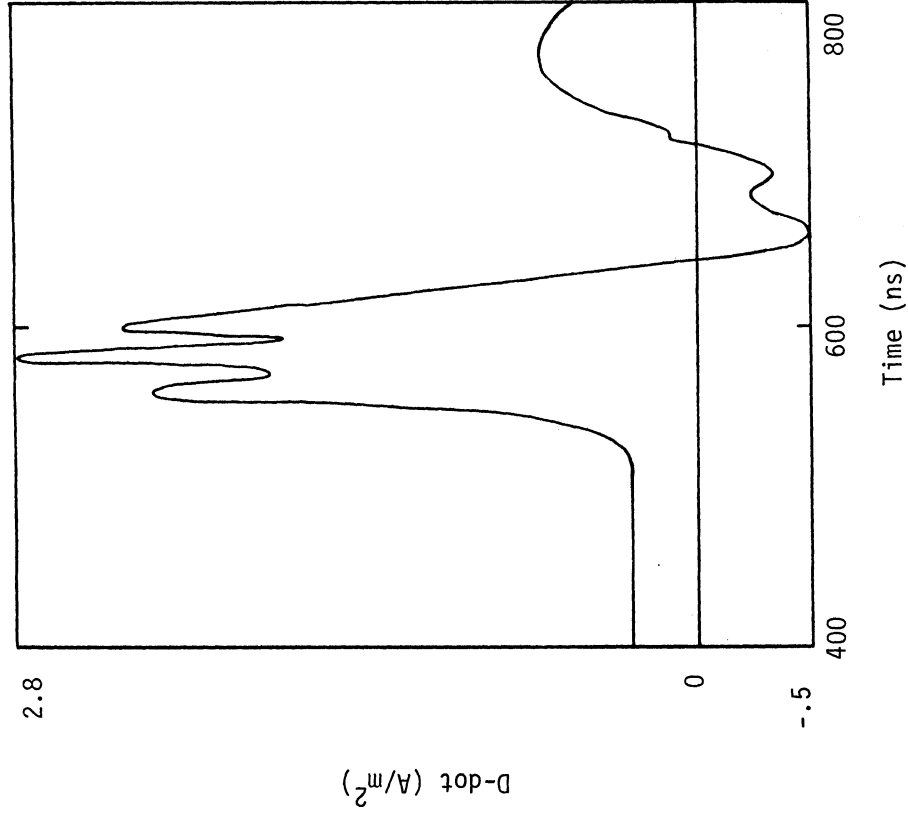
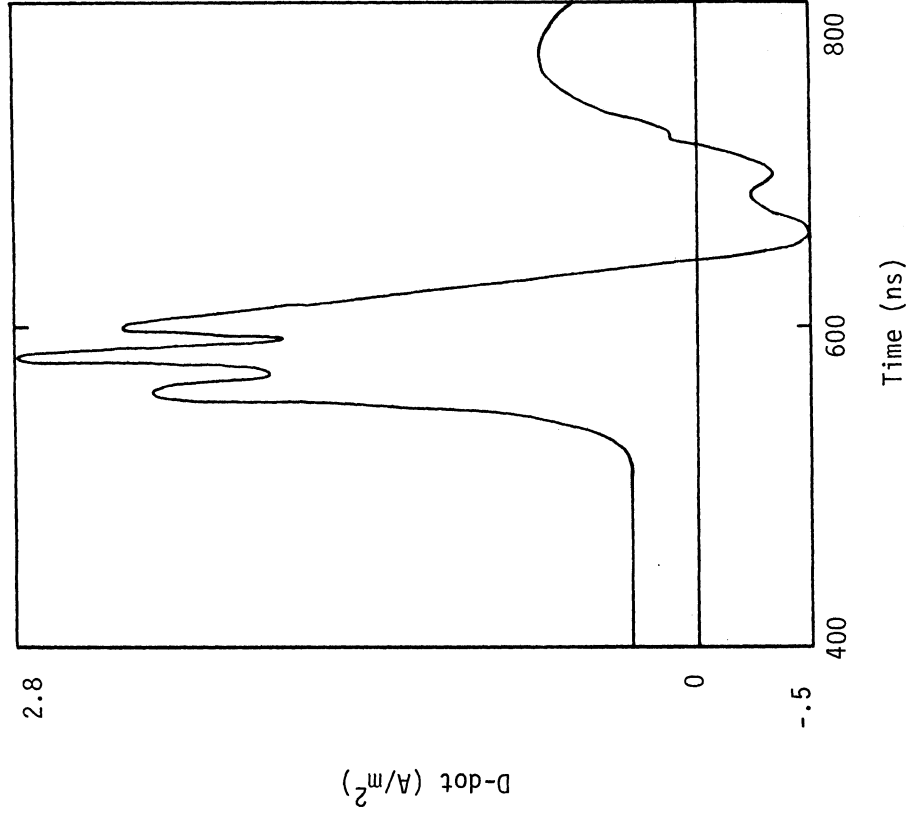


Figure 4.19e. Injected Current at Attachment Point



Charge - Negative
Attachment Point - Tail

Figure 4.20a. Electric Field at Forward Sensor Point



Charge - Negative
Attachment Point - Tail

Figure 4.20b. D-dot at Forward Sensor Point

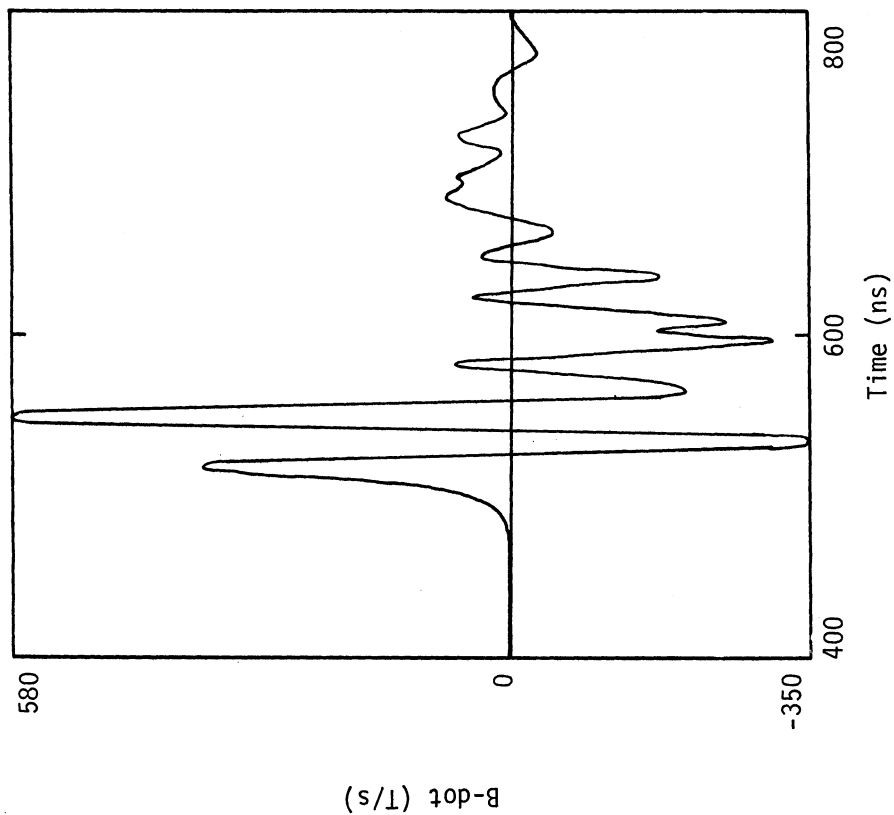


Figure 4.20d. B-dot at Longitudinal Fuselage Sensor Point

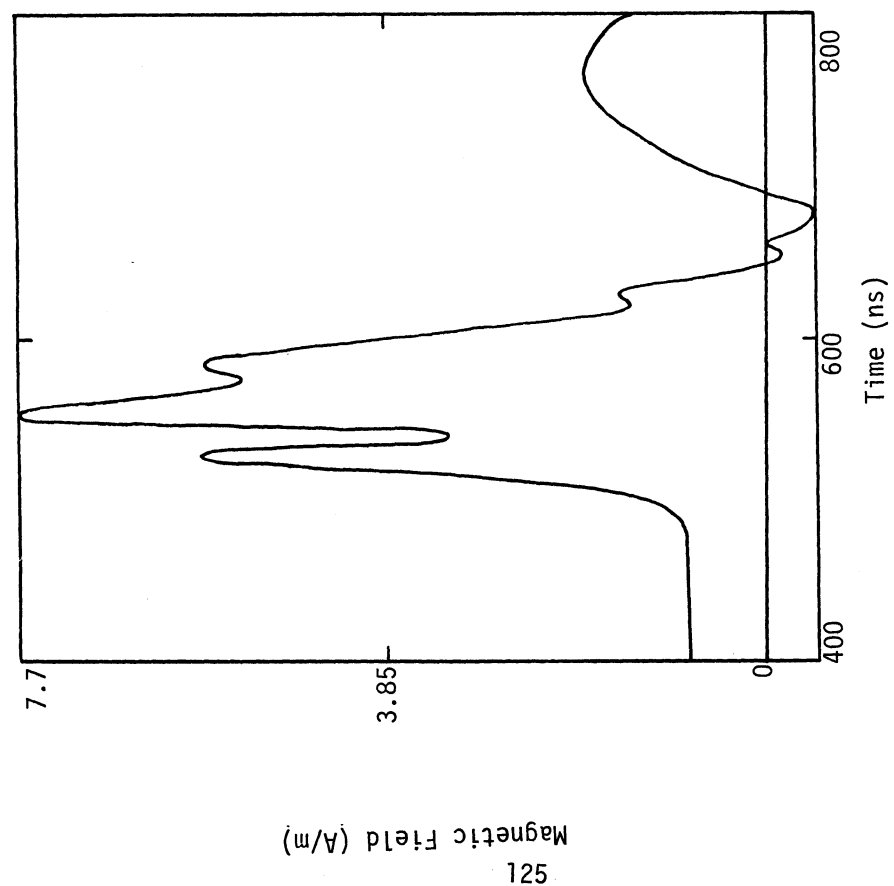


Figure 4.20c. Magnetic Field (H) at Longitudinal Fuselage Sensor Point

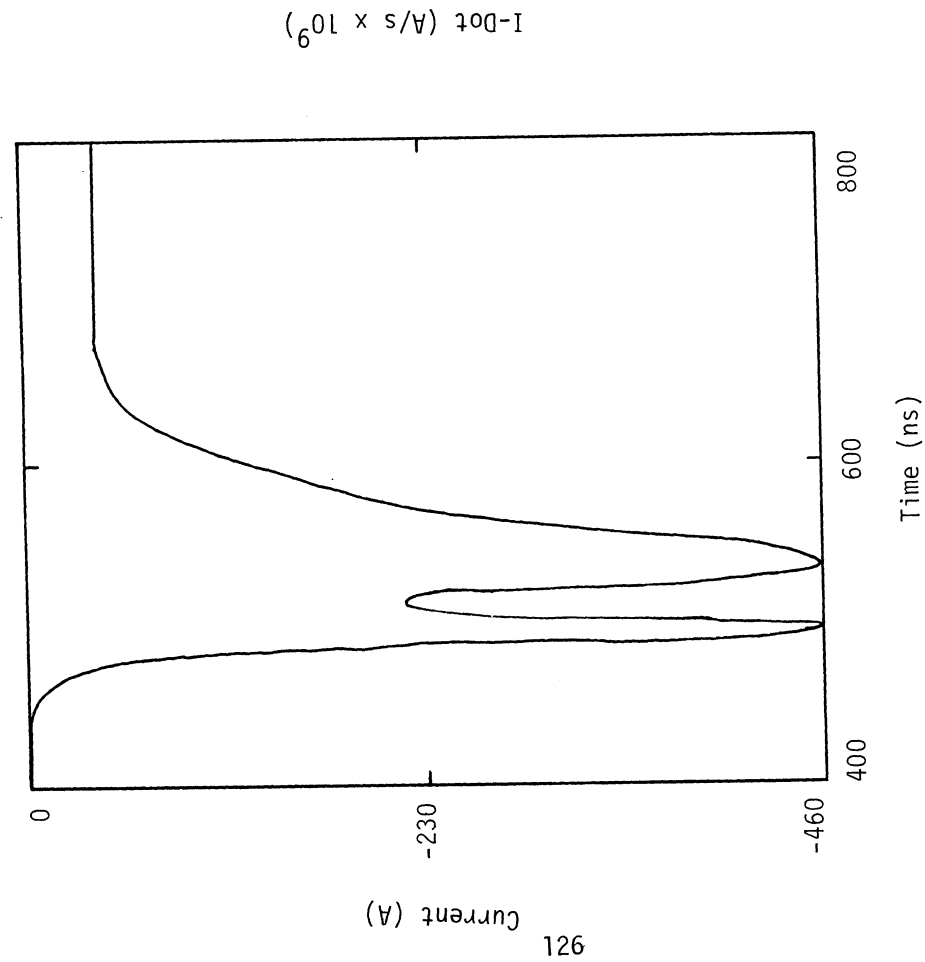


Figure 4.20e. Injected Current at Attachment Point

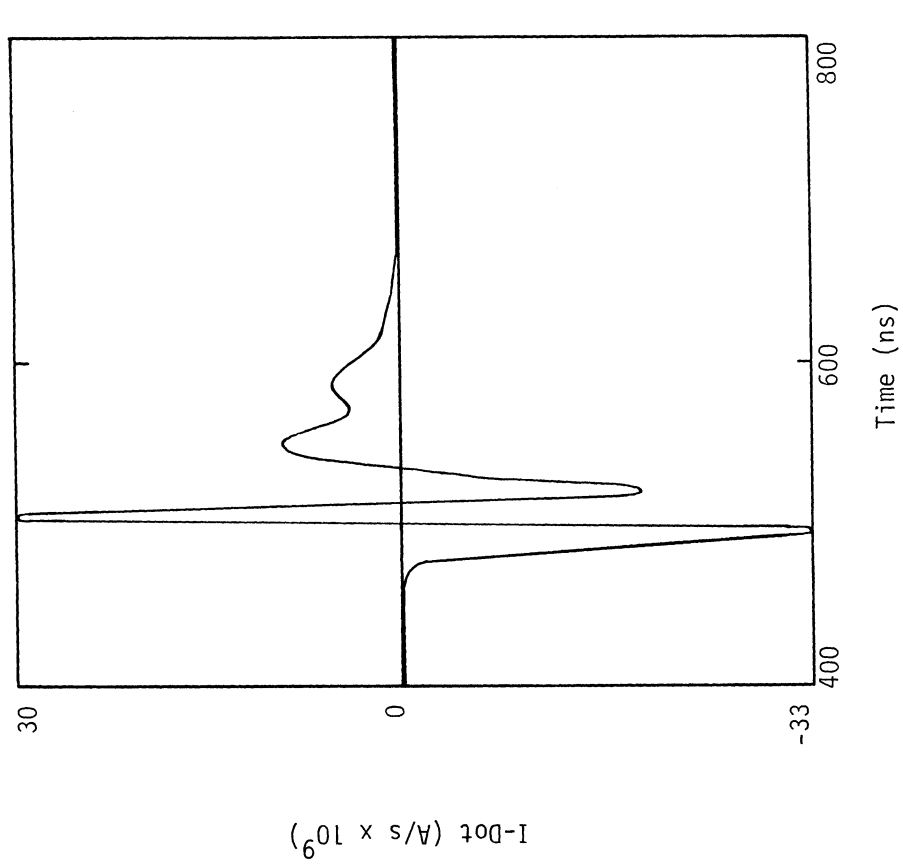
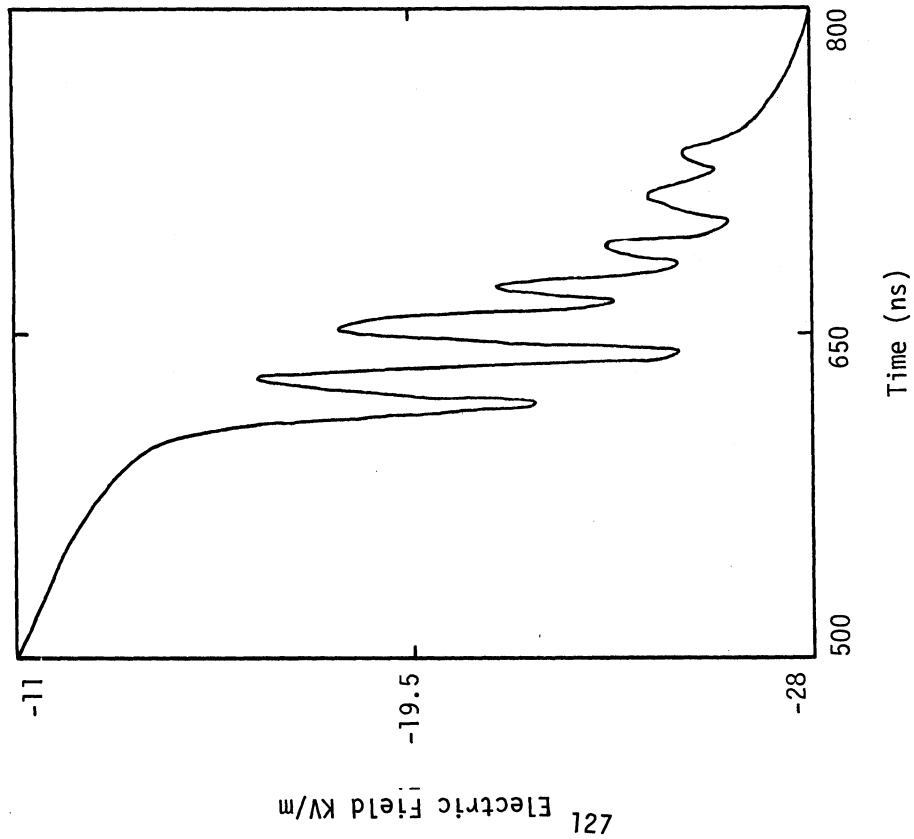


Figure 4.20f. I-dot at Attachment Point



4.21a. Electric Field at Forward Sensor Point

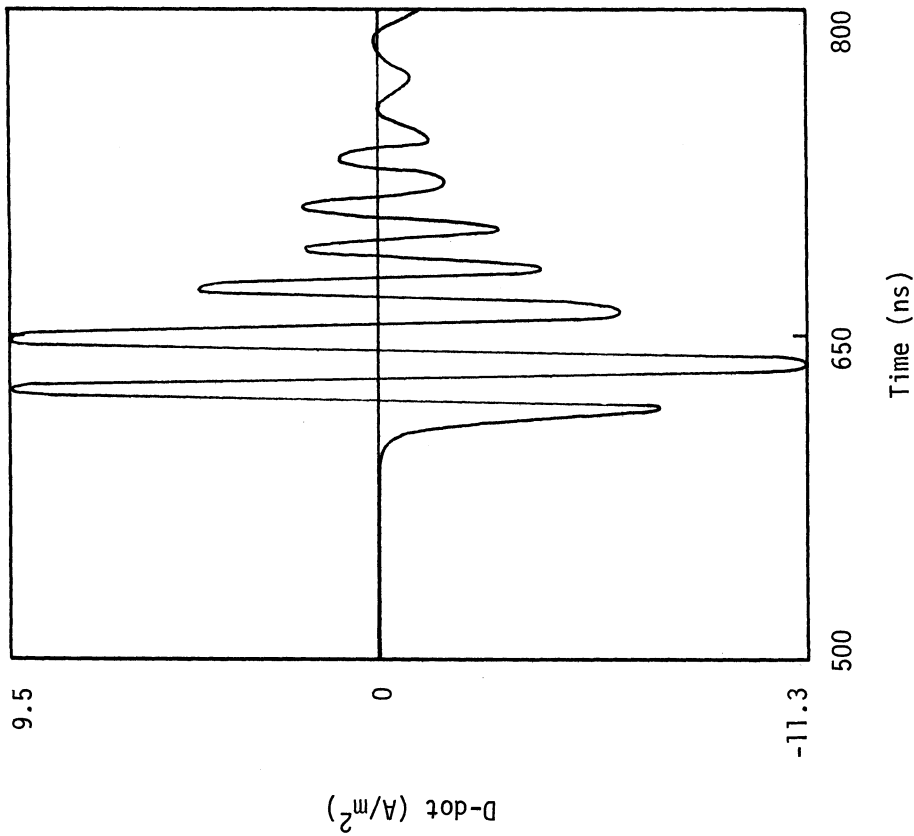
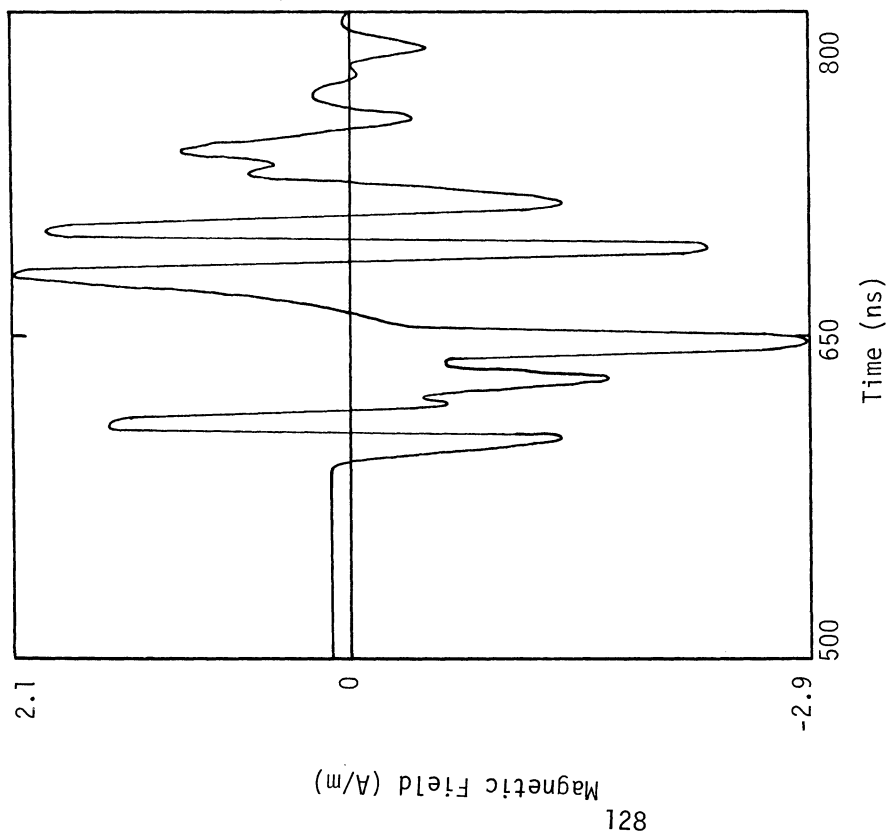
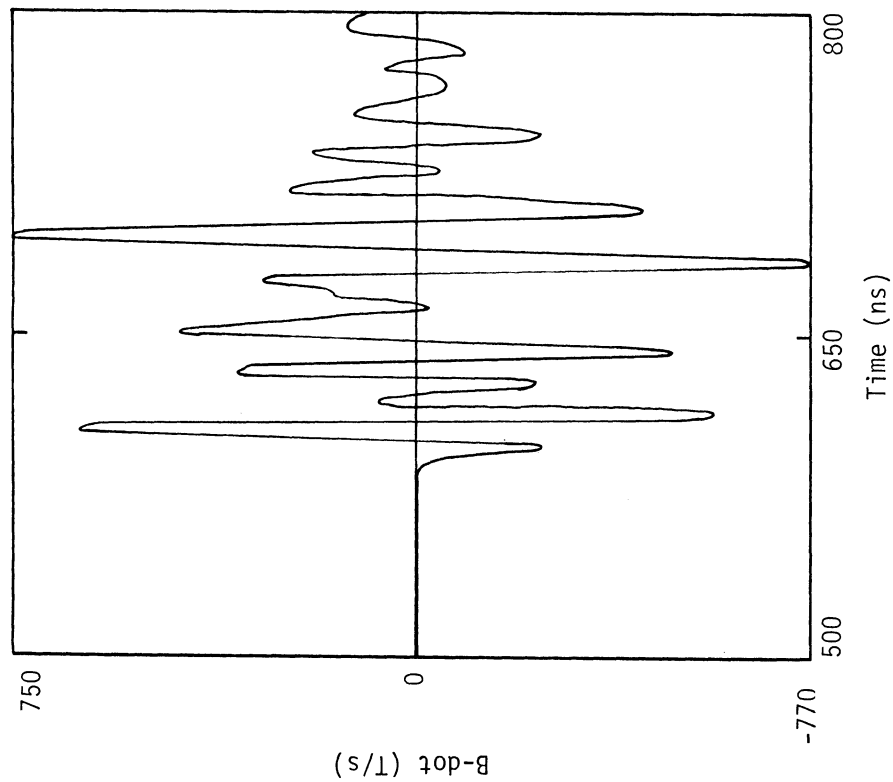


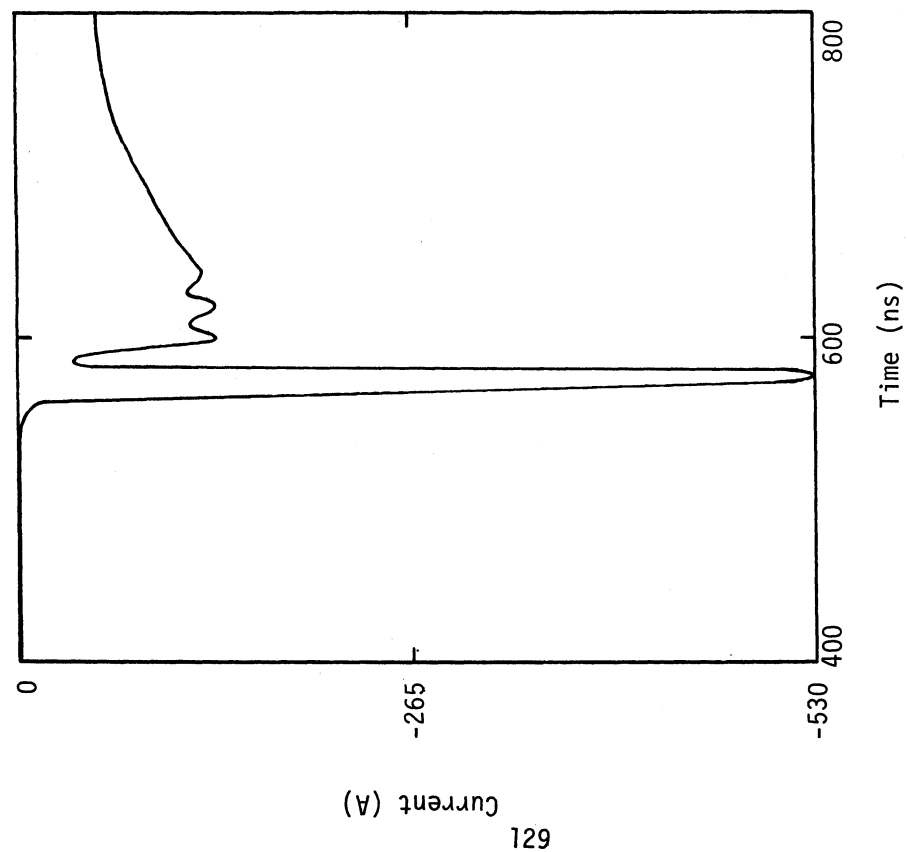
Figure 4.21b. D-dot at Forward Sensor Point



Charge - Positive
Attachment Point - Left Wing
Figure 4.21c. Magnetic Field (H) at Longitudinal
Fuselage Sensor Point

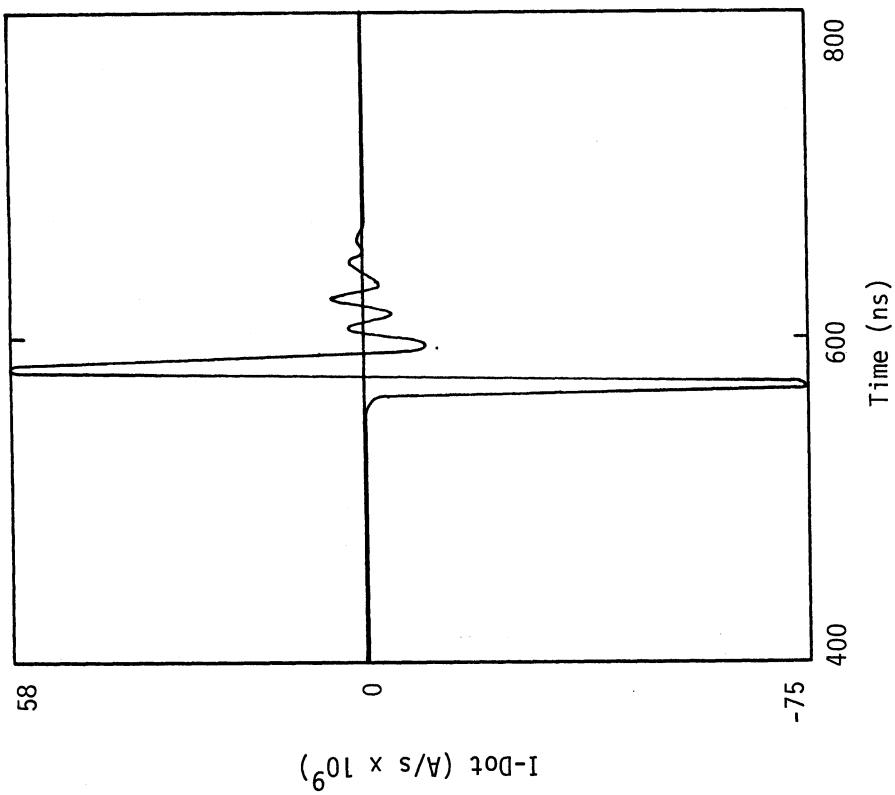


Charge - Positive
Attachment Point - Left Wing
Figure 4.21d. B-dot at Longitudinal Fuselage
Sensor Point



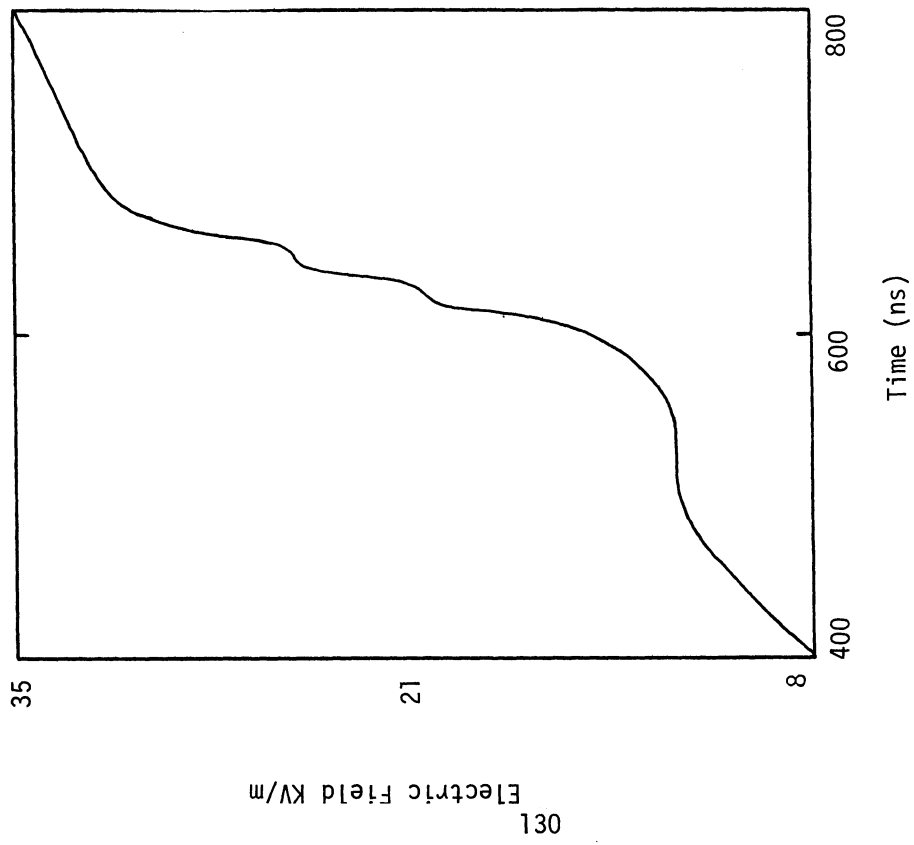
Charge - Positive
Attachment Point - Left Wing

Figure 4.21e. Injected Current at Attachment Point



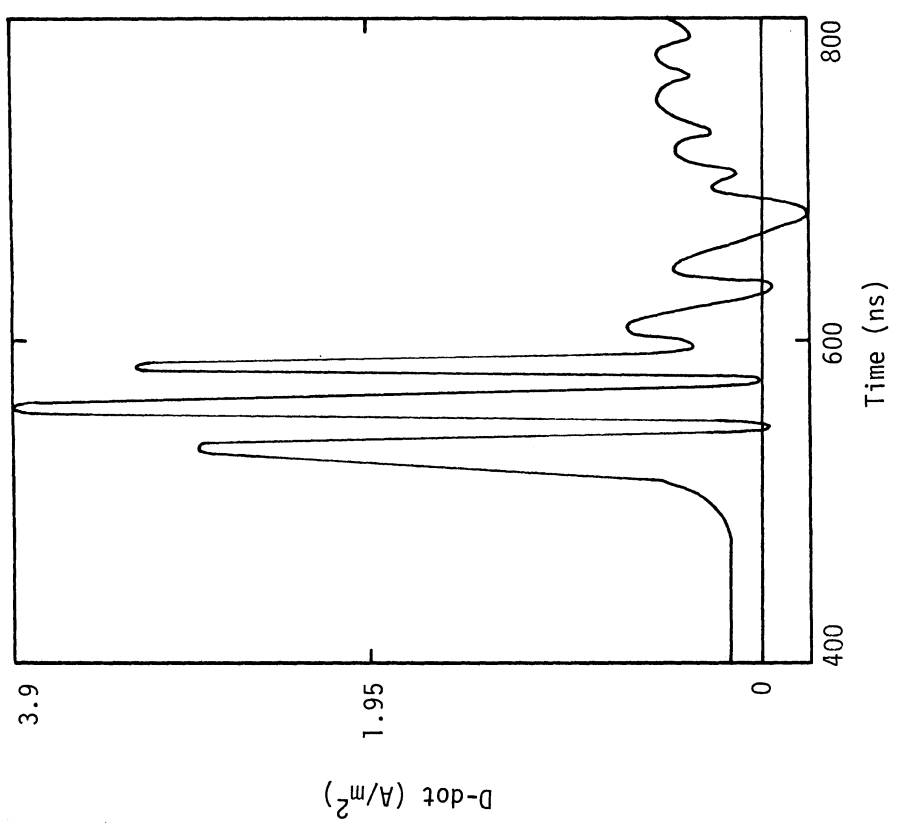
Charge - Positive
Attachment Point - Left Wing

Figure 4.21f. I-dot at Attachment Point



Charge - Negative
Attachment Point - Left Wing

Figure 4.22a. Electric Field at Forward Sensor Point



Charge - Negative
Attachment Point -left Wing

Figure 4.22b. D-dot at Forward Sensor Point

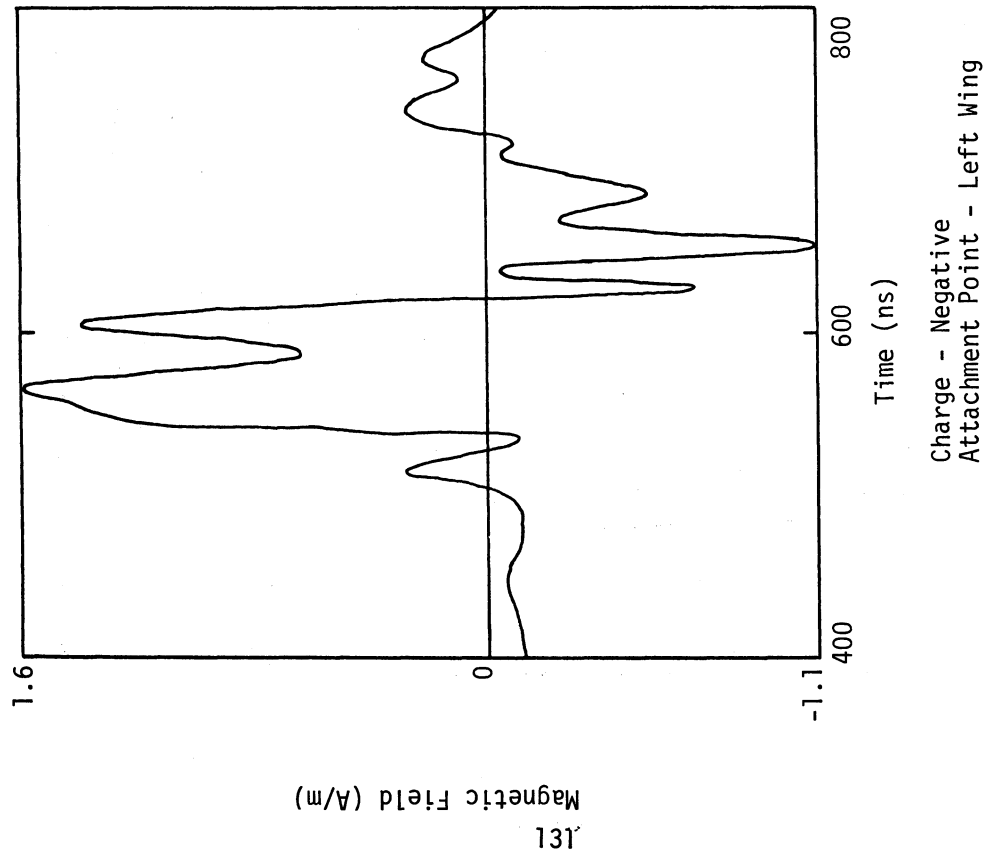


Figure 4.22c. Magnetic Field (H) at Longitudinal Fuselage Sensor Point

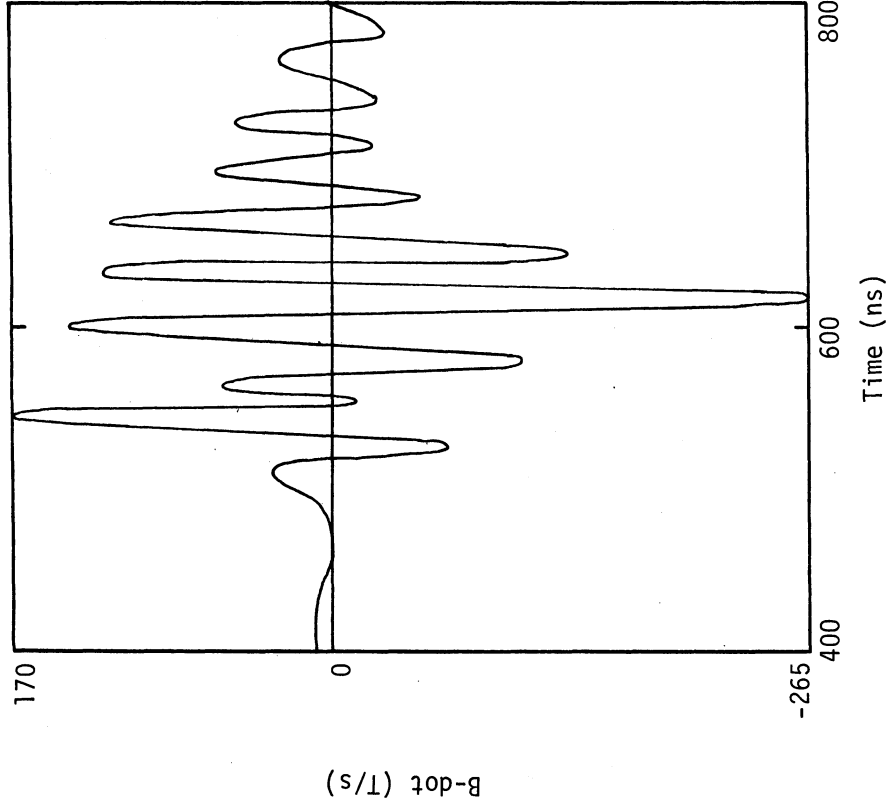
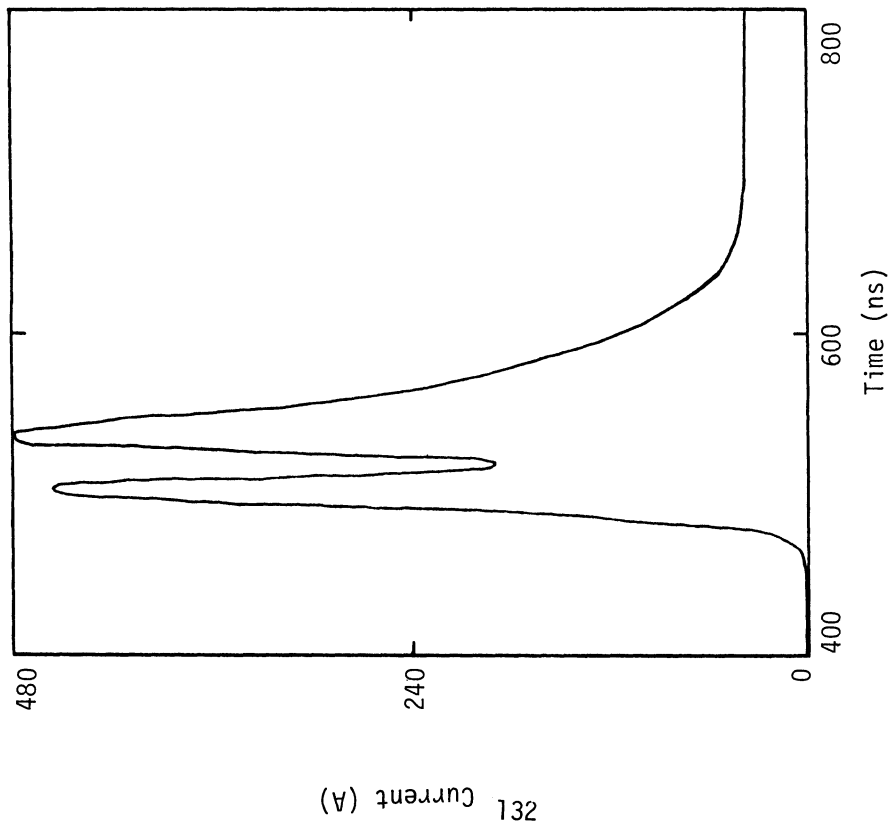
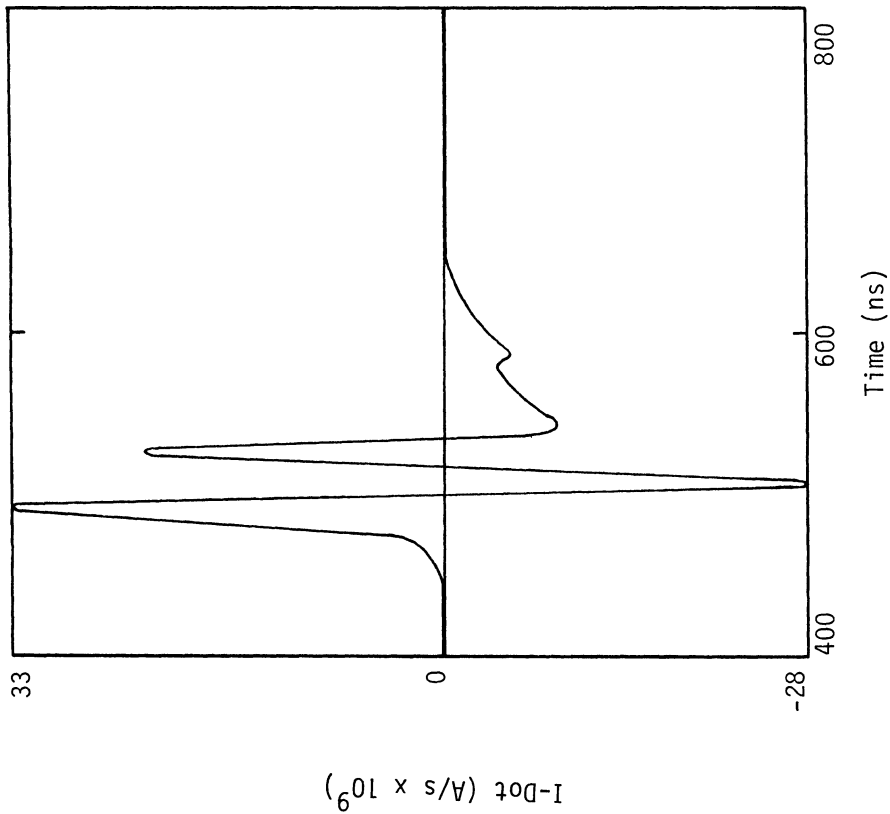


Figure 4.22d. B-dot at Longitudinal Fuselage Sensor Point



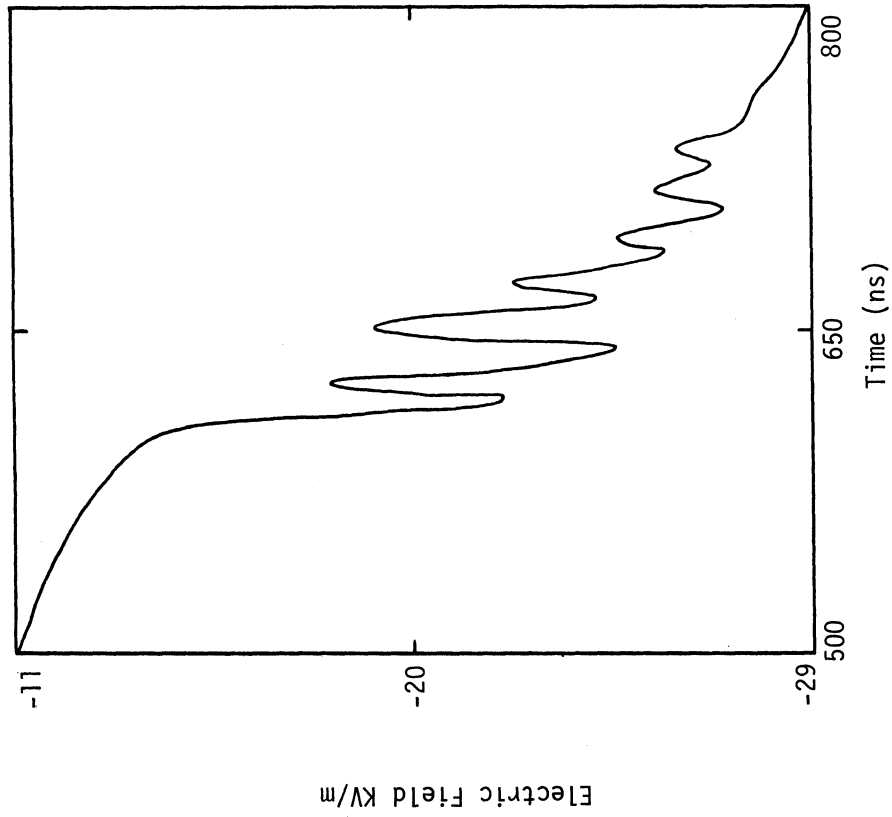
Charge - Negative
Attachment Point - Left Wing

Figure 4.22e. Injected Current at Attachment Point



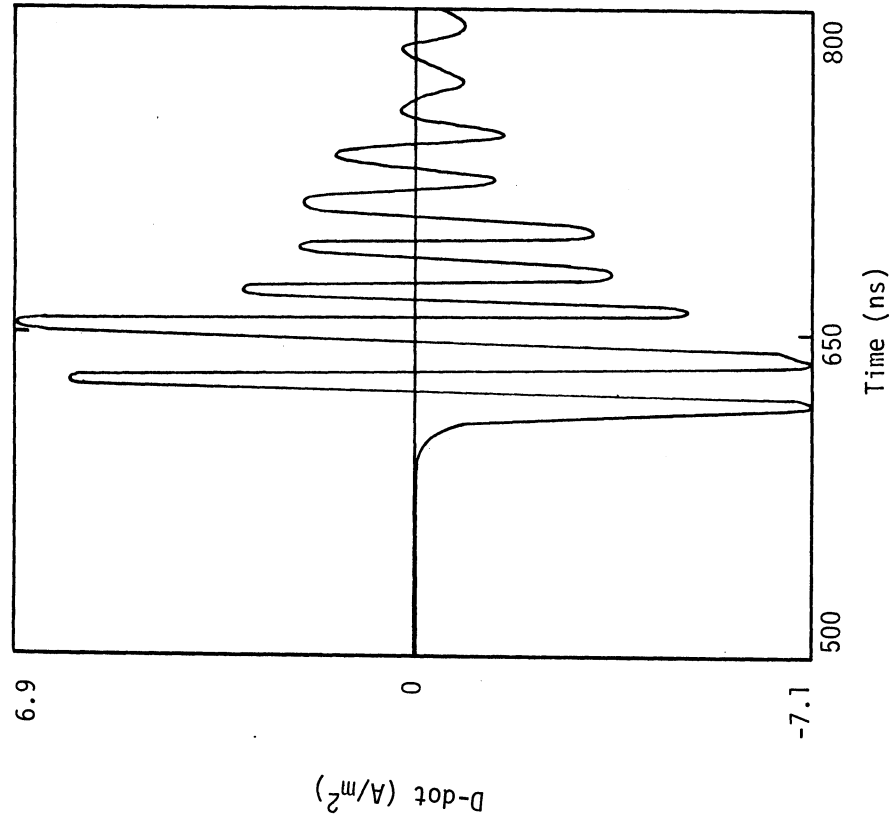
Charge - Negative
Attachment Point - Left Wing

Figure 4.22f. I-dot at Attachment Point



Charge - Positive
Attachment Point - Right Wing

Figure 4.23a. Electric Field at Forward Sensor Point



Charge - Positive
Attachment Point - Right Wing

Figure 4.23b. D-dot at Forward Sensor Point

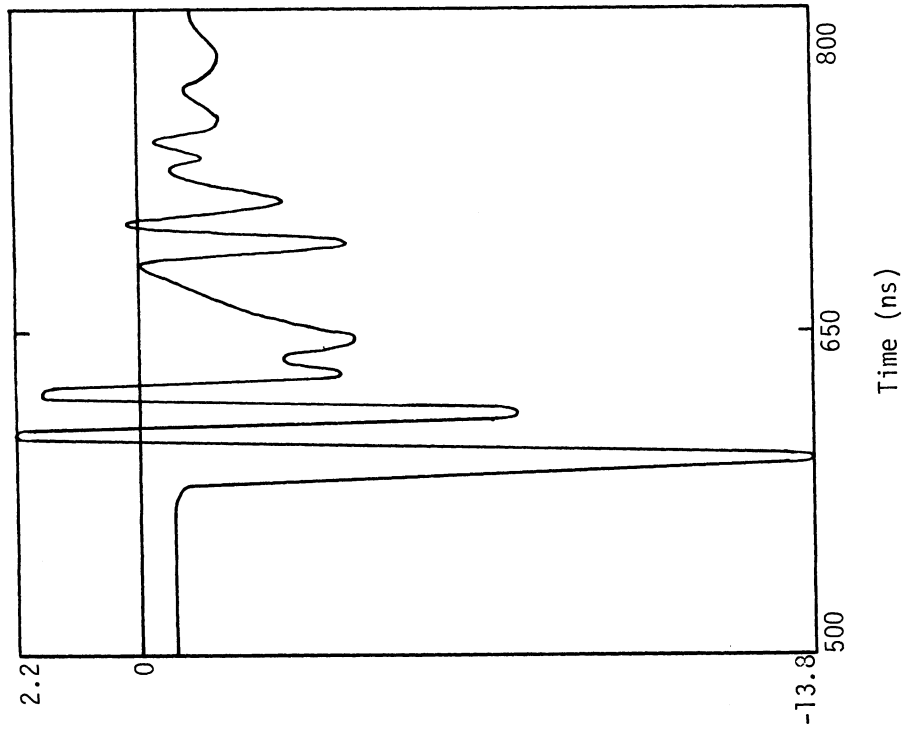


Figure 4.23c. Magnetic Field (H) at Longitudinal Fuselage Sensor Point

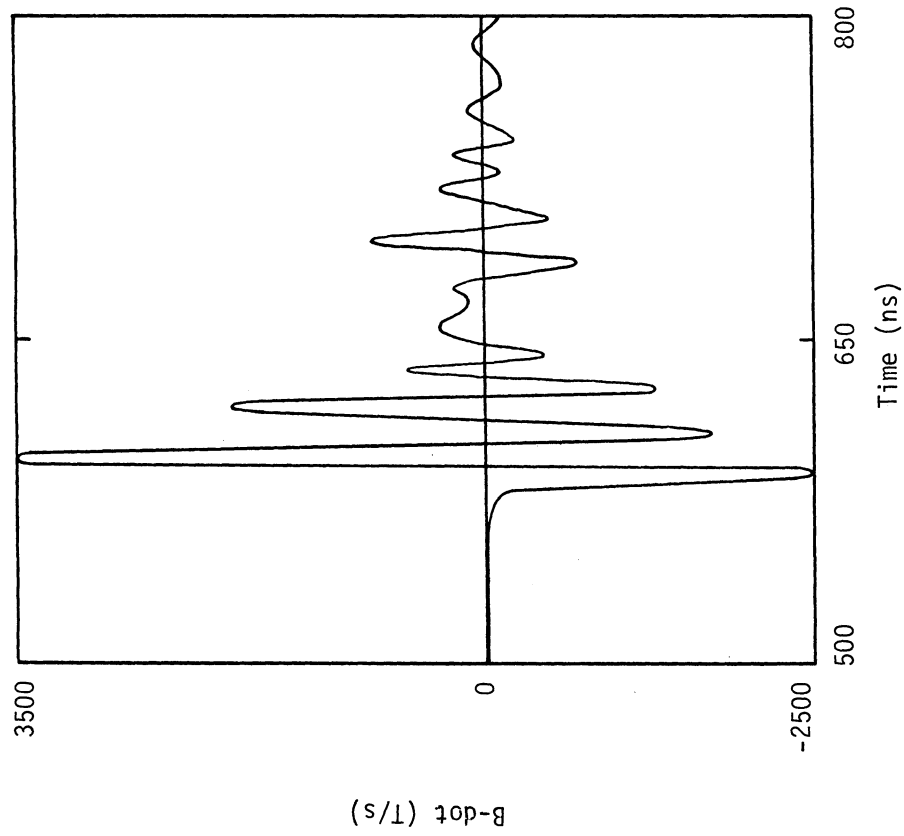


Figure 4.23d. B-dot at Longitudinal Fuselage Sensor Point

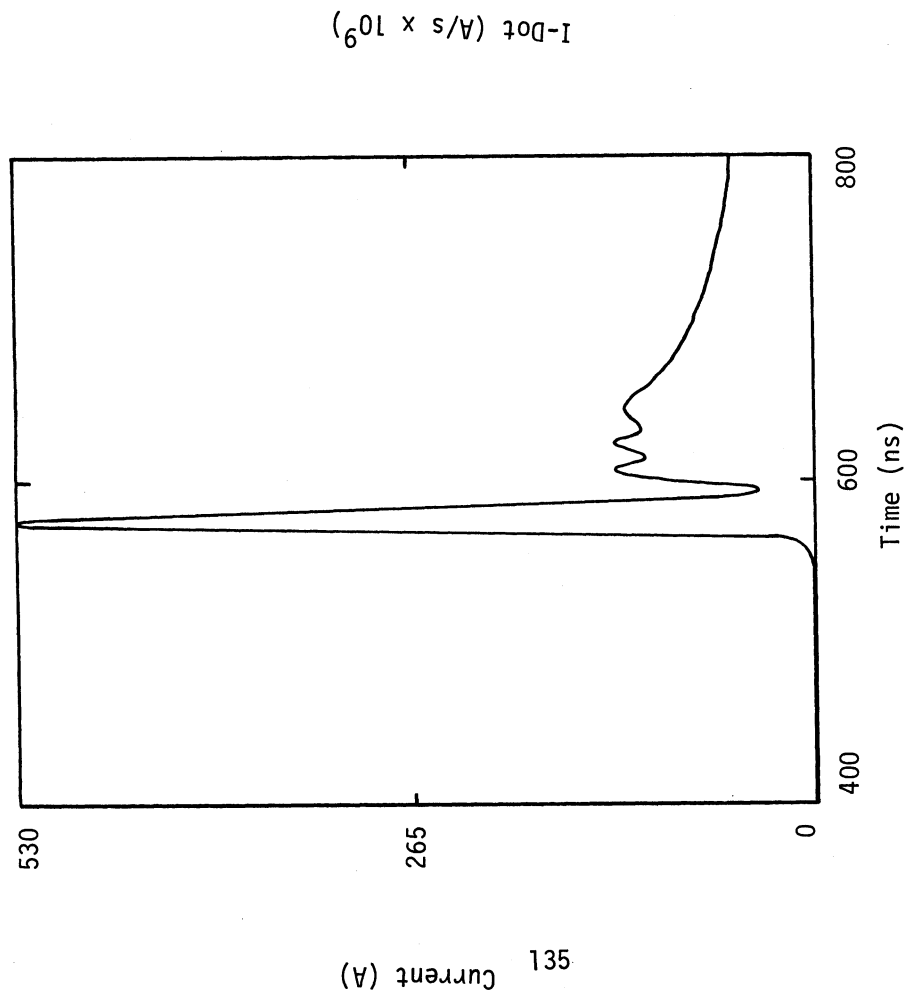


Figure 4.23e. Injected Current at Attachment Point

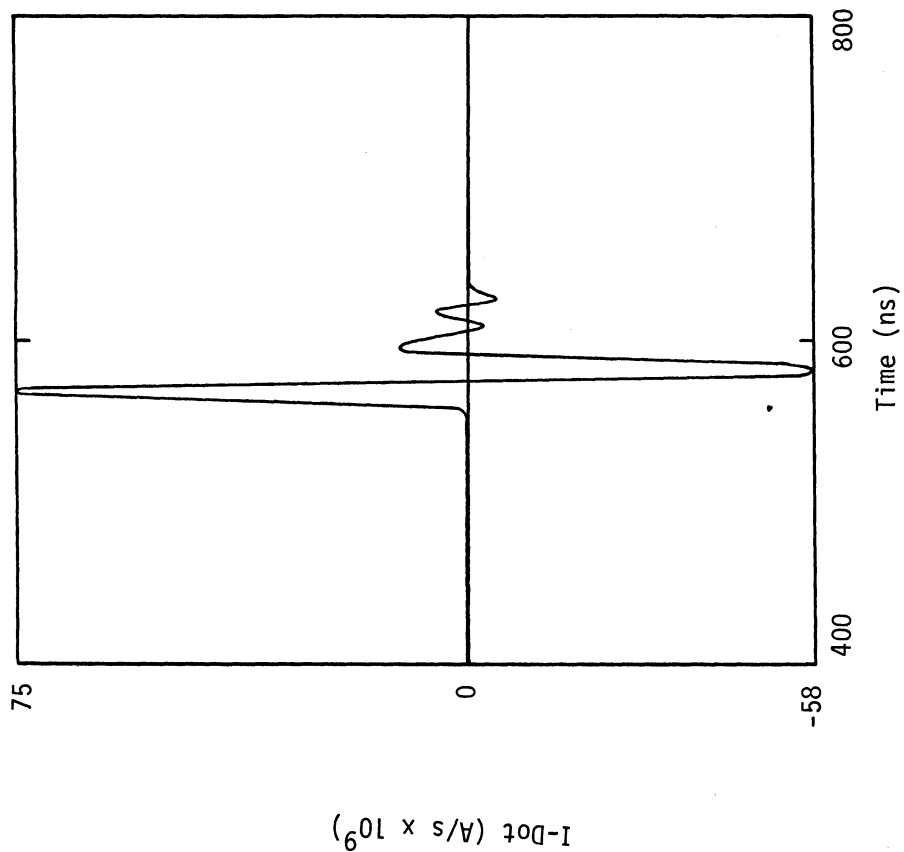
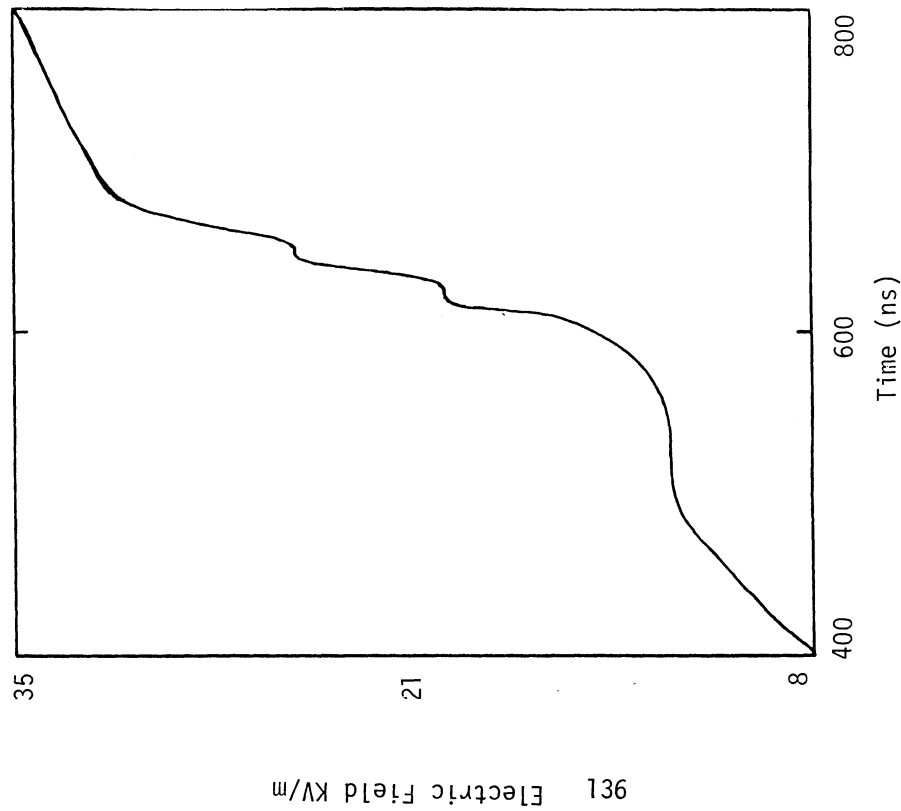
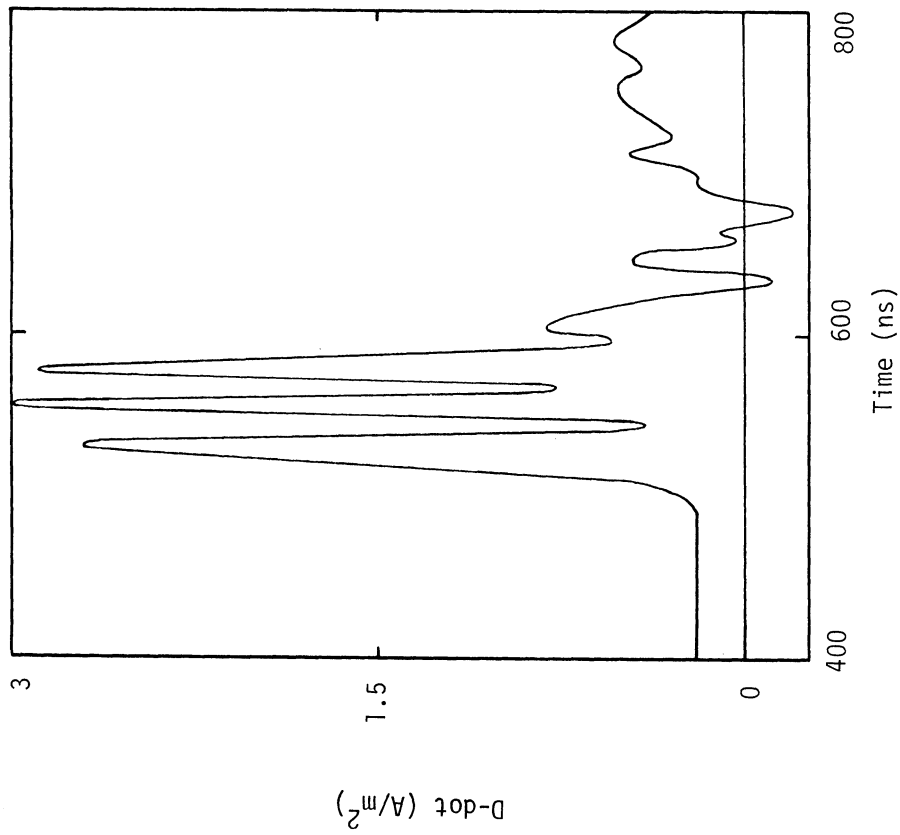


Figure 4.23f. I-dot at Attachment Point



Charge - Negative
Attachment Point - Right Wing

Figure 4.24a. Electric Field at Forward Sensor Point



Charge - Negative
Attachment Point - Right Wing

Figure 4.24b. D-dot at Forward Sensor Point

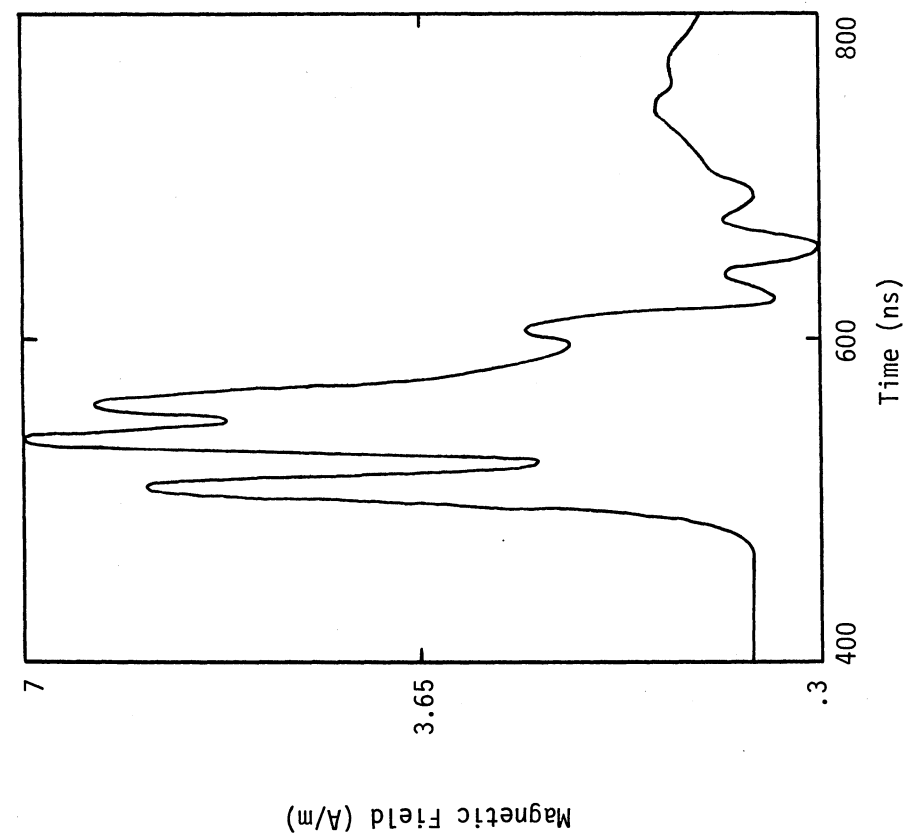


Figure 4.24c. Magnetic Field (H) at Longitudinal Fuselage Sensor Point

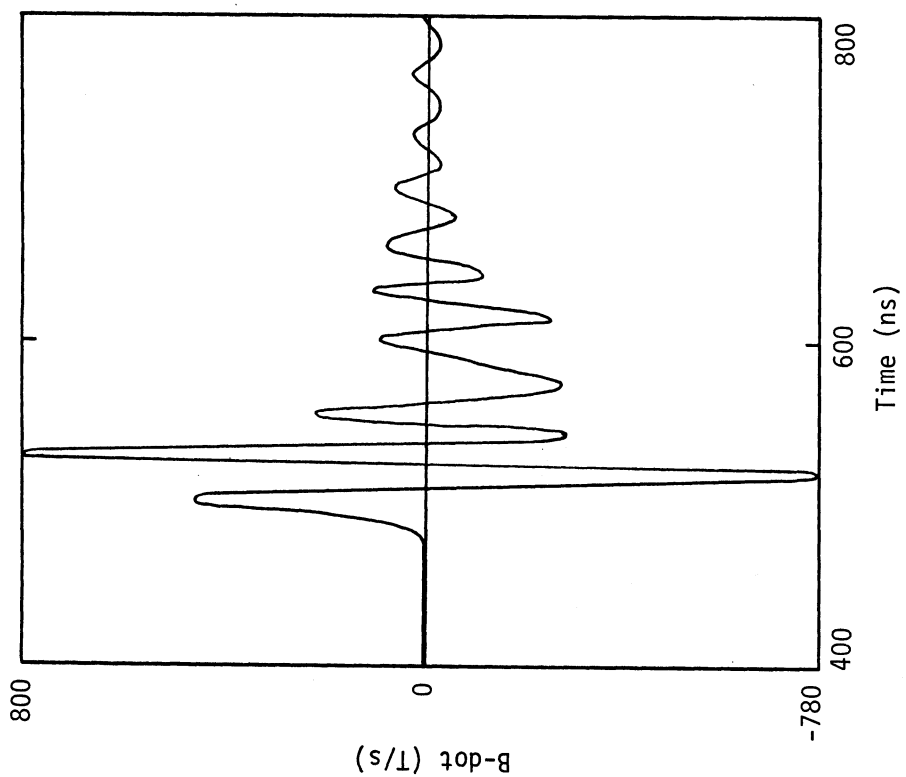


Figure 4.24d. B-dot at Longitudinal Fuselage Sensor Point

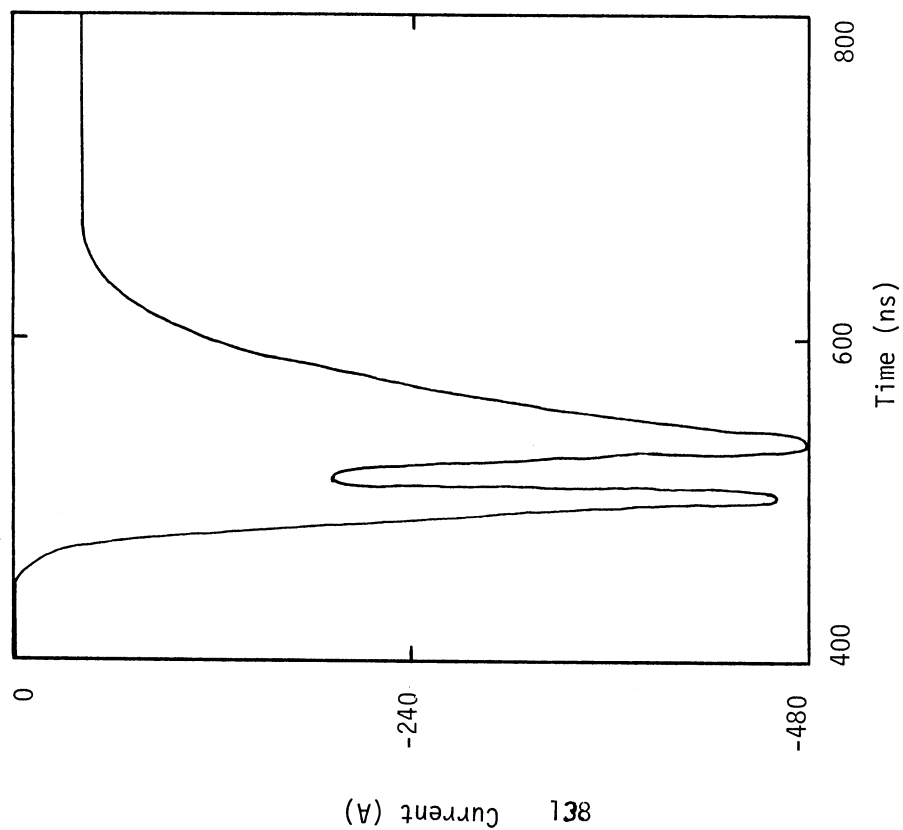


Figure 4.24e. Injected Current at Attachment Point

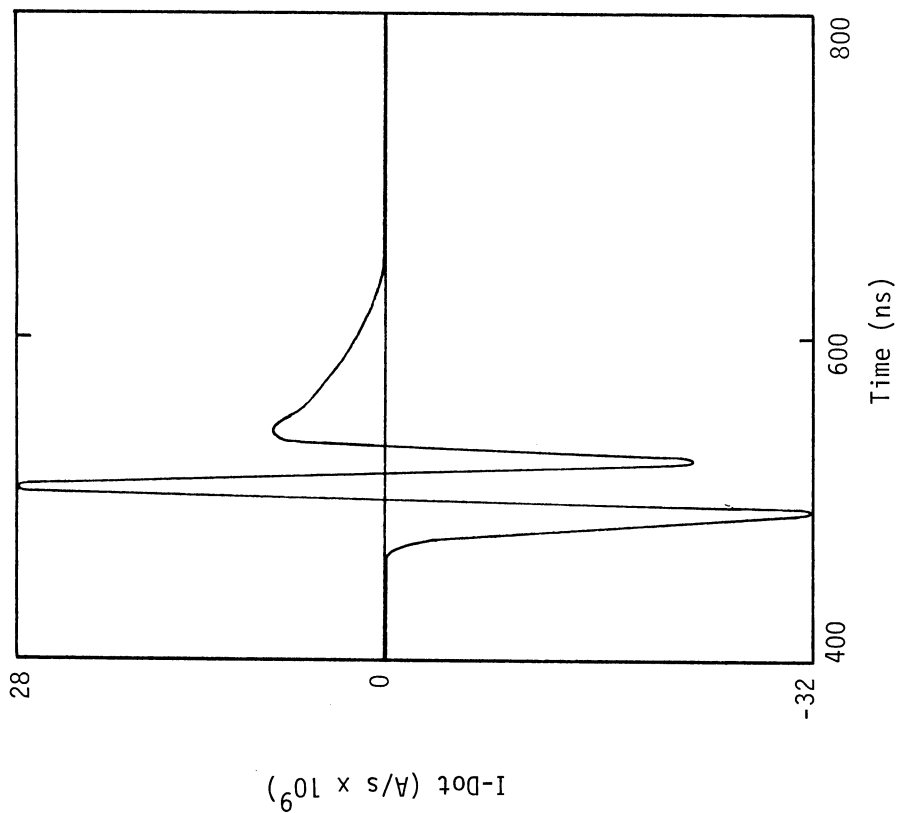


Figure 4.24f. I-dot at Attachment Point

Since the H and B-dot monitor locations are on the right side of the fuselage, these responses were expected to differ. The E and D-dot monitor locations, however, are also not exactly on the line of symmetry of the aircraft, because of finite differencing requirements. The actual location of these points is a quarter meter to the left of this line, and therefore approximately a half meter closer to the left wing attachment point. If these points were on the line of symmetry, no difference in E and D-dot response would be seen between left and right wing attachment.

The calculated nonlinear aircraft responses were also compared with the measured responses from 1982. The 1982 responses were used because of their time-coordinated character, which permits one to be sure that they were caused by the same lightning event. In particular, consider the measured D-dot and B-dot responses from Flight 82-039, shown in Figures 4.25 and 4.26, and the negative charge nose attachment of Figures 4.18b and 4.18d. Although the actual waveforms are different, the amplitudes and general character are very similar. By general character is meant lifetime of the response and also the time from peak to peak. In addition the calculated injected current of about 450 amperes is consistent within a factor of two of the linear current needed to produce the measured response, as found in Chapter 3. None of the other attachment points is able to reproduce both the measured D-dot and B-dot amplitudes, so it may be reasonably concluded that the measured records of Figures 4.25 and 4.26 came from a nose attachment. The observed differences in the detailed waveforms may be envisioned as resulting from a slightly different attachment point, lightning channel orientation, or line current waveform.

At present comparison of the measured data to nonlinear calculations is in a preliminary state. There is clearly no obvious technique for determining a current source such as that presented in Chapter 3 for the linear interaction. It may be necessary to begin by developing a data base of calculated nonlinear responses in order to recognize trends and tendencies in the measured data.

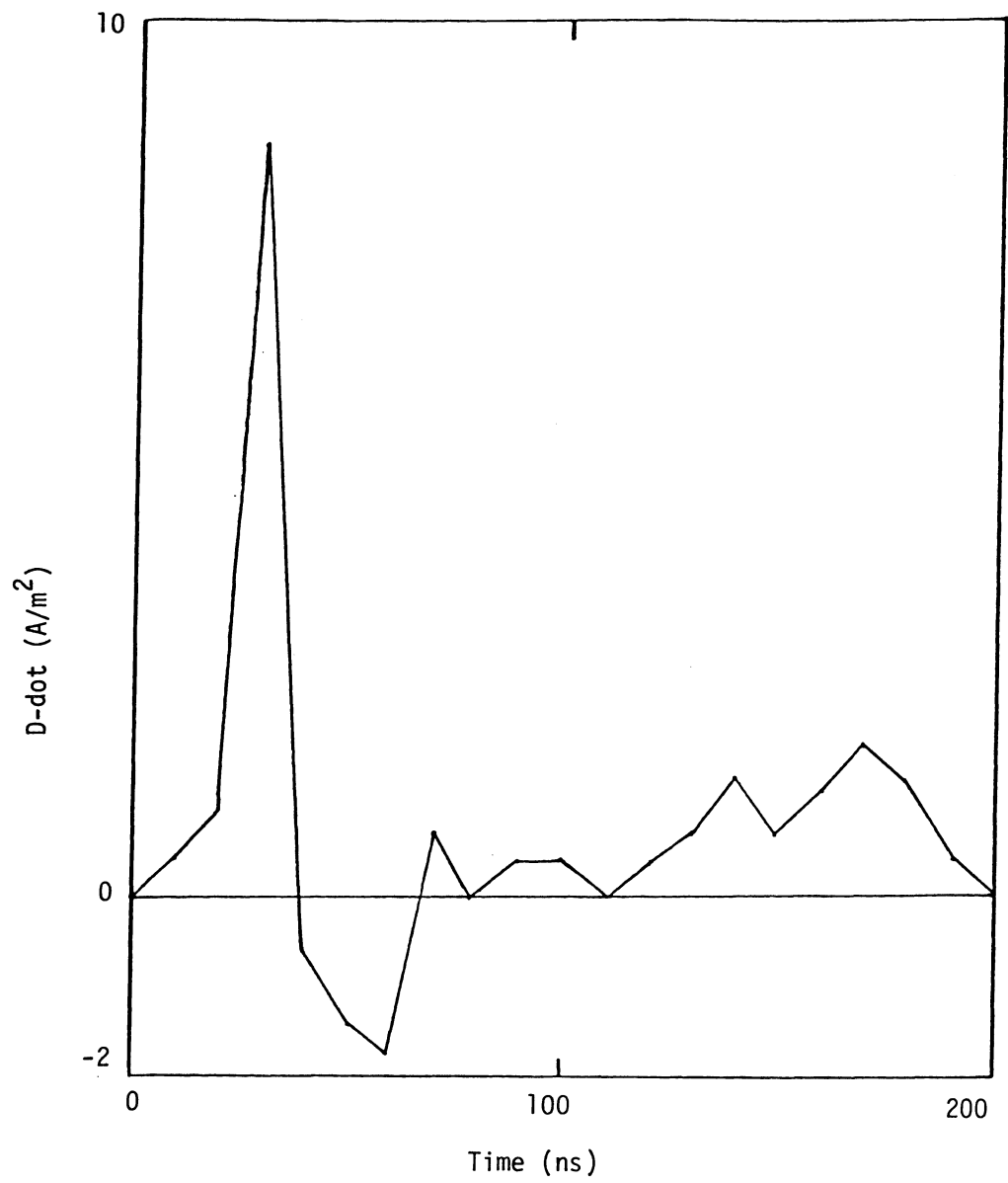


Figure 4.25 Measured D-dot of Flight 82-039

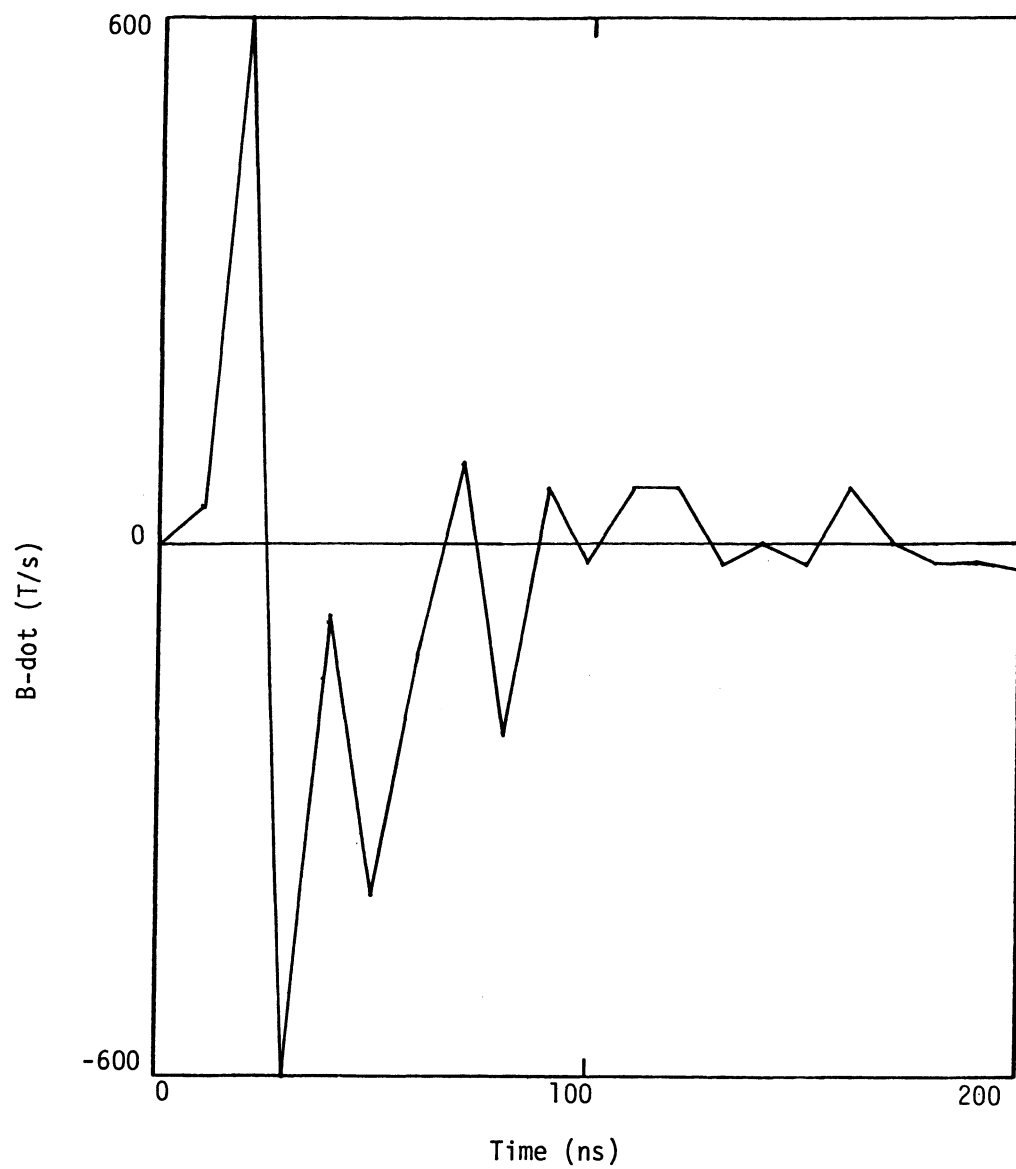


Figure 4.26 Measured B-dot of Flight 82-039

One encouraging note, however, is that on the basis of the small number of calculations that have been done so far it appears that linear and nonlinear analysis give approximately the same answer as far as the amplitude of the lightning current is concerned. If this could be established as true in general, analysis of the measured data would be greatly simplified.

CHAPTER 5

DISCUSSION AND RECOMMENDATIONS

5.0 Data Interpretation State of the Art

The research reported in the first four chapters is the continuation of initial efforts which were reported in [1]. The principal objective has been to develop a methodology whereby the lightning environment can be obtained from the measured data. A linear and time invariant approach based on a combination of Fourier transform and three dimensional finite difference techniques has been developed and demonstrated. This approach can obtain the lightning channel current in the absence of the aircraft for various channel characteristic impedances and resistive loading. When applied to a single measurement, however, the environment so obtained is not unique.

An interesting finding from this approach concerns the effect of the channel impedance on the response. From an environment interpretation point of view, it was found that the current waveform injected onto the aircraft is not greatly affected by the channel parameters, but that the channel current in the absence of the aircraft is.

Toward the end of this effort, time correlated 1982 B and D measurements were made available, and the approach was applied to one such data set. The results indicate that the initial selection of channel parameters (attach point, characteristic impedance, resistive loading, etc) did not reproduce both measurements simultaneously. Therefore more work needs to be done to understand simultaneous data.

In order to help with this problem the concept of response ratio was introduced. Ratios were computed for some measured and computed responses. Results are encouraging, although the concept needs to be more fully developed and applied.

It should be emphasized, however, that at this point there is no guarantee that linear analysis is sufficient to understand the

measured data. With this in mind, a nonlinear model of air breakdown based on air chemistry, photo-ionization, charge motion, and streamer theory has been developed and successfully compared with data published in the open literature. This model has been incorporated into the three-dimensional finite difference electromagnetic interaction model of the F106B aircraft. Attachment studies have been done for various parameters, and the results yield waveforms quite similar to, but not exactly the same as, those measured in flight. Indeed at the present time, it seems likely that the nonlinear attachment process could account for most of the in flight data obtained so far. More research and more simultaneous data is required to resolve the issue of whether or not the interaction can be successfully interpreted by linear analysis alone, or whether nonlinear modeling is required.

It should be noted here that the emphasis thus far has been on methodology and tool development. This includes the nonlinear model, the linear method development, and the concept of the response ratio. A major effort in future research will be to apply the methods to the data, especially the 1982 time correlated measurements.

5.1 Recommendations for Future Test Programs

a. Increased Dynamic Range

It has been shown in Chapter 2 how the digitization error limits the dynamic range of the data and thus its utility and accuracy in the data interpretation processes. Previous data has been obtained with a 6 bit recorder, and it is understood that an updated 8 bit version is planned. This will increase the available dynamic range by up to 12 dB, which should be a noticeable improvement.

b. Several Time Correlated Measurements

The 1982 data offers great hope in that \dot{B} , \dot{D} , and \dot{I} records caused by the same lightning event were obtained. However, the precise timing of these records with respect to each other is not known. It is desirable that several truly simultaneous measurements be made at widely separated (in space) measurement points. The relative timing of the records should be accurate to at least 10 ns, so that it can be

determined which record began first. Knowledge such as this would be greatly helpful in identifying attach and exit points.

c. Measurements of Fields

The data obtained on the surface of the aircraft consists of \dot{D} and \dot{B} measurements. It is difficult to determine the initial condition for these variables, but this makes a difference in the interpretation process. It is useful to know, for example, if the decrease in electric field is from a high level towards zero, or if it is from zero to a negative value. Thus, knowledge of the field levels themselves would be of great help.

d. Direct Strikes at Low Altitudes

Most of the data obtained thus far has been for relatively small events at high altitudes. It is certainly desirable to obtain data at lower elevations so that return stroke events can be recorded.

REFERENCES

1. Rudolph T.; and Perala, R.A., "Interpretation Methodology and Analysis of In-Flight Lightning Data," NASA CR-3590, October 1982.
2. Pitts, Felix, L.; and Thomas, Mitchel E.: 1981 Direct Strike Lightning Data. NASA TM-83273, 1982.
3. Turner, C.D.; and Trost, T.F.: "Laboratory Modeling and Analysis of Aircraft-Lightning Interaction," NASA CR-169455, August 1982.
4. Merewether, D.E.; and Fisher, R.: "Finite Difference Solution of Maxwell's Equation for EMP Applications." Electro-Magnetic Applications, Inc. (EMA), P.O.Box 8482, Albuquerque, NM 87198, Defense Nuclear Agency, DNA 5301F, April 1980.
5. Radasky, William, A.: "An Examination of the Adequacy of the Three Species Air Chemistry Treatment for the Prediction of Surface Burst EMP." Defense Nuclear Agency, DNA 3880T, Dec. 1975.
6. Gallimberti, I.: "The Mechanism of the Long Spark Formation," Journal de Physique, Colloque C7, supplément au No. 7, Tome 40, Juillet 1979.
7. Collins, M.M.C.; and Meek, J.M.: "Measurement of Field Changes Preceding Impulse Breakdown of Rod-Plane Gaps," Proceedings of the Seventh International Conference on Phenomena in Ionized Gases, August 22-27, Gradevinska Kujiga Publishing House, Belgrade, 22-27 August 1965.
8. Uman, M.A.; and Krider, E.P.: "Lightning Environment Modeling," Volume I of "Atmospheric Electricity Hazards Analytical Model Development and Application." Electro Magnetic Applications EMA 081-R-21, and AFWAL-TR-81-3084, August 1981. (Available from DTIC as AD A114 015.)
9. Uman, M.A.; and Krider, E.P.: "A Review of Natural Lightning: Experimental Data and Modeling," IEEE Transactions on Electromagnetic Compatibility, Vol. EMC-24, No.2, May 1982.

APPENDIX A

COMPARISON OF EXPERIMENTAL AND NUMERICAL RESULTS FOR THE INTERACTION OF A SCALE MODEL AIRCRAFT WITH A SIMULATED LIGHTNING CHANNEL*

R. A. Perala and T. H. Rudolph
Electro Magnetic Applications, Inc.
P. O. Box 26263
Denver, Colorado 80226

and

T. F. Trost and C. D. Turner
Department of Electrical Engineering
Texas Tech University
Lubbock, Texas 79409

Summary

Results are given which compare measured and computed responses for a scale model aircraft in a simulated attached lightning channel. A scale model of the NASA Langley F106 lightning research aircraft was suspended by a wire simulating the channel. A pulse was injected on the wire and subsequently interacted with the aircraft model. Sensors on the model recorded surface magnetic and electric field derivatives. Numerical simulations of this configuration were made with a three dimensional finite difference code for four entry/exit point configurations. Good agreement was obtained.

Introduction

One of the items of current interest in the lightning community is the knowledge of lightning's electromagnetic properties during a lightning/aircraft interaction event. This is of great importance because of the aircraft industry's move to new technologies such as digital fly by wire, advanced composite materials, and extensive use of low level integrated circuitry. Upset of digital circuits by lightning induced transients is therefore becoming a topic of increasing interest. Because of this concern, the NASA Langley Research Center has been sponsoring a research program to investigate the electromagnetic characteristics of natural lightning at aircraft altitudes. The principal means of accomplishing this investigation has been their F106 thunderstorm research aircraft which has been instrumented with electromagnetic sensors and recorders.^{1,2} The aircraft is flown into thunderstorms with the intent of being struck by lightning. Data on the interaction of the aircraft with both attached and nearby strikes has been obtained.³⁻⁶ In order to properly interpret the data, that is, to identify the nature of the lightning that cause the aircraft response, two accompanying supportive parallel efforts are being conducted. The first approach is experimental. A scale model of the F106 was constructed and suspended by wires which simulate the lightning channel. A pulse was injected up the wire and aircraft surface magnetic and electric field derivative responses were measured. The second approach involves numerical simulation of the scale model aircraft interaction by use of three dimensional finite difference solutions of Maxwell's equations. The results from the two approaches are then compared in order to enhance the understanding of the interaction process.

*Work performed under NASA Grant NAG 1-28 and contract NAS1-16489 and subcontract 1-43U-2094 to Research Triangle Institute.

Experimental Approach

An approximate scale model of the F-106B delta-wing aircraft has been constructed.⁷ The fuselage consists of a 3 foot length of aluminum cylinder, 4 inches in diameter. Flat end caps are machined to fit into each end and are secured with screws. The wings and tail are cut from 1/16 inch brass sheet to scale with the aluminum cylinder. The overall scale of the model is 1/18.8 of the actual F-106B.

The modeling apparatus is shown in Figure 1.

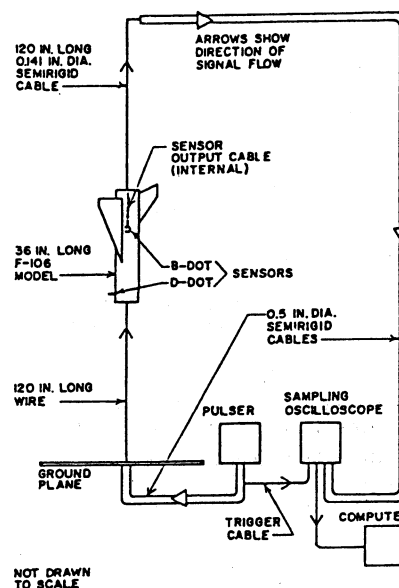


Figure 1 Apparatus for Aircraft-Lightning Modeling

A pulse of 0.75 ns duration is launched at the bottom of the lower wire. The magnetic (B) field measured six inches from the wire and 60 inches away from the model's nose is shown in Figure 2. To measure the resulting transient electromagnetic fields, time derivative sensors are used. Small B-dot (for longitudinal and transverse currents) and D-dot sensors have been placed on the model in the locations corresponding to their actual locations on the F-106B (on the fuselage over the starboard (axial current) and port wings (transverse current) and under the nose). The B-dot sensor is a loop made by bending 0.141 inch diameter semirigid coaxial cable into a 0.9 cm radius semicircle and cutting a gap in the outer conductor. The D-dot sensor is a monopole using a 1.65 cm wire.

The pulse travels up the lower wire, over the model, and on up the outer conductor of the upper wire, which is actually 0.141 coax. The sensor outputs are carried on the inside of this cable. No measurable leakage to the inside of the cable has been detected. When the top of the apparatus is reached, a transition is made to 0.5 inch diameter cable to complete the run back to the sampling oscilloscope. There, the waveforms are digitized and stored on magnetic disk. The equivalent risetime of the sampling scope is 25 ps. Although Figure 1 shows the attachment points in the center of the end caps, results have been obtained for other configurations as discussed in the last section.

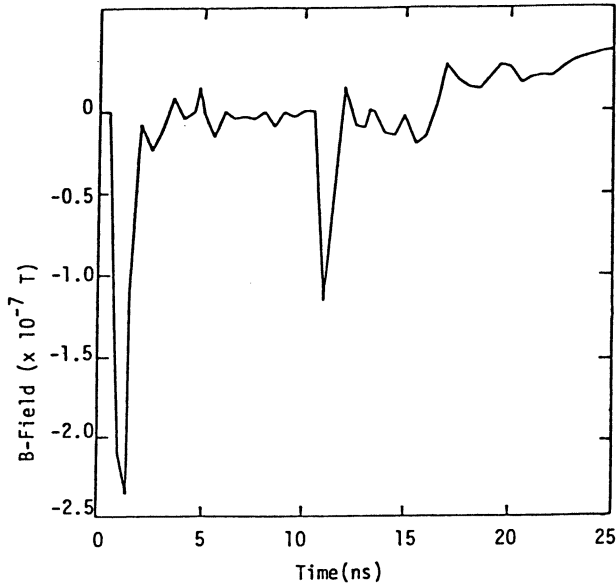


Figure 2 Magnetic Field Measured at a Radial Distance of 6 Inches from the Wire and 60 Inches from the Model Airplane's Nose

Numerical Approach

The numerical approach involves the use of a three dimensional time domain finite difference solution of Maxwell's equations in Cartesian coordinates. 9-12 The relationship of the numerical model geometry to the actual shape is shown in Figure 3.

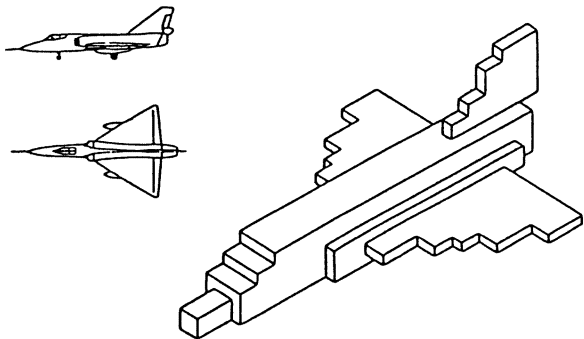


Figure 3 Three-Dimensional Finite Difference Model of F-106B

The spatial resolution of the solution space is one meter in the long dimension of the aircraft and one-half meter in the other two dimensions. The temporal step size is one nanosecond. The actual size of the solution space was chosen so that there are at least eight cells between any point on the aircraft and the boundary. The boundary conditions used on the outer boundary are the radiation boundary conditions of

Merewether.¹² Current was injected on the aircraft by specifying magnetic fields around the position of the input wire, and removed from the aircraft by zeroing a line of electric fields from the plane to the boundary at the position of the exit wire.

Figure 2, from which the injected current was deduced, needs further explanation. The measurement was taken at a point five feet from the nose of the model, and six inches from the wire, so the B field in the plot is an indication of the current at that point in the wire, which is not the same as the injected current. That this is true can be seen from the waveform of the B field, which shows a second peak approximately ten nanoseconds after the first peak. The ten nanosecond period corresponds to the travel time of the signal from the measuring point to the model and back, indicating that the second peak in Figure 2 is a reflection from the model travelling back along the wire. A reflection occurs at the injection point of the model because of the mismatch of impedances there. The model presents a lower impedance to the current than the wire does, and hence, more current is injected onto the model than is incident from the wire. This results in the reflected wave seen in the second peak of the plot. The actual injected current must then be determined from the sum of the two peaks, and not by the waveform of Figure 2 as it stands. For these studies the injected current was deduced by shifting the maximum of the second pulse of Figure 2 to the time position of the first maximum and then summing point by point.

A difficulty which arose in the analysis was in how to accurately determine the injected current from the magnetic field measurement. The most obvious way is to assume the simple expression $B(t) = \mu_0 I(t) / 2\pi r$, where r is the perpendicular distance of the measurement point from the wire. But this is really a magnetostatic assumption and at least requires that the pulse width be a much greater than the signal travel time from the wire to the measuring point. In the present case the pulse width is about .75 nanoseconds and the travel time is .5 nanoseconds, so the requirement is not satisfied. In order to solve the problem more accurately, an integral expression can be derived from the current in terms of the magnetic field.¹⁴ This approach is complex, and it would have required a significant amount of time to unfold the true current from the measured field. It was determined that the cost in time was not justified and the decision was made to use the simple formula $B(t) = \mu_0 I(t) / 2\pi r$, even though it may not be as accurate as one would like. Further measurements of the magnetic field closer to the wire are planned, but are not yet available.

Results and Conclusions

Results were compared for the four aircraft entry - exit point configurations shown in Figure 4. A comparison of the amplitudes of the initial peak is given in Table 1. Overlays of measured and computed results are shown in Figures 5 and 6.

The results show that in every case there is at least reasonable agreement between waveform shapes and in several cases the agreement is quite good.

Looking specifically at the measured waveforms of B_L and D for the nose-tail and nose-wing cases, one can observe reflections of the incident pulse from the trailing edge of the wing and from the rear of the fuselage (and trailing edge of the tail). These occur about 2.5 and 3.5 ns, respectively, after the incident pulse in B_L and about 5.0 and 5.2 ns after the pulse

in D . As the rear wire is moved from the fuselage to the wing tip, the reflections from these two locations are altered, the reflection from the trailing edge of the wings changing from being larger to being smaller than the reflection from the fuselage. This is expected because the wire carries away some of the current from the point to which it is attached, thus giving a smaller reflection.

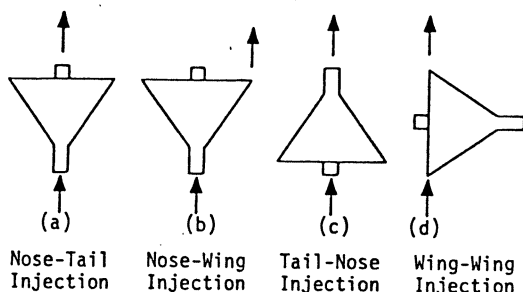


Figure 4 Aircraft Entry-Exit Point Configurations

Table 1 Comparison of Amplitudes of Initial Peaks, and Ratio in dB

	NOSE-TAIL			NOSE-WING			TAIL-NOSE			WING-WING		
	MEAS	NUM	dB	MEAS	NUM	dB	MEAS	NUM	dB	MEAS	NUM	dB
$B_L (1/s)$	560	343	4.3	540	343	3.9	250	89	11	340	184	5.3
$B_L (10^{-9}T)$	222	192	1.3	222	192	1.3	126	77	4.3	140	101	2.8
$B_T (1/s)$	125	192	3.7	122	192	3.9	150	165	.8	240	193	1.9
$B_T (10^{-9}T)$	50	102	6	51	102	6	62	100	4.8	112	102	.8
$D (C/m^2 \cdot s)$	7.2	5.9	1.7	7.2	5.9	1.7	3.6	.97	11.4	2.5	2.0	1.9
$D (10^{-9} C/m^2)$	2.2	2.6	1.5	2.2	2.6	1.5	1.1	.83	2.4	1.1	1.7	3.8

The results for the calculated B_L and D waveforms show less change in the reflections between these two cases evidently indicating somewhat less sensitivity to the location of the rear wire. For B_L , the reflection from the rear of the fuselage is decreased a bit in the nose-tail case, and for D there is no change.

The amplitude comparisons of Table 1 show an average agreement of 3.6 dB. It is noted that the B_T and B_L comparisons are usually the most divergent, which may indicate an unusual difficulty in the measurement or numerical technique at that location. The large differences of 11 dB are in two cases only. If these two 11 dB differences are not included, the average value of the absolute difference between measured and predicted peak amplitudes is 2.9 dB.

There are errors in both the measured and numerical results, although it is generally difficult to assign exact values. The measurement error in amplitude is expected to be less than 2 dB, and one could easily account for similar values for the numerical technique.

The main sources of error in the measured fields include the uncertainties in amplitude and time-base calibration of the sampling oscilloscope, the uncertainties in the sensitivities of the D-dot and B-dot sensors and the bandwidth limitations of the sensors and coaxial cables. The sensitivities of the sensors have been measured in a biconical transmission line calibrator which was constructed for this purpose. Smaller errors are introduced by digitization (12 bit A/D converter), timing, and noise ($S/N > 40 \text{ dB}^7$).

Errors in the numerical approach chiefly come from: 1) imperfect boundary conditions at the finite difference mesh outer boundary, 2) uncertainty in the exact knowledge of the input current waveform, 3) approximations associated with the ability to exactly model the aircraft shape with cell sizes $1m \times .5m \times .5m$. This also indicates some uncertainty in computing responses at exactly the corresponding locations used for the measured data.

The results are therefore felt to generally compare within experimental and numerical errors. The comparison therefore gives confidence that these methods can be applied to the F-106B data interpretation problem with the hope that valid conclusions about lightning interaction with aircraft can be made.

Acknowledgement

The authors would like to thank Mr. Felix Pitts, M.E. Thomas and K.P. Zaepfel of NASA Langley Research Center for their suggestions and encouragement regarding this project.

References

1. Thomas, Robert, M., Jr.: Expanded Interleaved Solid-State Memory for a Wide Bandwidth Transient Waveform Recorder. Lightning Technology, NASA CP-2128, 1980, pp. 119-129.
2. Pitts, F.L., et.al.: In-Flight Lightning Characteristics Measurements System. Federal Aviation Administration - Florida Institute of Technology Workshop on Grounding and Lightning Technology, FAA-RD-79-6, March 1979, pp. 105-111.
3. Pitts, Felix, L. and Mitchel E. Thomas: Initial Direct Strike Lightning Data. NASA TM-81867, 1980.
4. Pitts, Felix, L., "Electromagnetic Measurement of Lightning Strikes to Aircraft," AIAA Journal of Aircraft, Vol. 19, No.3, March 1982, p.246.
5. Pitts, Felix, L., and Mitchel E. Thomas: 1980 Direct Strike Lightning Data. NASA TM-81946, 1981.
6. Pitts, Felix, L., and Mitchel E. Thomas: 1981 Direct Strike Lightning Data. NASA TM-83273, 1982.
7. Trost, T.F. and C.D. Turner, "Transient Electromagnetic Fields on a Delta Wing Aircraft Model with Injected Currents," Proceedings of the International Aerospace Conference in Lightning and Static Electricity, St. Catherine's College, Oxford, 28 March 1982.
8. Baum, C.E., et.al., IEEE Transactions on Antennas and Propagation AP-26, (1), 22-35 (1978).
9. F. J. Eriksen, Rudolph, T.H., and R.A. Perala, "Electromagnetic Coupling Modeling of the Lightning/Aircraft Interaction Event," Volume III of "Atmospheric Electricity Hazards Analytical Model Development and Application," EMA-81-R-21, April, 1981.
10. Rymes, M.D., "T3DFD User's Manual," EMA-81-R-24, April 1981.

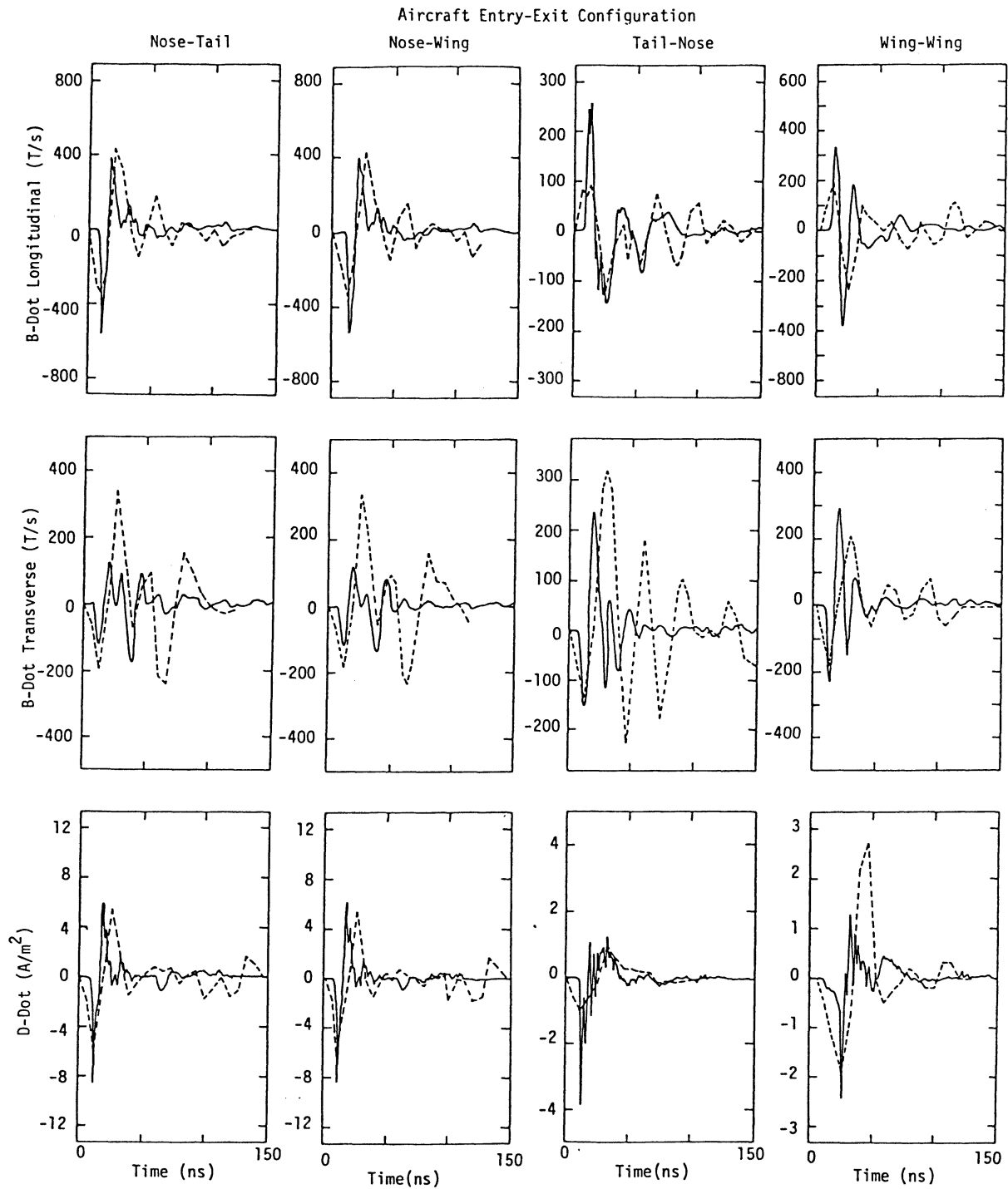


Figure 5 Overlays of Measured and Predicted Derivative Responses
(Predicted Responses Appear as Dashed Lines)

Aircraft Entry-Exit Configuration

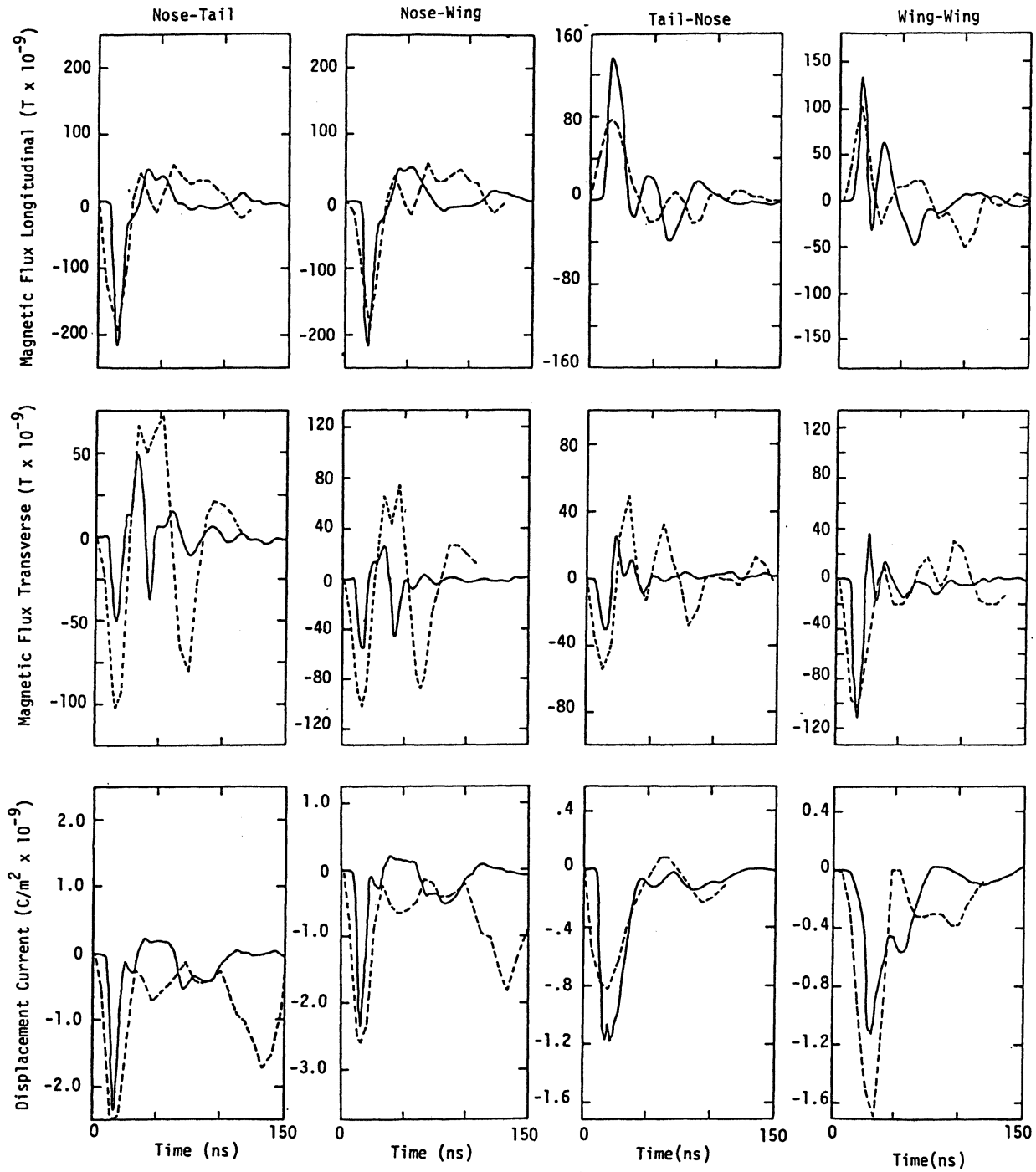


Figure 6. Overlays of Measured and Predicted Responses
(Predicted Responses Appear as Dashed Lines)

11. Yee, K.S., "Numerical Solution of Initial Boundary Value Problems Involving Maxwell's Equations in Isotropic Media," IEEE Transactions Ant. & Propagat., AP-14, May 1966, pp. 302-307.
12. Merewether, D.E. and R. Fisher, "Finite Difference Solution of Maxwell's Equation for EMP Applications," Report EMA-79-R-4 (Revised), Electro Magnetic Applications, Inc. (EMA), P.O. Box 8482 Albuquerque, NM 87198, 22 April 1980.
13. Perala, R.A., F.J. Eriksen, and T.H. Rudolph, "Electromagnetic Interaction of Lightning with Aircraft," IEEE Transactions, Electromagnetic Compatibility, May, 1982.
14. Harrington, R.F., Time Harmonic Electromagnetic Fields, McGraw-Hill: New York, 1971, p.34.

APPENDIX B

FOURIER TRANSFORM TECHNIQUE

The convention adopted for the Fourier transform used in the analysis is the following:

$$\text{Time to frequency: } F(\omega) = \int_{-\infty}^{\infty} f(t') e^{-j\omega t'} dt' \quad (\text{B-1})$$

$$\text{Frequency to time: } f(t) = \frac{1}{2\pi} \int_{-\infty}^{\infty} F(\omega') e^{j\omega' t} d\omega' \quad (\text{B-2})$$

For the time to frequency transform it is assumed that $f(t)$ is nonzero for only a finite time, $0 < t < \tau$, and is represented in this interval as a sequence of uniformly spaced points; $f_0, f_1, f_2, \dots, f_N$, where the uniform temporal spacing is Δt . It is also assumed that the sequence of points is chosen such that $f_0 = f_N = 0$. The function $f(t)$ is constructed from the points f_0, f_1, \dots, f_N , by connecting the points with straight lines. Therefore $f(t)$ is a continuous function with discontinuous derivative at each of the points f_0, f_1, \dots, f_N .

Equation (B-1) can be integrated by parts to yield,

$$F(\omega) = -\frac{f(t)}{j\omega} e^{-j\omega t} \Big|_0^\tau + \frac{1}{j\omega} \int_0^\tau f'(t') e^{-j\omega t'} dt'. \quad (\text{B-3})$$

But $f(\tau) = f_N = 0$ and $f(0) = f_0 = 0$, so,

$$F(\omega) = \frac{j}{\omega} \int_0^\tau f'(t') e^{-j\omega t'} dt'. \quad (\text{B-4})$$

Breaking the interval $0 < t < \tau$ into segments of length Δt ,

$$F(\omega) = \frac{j}{\omega} \sum_{n=0}^{N-1} \int_{t_n}^{t_{n+1}} f'(t') e^{-j\omega t'} dt'. \quad (\text{B-5})$$

Now $f'(t')$ is a constant for each interval and can be removed from the integral.

$$F(\omega) = \frac{j}{\omega} \sum_{n=0}^{N-1} f'_n \int_{t_n}^{t_{n+1}} e^{-j\omega t'} dt', \quad (\text{B-6})$$

where $f'_n \equiv \frac{f_{n+1} - f_n}{\Delta t}$.

The remaining integral can now be performed to give,

$$\begin{aligned}
 F(\omega) &= -\frac{j}{\omega} \sum_{n=0}^{N-1} f_n' \left(-\frac{1}{j\omega} \right) (e^{-j\omega t_{n+1}} - e^{-j\omega t_n}) \\
 &= \frac{1}{\omega} \sum_{n=0}^{N-1} f_n' e^{-j\omega t_n} (e^{-j\omega \Delta t} - 1) \\
 F(\omega) &= \frac{1}{\omega^2 \Delta t} (e^{-j\omega \Delta t} - 1) \sum_{n=0}^{N-1} (f_{n+1} - f_n) e^{-j\omega t_n} \quad (B-7)
 \end{aligned}$$

Note that $t_n = n\Delta t$ and $e^{-j\omega \Delta t}$ is a constant at each frequency, so that, defining $x \equiv e^{-j\omega \Delta t}$,

$$F(\omega) = \frac{x-1}{\omega^2 \Delta t} \sum_{n=0}^{N-1} (f_{n+1} - f_n) x^n. \quad (B-8)$$

The transform has thus been reduced to the evaluation of a polynomial at each frequency. Equation (B-8) is the form of the time to frequency transform which has been implemented for the analysis in this report. It should be noted that $F(\omega)$ as represented in Equation (B-8) is exact and known at all frequencies. This has come about because of the definition of $f(t)$ as a collection of straight line segments, which makes $f(t)$ known at all times. In reality the value of $f(t)$ is completely unknown except at the discrete points f_0, f_1, \dots, f_N . Hence, to avoid aliasing, Equation (B-8) should be trusted only in the range $\omega \leq \pi/\Delta t$. This ensures that at least two of the discrete known points of $f(t)$ will fall within the period $2\pi/\omega$.

The frequency to time transform, Equation (B-2), is implemented in much the same fashion as the time to frequency transform. It is complicated by a pair of things. First, $F(\omega)$ is in general nonzero as $\omega \rightarrow \infty$, so the integration in Equation (B-2) cannot in principle be truncated at some large ω_N . However, in practice, the contribution of frequencies beyond ω_N to the integral is usually very small, so Equation (B-2) is approximated by,

$$f(t) = \frac{1}{2\pi} \int_{-\infty}^{\infty} F(\omega') e^{j\omega' t} d\omega' \approx \frac{1}{2\pi} \int_{-\omega_N}^{\omega_N} F(\omega') e^{j\omega' t} d\omega'. \quad (B-9)$$

The second complication is that the discrete frequency points one is usually dealing with, F_0, F_1, \dots, F_N , are not in general uniformly spaced. This means that the final form of the frequency to time transform will not be as simple as that of the time to frequency transform.

To implement the frequency to time transform assume that the discrete points are known: $F_0, F_1, F_2, \dots, F_N$, where $F_0 = F(\omega_0)$, $F_1 = F(\omega_1)$, \dots , $F_N = F(\omega_N)$. Also choose ω_N large enough so that $F_N \approx 0$.

The first step in the implementation of Equation (B-9) is to eliminate the integration over the negative frequencies. Note first that from Equation (B-1), $F(-\omega) = \bar{F}(\omega)$, where the bar indicates complex conjugate.

$$\begin{aligned}
 f(t) &= \frac{1}{2\pi} \int_{-\omega_N}^{\omega_N} F(\omega') e^{j\omega' t} d\omega' \\
 &= \frac{1}{2\pi} \int_{-\omega_N}^0 F(\omega') e^{j\omega' t} d\omega' + \frac{1}{2\pi} \int_0^{\omega_N} F(\omega') e^{j\omega' t} d\omega' \\
 &= -\frac{1}{2\pi} \int_0^{\omega_N} F(-\omega') e^{-j\omega' t} d\omega' + \frac{1}{2\pi} \int_0^{\omega_N} F(\omega') e^{j\omega' t} d\omega' \\
 f(t) &= \frac{1}{2\pi} \int_0^{\omega_N} [\bar{F}(\omega') e^{-j\omega' t} + F(\omega') e^{j\omega' t}] d\omega'. \quad (B-10)
 \end{aligned}$$

$$\text{But } \bar{F}(\omega') e^{-j\omega' t} + F(\omega') e^{j\omega' t} = 2 \operatorname{Real} \{F(\omega') e^{j\omega' t}\}.$$

Therefore,

$$f(t) = \frac{1}{\pi} \operatorname{Real} \left\{ \int_0^{\omega_N} F(\omega') e^{j\omega' t} d\omega' \right\}. \quad (B-11)$$

From this point the development proceeds as in the time to frequency transform.

$$\begin{aligned}
 f(t) &= \frac{1}{\pi} \operatorname{Real} \left\{ \left. \frac{F(\omega')}{jt} e^{j\omega' t} \right|_0^{\omega_N} + \frac{1}{jt} \int_0^{\omega_N} F'(\omega') e^{j\omega' t} d\omega' \right\} \\
 &= \frac{1}{\pi} \operatorname{Real} \left\{ \frac{F(0)}{jt} + \frac{1}{jt} \sum_{n=0}^{N-1} F_n' \int_{\omega_n}^{\omega_{n+1}} e^{j\omega' t} d\omega' \right\} \\
 &= \frac{1}{\pi} \operatorname{Real} \left\{ \frac{F_0}{jt} - \frac{1}{t^2} \sum_{n=0}^{N-1} F_n' (e^{j\omega_{n+1} t} - e^{j\omega_n t}) \right\} \\
 f(t) &= -\frac{1}{\pi t} \operatorname{Real} \left\{ j F_0 + \frac{1}{t} \sum_{n=0}^{N-1} \frac{F_{n+1} - F_n}{\omega_{n+1} - \omega_n} (e^{j\omega_{n+1} t} - e^{j\omega_n t}) \right\} \quad (B-12)
 \end{aligned}$$

This is the form of the frequency to time transform that has been implemented for the analysis in this report. Note that Equation (B-12) is really an approximation because of the truncation of the integral in Equation (B-2) at ω_N .

1. Report No. NASA CR-3746		2. Government Accession No.		3. Recipient's Catalog No.	
4. Title and Subtitle LINEAR AND NONLINEAR INTERPRETATION OF THE DIRECT STRIKE LIGHTNING RESPONSE OF THE NASA F106B THUNDERSTORM RESEARCH AIRCRAFT				5. Report Date December 1983	
				6. Performing Organization Code	
7. Author(s) T. H. Rudolph and R. A. Perala				8. Performing Organization Report No. EMA-83-R-21	
9. Performing Organization Name and Address Electro Magnetic Applications, Inc. P. O. Box 26263 Denver, CO 80226				10. Work Unit No.	
				11. Contract or Grant No. NAS1-16984	
12. Sponsoring Agency Name and Address National Aeronautics and Space Administration Langley Research Center Hampton, Virginia 23665				13. Type of Report and Period Covered Contractor Report	
				14. Sponsoring Agency Code	
15. Supplementary Notes Langley technical monitor: Felix L. Pitts Final Report					
16. Abstract The objective of the work reported here is to develop a methodology by which electro-magnetic measurements of inflight lightning stroke data can be understood and extended to other aircraft. A linear and time invariant approach based on a combination of Fourier transform and three dimensional finite difference techniques is demonstrated. This approach can obtain the lightning channel current in the absence of the aircraft for given channel characteristic impedance and resistive loading. The model is applied to several measurements from the NASA F106B lightning research program. A non-linear three dimensional finite difference code has also been developed to study the response of the F106B to a lightning leader attachment. This model includes three species air chemistry and fluid continuity equations and can incorporate an experimentally based streamer formulation. Calculated responses are presented for various attachment locations and leader parameters. The results are compared qualitatively with measured inflight data.					
17. Key Words (Suggested by Author(s)) Lightning Electromagnetic Finite Difference Coupling Air Chemistry Maxwell's Equations Non-linear Modeling Data Analysis Attachment				18. Distribution Statement Unclassified - Unlimited RESTRICTED Subject Category 47	
19. Security Classif. (of this report) Unclassified		20. Security Classif. (of this page) Unclassified		21. No. of Pages 168	
22. Price					